frontiers | Research Topics

Disorder and superconductivity: A 21st-century update

Edited by
Ruslan Prozorov, James Avery Sauls, Nigel Hussey,
Peter Hirschfeld and Maria Iavarone

Published in
Frontiers in Physics

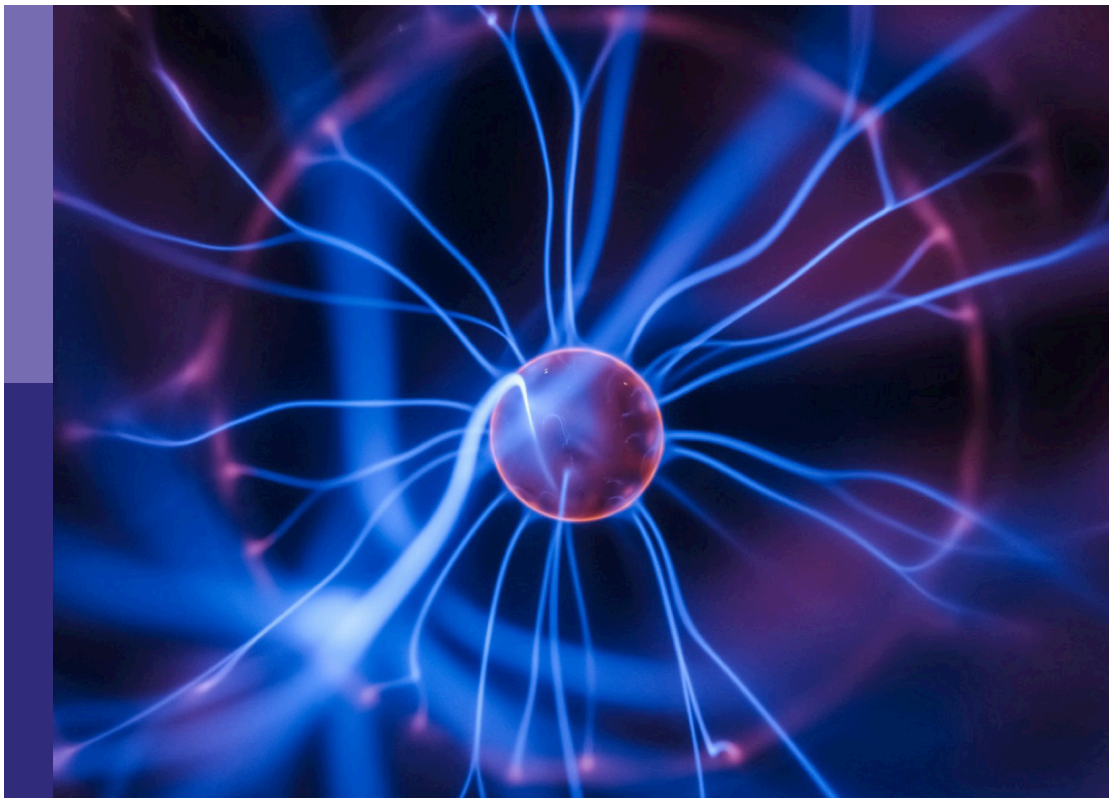

ISSN 1664-8714
ISBN 978-2-8325-5462-3
DOI 10.3389/978-2-8325-5462-3

About Frontiers

Frontiers is more than just an open access publisher of scholarly articles: it is a pioneering approach to the world of academia, radically improving the way scholarly research is managed. The grand vision of Frontiers is a world where all people have an equal opportunity to seek, share and generate knowledge. Frontiers provides immediate and permanent online open access to all its publications, but this alone is not enough to realize our grand goals.

Frontiers journal series

The Frontiers journal series is a multi-tier and interdisciplinary set of open-access, online journals, promising a paradigm shift from the current review, selection and dissemination processes in academic publishing. All Frontiers journals are driven by researchers for researchers; therefore, they constitute a service to the scholarly community. At the same time, the *Frontiers journal series* operates on a revolutionary invention, the tiered publishing system, initially addressing specific communities of scholars, and gradually climbing up to broader public understanding, thus serving the interests of the lay society, too.

Dedication to quality

Each Frontiers article is a landmark of the highest quality, thanks to genuinely collaborative interactions between authors and review editors, who include some of the world's best academicians. Research must be certified by peers before entering a stream of knowledge that may eventually reach the public - and shape society; therefore, Frontiers only applies the most rigorous and unbiased reviews. Frontiers revolutionizes research publishing by freely delivering the most outstanding research, evaluated with no bias from both the academic and social point of view. By applying the most advanced information technologies, Frontiers is catapulting scholarly publishing into a new generation.

What are Frontiers Research Topics?

Frontiers Research Topics are very popular trademarks of the *Frontiers journals series*: they are collections of at least ten articles, all centered on a particular subject. With their unique mix of varied contributions from Original Research to Review Articles, Frontiers Research Topics unify the most influential researchers, the latest key findings and historical advances in a hot research area.

Find out more on how to host your own Frontiers Research Topic or contribute to one as an author by contacting the Frontiers editorial office: frontiersin.org/about/contact

Disorder and superconductivity: A 21st-century update

Topic editors

Ruslan Prozorov — Iowa State University, United States
James Avery Sauls — Louisiana State University, United States
Nigel Hussey — University of Bristol, United Kingdom
Peter Hirschfeld — University of Florida, United States
Maria Iavarone — Temple University, United States

Citation

Prozorov, R., Sauls, J. A., Hussey, N., Hirschfeld, P., Iavarone, M., eds. (2024). *Disorder and superconductivity: A 21st-century update*. Lausanne: Frontiers Media SA.
doi: 10.3389/978-2-8325-5462-3

Table of contents

frontiers | Frontiers in Physics

TYPE Editorial
PUBLISHED 26 August 2024
DOI 10.3389/fphy.2024.1478445

OPEN ACCESS

EDITED AND REVIEWED BY
Matthias Eschrig,
University of Greifswald, Germany

*CORRESPONDENCE
Ruslan Prozorov,
prozorov@iastate.edu

RECEIVED 09 August 2024
ACCEPTED 19 August 2024
PUBLISHED 26 August 2024

CITATION
Prozorov R, Sauls JA, Hirschfeld P, Hussey NE and Iavarone M (2024) Editorial: Disorder and superconductivity: a 21st-century update. *Front. Phys.* 12:1478445.
doi: 10.3389/fphy.2024.1478445

Editorial: Disorder and superconductivity: a 21st-century update

Ruslan Prozorov[1]*, James Avery Sauls[2], Peter Hirschfeld[3], Nigel E. Hussey[4] and Maria Iavarone[5]

[1]Department of Physics and Astronomy, Iowa State University, Ames, IA, United States, [2]Department of Physics and Astronomy, Hearne Institute of Theoretical Physics, Louisiana State University, Baton Rouge, LA, United States, [3]Department of Physics, University of Florida, Gainesville, FL, United States, [4]School of Physics, University of Bristol, Bristol, United Kingdom, [5]Department of Physics, Temple University, Philadelphia, PA, United States

KEYWORDS

supeconductivity, supercondcutors, disorder, disorder-compounds, high-T_C

Editorial on the Research Topic
Disorder and superconductivity: a 21st-century update

Studying defects and imperfections in superconductors is paramount for fundamental and applied research. Defects play a multifaceted role, from decreasing quality and performance in some situations to enhancing desired properties in others. Disorder is also a unique probe to study the fundamental aspects of superconductivity. In classical s-wave isotropic superconductors, only pair-breaking (magnetic) scattering suppresses the order parameter, hence the transition temperature, T_c. In superconductors with an anisotropic gap, both potential and pair-breaking scattering suppress T_c, and in unconventional superconductors, the non-magnetic disorder can suppress superconductivity completely. Understanding the mechanisms through which defects influence the properties of superconductors is key to advancing the development and optimization of high-performance superconducting materials for modern technologies.

This Frontiers of Physics Research Topic–"*Disorder and superconductivity: a 21st-century update*"–contains an open-access Research Topic of three review articles and five original research articles highlighting several aspects of this broad area of modern research.

Alloul reviews the paramount role of disorder in determining some normal- and superconducting-state properties of high-T_c cuprate superconductors, in particular its effect on the T-doping phase diagram. Focusing on $YBa_2Cu_3O_{7-x}$ as the least disordered cuprate in the pristine state, controlled defects were introduced by spinless (Zn, Li) impurities substituted on the planar Cu sites. Another type of atomic disorder was introduced by electron irradiation. The review focuses on the Kondo-like physics emerging due to disorder and its connection to pseudogap and strange metal phases, and the use of isolated impurities to probe the correlations in the surrounding pure host.

Andersen et al. review spontaneous time-reversal symmetry breaking (TRSB) by disorder in superconductors. They discuss the possible nature of the superconducting ground state in materials where such TRSB was observed. While the most straightforward explanation comes from considering at least two different superconducting order parameters, it is shown that even in the case of a single order parameter TRSB may

occur locally due to localized orbital current patterns or spin-polarization near atomic-scale impurities, twin boundaries and other defects.

Mishra et al. both present new data and review existing data on the thermal conductivity of nonunitary triplet superconductors with specific application to UTe_2. Thermal conductivity is a unique bulk probe of nodal quasiparticles and in this paper the authors derive a general expression for the thermal conductivity of a spin triplet superconductor. By varying the direction of the heat flow it is possible to map out the structure of the order parameter, and particularly distinguish between line and point nodes. Their analysis is assisted by comparing theory to samples with varying levels of disorder.

Juskus et al. highlight the apparent insensitivity of T_c to residual resistivity in various single-layered cuprates. By analyzing the results of T_c suppression in Bi2201, LSCO and Tl2201, the authors suggest that either we do not understand the origins of residual resistivity in cuprates or that the accepted paradigm of dirty d-wave theory may be invalid. The authors then present an alternative, non-BCS interpretation for the different extents of the superconducting dome in the three cuprate families.

Curro et al. study critical dynamics near the quantum phase transition in $TmVO_4$ where ferroquadrupolar order is suppressed by a magnetic field and identify a unique form of the hyperfine coupling that exclusively probes the transverse field susceptibility. The results show that this quantity diverges at the critical field, in contrast to the mean-field prediction. Further analysis suggests the presence of quantum Griffiths phases. This form of inhomogeneous and correlated disorder is largely absent from theories of disordered superconductivity, except for superfluidity of ^3He in dilute random solids like silica aerogels.

Ngampruetikorn and Sauls develop a theory of thermal transport and anomalous thermal Hall effect as well as electrical conductivity for chiral superconductors belonging to even or odd-parity E_1 and E_2 representations of the tetragonal and hexagonal point groups. Chiral superconductors exhibit novel properties that depend on the topology of the order parameter and Fermi surface, and, importantly for our Research Topic, the structure of the impurity potential. An anomalous thermal Hall effect is predicted and shown to be sensitive to the winding number, ν, of the chiral order parameter via Andreev scattering. For heat transport in a chiral superconductor with point-like impurities, a transverse heat current is obtained for $\nu = \pm 1$, but vanishes for $|\nu| > 1$. Their theory provides quantitative formulae for analyzing and interpreting thermal transport measurements for superconductors with broken time-reversal and mirror symmetries.

Wang et al. present their experimental results on zinc-doped $Bi_2Sr_2CaCu_2O_{8+x}$ high-T_c cuprate superconductor. Zinc exchanged for copper strongly suppresses superconductivity and acts as impurities with a strong quasiparticle scattering resonance. Using scanning tunneling microscopy, they investigate the electronic structure on the atomic scale around a Zn impurity. They conclude that the measured impurity-induced bound state pattern is strongly influenced by Bi atoms on the surface and therefore supports the "filter" theoretical model of the nonlocal interlayer tunneling effect from the CuO_2 layer to the BiO layer on the surface.

Finally, Torsello et al. report unusually weak proton irradiation effects in the anisotropic superconductor $RbCa_2Fe_4As_4F_2$ with unusual properties in between those of the iron-based pnictides and the high-T_c cuprates. Combining a coplanar waveguide resonator technique with electrical transport and point-contact Andreev reflection spectroscopy, they study the effect of structural disorder on the critical temperature, the superfluid density and the superconducting gap. They find an unusually weak dependence of the superconducting properties on the amount of disorder in this material when compared to other iron-based superconductors under comparable irradiation conditions. Surprisingly, the nodal order parameter of $RbCa_2Fe_4As_4F_2$ is also robust against proton irradiation, with a two-band d-d model being the one that best fits the experimental data.

Author contributions

RP: Writing–original draft, Writing–review and editing. JS: Writing–original draft, Writing–review and editing. PH: Writing–original draft, Writing–review and editing. NH: Writing–original draft, Writing–review and editing. MI: Writing–original draft, Writing–review and editing.

Funding

The author(s) declare that no financial support was received for the research, authorship, and/or publication of this article.

Conflict of interest

The authors declare that the research was conducted in the absence of any commercial or financial relationships that could be construed as a potential conflict of interest.

Publisher's note

frontiers | Frontiers in Physics

TYPE Original Research
PUBLISHED 11 January 2024
DOI 10.3389/fphy.2023.1337271

OPEN ACCESS

EDITED BY
Ruslan Prozorov,
Iowa State University, United States

REVIEWED BY
Yuriy Yerin,
University of Perugia, Italy
Asish K. Kundu,
Brookhaven National Laboratory (DOE), United States

*CORRESPONDENCE
Huan Yang,
huanyang@nju.edu.cn
Hai-Hu Wen,
hhwen@nju.edu.cn

RECEIVED 12 November 2023
ACCEPTED 31 December 2023
PUBLISHED 11 January 2024

CITATION
Wang Z, Fan S, Li H, Li H, Yang H and Wen H-H (2024), Absence of the impurity-resonance spot at a Bi defect located near the Zn impurity in $Bi_2Sr_2Ca(Cu_{1-x}Zn_x)_2O_{8+\delta}$. *Front. Phys.* 11:1337271. doi: 10.3389/fphy.2023.1337271

Absence of the impurity-resonance spot at a Bi defect located near the Zn impurity in $Bi_2Sr_2Ca(Cu_{1-x}Zn_x)_2O_{8+\delta}$

Zhaohui Wang, Shengtai Fan, Han Li, Huazhou Li, Huan Yang* and Hai-Hu Wen*

National Laboratory of Solid State Microstructures and Department of Physics, Center for Superconducting Physics and Materials, Collaborative Innovation Center for Advanced Microstructures, Nanjing University, Nanjing, China

Zn dopants to Cu sites in high-T_c cuprates strongly suppress superconductivity and act as impurities with a strong quasiparticle scattering resonance. Using the scanning tunneling microscope, we investigate the electronic structure in the atomic scale around Zn impurities in $Bi_2Sr_2Ca(Cu_{1-x}Zn_x)_2O_{8+\delta}$. The intense scattering resonance of the Zn impurity in the CuO_2 layer strongly affects the measured local density of states of the BiO layer on the surface. The pattern of the bound state induced by a Zn impurity consists of a central spot at the Bi atom just above the Zn impurity and eight symmetric spots at the next nearest neighboring (NNN) and the third nearest neighboring (3NN) sites of Bi atoms. When the Bi atom above the NNN Cu atom is missing, the corresponding scattering spot is absent simultaneously. Our results indicate that the measured impurity-induced bound state pattern is strongly influenced by Bi atoms on the surface and therefore supports the "filter" theoretical model of the nonlocal interlayer tunneling effect from the CuO_2 layer to the BiO layer on the surface. Our research provides extra information about the impurity-induced bound state by Zn impurities.

KEYWORDS

unconventional high-temperature superconductors, cuprates, Bi2212, nonmagnetic impurity, impurity state, Bi defect

Introduction

High-T_c cuprates have been the focus of investigation in condensed matter physics for decades because of the potential application and underlying mechanism of unconventional high-T_c superconductivity. The parent compound of cuprates is a Mott insulator, and superconductivity is induced by the hole or electron doping [1]. The chemical doping is usually carried out to the 'charge-reservoir' layers in cuprates, while the charge carriers are transferred to the conducting and superconducting CuO_2 planes. However, substituting Cu atoms in the CuO_2 plane usually breaks the superconductivity and lowers T_c; meanwhile, the impurity bound state is induced at the substitution site [2–4]. This impurity effect provides critical insights into the underlying physics of high-T_c superconductivity. For instance, according to Anderson's theorem [5], the non-magnetic impurity does not influence superconductivity in an *s*-wave superconductor, however, it has a strong pair-breaking

effect in a *d*-wave superconductor with a gap sign change [6–8]. As a result, in a *d*-wave superconductor, T_c decreases rapidly with the increase in nonmagnetic impurities following the well-known Abrikosov-Gor'kov formula [9, 10]. This formula can apply to other superconductors with a sign-change order parameter like the *s*± or the *p* wave. Moreover, impurities in a *d*-wave superconductor can give rise to the so-called gapless superconductivity [11] and the phase transition to this state is proved to be a Lifshitz type of the 2.5 order [12, 13].

Among the various impurity substitutions into CuO_2 planes, Zn dopants have attracted much experimental and theoretical attention. Experimentally, a dramatic decrease of T_c is observed in Zn-doped cuprates, which is evidence of a *d*-wave gap if Zn dopants are regarded as non-magnetic impurities [14, 15]. Doping Zn impurities reduces the superfluid density [16, 17] and increases the residual specific heat coefficient [18], which can be explained by the non-superconducting regions induced by Zn dopants with the effective size of the coherence length [16]. The scanning tunneling microscopy/spectroscopy (STM/STS) experiments confirm the local effect of Zn impurities within a few nanometers [3], and the impurity-induced resonance behaves as a strong in-gap peak of density of states (DOS) located at about −2 meV near the Fermi energy. The hole doping level can influence the impurity resonance, and the bound state peak disappears in the underdoped sample with a larger gap [19, 20]. Zn dopants are usually regarded as nonmagnetic impurities. However, the staggered antiferromagnetic spin structure is observed near the Zn dopant [21–25], which may be due to the exposure of the antiferromagnetic background after the superconductivity is killed by the Zn impurities. These fascinating experimental findings demonstrate how Zn impurities locally disturb the surrounding electronic and spin structures. There are also theoretical interpretations to describe the scattering resonance pattern. It is calculated that impurity bound states are located at the four nearest Cu sites to the Zn impurity, and the complex interlayer tunneling effect makes the surface pattern on the BiO layer different from that on the CuO_2 layer [26, 27]. Based on the so-called 'filter' model, tunneling from the STM tip into the CuO_2 layer requires tunneling through the insulating BiO surface, effectively filtering the signal [26, 27]. The subsequently developed BdG-Wannier approach [28] further improves the model, and the theoretical result shows excellent agreement with the experiment.

Recently, the charge-reservoir layer has been argued to play an essential role in the unconventional superconductivity in cuprates. For example, the obtained gap feature on the exposed surface of the charge-reservoir layer is different from that on the CuO_2 plane [29, 30]. These experiment results provide another angle of view showing that the charge-reservoir layer may influence the detected local density of states (LDOS) on the surface.

Using STM/STS, we investigate the influence to the impurity-bound-state by Bi vacancies on the surface near the Zn impurity on the CuO_2 plane in $Bi_2Sr_2Ca(Cu_{1-x}Zn_x)_2O_{8+\delta}$ (Zn-Bi2212).A Bi vacancy above the next nearest neighboring Cu atom near the Zn impurity leads to the missing of the corresponding scattering resonance spot at the Bi vacancy. This result indicates that the measured impurity-induced bound state on the surface is significantly affected by the Bi atom in the BiO layer. Our observation provides a crucial clue for understanding the interaction between different layers in cuprates and facilitates the comprehension of the tunneling path in STM experiments.

Material and methods

$Bi_2Sr_2Ca(Cu_{1-x}Zn_x)_2O_{8+\delta}$ single crystals with a nominal doping level of x = 2% were grown by the self-flux method [31]. Stoichiometric proportional powders of Bi_2O_3, $SrCO_3$, CuO, $CaCO_3$, and ZnO compounds were used as starting material for growth. The mixed powder was calcined at 860°C for 48 h and ground to fine powder again. To ensure a complete solid-state reaction, the grinding and calcining procedure were repeated three times [32]. The obtained polycrystalline powder is a pure single phase examined by the powder x-ray diffraction. The polycrystalline powder was calcined at 1,020°C for 2 hours; it was cooled to 940°C at a rate of 2°C/h, then 840°C at a rate of 1°C/h, to 500°C at a rate of 1°C/min, and finally it is cooled to the room temperature with the furnace. The superconducting property was characterized by the magnetization measurement, and the transition is sharp, with a T_c of about 86 K. The STM/STS measurements were carried out in a scanning tunneling microscope (USM-1300, Unisoku Co., Ltd.). The Zn-Bi2212 samples were cleaved at room temperature in an ultra-high vacuum with a base pressure of about 2×10^{-10} torr and then transferred into the STM system working at 1.5 K. All the STM/STS measurements used the electrochemically etched chromium tips. The Cr tip was electrochemically etched by 3 mol/L NaOH solution with the immersed end covered by a polytetrafluoroethylene tube with a specific length [33]. The differential conductance is measured using the lock-in method with an AC modulation amplitude of 2 mV and frequency of 987.5 Hz. All the STM/STS data were taken at 1.5 K in this work. The setpoint conditions are V_{set} = −100 mV and I_{set} = 100 pA for all measurements of topographies and tunneling spectra.

Results and discussion

Figure 1A shows the crystal structure of the $Bi_2Sr_2CaCu_2O_{8+\delta}$ (Bi2212) unit cell. STM measurement is carried out after cleavage, and the exposed surface is universally the BiO layer because of the weak interaction between adjacent BiO planes. Cu atoms reside directly beneath the Bi atoms based on the crystal structure. When Zn impurities are doped into Bi2212, they replace the Cu atoms, and the situation of the BiO surface with an individual Zn impurity is shown in Figure 1B. To facilitate the discussion, we label the Bi atom positions as Bi0, Bi1, Bi2, and Bi3, representing the Bi atom directly above the Zn impurity, the nearest neighboring (NN) Cu atom, the next nearest neighboring (NNN) Cu atom, and the third nearest neighboring (3NN) Cu atom, respectively. Figure 1C shows the topography of the cleaved surface of Zn-Bi2212, and the atoms are Bi atoms. There are supermodulations on the surface along the diagonal direction. The Cu atoms are supposed to be just below the Bi atoms on the surface, even considering the impact of supermodulation [34]. Due to the supermodulation, the Zn impurity is unclear on the topographic image. Following a previous study [3], the bound-state pattern induced by a Zn impurity can be recognized by the differential conductance mapping at −2 mV, and the result is shown in Figure 1D. Here, the differential conductance is proportional to the LDOS, and the

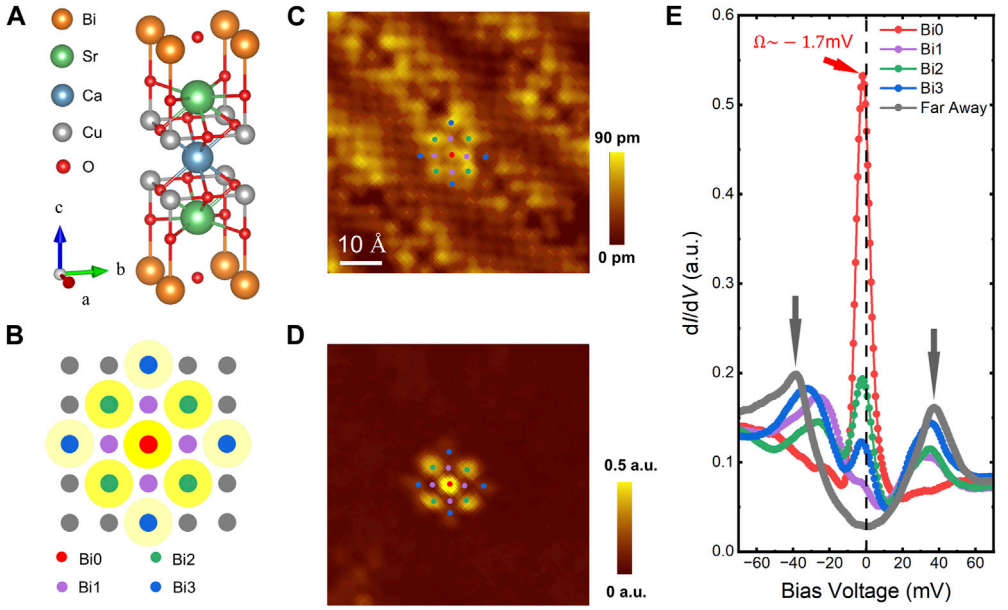

FIGURE 1
(A) Crystal structure of Bi2212 shown in a unit cell. **(B)** Schematic diagram of the BiO plane with a single Zn impurity (denoted by a red spot). The impurity bound state is also illustrated in the figure as yellow patterns, and different colors plot the neighbored Cu atoms in the central effective area by the Zn. **(C)** Atomically resolved topographic image near a Zn impurity. **(D)** Differential conductance mapping recorded at −2 mV in the same field of view of **(C)**. Locations of the Zn impurity and neighbored Cu atoms are shown in **(C)** and **(D)** by using some symbols in **(B)**. **(E)** Several tunneling spectra measured at specific positions. The shown spectra for Bi1, Bi2, and Bi3 sites are the average one of four spectra measured above the four corresponding Bi1, Bi2, and Bi3 sites.

brightest spot corresponds to the strongest in-gap density of states at −2 mV. Compared to a previous study [3], the center of the brightest spot is just above the Zn site. Eight bright spots also surround the Zn impurity symmetrically: four second-brightest spots near the NNN Cu atoms and four third-brightest spots near the 3NN Cu atoms. In contrast, no prominent spot is near the NN Cu atoms. Tunneling spectra are measured at Bi0 sites just above the Zn impurity, and the Bi atoms above the Cu atoms surrounding the Zn impurity; they are displayed in Figure 1E. The spectrum measured far away from the Zn impurity is also shown in the figure, and the superconducting coherence peaks are indicated by arrows at about ±37 meV. The finite zero-bias differential conductance is due to the impurity scattering in the *d*-wave superconductor [35–37]. On the spectrum measured at the Zn impurity, one can see the significant suppression of the coherence peak. Meanwhile, there is a solid bound state peak at $\Omega \approx -1.7$ mV, similar to the value from the previous report [3]. It should be noted that Ω slightly changes from −5 to 0 meV for different Zn impurities, and the peak amplitude also changes. This is possibly due to the slight difference in impurity scattering potential or the local superconducting gap [37, 38]. Nevertheless, a relatively small value of Ω compared to the superconducting gap suggests a strong scattering close to the unitary limit [7, 8]. The impurity bound state is weakened at the NNN and the 3NN Cu sites, and the peak is negligible at the NN Cu site. Meanwhile, the recovery of the coherence peak energy and the peak amplitude only correlates to the distance between the site and the Zn impurity.

The supermodulation structure in Bi2212 can spontaneously introduce lattice defects, particularly Bi defects, and it is interesting to investigate the influence on the Zn impurity by the missing Bi atoms. One example in the presence of Bi vacancies is shown in Figure 2, and the topography is shown in Figure 2A. Two Bi1 atoms are missing above two NN Cu sites around the Zn impurity, as illustrated in Figure 2D. This feature is more evident in the inverse Fourier transform result to the Bragg peaks and the vectors around $(\pm \frac{\pi}{a_0}, \pm \frac{\pi}{a_0})$, where a_0 is the lattice constant of Zn-Bi2212. The inverse Fourier transform image is shown in Figure 2B. Figure 2C shows the differential conductance mapping measured at −2 mV, similar to the one measured in the typical case of the Zn impurity without Bi vacancies (Figure 1D). We also measure the tunneling spectra at the Zn and Bi1 sites or vacancies above the NN Cu atom. The results are shown in Figure 2E. The spectrum measured at the Zn impurity shows a strong resonance peak at about −2.3 mV. It should be noted that impurity resonance peaks have different energies and amplitudes for different impurities. Therefore, the slight shift of the bound state energy and the decrease of the bound state peak is unlikely due to the B1 vacancies. For spectra measured at the Bi1 sites and Bi1 vacancies just above NN Cu sites, the impurity bound state peaks are weak at these two positions.

Although Bi1 vacancies have negligible influence on the bound state pattern on the surface, Bi2 vacancies seem to have a significant impact on the pattern. One example is shown in Figure 3. The Bi2 atom is missing from the topography shown in Figure 3A, while the resonance spot of the bound state pattern is missing simultaneously (Figure 3B). Figure 3D shows tunneling spectra measured at the Zn impurity, the Bi2 site above the NNN Cu atom, and the Bi2 vacancy above the NNN Cu atom. The resonance peak on the spectrum measured at the Bi2 site is similar to that shown in Figure 1E. However, the resonance peak is significantly weakened on the spectrum measure at the Bi2 vacancy. To

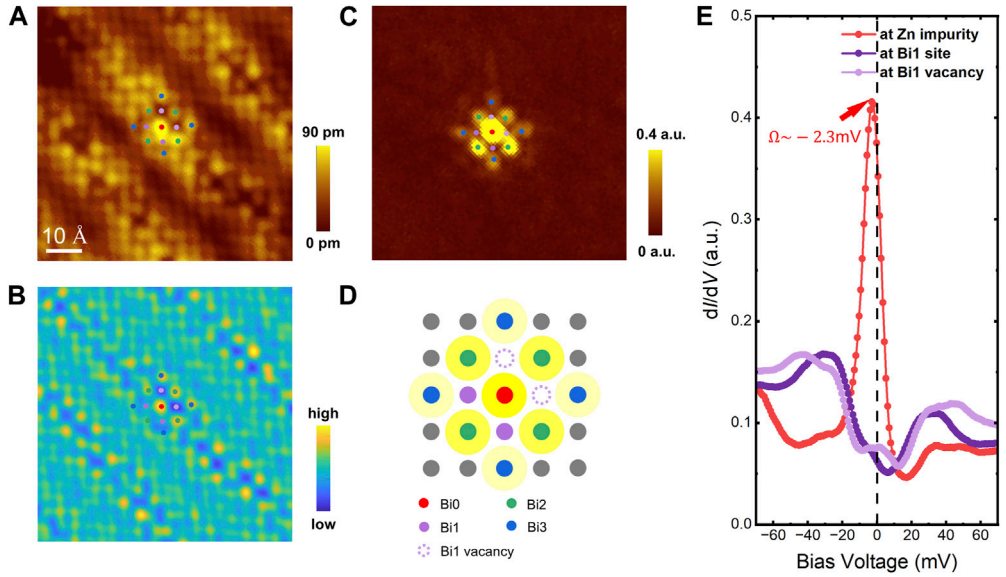

FIGURE 2
(A) Typical topographic image near a Zn impurity with two Bi1 vacancies on the surface. **(B)** Inverse Fourier transform results in the Bragg peaks and the vectors around $(\pm\frac{\pi}{a_0}, \pm\frac{\pi}{a_0})$ in the Fourier transform pattern of **(A)**. There are two Bi vacancies near the Zn impurity. **(C)** Differential conductance mapping measured at −2 mV in the same field of view as **(A)**. **(D)** Schematic illustration of the Zn impurity with two Bi1 vacancies, just above two NN Cu sites. **(E)** Tunneling spectra measured at Zn impurity and B1 sites or vacancies. The spectrum for Bi1 sites (or Bi1 vacancies) is the average of two spectra measured above two Bi1 sites (or two Bi1 vacancies).

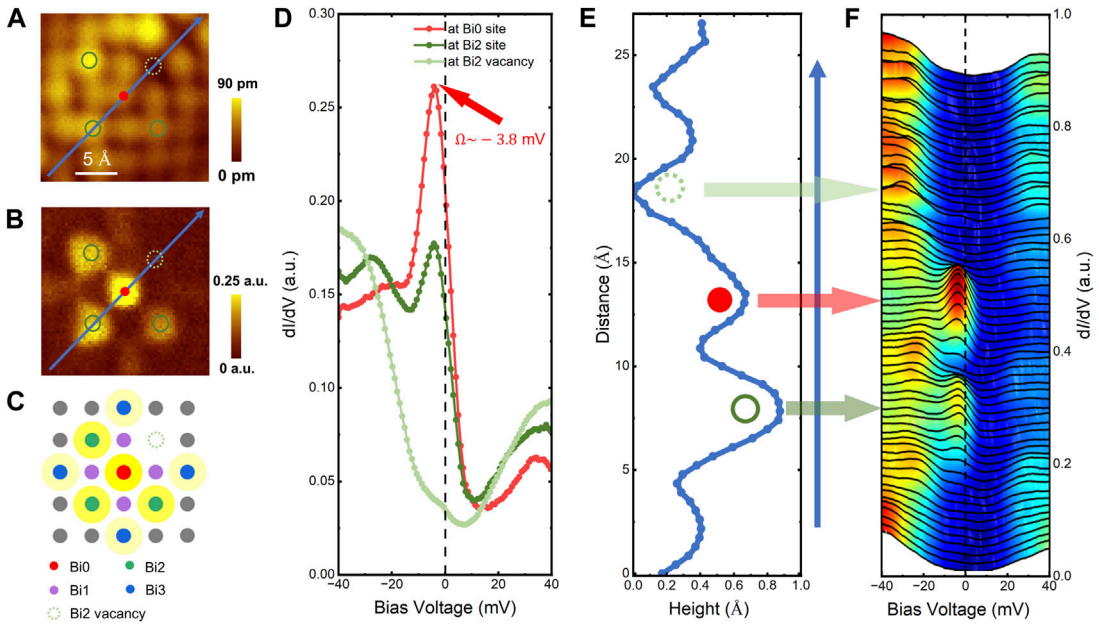

FIGURE 3
(A) Topographic image near a Zn impurity with a Bi2 vacancy on the surface. **(B)** Differential conductance mapping measured at −2 mV measured in the same area of **(A)**. The resonance spot of the bound state pattern is missing at the B2 vacancy site. **(C)** Schematic illustration of the Zn impurity with a Bi2 vacancy nearby. **(D)** Spectra measured at the Zn impurity, Bi2 sites above the NNN Cu atoms, and Bi2 vacancy above the NNN Cu atom. The spectrum of Bi2 sites is the average one of three spectra measured above three NNN Cu sites. The bound state peak behaves differently at the Bi2 vacancy and at Bi2 sites. **(E)** Height profile along the arrowed line in **(A)** or **(B)**. **(F)** A set of tunneling spectra measured along the arrowed line in **(A)** or **(B)**. The bound state peak is missing from the spectra measured near the Bi2 vacancy.

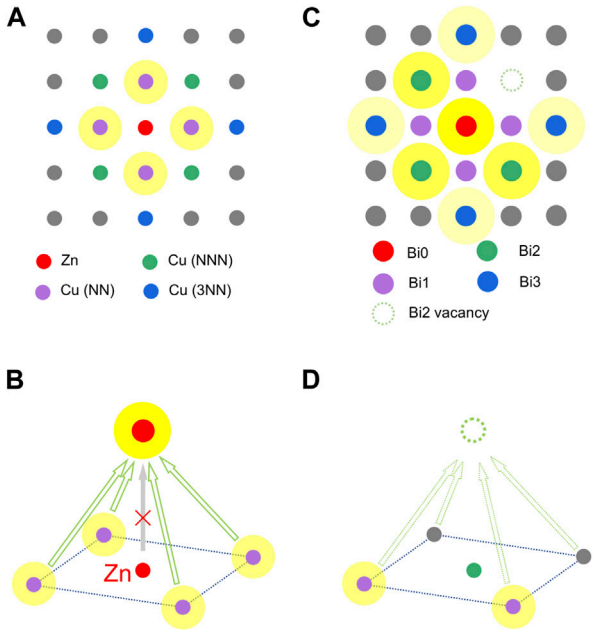

FIGURE 4
(A) Schematic illustration of CuO_2 plane with one Zn impurity. **(B)** Schematic illustration of the tunneling process when the STM tip is directly above the Bi0 site. **(C)** Schematic illustration of BiO plane corresponding to the case of one Zn impurity with one Bi2 defect. **(D)** Schematic illustration of the tunneling process when the STM tip is directly above the Bi2 vacancy. The dotted arrows indicate that the missing Bi atom will lead to the failure of the tunneling from the neighboring Cu-$3d_{x2-y2}$ to the surface and then to the STM tip.

investigate the electronic property of the Bi2 vacancy, we measure a set of tunneling spectra along an arrowed line in Figure 3A across a Bi2 site, a Zn impurity, and the Bi2 vacancy, and the result is shown in Figure 3F. Meanwhile, the corresponding height profile along the arrowed line is shown in Figure 3E, and the Bi2 vacancy can be observed as a valley. The superconducting gapped feature can be identified on spectra measured at the terminus of the arrowed line, indicating that the impurity scattering from the Zn dopant is localized. Above the Zn impurity, the bound state peak can be seen on the spectra measured at positions within the range with a diameter approximately equaling the size of a Bi atom. The bound state peak with a weakened amplitude can be seen on the spectra near the Bi2 atom. However, the bound state peak is absent on the spectra measured near the Bi2 vacancy. Consequently, one can robustly conclude that the Bi2 vacancy will strongly affect the Zn impurity-induced bound state pattern on the surface and cause the absence of the scattering resonance spot at the Bi vacancy.

Here we report the influence on the Zn impurity-induced bound states by the out-of-plane Bi defects on the surface, which has not been reported in previous works [3, 19, 20]. The detailed STM/STS measurement shows that the Bi2 vacancy significantly weakens the bound-state peak and the resonance spot measured at the impurity bound state energy. Besides, a similar phenomenon can also be observed in the case of the Bi3 vacancy, and the corresponding resonance spot also disappears in the presence of the Bi3 vacancy. In contrast, the Bi1 vacancy does not affect the bound state pattern at the bound state energy. However, it should be noted that the impurity bound state peak is negligible at the Bi1 site. Therefore, it is understandable that the Bi1 vacancy does not influence the impurity bound state pattern. Bi atoms are located in the charge-reservoir layer, and the Bi vacancy may induce a slight hole doping. Meanwhile, the Bi vacancy may increase the distance between the apical oxygen and the Cu atom underneath, which may be related to the superconductivity in the CuO_2 layer [39–41] and further modify the impurity bound state. These are the possible ways that the Bi vacancy in the charge-reservoir layer affects the impurity bound state in the CuO_2 layer. However, the resonance peak recorded just above the Zn impurity seems to be not affected by any Bi vacancies. In addition, the Bi1 site is closer to the Zn impurity than the Bi2 site, but the Bi1 vacancy has negligible influence on the impurity-bound-state peak or the bound-state pattern at the peak energy. Therefore, it is unlikely that the Bi vacancies will directly influence the Zn impurity state on the CuO_2 plane.

Based on theoretical calculations [26–28], the impurity bound state pattern behaves differently on the CuO_2 plane and the surface BiO layer because the measured pattern on the surface is affected by the interlayer tunneling matrix elements with the so-called "filter effects". In this picture, the hybridization of the in-plane $3d_{x^2-y^2}$ orbital of the metal atom (Zn or Cu) with p orbitals of apical O and Bi right above is forbidden by symmetry. Specifically, the strongest impurity bound state is located at four NN Cu atoms from the calculation [26–28], and the result is shown in Figure 4A. Figure 4B shows the tunneling process proposed by the theory, and the tunneling to the Bi atom through $6p_z$ orbital on the surface is from the in-plane $3d_{x^2-y^2}$ orbital of neighboring metal atoms (Zn or Cu) instead of the one right underneath. Additionally, the tunneling is assisted by the p orbital of apical O just below the surface Bi atom [28]. Based on this model, the obtained resonance pattern (Figure 4C) on the surface is very similar to the experimental result (Figure 3B) in the presence of a Bi2 vacancy since the impurity bound state in the CuO_2 plane cannot show up without the Bi2 atom (Figure 4D). Therefore, our experiment strongly supports the theoretical calculation results of the "filter effects" in the interlayer tunneling process.

Conclusion

In summary, we have carried out the studies on the influence of Bi defects on Zn impurity scattering resonance states in Zn-Bi2212 using STM/STS. Our findings reveal several intriguing characteristics: i) In the case of Bi1 defects, we observed no significant deviations compared to normal resonance states. ii) for the Bi2 defects situation, we detected a notable absence of LDOS at the corresponding Cu sites beneath these Bi defects. These observations collectively indicate that the BiO plane plays a crucial role in the impurity-induced bound state formation from a different perspective. Our research underscores how structural distortions and defects, even outside the CuO_2 plane, significantly impact resonance states we measured through STM/STS. These results shed new light on understanding the interaction between

different layers in cuprate and facilitate the comprehension of the tunneling process.

Data availability statement

The raw data supporting the conclusion of this article will be made available by the authors, without undue reservation.

Author contributions

ZW: Investigation, Visualization, Formal Analysis, Writing–original draft, Writing–review and editing. SF: Formal Analysis, Writing–original draft. HaL: Validation, Writing–original draft. HuL: Writing–original draft. HY: Investigation, Formal Analysis, Writing–review and editing, Writing–original draft. H-HW: Supervision, Investigation, Writing–review and editing, Project administration, Funding acquisition.

Funding

The author(s) declare financial support was received for the research, authorship, and/or publication of this article. This work was supported by National Key R&D Program of China (No. 2022YFA1403201), and National Natural Science Foundation of China (Nos. 12061131001 and 11927809).

Acknowledgments

We thank X. Zhu for the efforts in growing the single crystals, and we also acknowledge helpful discussions with S. Wan, X. Zhang and R. Yan.

Conflict of interest

The authors declare that the research was conducted in the absence of any commercial or financial relationships that could be construed as a potential conflict of interest.

Publisher's note

References

1. Keimer B, Kivelson SA, Norman MR, Uchida S, Zaanen J. From quantum matter to high-temperature superconductivity in copper oxides. *Nature* (2015) 518:179–86. doi:10.1038/nature14165

2. Alloul H, Bobroff J, Gabay M, Hirschfeld PJ. Defects in correlated metals and superconductors. *Rev Mod Phys* (2009) 81:45–108. doi:10.1103/revmodphys.81.45

3. Pan SH, Hudson EW, Lang KM, Eisaki H, Uchida S, Davis JC. Imaging the effects of individual zinc impurity atoms on superconductivity in $Bi_2Sr_2CaCu_2O_{8+\delta}$. *Nature* (2000) 403:746–50. doi:10.1038/35001534

4. Hudson EW, Lang KM, Madhavan V, Pan SH, Eisaki H, Uchida S, et al. Interplay of magnetism and high-T_c superconductivity at individual Ni impurity atoms in $Bi_2Sr_2CaCu_2O_{8+\delta}$. *Nature* (2001) 411:920–4. doi:10.1038/35082019

5. Anderson PW. Theory of dirty superconductors. *J Phys Chem Sol* (1959) 11:26–30. doi:10.1016/0022-3697(59)90036-8

6. Lee PA. Localized states in a d-wave superconductor. *Phys Rev Lett* (1993) 71: 1887–90. doi:10.1103/PhysRevLett.71.1887

7. Salkola MI, Balatsky AV, Scalapino DJ. Theory of scanning tunneling microscopy probe of impurity states in a *d*-wave superconductor. *Phys Rev Lett* (1996) 77:1841–4. doi:10.1103/PhysRevLett.77.1841

8. Balatsky AV, Salkola MI, Rosengren A. Impurity-induced virtual bound states in d-wave superconductors. *Phys Rev B* (1995) 51:15547–51. doi:10.1103/PhysRevB.51.15547

9. Abrikosov AA, Gor'kov LP. Contribution to the throry of superconducting alloys with paramagnetic impurities. *Sov Phys JETP* (1961) 12:1243–53.

10. Larkin A, Varlamov A. *Theory of fluctuations in superconductors*. New York: Oxford University Press (2005). doi:10.1093/acprof:oso/9780198528159.001.0001

11. Botelho SS, Sá de Melo CAR. Lifshitz transition in *d*-wave superconductors. *Phys Rev B* (2005) 71:134507. doi:10.1103/PhysRevB.71.134507

12. Yerin Y, Varlamov AA, Petrillo C. Topological nature of the transition between the gap and the gapless superconducting states. *Europhys Lett* (2022) 138:16005. doi:10.1209/0295-5075/ac64b9

13. Yerin Y, Petrillo C, Varlamov AA. Topological phase transition between the gap and the gapless superconductors. *Scipost Phys Core* (2022) 5:009. doi:10.21468/SciPostPhysCore.5.1.009

14. Fukuzumi Y, Mizuhashi K, Takenaka K, Uchida S. Universal superconductor-insulator transition and T_c depression in Zn-substituted high-T_c cuprates in the underdoped regime. *Phys Rev Lett* (1996) 76:684–7. doi:10.1103/PhysRevLett.76.684

15. Bonn DA, Kamal S, Zhang K, Liang R, Baar DJ, Klein E, et al. Comparison of the influence of Ni and Zn impurities on the electromagnetic properties of $YB_2Cu_3O_{6.95}$. *Phys Rev B* (1994) 50:4051–63. doi:10.1103/PhysRevB.50.4051

16. Nachumi B, Keren A, Kojima K, Larkin M, Luke GM, Merrin J, et al. Muon spin relaxation studies of Zn-substitution effects in high-T_c cuprate superconductors. *Phys Rev Lett* (1996) 77:5421–4. doi:10.1103/PhysRevLett.77.5421

17. Bernhard C, Tallon JL, Bucci C, De Renzi R, Guidi G, Williams GVM, et al. Suppression of the superconducting condensate in the high-T_c cuprates by Zn substitution and overdoping: evidence for an unconventional pairing state. *Phys Rev Lett* (1996) 77:2304–7. doi:10.1103/PhysRevLett.77.2304

18. Nakano T, Momono N, Nagata T, Oda M, Ido M. Contrasting Ni- and Zn-substitution effects on magnetic properties and superconductivity in $La_{2-x}Sr_xCuO_4$. *Phys Rev B* (1998) 58:5831–8. doi:10.1103/PhysRevB.58.5831

19. Machida T, Kato T, Nakamura H, Fujimoto M, Mochiku T, Ooi S, et al. Disappearance of zinc impurity resonance in large-gap regions of $Bi_2Sr_2CaCu_2O_{8+\delta}$ probed by scanning tunneling spectroscopy. *Phys Rev B* (2010) 82:180507. doi:10.1103/PhysRevB.82.180507

20. Machida T, Kato T, Nakamura H, Fujimoto M, Mochiku T, Ooi S, et al. Quantum interference of impurity bound states in $Bi_2Sr_2Ca(Cu_{1-x}Zn_x)_2O_{8+\delta}$ probed by scanning tunneling spectroscopy. *Phys Rev B* (2011) 84:064501. doi:10.1103/PhysRevB.84.064501

21. Mahajan AV, Alloul H, Collin G, Marucco JF. ^{89}Y NMR probe of Zn induced local moments in $YBa_2(Cu_{1-y}Zn_y)_3O_{6+x}$. *Phys Rev Lett* (1994) 72:3100–3. doi:10.1103/PhysRevLett.72.3100

22. Alloul H, Mendels P, Casalta H, Marucco JF, Arabski J. Correlations between magnetic and superconducting properties of Zn-substituted $YBa_2Cu_3O_{6+x}$. *Phys Rev Lett* (1991) 67:3140–3. doi:10.1103/physrevlett.67.3140

23. Hirota K. Neutron scattering studies of Zn-doped $La_{2-x}Sr_xCuO_4$. *Physica C* (2001) 357-360:61–8. doi:10.1016/S0921-4534(01)00195-2

24. Suchaneck A, Hinkov V, Haug D, Schulz L, Bernhard C, Ivanov A, et al. Incommensurate magnetic order and dynamics induced by spinless impurities in $YBa_2Cu_3O_{6.6}$. *Phys Rev Lett* (2010) 105:037207. doi:10.1103/PhysRevLett.105.037207

25. Kimura H, Hirota K, Matsushita H, Yamada K, Endoh Y, Lee S-H, et al. Neutron-scattering study of static antiferromagnetic correlations in $La_{2-x}Sr_xCu_{1-y}Zn_yO_4$. *Phys Rev B* (1999) 59:6517–23. doi:10.1103/PhysRevB.59.6517

26. Martin I, Balatsky AV, Zaanen J. Impurity states and interlayer tunneling in high temperature superconductors. *Phys Rev Lett* (2002) 88:097003. doi:10.1103/PhysRevLett.88.097003

27. Zhu J-X, Lee TK, Ting CS, Hu C-R. Quasiparticle resonant states induced by a unitary impurity in a d-wave superconductor. *Phys Rev B* (2000) 61:8667–70. doi:10.1103/PhysRevB.61.8667

28. Kreisel A, Choubey P, Berlijn T, Ku W, Andersen BM, Hirschfeld PJ. Interpretation of scanning tunneling quasiparticle interference and impurity states in cuprates. *Phys Rev Lett* (2015) 114:217002. doi:10.1103/PhysRevLett.114.217002

29. Lv Y-F, Wang W-L, Peng J-P, Ding H, Wang Y, Wang L, et al. Mapping the electronic structure of each ingredient oxide layer of high-T_c cuprate superconductor $Bi_2Sr_2CaCu_2O_{8+\delta}$. *Phys Rev Lett* (2015) 115:237002. doi:10.1103/PhysRevLett.115.237002

30. Fan J-Q, Yu X-Q, Cheng F-J, Wang H, Wang R, Ma X, et al. Direct observation of nodeless superconductivity and phonon modes in electron-doped copper oxide $Sr_{1-x}Nd_xCuO_2$. *Natl Sci Rev* (2022) 9:nwab225. doi:10.1093/nsr/nwab225

31. Lovleena BIK, Kholkin AL, Kumar B. Structural changes in ab-plane of Zn doped Bi-2212 HTSC single crystals. *Physica C* (2007) 451:44–8. doi:10.1016/j.physc.2006.10.003

32. Liu S-Y, Zhang W-T, Zhao L, Liu H-Y, Wu Y, Liu G-D, et al. Growth and characterization of high-quality single crystals of Ni- and Zn-doped $Bi_2Sr_2Ca(Cu_{2-x}M_x)O_{8+\delta}$ (M = Ni or Zn) high-temperature superconductors. *Chin Phys Lett* (2012) 29:087401. doi:10.1088/0256-307X/29/8/087401

33. Huang D, Liu S, Zeljkovic I, Mitchell JF, Hoffman JE. Etching of Cr tips for scanning tunneling microscopy of cleavable oxides. *Rev Sci Instrum* (2017) 88:023705. doi:10.1063/1.4976567

34. Hamidian MH, Firmo IA, Fujita K, Mukhopadhyay S, Orenstein JW, Eisaki H, et al. Picometer registration of zinc impurity states in $Bi_2Sr_2CaCu_2O_{8+\delta}$ for phase determination in intra-unit-cell Fourier transform STM. *New J Phys* (2012) 14:053017. doi:10.1088/1367-2630/14/5/053017

35. Pan SH, O'Neal JP, Badzey RL, Chamon C, Ding H, Engelbrecht JR, et al. Microscopic electronic inhomogeneity in the high-Tc superconductor $Bi_2Sr_2CaCu_2O_{8+\delta}$. *Nature* (2001) 413:282–5. doi:10.1038/35095012

36. Renner C, Fischer O. Vacuum tunneling spectroscopy and asymmetric density of states of $Bi_2Sr_2CaCu_2O_{8+\delta}$. *Phys Rev B* (1995) 51:9208–18. doi:10.1103/PhysRevB.51.9208

37. McElroy K, Lee J, Slezak JA, Lee D-H, Eisaki H, Uchida S, et al. Atomic-scale sources and mechanism of nanoscale electronic disorder in $Bi_2Sr_2CaCu_2O_{8+\delta}$. *Science* (2005) 309:1048–52. doi:10.1126/science.1113095

38. McElroy K, Lee D-H, Hoffman JE, Lang KM, Lee J, Hudson EW, et al. Coincidence of checkerboard charge order and antinodal state decoherence in strongly underdoped superconducting $Bi_2Sr_2CaCu_2O_{8+\delta}$. *Phys Rev Lett* (2005) 94:197005. doi:10.1103/PhysRevLett.94.197005

39. O'Mahony SM, Ren W, Chen W, Chong YX, Liu X, Eisaki H, et al. On the electron pairing mechanism of copper-oxide high temperature superconductivity. *Proc Natl Acad Sci USA* (2022) 119:e2207449119. doi:10.1073/pnas.2207449119

40. Zou C, Hao Z, Li H, Li X, Ye S, Yu L, et al. Effect of structural supermodulation on superconductivity in trilayer cuprate $Bi_2Sr_2Ca_2Cu_3O_{10+\delta}$. *Phys Rev Lett* (2020) 124:047003. doi:10.1103/PhysRevLett.124.047003

41. Slezak JA, Lee J, Wang M, McElroy K, Fujita K, Andersen BM, et al. Imaging the impact on cuprate superconductivity of varying the interatomic distances within individual crystal unit cells. *Proc Natl Acad Sci USA* (2008) 105:3203–8. doi:10.1073/pnas.0706795105

frontiers | Frontiers in Physics

TYPE Original Research
PUBLISHED 16 January 2024
DOI 10.3389/fphy.2023.1336501

OPEN ACCESS

EDITED BY
Ruslan Prozorov,
Iowa State University, United States

REVIEWED BY
Krastyo Buchkov,
Georgi Nadjakov Institute of Solid State Physics (BAS), Bulgaria
Ioan Adrian Crisan,
National Institute of Materials Physics, Romania

*CORRESPONDENCE
Daniele Torsello,
daniele.torsello@polito.it

RECEIVED 10 November 2023
ACCEPTED 31 December 2023
PUBLISHED 16 January 2024

CITATION
Torsello D, Piatti E, Fracasso M, Gerbaldo R, Gozzelino L, Yi X, Xing X, Shi Z, Daghero D and Ghigo G (2024), Unusually weak irradiation effects in anisotropic iron-based superconductor $RbCa_2Fe_4As_4F_2$. *Front. Phys.* 11:1336501. doi: 10.3389/fphy.2023.1336501

Unusually weak irradiation effects in anisotropic iron-based superconductor $RbCa_2Fe_4As_4F_2$

Daniele Torsello[1,2]*, Erik Piatti[1], Michela Fracasso[1,2], Roberto Gerbaldo[1,2], Laura Gozzelino[1,2], Xiaolei Yi[3], Xiangzhuo Xing[4], Zhixiang Shi[3], Dario Daghero[1] and Gianluca Ghigo[1,2]

[1]Department of Applied Science and Technology, Politecnico di Torino, Torino, Italy, [2]Istituto Nazionale di Fisica Nucleare, Sezione di Torino, Torino, Italy, [3]School of Physics, Southeast University, Nanjing, China, [4]School of Physics and Physical Engineering, Qufu Normal University, Qufu, China

We report on the effects of 3.5 MeV proton irradiation in $RbCa_2Fe_4As_4F_2$, an iron-based superconductor with unusual properties in between those of the pnictides and of the cuprate high-temperature superconductors. We studied how structural disorder introduced by ion bombardment affects the critical temperature, superfluid density and gap values by combining a coplanar waveguide resonator technique, electric transport measurements and point-contact Andreev-reflection spectroscopy. We find an unusually weak dependence of the superconducting properties on the amount of disorder in this material when compared to other iron-based superconductors under comparable irradiation conditions. The nodal multigap state exhibited by pristine $RbCa_2Fe_4As_4F_2$ is also robust against proton irradiation, with a two-band *d*-*d* model being the one that best fits the experimental data.

KEYWORDS

12442 iron-based superconductors, proton irradiation, superfluid density, order parameter symmetry, point-contact spectroscopy

1 Introduction

Ion irradiation has proven to be an extremely useful tool for the investigation of fundamental properties of superconductors [1–3]. In recent years, significant efforts have been devoted to the study of iron-based superconductors (IBSs) [4–7], hoping that understanding their pairing mechanism could lead to a comprehensive understanding of unconventional superconductivity [8]. Although this high goal is still far from being achieved, several interesting findings were reported on these intriguing materials, contributing to deepen the knowledge of the effects of disorder on the superconducting condensate and related phenomena. In particular, besides the more standard result of enhancing the vortex pinning capability [7], an irradiation-disorder-induced transition was observed between $s_{\pm}$ and s_{++} states in two-band IBSs of the 122 family [3], that contributed to confirm the $s_{\pm}$ state for the pristine compound, as predicted theoretically [1].

In the last few years, the attention moved to a newly discovered family of IBSs, the 12442 pnictide family [9–11], that shows some peculiar properties resembling those of the cuprates [12–15]. The 12442-type $ACa_2Fe_4As_4F_2$ (where A = K, Rb, Cs) compounds are obtained by the intergrowth of 1111-type CaFeAsF and 122-type AFe_2As_2. While in most IBSs superconductivity emerges after the suppression of antiferromagnetic order in the

parent compound by carrier doping, the 12442 compounds are superconducting in their stoichiometric state, with a critical temperature ranging from 28 to 33 K, without the need for chemical substitution to achieve extra carrier doping. These compounds consist of alternate stacking of conducting Fe_2As_2 layers and insulating Ca_2F_2 blocks, and contrary to other IBSs, they have double FeAs layers between neighboring insulating layers, thus mimicking the case of double CuO_2 layers in the cuprates. As the cuprates (and contrary to 122 and 1144 IBSs), these compounds show a large anisotropy in the upper critical field and penetration depth [16]. As for the pairing symmetry and gap structure, to date it is still controversial whether in 12442 there exist gap nodes or not, and, in the former case, whether nodal *d*-wave-like or accidental nodal *s*-wave gaps should be expected. Recently, a study of the gap structure of $RbCa_2Fe_4As_4F_2$ (Rb-12442) led to the identification of two gaps with signatures of *d*-wave-like nodal behavior [16]. Data are well described by a two-band *d*-*d* state with symmetry-imposed nodes, since they persist upon Ni doping. Within this framework, the need emerges to investigate the role of disorder of nonchemical origin, e.g., induced by ion irradiation. In fact, in this case it is possible to compare measurements on the very same crystals before and after irradiation, i.e., after the introduction of structural defects with defined shape and dimensions, and controlled density. This could help in completing the picture and give hints toward an overall interpretation of the superconductivity mechanism in the 12442 IBSs.

In this work, we report on the effects of disorder introduced via 3.5 MeV proton irradiation on the critical temperature, superfluid density and gap values of Rb-12442 single crystals, investigated by a combination of the complementary techniques of electric transport measurements, coplanar waveguide resonator (CPWR) measurements and point-contact Andreev-reflection spectroscopy (PCARS).

Transport measurements allow the determination of the resistivity as a function of temperature, of the residual resistivity ratio RRR, and of the superconducting transition temperature T_c^ρ, and thus provide information on how irradiation affects the scattering of electrons by defects and the onset of the superconducting state.

CPWR measurements allow a direct determination of the London penetration depth λ_L as a function of temperature, and consequently of the superfluid density ρ_s and of the critical temperature T_c^λ at which it vanishes. The temperature dependence of ρ_s provides indications on the symmetry of the superconducting gap(s), and in particular on whether unpaired quasiparticles persist down to the lowest temperatures, which is associated to an incomplete gapping of the Fermi surface typical for example, of *d*-wave superconductivity.

PCARS allows a direct determination of the amplitude and symmetry of the superconducting gap(s) and of the temperature at which they close, T_c^A, by measuring the differential conductance dI/dV of a small (point-like) contact between a normal metal (N) and the superconductor under study (S), as a function of the bias voltage V applied across the NS junction [17–19]. The absence of an insulating barrier between the N and S banks enables Andreev reflection at the interface [17–19], which enhances the dI/dV for $V \leq \Delta/e$ (Δ being the superconducting gap) and makes it sensitive to the coherence of the superconducting condensate—unlike tunnelling spectroscopy that probes the density of states of unpaired quasiparticles. Finally, the dependence of the critical temperature (T_c^ρ or T_c^λ) on the disorder (which is directly related to the symmetry of the energy gap in single-band systems) can be compared to that observed in other, more widely-studied IBS systems.

The conclusion of this extensive study is that the critical temperature of 12442 decreases on increasing disorder in an unusually weak (if compared to other IBSs) and nonlinear manner, while the London penetration depth increases in an approximately linear way. The joint analysis of PCARS spectra and CPWR measurements supports the existence of nodes in at least one gap, and most probably indicates the persistence of the same gap symmetry observed in the pristine, non-irradiated compound.

2 Materials and methods

2.1 Crystal growth and basic characterization

Single crystals of Rb-12442 were grown by the self-flux method [14, 20, 21] and their high quality was assessed through X-ray diffraction and energy-dispersive X-ray spectroscopy as detailed in Refs. [14, 16].

2.2 Electrical resistivity measurements

The temperature dependence of the electrical resistivity was measured on selected single crystals by means of the van der Pauw method [22] after having electrically contacted them with thin gold wires and conducting silver paste. Each resistance measurement was performed by sourcing a small DC current ≈ 100 μA between two adjacent contacts and measuring the resulting voltage drop across the opposite pair of contacts. Common-mode offsets including thermoelectric voltages were removed using the current-reversal method.

2.3 CPWR measurements

The London penetration depth and superfluid density were measured by means of a coplanar waveguide resonator (CPWR) technique, particularly suitable to study small IBS crystals for irradiation experiments since it is minimally invasive and the same samples can be characterized several times before and after different irradiation steps [23]. The measurement was carried out within a resonator perturbation approach. A coplanar waveguide resonator obtained by patterning an $YBa_2Cu_3O_{7-\delta}$ thin film deposited on MgO substrate was coupled to a vector network analyzer for the measurement of the scattering matrix at low input power. The transmitted power shows a resonance that can be fitted by a modified Lorentzian function, yielding the resonance frequency and quality factor. Measurements were carried out as a function of the temperature for the empty resonator and with the investigated samples coupled to it (i.e., placed on the central stripline, far from the edges). The presence of the sample causes

shifts of the resonance frequency and of the quality factor that are due to the electromagnetic properties of the sample: from these shifts, after a self-consistent calibration procedure, the absolute value of the penetration depth and its temperature dependence can be assessed [24].

2.4 PCARS measurements

The structure of the superconducting gap was assessed via point-contact Andreev reflection spectroscopy (PCARS), by measuring the differential conductance (dI/dV) of point-like contacts made between a normal metal (N) and the superconducting sample (S). Unlike in tunnelling spectroscopy, in a direct N/S contact without insulating barrier, electrons impinging on the N/S interface are either transmitted from the metal to the superconductor—if their energy eV is higher than the gap Δ in the S side—or experience Andreev reflection, i.e., are transmitted as a Cooper pair in S while a hole is reflected back in N [17–19]. As a result, the differential conductance of the junction is enhanced for V smaller than Δ/e. In real junctions, a small potential barrier can be present at the interface, which makes a tunneling contribution be present in addition to the Andreev-reflection signal. The shape of the resulting dI/dV vs. V curve depends not only on the gap amplitude, but also on its symmetry in the reciprocal space. In particular, isotropic gaps give rise to conductance curves with a zero-bias minimum and two symmetric maxima at the gap edges, no matter what is the direction of current injection with respect to the crystallographic axes [18]. Instead, anisotropic nodal gaps (especially in the case of a d-wave symmetry) can give rise to a variety of different curves depending on the angle of current injection [25]. For example, zero-bias cusps or peaks are typical features that can be associated to a d-wave gap, in specific conditions of barrier height and current direction [19]. In multigap systems, features such as peaks or shoulders are observed in the differential conductance, which are the hallmarks of the different gaps [19].

Point contacts were fabricated by using the so-called soft technique [18, 19], i.e., by using a thin gold wire ($\varnothing \approx 12.7\ \mu m$) stretched over the platelet-like sample and touching its very thin and flat side surface in a single point. These contacts were (optionally) mechanically stabilized by small ($\varnothing \approx 50\ \mu m$) drop-cast droplets of silver paste. In either case, the "macroscopic" contact actually consists of several parallel nanoscopic N/S contacts.

The differential conductance was obtained by numerical derivation of the $I - V$ characteristics of the contact, measured in the pseudo-four-probe configuration as detailed in Refs. [12, 16]. Within the present paper, the direction of (main) current injection was confined along the ab planes of the crystals by making the point contacts on the thin, but smooth and flat side surfaces of the crystals. For the dI/dV vs. V curves to contain spectroscopic information, the (maximum) energy of the injected electrons must be directly related to the bias voltage applied through the junction, i.e., $E = eV$. This requires that the resistance of the contact is much larger than the resistance of the normal bank, and that electrons do not lose energy while crossing the interface. The latter condition means that there is no Joule dissipation in the contact, and is fulfilled if the individual nanocontacts are in the ballistic or at most diffusive regime [18, 26], i.e., their radius is smaller than the (inelastic) electronic mean free path.

Information about the gap number, amplitude and symmetry were extracted from the experimental dI/dV vs. V curves of spectroscopic contacts by fitting them with suitable models. Before fitting, the experimental curves at any temperature were normalized to the normal-state curve measured just above the superconducting transition—as customary in IBSs [18, 27, 28]—after this was rescaled by subtracting the contribution of the so-called spreading resistance R_s, i.e., normal-state resistance of the crystal that appears, in series with the contact, in the proximity of the resistive transition and results in a horizontal stretching and a downward shift of the dI/dV spectra with respect to those at low temperature [29]. As discussed in Refs. [12, 16], for each contact we typically selected the value of R_s that allows matching the tails of the normal and superconducting dI/dV spectra. Since this choice remains somewhat arbitrary, we used multiple reasonable values of R_s to obtain the normalized spectra, and repeated each time the fitting procedure. The resulting values of the fit parameters were then averaged and their maximum differences taken as the uncertainty of the procedure.

The normalized dI/dV spectra were then fitted to the two-band version [18, 19] of the appropriate anisotropic Blonder-Tinkham-Klapwijk model [30–32], as extensively discussed in Refs. [12, 16]. The reason why we used an effective two-band model even if we expect more than two gaps to be present in this compound is due to the necessity to limit the number of adjustable parameters. Indeed, for each gap i the model includes as adjustable parameters the gap amplitude Δ_i, the broadening parameter Γ_i, and the barrier parameter Z_i. The model also contains the relative weight of the large-gap band in the conductance w_1 and the direction α between the direction of (main) current injection and the antinodal line. The latter is crucial in reproducing zero-bias peaks in the experimental spectra arising from the interference effects occurring when electron-like and hole-like quasiparticles experience order parameters of opposite sign. Being based on the weak-coupling BCS theory, the model does not capture strong-coupling features such as electron-boson-derived shoulders appearing at energies higher than the largest gap, which must therefore be excluded from the fitting procedure [19, 27, 29].

2.5 Ion irradiation

Ion irradiation was carried out at the CN facility of the Legnaro National Laboratories of INFN, at room temperature, in high vacuum, with a defocused 3.5 MeV proton beam incident parallel to the c axis of the samples. This energy ensures that ion implantation is avoided in all the investigated samples. The beam current was kept below 60 nA on a spot of 7 mm of diameter, to avoid excessive sample heating.

Irradiation with MeV-protons in IBSs is known to produce point-like defects (Frenkel pairs) and small clusters of nanometric size [33], that in the present case are quite uniformly distributed in the sample, since the Bragg peak is avoided. Such defects are efficient scattering centers that can strongly affect the superconducting state by suppressing the superfluid density.

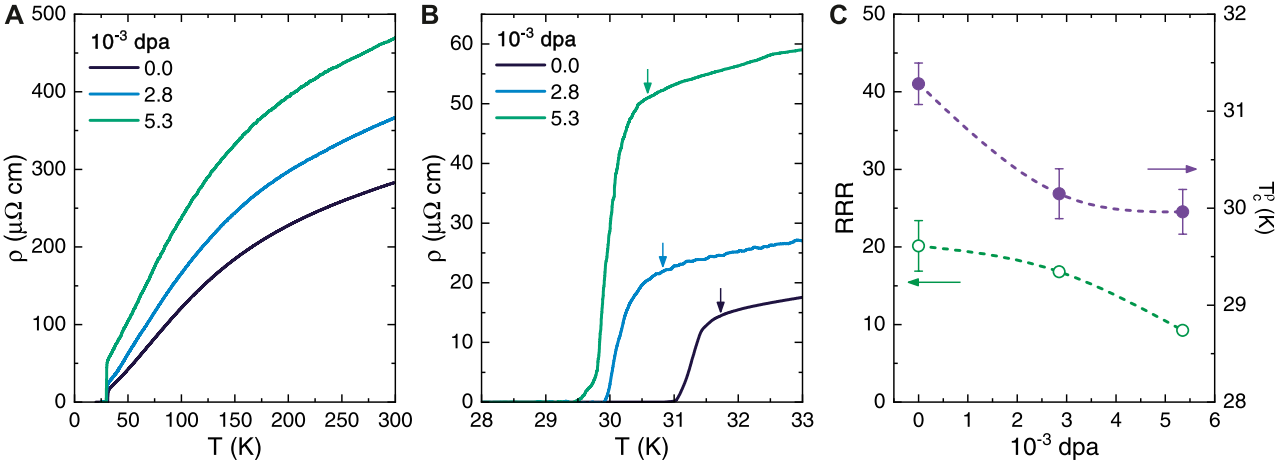

FIGURE 1
(A) Resistivity ρ as a function of temperature T for three Rb-12442 crystals in the pristine state (corresponding to dpa = 0) and at increasing proton irradiation levels. **(B)** Magnification of the curves shown in **(A)** in the vicinity of the superconducting transition. The arrows highlight the onset temperature of the resistive transition T_c^{on} (see text for details). **(C)** Superconducting transition temperature T_c^{ρ} (filled violet circles, right scale) and residual resistivity ratios *RRR* (hollow green circles, left scale) of the same crystals as a function of the disorder level measured in displacements per atom (dpa). Dashed lines are guides to the eye.

In order to compare the effects of irradiation on the superconducting properties of our samples with other materials and irradiation conditions we computed the displacements per atom (dpa) through Monte Carlo simulations with the SRIM code [34]. This approach has proven useful to study the effects of ion-irradiation-induced disorder because dpa is a good parameter to characterize the amount of scattering centers introduced in the sample [35]. The dpa value is proportional to the proton fluence, that was evaluated through the total deposited charge obtained by integrating the measured beam current at the beam spot on the sample.

3 Results

We first investigate the effects of ion irradiation on the electric transport properties of the Rb-12442 crystals. Figure 1A shows the electrical resistivity ρ as a function of temperature T of three crystals at different dpa values, and Figure 1B a magnification close to the superconducting transitions. The normal state of the pristine crystal exhibits the typical behaviour as reported in the literature [14, 16]: the residual resistivity ratio, defined as $RRR = \rho(300\,\mathrm{K})/\rho(T_c^{on})$, is $RRR = 20 \pm 3$ and larger than the literature values (12–16) [14, 16, 36]; whereas the resistivity at room T is $\rho(300\,\mathrm{K}) = 290 \pm 30\,\mu\Omega\,\mathrm{cm}$ and lower than the previously-reported values ($\approx 1.1\,\mathrm{m}\Omega\,\mathrm{cm}$) [14]. Both features attest the high crystalline quality of our present samples. Here, T_c^{on} is defined as the onset of the superconducting transition, i.e., the temperature at which the resistivity starts to deviate from a linear extrapolation of the normal state (highlighted by the arrows in Figure 1B). The resistive superconducting transition temperature is defined as $T_c^{\rho} = T_c^{50} \pm \frac{T_c^{90} - T_c^{10}}{2}$, where T_c^{α} is the temperature at which the resistivity reaches $\alpha\%$ of $\rho(T_c^{on})$, and is equal to $T_c^{\rho} = 31.3 \pm 0.2\,\mathrm{K}$ for the pristine crystal, in good agreement with the previous reports [12, 14, 16].

At the increase of the irradiation level, the resistivity increases in the entire temperature range up to $\rho(300\,K) = 470 \pm 50\,\mu\Omega\,\mathrm{cm}$ in the crystal at 5.3×10^{-3} dpa, and at the same time both T_c^{ρ} and *RRR* are suppressed. As shown in Figure 1C, the suppression of T_c^{ρ} introduced by irradiation is significantly faster at lower dpa than at higher dpa values, and for both quantities it is minute with respect to those introduced by substitutional Ni doping. Specifically, we observe a maximum T_c^{ρ} suppression of 4.2% and a minimum $RRR = 9$ in our irradiated samples, against a complete disappearance of superconductivity and a minimum $RRR \approx 1$ in Ni-doped samples. This indicates that the perturbations to the structural and electronic properties of Rb-12442 crystals introduced by irradiation are minimal with respect to those attained by substitutional doping.

A more extensive characterization of the superconducting properties of the Rb-12442 crystals upon increasing ion irradiation was carried out by analyzing the data from CPWR measurements. Figure 2A shows the temperature dependence of the London penetration depth λ_L for the pristine crystal and for five irradiated crystals with increasing dpa values, from 1.7 up to 7.8×10^{-3} dpa. It can clearly be seen that ion irradiation increases λ_L in the entire T range and suppresses the onset temperature below which superconducting behaviour is observed. In particular, the superconducting critical temperature T_c^{λ} can be obtained as the value of T at which λ_L diverges (or equivalently, at which the superfluid density $\rho_s = \lambda_L^{-2}$ goes to 0). Figure 2B shows how this definition correlates extremely well to the midpoint of the resistive transition in transport measurements, for both pristine and irradiated samples.

Figure 2C tracks the evolution of T_c^{λ} upon increasing irradiation level, which confirms both its small suppression as compared with those attained via substitutional doping (maximum T_c^{λ} suppression of 4.5% at 7.8×10^{-3} dpa) and the progressive reduction in its suppression rate at higher dpa values. Figure 2D shows λ_L measured at $T = 10$ K and the corresponding values of ρ_s as a function of the dpa values: $\lambda_L(10\,\mathrm{K})$ increases from 211 to 790 nm from the pristine

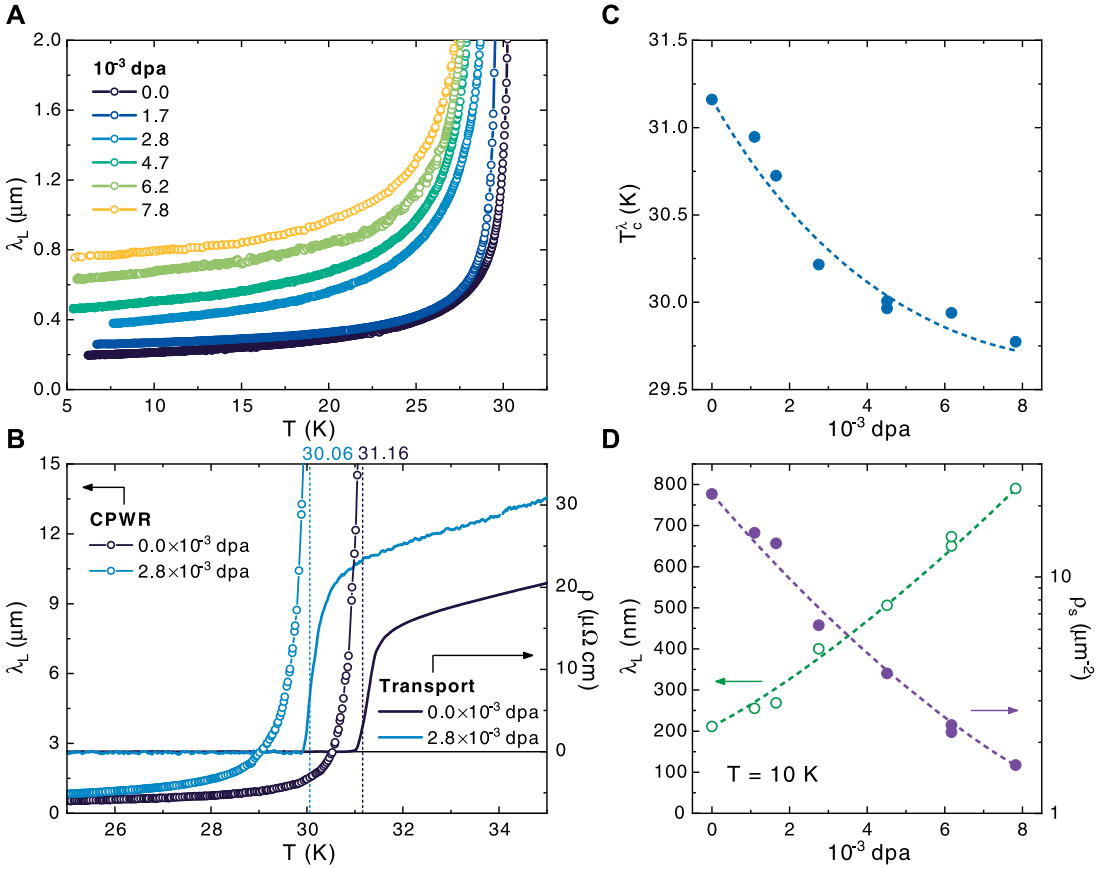

FIGURE 2
(A) Temperature (T) dependence of the London penetration depth λ_L determined from CPWR measurements for pristine and irradiated crystals for increasing proton irradiation levels, measured as displacements per atom (dpa). **(B)** Comparison of the T dependencies of λ_L (hollow circles, left scale) and of the electrical resistivity ρ (solid lines, right scale) measured in the same two samples (a pristine crystal and an irradiated crystals at 2.8×10^{-3}dpa). The superconducting critical temperature determined from CPWR measurements, T_c^{λ}, (defined as the T at which λ_L diverges) correlates well with the midpoint of the resistive transition. **(C)** T_c^{λ} and **(D)** λ_L (hollow green circles, left scale) and ρ_s (filled violet circles, right scales) measured at 10 K determined from the curves shown in panel **(A)** as a function of the disorder level measured in dpa. Dashed lines are guides to the eye.

crystal to the crystal irradiated at 7.8×10^{-3} dpa, corresponding to a reduction in $\rho_s(10\,\mathrm{K})$ from 22.4 to 7.8 μm^{-2}. This shows that ion irradiation is much more effective at tuning the magnetic penetration depth of the Rb-12442 crystals with respect to their superconducting transition temperatures, also when compared with Ni substitutional doping: for instance, 5% Ni-doped crystals—where T_c^{λ} was suppressed by ~ 34% with respect to the pristine crystals—exhibited an increase of $\lambda_L(10\,\mathrm{K})$ only up to ~ 600 nm [16].

Now we turn our attention to the effect of ion irradiation on the values of the superconducting energy gaps as measured by PCARS. Figures 3A, B, C show some examples of low-temperature PCARS spectra of different point contacts (with different normal-state resistance) made on the sample with a disorder level of 5.3×10^{-3} dpa. Most spectra (Figure 3A) show a zero-bias cusp or maximum, which is suggestive of a nodal gap [18, 19, 30–32], and is perfectly consistent with the observations made on pristine Rb-12442 [12, 16]. Others, instead, show a broad maximum (Figure 3B) or even two symmetric maxima at low bias (Figure 3C) that are usually associated to an isotropic gap, but can be observed even in d-wave gap symmetry when the current is injected (mainly) along the antinodal direction [18, 19, 30–32].

More detailed information about the energy gap can be extracted by normalizing the experimental spectra to the normal-state curve measured immediately above T_c [18, 27, 28], and fitting the normalized spectra to a suitable model for Andreev reflection at a normal metal/superconductor interface [18, 19]. Figures 3D, E, F show three different normalized spectra (black lines). None of these could be fitted by using a single gap, either in s-wave or d-wave symmetry, indicating that irradiation does not change the multiband nature of superconductivity in this compound. We then used an effective two-band model, in which the relative weight of the gaps is an adjustable parameter. Based on the results found in pristine, unirradiated Rb-12442 [12, 16] and on the fact that some of the curves (Figure 3D) display a zero-bias cusp, we tried to fit the curves using either an isotropic s-wave gap and a nodal d-wave gap (s-d model in the following) or two d-wave gaps (d-d model). As discussed in Ref. [12], the s-d model actually mimics the nodal $s_{\pm}$ and the $d_{x^2-y^2}$ symmetries, whereas the d-d model mimics the d_{xy} symmetry, all compatible with the tetragonal structure of Rb-12442 [8]. In both the models, the partial conductance associated to each gap is modelled as in Ref. [32]. The fitting parameters are then, in addition to the gap amplitudes Δ_s and Δ_d (in the s-d model) or Δ_{d1}

10.3389/fphy.2023.1336501

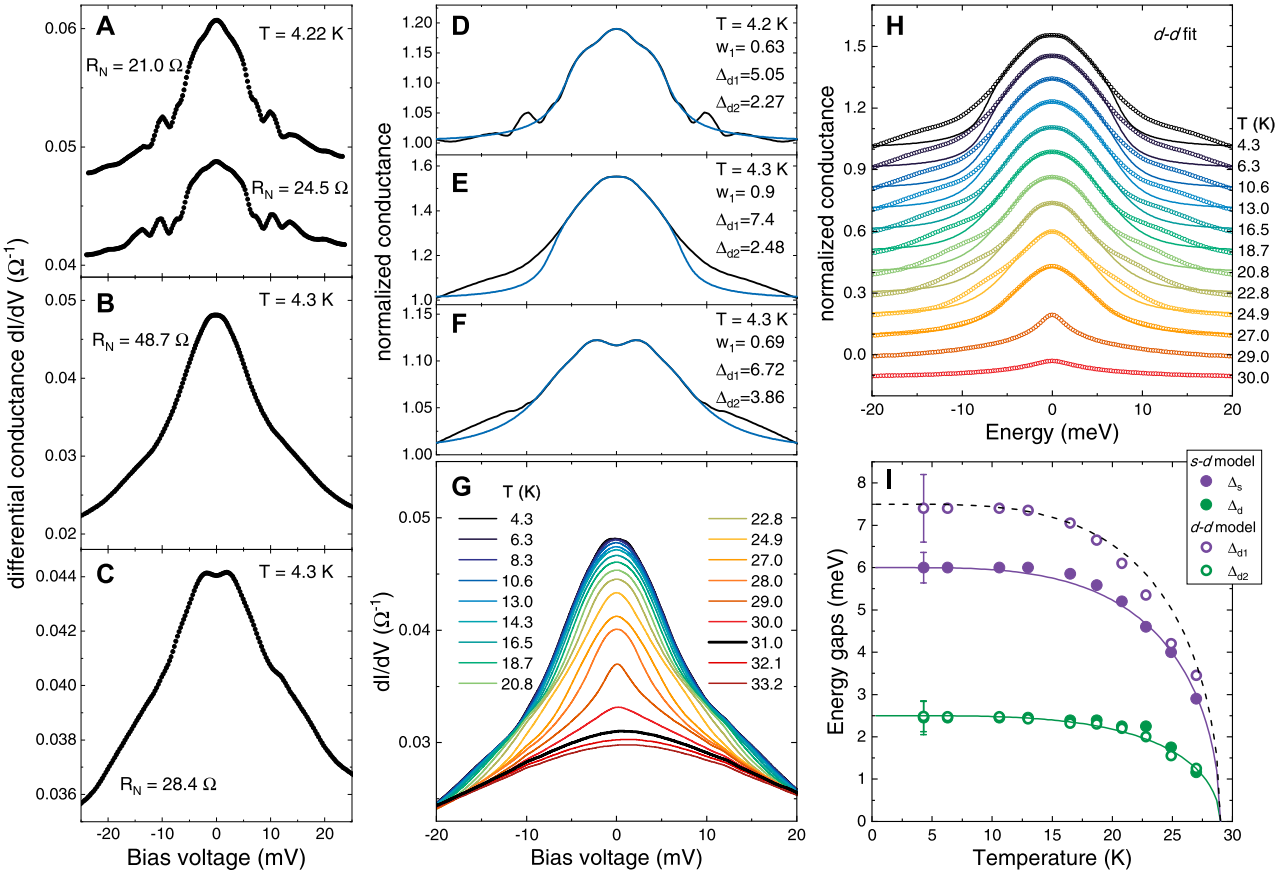

FIGURE 3
(A, B, C) Some examples of as-measured conductance curves (dI/dV vs. V) of ab-plane contacts made on the irradiated crystal for which the disorder level is 5.3×10^{-3} dpa. The normal-state resistance of each contact is indicated in the labels. **(D, E, F)** Examples of normalized conductance curves (black lines) with the relevant d-d fit (blue lines). The labels indicate the temperature at which the spectra were acquired, the value of the weight w_1 given by the fit, and the amplitude of the two gaps. **(G)** Temperature dependence of the raw conductance spectra of the contact with R_N = 48.7 Ω. The black curve (at T = 31 K) is the first that does not show zero-bias features and corresponds to the attainment of the bulk normal state. **(H)** The same conductance curves of panel **(G)** after normalization (symbols) and the relevant best-fitting curves (lines) calculated within the d-d model. **(I)** Temperature dependence of the energy gaps extracted from the fit of the curves in panel **(G)** using the s-d model (filled circles) and the d-d model (hollow circles). Solid lines are functions of the form of Eq. 1.

and Δ_{d2} (in the d-d model), the weight w_1 of the large gap (such that $w_2 = 1 - w_1$), the barrier parameters Z_1 and Z_2, the broadening parameters Γ_1 and Γ_2, and the angle α between the direction of (main) current injection and the antinodal direction of the d-wave gap. In the case of the d-d model, we assume $\alpha_1 = \alpha_2$, that implies that both the gaps have nodes in the same direction.

It turns out that both the models allow a good fit of the curves, as already pointed out in the case of pristine Rb-12442 and of the Ni-doped compound [12, 16]. The fact that irradiation does not change the gap structure is compatible both with the small effect on the critical temperature, and with the observed persistence of the same structure even in Ni-doped samples [12, 16] where the dopants introduce disorder and give rise to a much more significant T_c suppression (about 10 K). It is worth noting that, in order to reproduce the shape of the curves in panels E and F, the current injection has to be assumed to occur along the antinodal direction of the d-wave gap (i.e., $\alpha \simeq 0$). Just as an example, Figures 3D, E, F show the results of the d-d fit of three different curves measured at the lowest temperature. The fit is very good in the central part of the curves, while for higher energies (starting at about 10 meV) it fails due to an excess conductance probably due to the coupling of charge carriers with some bosonic mode involved in the superconducting pairing, as always observed in IBSs [19, 27, 29, 37]. The amplitudes of the superconducting gaps vary from one contact to another, probably due to the fact that the compound features more than two gaps, while we are using here a minimal (effective) two-gap model in order to keep the number of adjustable parameters to a minimum; moreover, the presence of the bosonic structures prevents an accurate determination of the larger gap, presumably causing its overestimation. The same happened in pristine Rb-12442, where the gap amplitudes were spread over a rather wide band of energies. In particular we found, for the d-d model, $\Delta_{d1} \in [4.8, 7.3]$ meV and $\Delta_{d2} \in [1.3, 3.0]$ meV. The gap amplitudes that result from the d-d fit of the curves in irradiated Rb-12442 are still generally compatible with the same distribution of gap values, meaning that no significant change in the gap amplitudes has been produced by irradiation. The same happens in the case of the s-d fit.

Figure 3G reports, as an example, the temperature dependence of the conductance curves of a point-contact whose normal-state resistance is 48.7 Ω. Above 31 K (black curve) the conductance

curves are smooth and do not show any feature at zero bias. This means that, at this temperature, the transition to the normal state is complete (in accordance with the green curve in Figure 1B). We thus chose this curve as the normal-state conductance and used it to normalize all the others at lower temperatures, with no need of any further rescaling or shift. The resulting normalized curves are shown in Figure 3H (symbols), vertically offset for clarity (apart from the lowest-temperature curve). The best-fitting curves, obtained within the *d*-*d* model, are shown as well as solid lines. The fit follows rather well the temperature evolution of the experimental curves; up to 23 K, it was possible to fit them by keeping all the parameters of the model (apart from the gaps) fixed to their lowest-temperature values, which is always a good indication of both the reliability of the curves (and of the normalization) and of the ability of the model to grasp the physics of the system. In particular, we used $w = 0.9$, $\Gamma_1 = 0.45$ meV, $Z_1 = 0.14$, $\Gamma_2 = 0.25$ meV, $Z_2 = 0.32$. Above 23 K, instead, the conductance curves start to shrink, becoming too narrow with respect to what predicted by the model; if one wants to reproduce this shrinking, the values of the barrier parameters and of the broadening parameters must be reduced. The possible reason for this behaviour can be understood by plotting the gap amplitudes resulting from the fit as a function of the temperature, as in Figure 3I. This plot shows that the small gap amplitude is rather robust against the model used (either *s*-*d* or *d*-*d*) which is natural since in either case the small gap has the *d*-wave symmetry. The amplitude of the larger gap instead depends on whether it is *s*-wave or *d*-wave, which is perfectly natural due to the different shape of the Andreev-reflection features that these two symmetries produce. The most relevant thing is that, no matter what the model is, the gap amplitudes follow a very clear trend which can be approximated by the solid and dashed curves, whose expression is

$$\Delta_i(T) = \Delta_i(0)\tanh\left(2.0\sqrt{\frac{T_c^A}{T}-1}\right) \quad (1)$$

where Δ_i is the gap of the i-th band and $T_c^A = 29$ K. This indicates that the behaviour is not exactly BCS, and that the Andreev critical temperature T_c^A (i.e., the temperature at which the Andreev signal disappears, and at which the superconducting bank of the junction becomes normal) is about 29 K, and thus smaller than $T_c = 31$ K at which the narrow zero-bias maximum in the experimental curves disappears (see Figure 3G). As is clear from Figure 1B, T_c^A falls in the proximity of the superconducting transition, but still in a region where the resistivity is zero. This is likely to be due to the non perfectly ballistic nature of the contact, so that a very small heating occurs in the contact region giving rise to a small mismatch between the "bulk" T_c^ρ and T_c^A. The same effect explains the narrow zero-bias peak that emerges at high temperature in the conductance curves: while at zero bias the temperature of the contact is equal to that of the bulk, on increasing the bias voltage the current gives rise to heating and, being close to the normal transition, this produces an increase in resistance (and thus a decrease in conductance). Such an effect ceases when the temperature at which the curve is acquired is already in a region where the normal transition (as measured by transport) is complete, since here the resistivity has a much weaker dependence on temperature. Figure 4 displays the temperature dependence of the zero-bias resistance (main panel) and conductance (inset). It is clear that the high-temperature behaviour of both these quantities is no longer due to the temperature dependence of the superconducting gap, but is related instead to the temperature dependence of the crystal's resistivity.

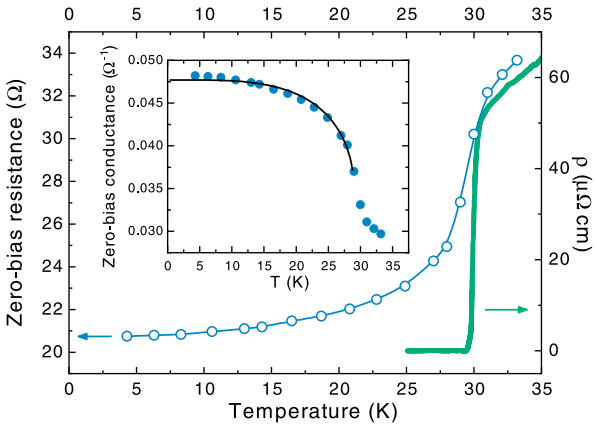

FIGURE 4
Temperature dependence of the zero-bias resistance extracted from the curves in Figure 3G (blue hollow circles, left scale) compared to the resistivity of the same crystal (solid green line, right scale). The inset shows the zero-bias conductance (filled blue circles), that follows the same temperature dependence of the gaps up to 29 K (solid black line).

4 Discussion

The response to proton-irradiation-induced disorder of Rb-12442 is qualitatively as expected for the IBSs, showing a suppression of the critical temperature and of the superfluid density due to the enhanced scattering of carriers in a multiband system. However, there is a relevant quantitative difference: below about 4–5 × 10^{-3} dpa, the T_c suppression rate with dpa in optimally-doped (Ba,K)Fe_2As_2 is about twice than for Rb-12442 samples, despite the similar pristine critical temperature of the two compositions. This is reported in Figure 5A, where the data obtained in this work on Rb-12442 are compared to the typical behavior exhibited by the 122 family of IBSs when exposed to the same irradiation process [35]. It is also evident that the T_c vs. dpa curve of Rb-12442 shows an upward curvature (or alternatively, that it can be divided in two separate linear trends with different slopes), implying an even lower dpa dependence at higher disorder levels. This behavior is quite unexpected, and could—in principle—be the result of an important change in the symmetry of the superconducting gap of the system. However, the fact that the experimental PCARS spectra measured on a sample with a disorder level of 5.3 × 10^{-3} dpa can be satisfactorily fitted using models employing the same gap symmetry describing pristine and Ni-doped Rb-12442 [12, 16] makes this scenario highly unlikely. Similarly to T_c, also the low-temperature value of the London penetration depth, as shown in Figure 5B, has a much smaller variation with dpa when compared to other IBSs. In this case, the modification with dpa is approximately linear in the whole investigated range.

These two observations indicate that the condensate in this system is affected much less than similar systems by the exposition to the same proton irradiation conditions. Since the composition, density and chemical nature of the 12442 and 122 families of IBSs is

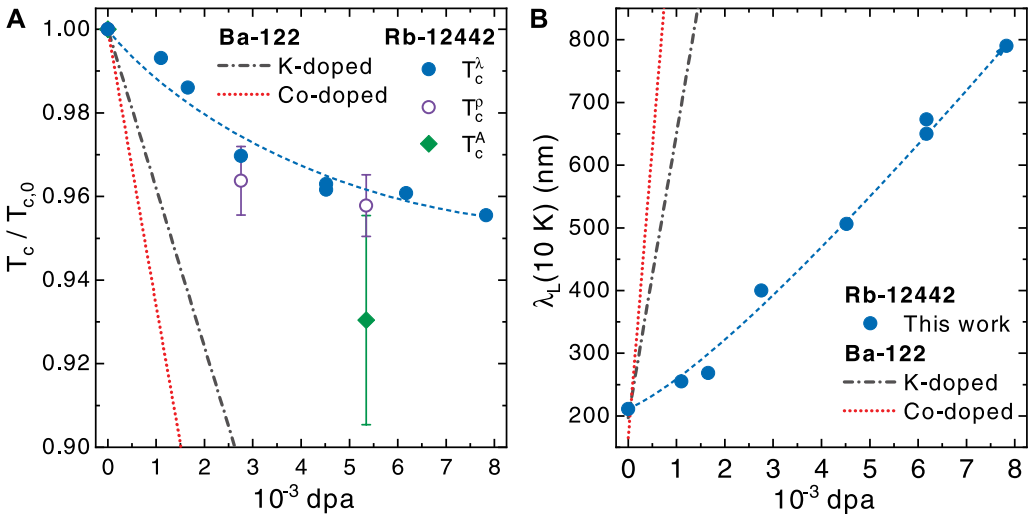

FIGURE 5
(A) Proton-irradiation-induced suppression of the superconducting critical temperature T_c for Rb-12442 samples, determined from CPWR analysis (T_c^λ, filled blue circles), from dc resistivity (T_c^ρ, hollow violet circles) and from PCARS measurements (T_c^A, filled green diamonds–the smaller value is due to localized contact heating as explained in the text). The dashed line is a guide for the eye. Data are normalized to the corresponding transition temperature at 0 dpa ($T_{c,0}$) and compared to the trend (black and red lines) showed by two optimally-doped systems of the 122 IBS family (K and Co-doped $BaFe_2As_2$), for which the scaling laws with dpa were reported [35]. **(B)** Proton irradiation-induced increase of the London penetration depth λ_L at $T = 10$ K for Rb-12442 samples (symbols, dashed line is a guide to the eye), compared to the trends shown by the same two IBS Ba-122 systems shown in **(A)** [35].

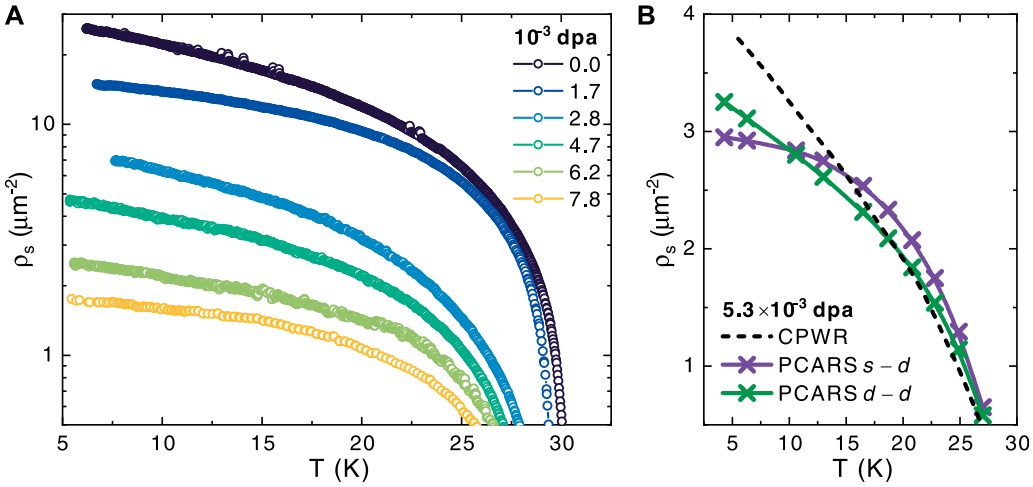

FIGURE 6
(A) Superfluid density ($\rho_s = \lambda_L^{-2}$) as a function of temperature T for increasing values of proton irradiation-induced disorder measured in displacements per atom (dpa), from CPWR measurements. **(B)** Data calculated from the gap values measured by PCARS (crosses) are compared to the temperature dependence of ρ_s deduced starting from CPWR data for the disorder level of 5.3×10^{-3} dpa.

similar, a similar defects morphology is induced in the samples. Therefore, either the recombination rate of the created defects is much higher in the 12442 family (possibly due to the more layered and anisotropic structure), or the superconducting state itself is more radiation-hard. The latter option could be related to the other peculiarities observed in this system, such as the observation of nodal behavior [16, 38–40] and its vicinity to the disappearance of the electron-like pockets [12].

A further confirmation of the robustness of nodal behavior in Rb-12442 against the introduction of disorder via proton irradiation can be obtained from the temperature dependence of the superfluid density. Figure 6A shows $\rho_s = \lambda_L^{-2}$ as a function of T determined from the $\lambda_L(T)$ curves shown in Figure 2A: beyond the suppression of the superfluid density in the entire temperature range with increasing dpa, it can be seen that all the $\rho_s(T)$ curves exhibit a smooth, kink-less behavior in the experimentally-accessible temperature range, and a clear linear dependence at low temperatures. Both features are consistent with the previous reports in pristine and Ni-doped Rb-12442 crystals [12, 16] and are typically associated with multigap superconductivity with

mainly interband coupling [41] and with the existence of at least one nodal gap [38, 39] respectively.

This interpretation can be further corroborated by combining the results obtained independently by means of the CPWR and PCARS measurements. As a matter of fact, the superfluid density can also be computed from the zero-temperature London penetration depth, $\lambda_L(0)$, and from the temperature-dependence of the gap values extracted from PCARS, $\Delta_i(T)$, as [42]:

$$\rho_s(T) = \frac{1}{\lambda_L(0)^2} \sum_i w_i \left[1 + \frac{1}{\pi} \int_0^{2\pi} \int_{\Delta_i(\phi,T)}^{\infty} \frac{\partial f}{\partial E} \frac{E dE d\phi}{\sqrt{E^2 - \Delta_i^2(\phi,T)}} \right]$$

where i identifies the band, $\Delta_i(\phi, T)$ is the angle-dependent superconducting gap function, $f = [1 + \exp(E/k_B T)]^{-1}$ is the Fermi function and w_i is the mixing weight of the i-th gap contribution (constrained by $w_1 + w_2 = 1$). For this latter parameter we use the same value previously employed for pristine undoped Rb-12442 [16] and consider it as a fixed parameter. One can factorize the angular and temperature dependencies of the gap as $\Delta_i(\phi, T) = \Delta_{0,i} f_\phi(\phi) f_T(T)$, where the angular function for d-wave (nodal) superconductors is $f_\phi(\phi) = \cos(2\phi)$ and the gap amplitude is the one measured by PCARS. To obtain the $\lambda_L(0)$ value for the disorder level of the sample measured by PCARS we linearly interpolate the data shown in Figure 5B.

The comparison between the superfluid data from PCARS obtained within this approach and the data from the CPWR technique is shown in Figure 6B, for the disorder level of 5.3×10^{-3} dpa. Violet (green) crosses indicate the values of ρ_s calculated by starting from the PCARS gaps extracted from the s-d (d-d) fit, while the black dotted line represents the $\rho_s(T)$ curve deduced from the CPWR analysis for a disorder level of 5.3×10^{-3} dpa. The PCARS d-d case seems to yield the best qualitative match with the CPWR trend since it reproduces the linear behavior at low temperatures (even though with a lower slope), contrarily to what is found for the s-d case, where the s-wave component forces the curve to saturate.

In summary, we reported on the unusually weak irradiation effects on the superconducting properties of the IBS Rb-12442. The analysis was performed by CPWR and PCARS on single crystals before and after 3.5-MeV proton irradiation, at different damage levels up to 7.8×10^{-3} dpa. Both the critical temperature and the superfluid density are shown to decrease with disorder, but at a much lower rate than for other IBS systems with similar pristine values of T_c and ρ_s. Moreover, the critical temperature degradation shows also a qualitatively different trend with respect to the other mentioned IBSs, i.e., a change of linear slope or possibly an upward curvature, implying an even smaller disorder dependence for higher irradiation doses. A comparison between results from the two measurement techniques allowed us to elaborate about the order parameter symmetry, in an effective two-gap approach. The evidence of a nodal behavior is confirmed also for the irradiated crystal and on the basis of the comparison we are inclined to select the d-d scenario rather than the s-d one, even though an ultimate evidence is still needed, which encourages further investigation.

Data availability statement

The original contributions presented in the study are included in the article/Supplementary Material, further inquiries can be directed to the corresponding author.

Author contributions

DT: Conceptualization, Investigation, Writing–original draft, Writing–review and editing. EP: Data curation, Investigation, Visualization, Writing–original draft, Writing–review and editing. MF: Investigation, Writing–review and editing. RG: Investigation, Writing–review and editing. LG: Investigation, Writing–review and editing. XY: Investigation, Writing–review and editing. XX: Investigation, Writing–review and editing. ZS: Investigation, Writing–review and editing. DD: Formal Analysis, Funding acquisition, Investigation, Resources, Writing–original draft, Writing–review and editing. GG: Conceptualization, Formal Analysis, Funding acquisition, Investigation, Resources, Writing–original draft, Writing–review and editing.

Funding

The author(s) declare financial support was received for the research, authorship, and/or publication of this article. This work was supported by the Italian Ministry of Education, University, and Research through the PRIN-2017 program: DT, MF, RG, LG, and GG acknowledge support from project "HIBiSCUS", Grant No. 201785KWLE; EP and DD acknowledge support from project "Quantum2D", Grant No. 2017Z8TS5B). DT also acknowledges that this study was carried out within the Ministerial Decree no. 1062/2021 and received funding from the FSE REACT-EU—PON Ricerca e Innovazione 2014-2020.

Acknowledgments

Support by INFN CSN5 and by the European Cooperation in Science and Technology (COST) action CA21144 "SUPERQUMAP" is also acknowledged.

Conflict of interest

The authors declare that the research was conducted in the absence of any commercial or financial relationships that could be construed as a potential conflict of interest.

Publisher's note

Author disclaimer

This manuscript reflects only the authors' views and opinions, neither the European Union nor the European Commission can be considered responsible for them.

References

1. Korshunov MM, Togushova YN, Dolgov OV. Impurities in multiband superconductors. *Physics-Uspekhi* (2016) 59:1211–40. doi:10.3367/UFNe.2016.07.037863

2. Efremov DV, Korshunov MM, Dolgov OV, Golubov AA, Hirschfeld PJ. Disorder-induced transition between $s_{\pm}$ and s_{++} states in two-band superconductors. *Phys Rev B* (2011) 84:180512. (R). doi:10.1103/physrevb.84.180512

3. Ghigo G, Torsello D, Ummarino GA, Gozzelino L, Tanatar MA, Prozorov R, et al. Disorder-driven transition from $s_{\pm}$ to s_{++} superconducting order parameter in proton irradiated $Ba(Fe_{1-x}Rh_x)_2As_2$ single crystals. *Phys Rev Lett* (2018) 121:107001. doi:10.1103/PhysRevLett.121.107001

4. Ghigo G, Ummarino GA, Gozzelino L, Gerbaldo R, Laviano F, Torsello D, et al. Effects of disorder induced by heavy-ion irradiation on $(Ba_{1-x}K_x)Fe_2As_2$ single crystals, within the three-band Eliashberg $s_{\pm}$ wave model. *Sci Rep* (2017) 7:13029. doi:10.1038/s41598-017-13303-5

5. Ghigo G, Torsello D, Gerbaldo R, Gozzelino L, Pyon S, Veshchunov IS, et al. Effects of proton irradiation on the magnetic superconductor $EuFe_2(As_{1-x}P_x)_2$. *Supercond Sci Technol* (2020) 33:094011. doi:10.1088/1361-6668/aba355

6. Torsello D, Ummarino G, Bekaert J, Gozzelino L, Gerbaldo R, Tanatar M, et al. Tuning the intrinsic anisotropy with disorder in the $CaKFe_4As_4$ superconductor. *Phys Rev Appl* (2020) 13:064046. doi:10.1103/PhysRevApplied.13.064046

7. Torsello D, Gerbaldo R, Gozzelino L, Laviano F, Takahashi A, Park A, et al. Twofold role of columnar defects in iron based superconductors. *Supercond Sci Technol* (2020) 33:094012. doi:10.1088/1361-6668/aba350

8. Hirschfeld PJ, Korshunov MM, Mazin II. Gap symmetry and structure of Fe-based superconductors. *Rep Prog Phys* (2011) 74:124508. doi:10.1088/0034-4885/74/12/124508

9. Wang ZC, He CY, Wu SQ, Tang ZT, Liu Y, Ablimit A, et al. Superconductivity in $KCa_2Fe_4As_4F_2$ with separate double Fe_2As_2 layers. *J Am Chem Soc* (2016) 138:7856–9. doi:10.1021/jacs.6b04538

10. Wang Z, He C, Tang Z, Wu S, Cao G. Crystal structure and superconductivity at about 30 K in $ACa_2Fe_4As_4F_2$ (A= Rb, Cs). *Sci China Mater* (2017) 60:83–9. doi:10.1007/s40843-016-5150-x

11. Wu SQ, Wang ZC, He CY, Tang ZT, Liu Y, Cao GH. Superconductivity at 33–37 K in $ALn_2Fe_4As_4O_2$ (A = K and Cs; Ln = lanthanides). *Phys Rev Mater* (2017) 1:044804. doi:10.1103/PhysRevMaterials.1.044804

12. Piatti E, Torsello D, Ghigo G, Daghero D. Spectroscopic studies of the superconducting gap in the 12442 family of iron-based compounds (Review article). *Low Temp Phys* (2023) 49:770–85. doi:10.1063/10.0019688

13. Wang T, Zhang C, Xu L, Wang J, Jiang S, Zhu Z, et al. Strong Pauli paramagnetic effect in the upper critical field of $KCa_2Fe_4As_4F_2$. *Science China Phys Mech Astron* (2020) 63:227412–6. doi:10.1007/s11433-019-1441-4

14. Yi X, Li M, Xing X, Meng Y, Zhao C, Shi Z. Single crystal growth and effects of Ni doping on the novel 12442-type iron-based superconductor $RbCa_2Fe_4As_4F_2$. *New J Phys* (2020) 22:073007. doi:10.1088/1367-2630/ab9427

15. Wang ZC, Liu Y, Wu SQ, Shao YT, Ren Z, Cao GH. Giant anisotropy in superconducting single crystals of $CsCa_2Fe_4As_4F_2$. *Phys Rev B* (2019) 99:144501. doi:10.1103/PhysRevB.99.144501

16. Torsello D, Piatti E, Ummarino GA, Yi X, Xing X, Shi Z, et al. Nodal multigap superconductivity in the anisotropic iron-based compound $RbCa_2Fe_4As_4F_2$. *npj Quantum Mater* (2022) 7:10–7. doi:10.1038/s41535-021-00419-1

17. Blonder GE, Tinkham M, Klapwijk TM. Transition from metallic to tunneling regimes in superconducting microconstrictions: excess current, charge imbalance, and supercurrent conversion. *Phys Rev B* (1982) 25:4515–32. doi:10.1103/PhysRevB.25.4515

18. Daghero D, Gonnelli RS. Probing multiband superconductivity by point-contact spectroscopy. *Supercond Sci Technol* (2010) 23:043001. doi:10.1088/0953-2048/23/4/043001

19. Daghero D, Tortello M, Ummarino GA, Gonnelli RS. Directional point-contact Andreev-reflection spectroscopy of Fe-based superconductors: Fermi surface topology, gap symmetry, and electron–boson interaction. *Rep Prog Phys* (2011) 74:124509. doi:10.1088/0034-4885/74/12/124509

20. Wang T, Chu J, Jin H, Feng J, Wang L, Song Y, et al. Single-crystal growth and extremely high H_{c2} of 12442-type Fe-based superconductor $KCa_2Fe_4As_4F_2$. *The J Phys Chem C* (2019) 123:13925–9. doi:10.1021/acs.jpcc.9b04624

21. Xing X, Yi X, Li M, Meng Y, Mu G, Ge JY, et al. Vortex phase diagram in 12442-type $RbCa_2Fe_4As_4F_2$ single crystal revealed by magneto-transport and magnetization measurements. *Supercond Sci Technol* (2020) 33:114005. doi:10.1088/1361-6668/abb35f

22. Lim SHN, McKenzie DR, Bilek MMM. Van der Pauw method for measuring resistivity of a plane sample with distant boundaries. *Rev Sci Instrum* (2009) 80:075109. doi:10.1063/1.3183503

23. Ghigo G, Torsello D. *Analysis of microwave conductivity and penetration depth of iron based superconductors families*. Cham: Springer International Publishing (2022). p. 61–75. doi:10.1007/978-3-030-93910-6_3

24. Ghigo G, Fracasso M, Gerbaldo R, Gozzelino L, Laviano F, Napolitano A, et al. High-frequency ac susceptibility of iron-based superconductors. *Materials* (2022) 15:1079. doi:10.3390/ma15031079

25. Daghero D, Tortello M, Ummarino GA, Griveau JC, Colineau E, Eloirdi R, et al. Strong-coupling d-wave superconductivity in $PuCoGa_5$ probed by point-contact spectroscopy. *Nat Commun* (2012) 3:786. doi:10.1038/ncomms1785

26. Naidyuk YG, Yanson I. *Point-contact spectroscopy*. New York, NY: Springer (2005).

27. Daghero D, Piatti E, Zhigadlo ND, Ummarino GA, Barbero N, Shiroka T. Superconductivity of underdoped PrFeAs(O,F) investigated via point-contact spectroscopy and nuclear magnetic resonance. *Phys Rev B* (2020) 102:104513. doi:10.1103/physrevb.102.104513

28. Daghero D, Tortello M, Ummarino GA, Piatti E, Ghigo G, Hatano T, et al. Decoupling of critical temperature and superconducting gaps in irradiated films of a Fe-based superconductor. *Supercond Sci Technol* (2018) 31:034005. doi:10.1088/1361-6668/aaa8b9

29. Daghero D, Pecchio P, Ummarino G, Nabeshima F, Imai Y, Maeda A, et al. Point-contact Andreev-reflection spectroscopy in Fe(Te,Se) films: multiband superconductivity and electron-boson coupling. *Supercond Sci Technol* (2014) 27:124014. doi:10.1088/0953-2048/27/12/124014

30. Tanaka Y, Kashiwaya S. Theory of tunneling spectroscopy of *d*-wave superconductors. *Phys Rev Lett* (1995) 74:3451–4. doi:10.1103/physrevlett.74.3451

31. Kashiwaya S, Tanaka Y, Koyanagi M, Takashima H, Kajimura K. Origin of zero-bias conductance peaks in high-T_c superconductors. *Phys Rev B* (1995) 51:1350–3. doi:10.1103/physrevb.51.1350

32. Kashiwaya S, Tanaka Y, Koyanagi M, Kajimura K. Theory for tunneling spectroscopy of anisotropic superconductors. *Phys Rev B* (1996) 53:2667–76. doi:10.1103/physrevb.53.2667

33. Park A, Pyon S, Sun Y, Veshchunov I, Chen J, Ito N, et al. Quasiparticle scattering in 3 MeV proton irradiated $BaFe_2(As_{0.67}P_{0.33})_2$. *Phys Rev B* (2018) 98:054512. doi:10.1103/PhysRevB.98.054512

34. Ziegler JF, Ziegler M, Biersack J. SRIM – the stopping and range of ions in matter. *Nucl Instrum Meth B* (2010) 268:1818–23. doi:10.1016/j.nimb.2010.02.091

35. Torsello D, Gozzelino L, Gerbaldo R, Tamegai T, Ghigo G. Scaling laws for ion irradiation effects in iron-based superconductors. *Sci Rep* (2021) 11:5818. doi:10.1038/s41598-021-84699-4

36. Yi X, Xing X, Meng Y, Zhou N, Wang C, Sun Y, et al. Anomalous second magnetization peak in 12442-type $RbCa_2Fe_4As_4F_2$ superconductors. *Chin Phys Lett* (2023) 40:027401. doi:10.1088/0256-307X/40/2/027401

37. Tortello M, Daghero D, Ummarino GA, Stepanov VA, Jiang J, Weiss JD, et al. Multigap superconductivity and strong electron-boson coupling in Fe-based superconductors: a point-contact Andreev-reflection study of $BaFe_{1-x}Co_xAs_2$ single crystals. *Phys Rev Lett* (2010) 105:237002. doi:10.1103/PhysRevLett.105.237002

38. Smidman M, Kirschner FKK, Adroja DT, Hillier AD, Lang F, Wang ZC, et al. Nodal multigap superconductivity in $KCa_2Fe_4As_4F_2$. *Phys Rev B* (2018) 97:060509. doi:10.1103/PhysRevB.97.060509

39. Kirschner FKK, Adroja DT, Wang ZC, Lang F, Smidman M, Baker PJ, et al. Two-gap superconductivity with line nodes in $CsCa_2Fe_4As_4F_2$. *Phys Rev B* (2018) 97:060506. doi:10.1103/PhysRevB.97.060506

40. Wang T, Chu J, Feng J, Wang L, Xu X, Li W, et al. Low temperature specific heat of 12442-type $KCa_2Fe_4As_4F_2$ single crystals. *Sci China Phys Mech Astron* (2020) 63:297412–6. doi:10.1007/s11433-020-1549-9

41. Torsello D, Ummarino GA, Gozzelino L, Tamegai T, Ghigo G. Comprehensive Eliashberg analysis of microwave conductivity and penetration depth of K-Co-and P-substituted $BaFe_2As_2$. *Phys Rev B* (2019) 99:134518. doi:10.1103/PhysRevB.99.134518

42. Chandrasekhar BS, Einzel D. The superconducting penetration depth from the semiclassical model. *Ann Phys* (1993) 505:535–46. doi:10.1002/andp.19935050604

frontiers | Frontiers in Physics

TYPE Original Research
PUBLISHED 03 May 2024
DOI 10.3389/fphy.2024.1384275

OPEN ACCESS

EDITED BY
Takeshi Mizushima,
Osaka University, Japan

REVIEWED BY
Mario Cuoco,
National Research Council (CNR), Italy
Philip Brydon,
University of Otago, New Zealand

*CORRESPONDENCE
Vudtiwat Ngampruetikorn,
vudtiwat.ngampruetikorn@sydney.edu.au
J. A. Sauls,
sauls@lsu.edu

RECEIVED 09 February 2024
ACCEPTED 08 March 2024
PUBLISHED 03 May 2024

CITATION
Ngampruetikorn V and Sauls JA (2024), Anomalous Hall effects in chiral superconductors.
Front. Phys. 12:1384275.
doi: 10.3389/fphy.2024.1384275

Anomalous Hall effects in chiral superconductors

Vudtiwat Ngampruetikorn[1,2,3,4]* and J. A. Sauls[1,2,5]*

[1]Center for Applied Physics and Superconducting Technologies, Department of Physics, Northwestern University, Evanston, IL, United States, [2]Fermi National Accelerator Laboratory, Batavia, IL, United States, [3]Initiative for the Theoretical Sciences, The Graduate Center, City University of New York, New York, NY, United States, [4]School of Physics, University of Sydney, Sydney, NSW, Australia, [5]Hearne Institute of Theoretical Physics, Department of Physics and Astronomy, Louisiana State University, Baton Rouge, LA, United States

We report theoretical results for the electronic contribution to thermal and electrical transport for chiral superconductors belonging to even or odd-parity E_1 and E_2 representations of the tetragonal and hexagonal point groups. Chiral superconductors exhibit novel properties that depend on the topology of the order parameter and Fermi surface, and—as we highlight—the structure of the impurity potential. An anomalous thermal Hall effect is predicted and shown to be sensitive to the winding number, ν, of the chiral order parameter via Andreev scattering that transfers angular momentum from the chiral condensate to excitations that scatter off the random potential. For heat transport in a chiral superconductor with isotropic impurity scattering, i.e., point-like impurities, a transverse heat current is obtained for $\nu = \pm 1$, but vanishes for $|\nu| > 1$. This is not a universal result. For finite-size impurities with radii of order or greater than the Fermi wavelength, $R \geq \hbar/p_f$, the thermal Hall conductivity is finite for chiral order with $|\nu| \geq 2$, and determined by a specific Fermi-surface average of the differential cross-section for electron-impurity scattering. Our results also provide quantitative formulae for analyzing and interpreting thermal transport measurements for superconductors predicted to exhibit broken time-reversal and mirror symmetries.

KEYWORDS

topological superconductivity, chiral superconductors, broken time-reversal symmetry, broken mirror symmetry, thermal transport, anomalous Hall transport, Hall effects, impurity disorder

1 Introduction

The remarkable properties of the spin-triplet, p-wave phases of superfluid ^{3}He have stimulated research efforts to discover and identify electronic superconductors with novel broken symmetries and non-trivial ground-state topology [1–6], driven in part by predictions of novel transport properties. *Chiral* superfluids and superconductors are topological phases with gapless Fermionic excitations that reflect the momentum-space topology of the condensate of Cooper pairs. The A-phase of superfluid ^{3}He was definitively identified as a chiral p-wave superfluid by the observation of anomalous Hall transport of electrons moving through a quasiparticle fluid of chiral Fermions [7, 8]. A chiral d-wave state was proposed for doped graphene [9, 10], while a chiral p-wave state is proposed for MoS [11]. There is evidence from μSR of broken time-reversal symmetry onsetting at the superconducting transition for the pnictide SrPtAs [12], and a chiral d-wave state has been proposed as the ground state [13]. Recent μSR experiments also provide evidence for chiral d-wave superconductivity in the pnictide $LaPt_3P$ [14]. The perovskite, Sr_2RuO_4, has been

studied extensively and was proposed as a promising candidate for chiral p-wave superconductivity (E_u pairing with $\vec{\Delta} = \hat{\mathbf{d}}(p_x + ip_y)$), in part based on similarities of its normal-state Fermi-liquid properties with those of liquid ^{3}He [15, 16]. Evidence of broken time-reversal symmetry from both μSR and Kerr rotation measurements support an identification of Sr_2RuO_4 as a chiral superconductor [17, 18]. However, experiments designed to detect the theoretically predicted chiral edge currents [19], or to test for the two-dimensionality of the E_u representation that is a necessary requirement to support a chiral ground state, are so far inconclusive, or report null results [20–23]. Recent transport measurements also appear to conflict with the chiral p-wave identification based on the E_u representation; i.e., thermal conductivity measurements at low temperatures and as a function of magnetic field, which probe the low-energy quasiparticle excitation spectrum, are consistent with the nodal line structure of a d-wave order parameter, and inconsistent with the gap structure expected based on the E_u representation [24, 25]. The possibility that Sr_2RuO_4 is an even parity chiral superconductor has so far not been ruled out (see, e.g., Refs. [26–30]).

The first superconductor reported to show experimental evidence of broken time-reversal symmetry was the heavy fermion superconductor, UPt_3, based on μSR linewidth measurements [31]. This experiment followed theoretical predictions of broken time-reversal symmetry in the B-phase of UPt_3, i.e., the lower temperature superconducting phase [32]. Another notable signature of broken time-reversal symmetry is the onset of Kerr rotation as UPt_3 enters its low-temperature B-phase [33]. More recently, a neutron scattering experiment, using vortices as a probe for the superconducting state in the bulk, offers yet another piece of evidence for broken time-reversal symmetry in UPt_3 [6]. These results support the identification of a chiral superconducting phase of UPt_3, and they also support the basic theoretical model of a multi-component order parameter belonging to a two-dimensional representation of the hexagonal point group, D_{6h}, in which a weak symmetry breaking field lifts the degeneracy of the two-component order stabilizing two distinct superconducting phases in zero magnetic field [32, 34]. In this theory the predicted A phase of UPt_3 is time-reversal symmetric with pronounced anisotropic pairing correlations in the hexagonal plane [35, 36], is preferentially selected by the symmetry breaking field, and nucleates at $T_{c_1} = 560\,\mathrm{mK}$ as the first superconducting phase. The B-phase develops as the sub-dominant partner of the two-dimensional representation nucleates at $T_{c_2} \approx 470\,\mathrm{mK}$, such that the low-temperature superconducting phase spontaneously breaks both time-reversal and mirror-reflection symmetries, the latter defined by a plane containing the chiral axis which is aligned parallel (or anti-parallel) to the c-axis of UPt_3.

There are four two-dimensional representations of D_{6h}: two even-parity representations, E_{1g} and E_{2g}, and two odd-parity representations, E_{1u} and E_{2u}, all of which allow for chiral ground states [37, 38]. The chiral ground states belonging to the E_1 and E_2 representations are defined by zeroes of the Cooper pair amplitude at points $\mathbf{p} = \pm p_f \hat{\mathbf{z}}$ on the Fermi surface that are protected by the topology of the orbital order parameter in momentum space, i.e., $\Delta(\mathbf{p}) = |\Delta(\mathbf{p})|\, e^{i\nu\phi_{\mathbf{p}}}$, where $\phi_{\mathbf{p}}$ is the azimuthal angle defining a point $\mathbf{p}$ on the Fermi surface, and $\nu = \pm 1$ ($\nu = \pm 2$) for the E_1 (E_2) representations[1] The bulk of the experimental evidence—thermodynamic, H-T phase diagram [37, 39, 40], thermal transport [41, 42], ultra-sound [43], Josephson tunneling [3], SANS [5] and optical spectroscopy measurements [33]—supports the identification of UPt_3 as an odd-parity superconductor with an order parameter belonging to the E_{2u} representation, *and* a chiral B-phase order parameter of the form, $\vec{\Delta}_{\pm}(\mathbf{p}) = \Delta_B(T)\hat{\mathbf{d}}\hat{p}_z(\hat{p}_x \pm i\hat{p}_y)^2 \sim \hat{\mathbf{d}}e^{\pm i2\phi_{\mathbf{p}}}$. The vector $\hat{\mathbf{d}}$ is the quantization axis along which the spin-triplet Cooper pairs have zero spin projection, i.e., an equal-spin-pairing (ESP) state [39]. A key feature of the E_{2u} chiral order parameter is the winding number $\nu = \pm 2$. The Josephson interference experiment described in Ref. [3] can discriminate between $|\nu| = 1$ and $|\nu| = 2$ chiral ground states. Indeed the report of a π phase shift in the Fraunhofer pattern for the corner-SQUID geometry, combined with the observations of broken time-reversal symmetry [31, 33], provides strong evidence in favor a $|\nu| = 2\,(E_{2u})$ chiral B-phase of UPt_3. However, conclusive evidence for *bulk* chiral superconductivity remains elusive. A zero-field Hall transport measurement is an ideal experiment to confirm broken time-reversal and mirror symmetries in the bulk of a chiral superconductor candidate.

2 Anomalous Hall transport

The winding number of the order parameter for a chiral superconductor reflects the topology of the superconducting ground state. For a fully gapped chiral superconductor ν is related to the Chern number defined in terms of the Bogoliubov-Nambu Hamiltonian in 2D momentum space, or for chiral superconductors defined on a 3D Fermi surface the effective two-dimensional spectrum at fixed $p_z \neq 0$, $\mathcal{C}(p_z) = \frac{1}{2\pi}\int d^2p\,\Omega_z(\mathbf{p})$, where $\Omega_z(\mathbf{p})$ is the Berry curvature [44]. The result for the Chern number is $\mathcal{C}(p_z) = \nu$, which provides topological protection for a spectrum of chiral Fermions.

For 2D chiral phases there is a spectrum of massless chiral Fermions confined on the boundary (edge states) with the zero-energy state enforced by the bulk topology. However, for a chiral order parameter defined on a closed 3D Fermi surface there is also a bulk spectrum of gapless Weyl-Majorana Fermions with momenta near the nodal points $p_z = \pm p_f$, in addition to a *spectrum* of massless chiral Fermions confined on surfaces normal to the [1,0,0] and [0,1,0] planes [45].

2.1 Anomalous edge transport

For a fully gapped chiral p-wave ground state in two dimensions the spectrum of chiral edge Fermions is predicted to give rise to quantized heat and mass transport in chiral

1 More complex chiral order parameters with large winding numbers are allowed by the point group symmetry, c.f. Ref. [51]; $\nu = \pm 1, \pm 2$ are the loweset order harmonics consistent with the E_1 and E_2 representations, respectively.

superfluids and superconductors [45–49]. In particular, an anomalous thermal Hall conductance is predicted to be quantized, $K_{xy}/k_BT = \frac{\pi}{12}k_B/\hbar$ based on the low-energy effective field theory of the chiral edge states [46, 50]. This result is also obtained from the topology of the bulk order parameter combined with linear response theory based on the Bogoliubov Hamiltonian for 2D $p_x + ip_y$ topological superconductors [49].

For a chiral superconductor defined on a 3D Fermi surface an anamolous thermal Hall current is predicted, but is not quantized in units of a fundamental quantum of conductance. Based on the linear response theory of Qin et al. [50] Goswami and Nevidomsky obtained a result for the anomalous thermal Hall conductivity of the B-phase of UPt_3 for $T \ll T_{c_2}$ [44],

$$\kappa_{xy}\Big/k_BT = \nu\frac{\pi}{6}\frac{k_B}{\hbar}\left(\frac{\Delta p}{2\pi\hbar}\right). \tag{1}$$

The anomalous thermal Hall conductivity reflects the number of branches of chiral Fermions confined on the [1,0,0] or [0,1,0] surface, i.e., $|\nu| = 2$ for the E_{2u} chiral ground state. The non-universality of the thermal Hall conductivity is reflected by the term Δp, which is the "distance" between the two topologically protected $\nu = 2$ Weyl points at $\hat{p}_z = \pm 1$ on a projected surface containing the chiral axis; e.g., $\Delta p = 2p_f$ for a spherical Fermi surface [44].

Thus, heat transport experiments could decisively identify the broken symmetries and topology of superconductors predicted to exhibit chiral order. The thermal conductivity depends on both the topology of the order parameter and the Fermi surface. The anomalous thermal Hall effect, in which a temperature gradient generates heat currents perpendicular to it, results from broken time-reversal and mirror symmetries—a direct signature of chiral pairing[2]. A zero-field thermal Hall experiment can also be used as a signature of chiral edge states. However, zero-field thermal Hall transport has remained elusive thus far.

2.2 Impurity-induced anomalous transport

Here we consider zero-field Hall transport resulting from electron-impurity interactions in the bulk of the superconductor, which we show are easily several orders of magnitude larger than the edge contribution [52]. There are earlier theoretical predictions for impurity-induced anomalous thermal Hall effects in chiral superconductors based on point-like impurities by several authors [53–55]. As we show, the point-like impurity model, which includes only s-wave quasiparticle-impurity scattering, predicts zero Hall response except for Chern number $\nu = \pm 1$ [52], i.e., only for chiral p-wave superconductors [53].

In the following we present a self-consistent theory incorporating the effects of finite-size impurities and show that such effects are essential for a quantitative description of Hall transport in chiral superconductors. Experimental observation of an impurity-induced anomalous thermal Hall effect would provide a definitive signature of chiral superconductivity. The bulk effect can easily dominate the edge state contribution to the anomalous Hall current, except in ultra-pure fully gapped chiral superconductors.

3 Transport theory

We start from the Keldysh extension [56] of the transport-like equations originally developed by Eilenberger, Larkin and Ovchinnikov for equilibrium states of superconductors [57, 58], and extended by Larkin and Ovchinnikov to describe superconductors out of equilibrium [59]. This formalism is referred to as "quasiclassical theory". For reviews see Refs. [61–63]. The quasiclassical theory is formulated in terms of 4×4 matrix propagators for Fermionic quasiparticles and Cooper pairs that describe the space-time evolution of the their non-equilibrium distribution functions, as well as the dynamical response of the low-energy spectral functions and the superconducting order parameter. Here we are interested in the response to static, or low-frequency, thermal gradients and external forces that couple to energy, mass and charge currents. We follow as much as possible the notation and conventions of theory developed for thermal transport in unconventional superconductors by Graf et al. [64].

3.1 Keldysh-Eilenberger equations

The quasiclassical transport equations are matrix equations in particle-hole (Nambu) space which describe the dynamics of quasiparticle excitations and Cooper pairs. Physical properties, such as the spectral density, currents or response functions are expressed in terms of components of the Keldysh matrix propagator,

$$\check{G}(\mathbf{p},\varepsilon;\mathbf{r},t) = \begin{pmatrix} \hat{g}^R & \hat{g}^K \\ 0 & \hat{g}^A \end{pmatrix}, \tag{2}$$

where $\hat{g}^{R,A,K}(\mathbf{p},\varepsilon;\mathbf{r},t)$ are the 4×4 retarded (R), advanced (A) and Keldysh (K) matrix propagators.

The nonequilibrium dynamics is described by a transport equation for the Keldysh propagator,

$$\begin{aligned}\hat{H}^R \circ \hat{g}^K(\mathbf{p},\mathbf{r};\varepsilon,t) - \hat{g}^K \circ \hat{H}^A(\mathbf{p},\mathbf{r};\varepsilon,t) + \hat{g}^R \circ \hat{\Sigma}^K(\mathbf{p},\mathbf{r};\varepsilon,t) \\ -\hat{\Sigma}^K \circ \hat{g}^A(\mathbf{p},\mathbf{r};\varepsilon,t) + i\mathbf{v}_\mathbf{p}\cdot\boldsymbol{\nabla}\hat{g}^K(\mathbf{p},\mathbf{r};\varepsilon,t) = 0,\end{aligned} \tag{3}$$

as well as transport equations for the retarded and advanced propagators,

$$\left[\hat{H}^{R,A},\hat{g}^{R,A}\right]_\circ + i\mathbf{v}_\mathbf{p}\cdot\boldsymbol{\nabla}\hat{g}^{R,A}(\mathbf{p},\mathbf{r};\varepsilon,t) = 0, \tag{4}$$

where

$$\hat{H}^{R,A}(\mathbf{p},\mathbf{r};\varepsilon,t) = \varepsilon\hat{\tau}_3 - \hat{v}(\mathbf{p},\mathbf{r};t) - \hat{\Sigma}^{R,A}(\mathbf{p},\mathbf{r};\varepsilon,t) \tag{5}$$

is defined in terms of the excitation energy, ε, the coupling to external fields, $\hat{v}$, and the self-energies, $\hat{\Sigma}^{R,A}$. Pairing correlations, as well as effects of scattering by impurities, phonons and quasiparticles are described by the self-energies, $\hat{\Sigma}^{R,A,K}$. The

2 Note that time-reversal and mirror symmetries need not be broken simultaneously. For example, a three-band superconductor may break timereversal symmetry when the order parameter defined on each band has a different phase [60]. Mirror symmetry is however preserved and Hall effects are therefore not expected in this system.

convolution product ($\circ$-product) appearing in Eqs. 3, 4, in the mixed energy-time representation, is defined by,

$$\hat{A}\circ\hat{B}(\varepsilon;t)=e^{\frac{i}{2}\left[\partial_\varepsilon^A\partial_t^B-\partial_t^A\partial_\varepsilon^B\right]}\hat{A}(\varepsilon;t)\hat{B}(\varepsilon;t). \tag{6}$$

Note that ε is the excitation energy and t is the external time variable. The operator expansion for the convolution product is particularly useful if the external timescale, $t\sim\omega^{-1}$ is slow compared to the typical internal dynamical timescales, $\hbar/\Delta$ and τ, i.e., $\omega\ll|\varepsilon|\sim\Delta$ and $\omega\ll 1/\tau$. In this limit we can expand Eq. 6,

$$\hat{A}\circ\hat{B}(\varepsilon;t)\approx\hat{A}(\varepsilon;t)\hat{B}(\varepsilon;t)+\frac{i}{2}\left[\frac{\partial\hat{A}}{\partial\varepsilon}\frac{\partial\hat{B}}{\partial t}-\frac{\partial\hat{A}}{\partial t}\frac{\partial\hat{B}}{\partial\varepsilon}\right]. \tag{7}$$

The quasiclassical transport equations are supplemented by the normalization conditions [57, 58],

$$\hat{g}^{R,A}\circ\hat{g}^{R,A}=-\pi^2\,\hat{1} \tag{8}$$

$$\hat{g}^{R}\circ\hat{g}^{K}-\hat{g}^{K}\circ\hat{g}^{A}=0. \tag{9}$$

3.2 Quasiclassical propagators

The quasiclassical propagators are 4×4-matrices whose structure describes the internal quantum-mechanical degrees of freedom of quasiparticles and quasiholes. In addition to spin, the particle-hole degree of freedom is of fundamental importance to our understanding of superconductivity. In the normal state of a metal or Fermi liquid there is no quantum-mechanical coherence between particle and hole excitations. By contrast, the distinguishing feature of the superconducting state is the existence of quantum mechanical coherence between normal-state particle and hole excitations. Particle-hole coherence is the origin of persistent currents, Josephson effects, Andreev scattering, flux quantization, and all other nonclassical superconducting effects. The quasiclassical propagators are directly related to density matrices which describe the quantum-statistical state of the internal degrees of freedom. Nonvanishing off-diagonal elements in the particle-hole density matrix are indicative of superconductivity, indeed the onset of non-vanishing off-diagonal elements is the signature of the superconducting transition.

The Nambu matrix structure of the propagators and self energies is

$$\hat{g}^{R,A,K}=\begin{pmatrix} g^{R,A,K}+\mathbf{g}^{R,A,K}\cdot\boldsymbol{\sigma} & (f^{R,A,K}+\mathbf{f}^{R,A,K}\cdot\boldsymbol{\sigma})i\sigma_y \\ i\sigma_y(\bar{f}^{R,A,K}+\bar{\mathbf{f}}^{R,A,K}\cdot\boldsymbol{\sigma}) & \bar{g}^{R,A,K}-\bar{\mathbf{g}}^{R,A,K}\cdot\sigma_y\boldsymbol{\sigma}\sigma_y\end{pmatrix}. \tag{10}$$

The 16 matrix elements of $\hat{g}^{R,A,K}$ are expressed in terms of four spin-scalars ($g^{R,A,K}$, $\bar{g}^{R,A,K}$, $f^{R,A,K}$, $\bar{f}^{R,A,K}$) and four spin-vectors ($\mathbf{g}^{R,A,K}$, $\bar{\mathbf{g}}^{R,A,K}$, $\mathbf{f}^{R,A,K}$, $\bar{\mathbf{f}}^{R,A,K}$). All matrix elements are functions of $\mathbf{p}$, ε, $\mathbf{r}$ and t. The spin scalars $g^{R,A,K}$, $\bar{g}^{R,A,K}$ determine spin-independent properties such as the charge, mass and heat current densities, $\mathbf{j}_e(\mathbf{r},t)$, $\mathbf{j}_m(\mathbf{r},t)$ and $\mathbf{j}_q(\mathbf{r},t)$, as well as the local density of states

$$N(\varepsilon;\mathbf{r},t)=N_f\int d\mathbf{p}\left[-\frac{1}{\pi}\mathrm{Im}\frac{1}{2}\mathrm{Tr}\left\{\hat{\tau}_3\hat{g}^R(\mathbf{p},\varepsilon;\mathbf{r},t)\right\}\right], \tag{11}$$

where N_f is the normal-state density of states at the Fermi energy. The integration is over the Fermi surface *weighted* by the angle-resolved normal density of states at the Fermi surface, $n(\mathbf{p})$, normalized to

$$\int d\mathbf{p}(\ldots)\equiv\int dS_{\mathbf{p}}n(\mathbf{p})(\ldots)\ \text{with}\int dS_{\mathbf{p}}n(\mathbf{p})=1. \tag{12}$$

The current densities are determined from Fermi-surface averages over the elementary currents, $[e\mathbf{v}_{\mathbf{p}}]$, mass, $[m\mathbf{v}_{\mathbf{p}}]$, and energy, $[\varepsilon\mathbf{v}_{\mathbf{p}}]$, weighted by the scalar components of the diagonal Keldysh propagator. In particular, the charge and heat current densities are given by

$$\mathbf{j}^{(e)}(\mathbf{r},t)=N_f\int d\mathbf{p}\int\frac{d\varepsilon}{4\pi i}[e\mathbf{v}_{\mathbf{p}}]\mathrm{Tr}\left\{\hat{\tau}_3\,\hat{g}^K(\mathbf{p},\varepsilon;\mathbf{r},t)\right\}, \tag{13}$$

$$\mathbf{j}^{(q)}(\mathbf{r},t)=N_f\int d\mathbf{p}\int\frac{d\varepsilon}{4\pi i}[\varepsilon\mathbf{v}_{\mathbf{p}}]\mathrm{Tr}\left\{\hat{g}^K(\mathbf{p},\varepsilon;\mathbf{r},t)\right\}. \tag{14}$$

The off-diagonal components, $f^{R,A,K}$ and $\mathbf{f}^{R,A,K}$, are the anomalous propagators that characterize the pairing correlations of the superconducting state. Spin-singlet pairing correlations are encoded in f^K, while $\mathbf{f}^K$ is the measure of spin-triplet pairing correlations. Pair correlations develop spontaneously at temperatures below the superconducting transition temperature T_c. The anomalous propagators are not directly measurable, but the correlations they describe are observable via their coupling to the "diagonal" propagators, $g^{R,A,K}$ and $\mathbf{g}^{R,A,K}$, through the transport equations.

3.3 Coupling to external and internal forces

The couplings of low-energy excitations to electromagnetic fields are defined in terms of the scalar and vector potentials,

$$\hat{v}_{\mathrm{EM}}=e\,\varphi(\mathbf{r},t)\hat{\tau}_3+\frac{e}{c}\mathbf{v}_{\mathbf{p}}\cdot\mathbf{A}(\mathbf{r},t)\hat{\tau}_3. \tag{15}$$

Note that $e\hat{\tau}_3$ encodes the charge coupling of both particle and hole excitations to the electromagnetic field. The magnetic field also couples to the quasiparticles and pairs via the Zeeman energy, $\hat{v}_Z=\gamma\hat{\mathbf{S}}\cdot\mathbf{B}(\mathbf{r},t)$, where $\mathbf{B}=\boldsymbol{\nabla}\times\mathbf{A}$, γ is the gyromagnetic ratio of the normal-state quasiparticles, and $\hat{\mathbf{S}}=\frac{1}{2}(\hat{1}+\hat{\tau}_3)\boldsymbol{\sigma}-\frac{1}{2}(\hat{1}-\hat{\tau}_3)\sigma_y\boldsymbol{\sigma}\sigma_y$ is the Nambu representation of the Fermion spin operator.

3.3.1 Mean-field self-energies

Superconductors driven out of equilibrium are also subject to internal forces on quasiparticles and Cooper pairs, originating from electron-electron, electron-phonon and electron-impurity interactions. These interactions enter the quasiclassical theory as self-energy terms, $\hat{\Sigma}^{R,A,K}$, in the transport Eqs. 3, 4, 5. We include self-energies that contribute to leading order in expansion parameters, $\mathbf{s}=\{1/k_f\xi,\ k_BT_c/E_f,1/k_f\ell,\hbar/\tau E_f,\Delta/E_f\ \ldots\}\ll1$, that define the low-energy, long-wavelength region of validity of Landau Fermi-liquid theory, and its extension to include BCS condensation [61, 63, 65].

The leading order contributions to the self-energy from quasiparticle-quasiparticle interactions correspond the mean-field

self-energies, $\hat{\Sigma}^{R,A,K}_{\rm mf}$, in the particle-hole (Landau) and particle-particle (Cooper) channels, and are represented by Eqs. 16, 17, respectively,[3]

$$\hat{\Sigma}(\mathbf{p}) = \int d\mathbf{p}' \fint \frac{d\varepsilon'}{4\pi i} \left[A^s(\mathbf{p},\mathbf{p}')\, g^K(\mathbf{p}',\varepsilon')\hat{1} + A^a(\mathbf{p},\mathbf{p}')\, \mathbf{g}^K(\mathbf{p}',\varepsilon')\cdot\boldsymbol{\sigma} \right], \tag{16}$$

$$\hat{\Delta}(\mathbf{p}) = \int d\mathbf{p}' \fint \frac{d\varepsilon'}{4\pi i} \left[\lambda^s(\mathbf{p},\mathbf{p}')\, f^K(\mathbf{p}',\varepsilon')\, i\sigma_y + \lambda^t(\mathbf{p},\mathbf{p}')\, \mathbf{f}^K(\mathbf{p}',\varepsilon')\cdot i\boldsymbol{\sigma}\sigma_y \right]. \tag{17}$$

Note that $\hat{\Sigma}$ and $\hat{\Delta}$ represent the upper row of the Nambu matrix, $\hat{\Sigma}_{\rm mf}$. Since the mean-field self-energies are independent of ε, $\hat{\Sigma}^R_{\rm mf} = \hat{\Sigma}^A_{\rm mf} = \hat{\Sigma}_{\rm mf}$, and $\hat{\Sigma}^K_{\rm mf} = 0$. The interaction vertices, $A^{s,a}(\mathbf{p},\mathbf{p}')$, in Eq. 16 represent the quasiparticle interactions in the particle-hole channel. In the non-relativistic limit these interactions are spin-rotation invariant, in which case there are two real amplitudes: the spin-independent quasiparticle-quasiparticle interaction, $A^s(\mathbf{p},\mathbf{p}')$, the *exchange* term, $A^a(\mathbf{p},\mathbf{p}')$, describing the spin-dependent quasiparticle-quasiparticle interaction. These interactions are defined by the renormalized four-point vertex in the forward-scattering limit for quasiparticles with momenta and energies confined to the Fermi surface, i.e., $|\mathbf{p}| = |\mathbf{p}'| = p_f$ and $\varepsilon = \varepsilon' = 0$, which is a good approximation in the Fermi-liquid regime far from a quantum critical point. Thus, the propagator is integrated over the low-energy bandwidth defined by $\fint(\ldots) \equiv \int_{-\varepsilon_c}^{+\varepsilon_c}(\ldots)$, and the corresponding self-energies depend on the direction of the quasiparticle momentum on the Fermi surface, but are independent of ε.

In the Cooper channel the mean-field self energy from quasiparticle interactions is given by Eq. 17. The interaction vertex separates in terms of an even-parity, spin-singlet interaction, $\lambda^s(\mathbf{p},\mathbf{p}')$, and an odd-parity, spin-triplet interaction, $\lambda^t(\mathbf{p},\mathbf{p}')$, the latter resulting from exchange symmetry in the non-relativistic limit.[4] In a rotationally invariant Fermi liquid like liquid ^{3}He, the interactions in the Cooper channel further separates according to the irreducible representations of the rotation group in three dimensions, $SO(3)_L$,

$$\lambda^{s(t)}(\mathbf{p},\mathbf{p}') = \sum_{l}^{\text{even (odd)}} \lambda_l \sum_{m=-l}^{+l} \mathcal{Y}^\star_{l,m}(\hat{\mathbf{p}})\mathcal{Y}_{l,m}(\hat{\mathbf{p}}'), \tag{18}$$

which are labeled by the orbital angular momentum quantum number $l \in \{0,1,2,\ldots\}$, with the basis functions given by the spherical harmonics $\{\mathcal{Y}_{lm}(\hat{\mathbf{p}})\}$, normalized to $\int d\mathbf{p}\mathcal{Y}_{lm}(\hat{\mathbf{p}})\mathcal{Y}_{l'm'}(\hat{\mathbf{p}}') = \delta_{ll'}\delta_{mm'}$. The Cooper instability occurs in the pairing channel defined by the most attractive interaction, λ_l, which for ^{3}He is the odd-parity, spin-triplet ($S = 1$), $l = 1$ (p-wave) channel. For strongly correlated materials Cooper pairing is mediated by quasiparticle-quasiparticle interactions. This is necessarily the case in a single-component Fermi system like liquid ^{3}He, and is prevalent in strongly correlated electronic compounds such as the heavy-fermion superconductors, UPt_3 and URu_2Si_2, and unconventional superconductors like Sr_2RuO_4, all of which exhibit experimental signatures of broken time-reversal symmetry by the superconducting state. For these superconductors the pairing channel belongs to an irreducible representation of the crystal point group. Eq. 18 holds with l summed over the irreducible representations of the point group, the second sum m is over the set of orthogonal basis functions, $\{\mathcal{Y}_{lm}(\mathbf{p})|m \in \text{irrep}_l\}$, that span the irrep labeled by l. For materials with hexagonal point symmetry, e.g., UPt_3, we consider the four two-dimensional "E-reps": even parity E_{1g} and E_{2g} representations and odd-parity E_{1u} and E_{2u}. All four E-reps allow for a chiral ground state with minimum Chern numbers of $\nu = \pm 1$ ($E_{1g(u)}$) or $\nu = \pm 2$ ($E_{2g(u)}$).

3.3.2 Impurity self-energy

The effects of impurity disorder originate from the quasiparticle-impurity interaction, $\check{u}(\mathbf{p},\mathbf{p}')$, which corresponds to the transition matrix element for elastic scattering of a quasiparticle with momentum $\mathbf{p}$ to the point $\mathbf{p}'$ on the Fermi surface. Multiple scattering of quasiparticles and quasiholes by an impurity is described by the Bethe-Salpeter equation,

$$\check{t}(\mathbf{p}',\mathbf{p};\epsilon) = \check{u}(\mathbf{p}',\mathbf{p}) + N_f \int d\mathbf{p}''\, \check{u}(\mathbf{p}',\mathbf{p}'')\, \check{g}(\mathbf{p}'';\epsilon)\check{t}(\mathbf{p}'',\mathbf{p};\epsilon), \tag{19}$$

where $\check{t}(\mathbf{p}',\mathbf{p};\varepsilon)$ is the t-matrix for quasiparticle-impurity scattering, and $\check{g}(\mathbf{p};\varepsilon)$ is the quasiclassical Keldysh matrix propagator for particles, holes and Cooper pairs. The leading-order contribution to the configurational-averaged self energy is then determined by scattering of quasiparticles off an uncorrelated, random distribution of statistically equivalent impurities with average density, $n_{\rm imp}$,

$$\check{\Sigma}_{\rm imp}(\mathbf{p};\epsilon) = n_{\rm imp}\,\check{t}(\mathbf{p},\mathbf{p};\epsilon) = \begin{pmatrix} \hat{\Sigma}^R_{\rm imp} & \hat{\Sigma}^K_{\rm imp} \\ 0 & \hat{\Sigma}^A_{\rm imp} \end{pmatrix}, \tag{20}$$

where $\check{t}(\mathbf{p},\mathbf{p};\varepsilon)$ is the t-matrix evaluated self-consistently in the forward-scattering limit. Thus, the Nambu-matrix components of the impurity Keldysh self energy, $\hat{\Sigma}^{R,A,K}_{\rm imp}(\mathbf{p},\mathbf{r};\varepsilon,t) = n_{\rm imp}\hat{t}^{R,A,K}(\mathbf{p},\mathbf{p},\mathbf{r};\varepsilon,t)$, are determined by the corresponding components of the t-matrix,

$$\hat{t}^{R,A}(\mathbf{p}',\mathbf{p},\mathbf{r};\varepsilon,t) = u(\mathbf{p}',\mathbf{p}) + N_f \int d\mathbf{p}''\, u(\mathbf{p}',\mathbf{p}'')\, \hat{g}^{R,A}(\mathbf{p}'',\mathbf{r};\varepsilon,t) \circ \hat{t}^{R,A}(\mathbf{p}'',\mathbf{p},\mathbf{r};\varepsilon,t) \tag{21}$$

$$\hat{t}^{K}(\mathbf{p}',\mathbf{p},\mathbf{r};\varepsilon,t) = N_f \int d\mathbf{p}''\, \hat{t}^{R}(\mathbf{p}',\mathbf{p}'',\mathbf{r};\varepsilon,t) \circ \hat{g}^{K}(\mathbf{p}'',\mathbf{r};\varepsilon,t) \circ \hat{t}^{A}(\mathbf{p}'',\mathbf{p},\mathbf{r};\varepsilon,t). \tag{22}$$

Before proceeding to non-equilibrium quasiparticle transport we need to discuss the equilibrium state, including the effects of impurity scattering, on the equilibrium states of chiral superconductors and superfluids.

4 Equilibrium

For homogeneous systems in equilibrium the transport equations for the retarded and advanced propagators reduce to

3 The sign in Eq. (17) is such that $\lambda^{s(t)} > 0$ corresponds to an attractive pairing interaction.

4 This separation does not apply to superconducting materials without an inversion center, i.e. non-centrosymmetric superconductors.

TABLE 1 Representative orbital basis functions, expressed in the chiral basis, for the point groups D_{4h} and D_{6h}.

Point group	Irrep Γ	Basis functions $\eta_{\Gamma,\nu}(\hat{\mathbf{p}})$	Winding number ν	Parity
D_{4h}	E_g	$\hat{p}_z(\hat{p}_x \pm i\hat{p}_y) \propto \mathcal{Y}_2^{\pm 1}(\hat{\mathbf{p}})$	±1	+
	E_u	$\hat{p}_x \pm i\hat{p}_y \propto \mathcal{Y}_1^{\pm 1}(\hat{\mathbf{p}})$	±1	−
D_{6h}	E_{1g}	$\hat{p}_z(\hat{p}_x \pm i\hat{p}_y) \propto \mathcal{Y}_2^{\pm 1}(\hat{\mathbf{p}})$	±1	+
	E_{2g}	$(\hat{p}_x \pm i\hat{p}_y)^2 \propto \mathcal{Y}_2^{\pm 2}(\hat{\mathbf{p}})$	±2	+
	E_{1u}	$\hat{p}_x \pm i\hat{p}_y \propto \mathcal{Y}_1^{\pm 1}(\hat{\mathbf{p}})$	±1	−
	E_{2u}	$\hat{p}_z(\hat{p}_x \pm i\hat{p}_y)^2 \propto \mathcal{Y}_3^{\pm 2}(\hat{\mathbf{p}})$	±2	−

$$\left[\varepsilon\hat{\tau}_3 - \hat{\Delta}(\mathbf{p}) - \hat{\Sigma}_{\rm imp}^{R,A}(\mathbf{p};\varepsilon), \hat{g}^{R,A}(\mathbf{p};\varepsilon)\right] = 0, \tag{23}$$

where $\hat{\Delta}(\mathbf{p})$ is the mean-field order parameter and $\hat{\Sigma}_{\rm imp}^{R,A}(\mathbf{p};\varepsilon)$ are the equilibrium self-energies resulting from quasiparticle-impurity scattering. We consider the low-temperature limit in which the thermal populations of quasiparticles and phonons are sufficiently small that we can neglect quasiparticle-quasiparticle scattering and quasiparticle-phonon scattering contributions to the self energy. Thus, we retain only the mean-field pairing self energy and impurity self energy resulting from elastic quasiparticle-impurity scattering. The propagator is also constrained by the normalization condition, which for equilibrium reduces to matrix multiplication,

$$\left[\hat{g}^{R,A}(\mathbf{p},\varepsilon)\right]^2 = -\pi^2\hat{1}. \tag{24}$$

A chiral superconducting ground state is defined by spontaneous breaking of time-reversal and mirror symmetries by the orbital state of the Cooper pairs. We restrict our analysis to *unitary* superconductors in which the 4×4 Nambu matrix order parameter obeys the condition,

$$\hat{\Delta}(\mathbf{p})^2 = -|\Delta(\mathbf{p})|^2\hat{1}. \tag{25}$$

Unitary states preserve time-reversal symmetry with respect to the spin-correlations of the pairing state. In the clean limit $|\Delta(\mathbf{p})|$ is the energy gap for quasiparticles with momentum $\mathbf{p}$ near the Fermi surface, i.e., the Bogoliubov quasiparticle excitation energy is doubly degenerate with respect to spin and given by $E_{\mathbf{p}} = \sqrt{\xi_{\mathbf{p}}^2 + |\Delta(\mathbf{p})|^2}$, with $\xi_{\mathbf{p}} = v_f(|\mathbf{p}| - p_f)$ and $\Delta(\mathbf{p})$ defined for $\mathbf{p}$ on the Fermi surface. The unitarity condition is necessarily satisfied by spin-singlet pairing states, and is also the case for all known spin-triplet superconductors in which the parent state in zero external field is non-magnetic.[5] An important class of unitary triplet states are the equal-spin-pairing (ESP) states defined by the 2×2 spin-matrix order parameter, $\hat{\Delta}(\mathbf{p}) = \Delta(\mathbf{p})\hat{\mathbf{d}}\cdot(i\boldsymbol{\sigma}\sigma_y)$, in which $\hat{\mathbf{d}}$ is the direction in spin space along which the Cooper pairs have zero spin projection. Equivalently, this state corresponds to equal amplitudes for the spin projections $S_u = +1$ and $S_u = -1$ with $\hat{\mathbf{u}} \perp \hat{\mathbf{d}}$. For the chiral A-phase of ^{3}He, the direction $\hat{\mathbf{d}}$ can be controlled by a small magnetic field, $\mathbf{B}$, through the nuclear Zeeman energy that orients $\mathbf{d} \perp \mathbf{B}$. For chiral superconductors spin-orbit coupling and the crystalline field typically lock $\mathbf{d}$ along a high-symmetry direction of the crystal.

We consider four classes of chiral ground states corresponding to the even-parity, spin-singlet, E_{1g} and E_{2g}, and odd-parity, spin-triplet, E_{1u} and E_{2u} representations of the hexagonal point group, D_{6h}. These representations all allow for chiral ground states with principle winding numbers, $\nu = \pm1$ ($\nu = \pm2$) for the E_1 (E_2) representations.[6] Table 1 provides representative basis functions for these two-dimensional representations.

For even-parity, spin-singlet pairing the Nambu-matrix order parameter has the form, $\hat{\Delta}(\mathbf{p}) = (\Delta(\mathbf{p})\hat{\tau}_+ + \Delta^*(\mathbf{p})\hat{\tau}_-)\otimes(i\sigma_y)$, where $\hat{\tau}_\pm = (\hat{\tau}_1 \pm i\hat{\tau}_2)/2$ and $\{\hat{1}, \hat{\tau}_1, \hat{\tau}_2, \hat{\tau}_3\}$ are 2×2 matrices spanning particle-hole (Nambu) space. The spin-singlet correlations are represented by the Pauli matrix $i\sigma_y$, which is anti-symmetric under exchange. The orbital order parameter, $\Delta(\mathbf{p})$, is symmetric under exchange implying $\Delta(-\mathbf{p}) = +\Delta(\mathbf{p})$. The general form of the orbital order parameter is spanned by the two-dimensional space of $E_{1(2)g}$ basis functions. For E_{1g} the chiral basis $\{\mathcal{Y}_\nu(\mathbf{p})|\nu = \pm1\}$ can be constructed from the 2D vector representation: $\mathcal{Y}_\nu(\mathbf{p}) = \mathcal{Y}_{zx}(\mathbf{p}) + i\nu\mathcal{Y}_{zy}(\mathbf{p}) = \sin(p_z a_z)(\hat{p}_x + i\nu\hat{p}_y) = \sin(p_z a_z)e^{i\nu\phi_{\mathbf{p}}}$, where the latter two forms correspond to E_{1g} basis functions defined on a cylindrical Fermi surface with $\phi_{\mathbf{p}}$ corresponding to the azimuthal angle of $\mathbf{p}$. Note that chiral E_{1g} pairing also breaks reflection symmetry in the plane normal to the chiral axis, and has a line of nodes in the energy gap for momenta in the plane $p_z = 0$. Thus, E_{1g} pairing is not realized in 2D, but is defined on a 3D Fermi surface.

5 The A_1 phase of superfluid ^{3}He, which is stabilized by an externally applied magnetic field, is a non-unitary spin-triplet state [66]. The Uranium-based ferromagnetic superconductors are also believed to be non-unitary, spin-polarized, triplet superconductors.

6 $D_{\infty h}$, chiral ground states with any integer winding number $\nu\in$ Z are possible. For the discrete point group D_{6h} higher winding numbers with $\nu = \pm1 + \text{mod}(6)$ (E_1) or ($\nu = \pm2$) + mod(6) (E_2) are possible for pairing basis functions exhibiting strong hexagonal anisotropy, but in general the chiral basis functions with higher winding numbers will mix with $\nu = \pm1$ $\nu = \pm2$.

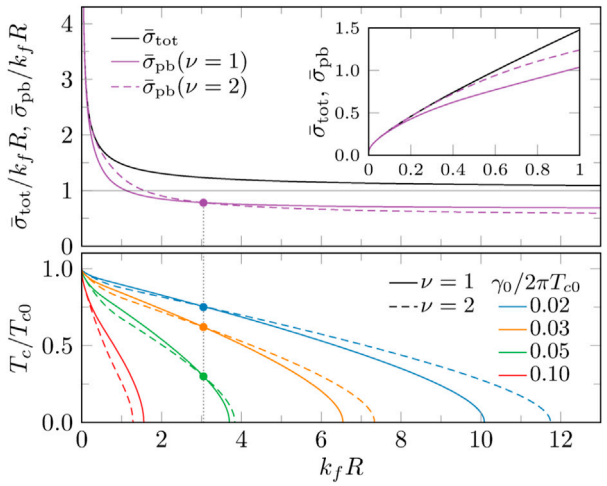

FIGURE 1
Impurity cross sections and critical temperature *versus* hard-disc radius for chiral states: $\nu = 1$ (solid) and $\nu = 2$ (dashed). For hard-disc radius $k_fR \approx 3.05$, pair-breaking cross sections and critical temperature of the two states coincide (filled circles). (Upper) Total cross section (black), transport cross section (solid purple) and pair-breaking cross section (purple). (Lower) Critical temperature for various impurity densities: $\gamma_0/2\pi T_{c_0} \equiv n_{\rm imp}\xi_0/k_f$ (see legend). Figure reproduced from Ref. [52] with permission of the American Physical Society (APS) and the authors.

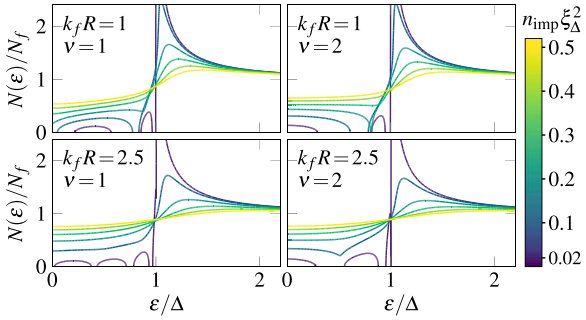

FIGURE 2
Density of states for chiral order $\nu = 1$ (left) and $\nu = 2$ (right), various impurity densities normalized by $\xi_\Delta^2 = (\pi N_f \Delta)^{-1}$ (see color bar), and impurity radii: $k_fR = 1$ (top) and 2.5 (bottom). Figure reproduced from Ref. [52] with permission of the APS and the authors.

For chiral E_{2g} pairing the basis functions can be defined as $\mathcal{Y}_\nu(\mathbf{p}) = \mathcal{Y}_{x^2-y^2}(\mathbf{p}) + i\,\mathrm{sgn}(\nu)\mathcal{Y}_{xy}(\mathbf{p}) = (\hat{p}_x + i\mathrm{sgn}(\nu)\hat{p}_y)^{|\nu|} = e^{i\nu\phi_{\mathbf{p}}}$, with $\nu = \pm 2$. The latter two forms correspond to E_{2g} pairing defined on a cylindrical Fermi surface. Note that the chiral ground state for E_{2g} also breaks reflection symmetry in one or more planes containing the chiral axis, $\hat{\boldsymbol{\ell}} = \hat{\mathbf{z}}$, but, in contrast to E_{1g}, preserves reflection symmetry in the plane normal to the chiral axis. Thus, a fully-gapped chiral ground state is possible in 2D, as well as a 3D Fermi surface that is open in the p_z direction. For a 3D Fermi surface that is closed in the p_z direction, the chiral E_{2g} ground state has topologically protected nodal points of $\Delta(\mathbf{p})$ at $\mathbf{p}_\pm = \pm p_f\hat{\mathbf{z}}$, and a corresponding spectrum of massless chiral Fermions in the bulk phase [44].

For odd-parity, ESP triplet states the Nambu-matrix order parameter takes the form, $\hat{\Delta}(\mathbf{p}) = (\Delta(\mathbf{p})\,\hat{\tau}_+ - \Delta^\star(\mathbf{p})\,\hat{\tau}_-) \otimes (\sigma_x)$, where we have chosen the ESP state with $\hat{\mathbf{d}} = \hat{\mathbf{z}}$.[7] The ESP triplet-correlations are represented by the symmetric Pauli matrix σ_x, and the odd-parity orbital order parameter, $\Delta(\mathbf{p})$, which is necessarily anti-symmetric under exchange, i.e., $\Delta(-\mathbf{p}) = -\Delta(\mathbf{p})$. For E_{1u} pairing the chiral basis $\{\mathcal{Y}_\nu(\mathbf{p})|\nu = \pm 1\}$ is constructed from the odd-parity 2D vector representation: $\mathcal{Y}_\nu(\mathbf{p}) = \mathcal{Y}_x(\mathbf{p}) + i\nu\mathcal{Y}_y(\mathbf{p}) = (\hat{p}_x + i\nu\hat{p}_y) = e^{i\nu\phi_{\mathbf{p}}}$, the latter two forms correspond to E_{1u} basis functions defined on a cylindrical Fermi surface with $\phi_{\mathbf{p}}$ corresponding to the azimuthal angle of $\mathbf{p}$. In contrast to E_{1g}, the E_{1u} chiral ground states are fully gapped in 2D, and in 3D for an open Fermi surface in the p_z direction. For chiral E_{2u} pairing the basis functions are constructed from those of E_{2g} by multiplying by odd-parity function of p_z. Thus, $\mathcal{Y}_\nu(\mathbf{p}) = \mathcal{Y}_{z(x^2-y^2)}(\mathbf{p}) + i\mathrm{sgn}(\nu)\mathcal{Y}_{z(xy)}(\mathbf{p}) = \sin(p_za_z)(\hat{p}_x + i\mathrm{sgn}(\nu)\hat{p}_y)^2 = \sin(p_za_z)\,e^{i\nu\phi_{\mathbf{p}}}$, with $\nu = \pm 2$. These chiral states correspond to the E_{2u} pairing model for the B-phase of UPt_3.

4.1 2D chiral superconductors

Here we consider the fully gapped E_{1u} and E_{2g} chiral ground states defined on a 2D cylindrical Fermi surface. These two cases illustrate nearly all of the key physical phenomena responsible for anomalous thermal and electrical transport mediated by non-magnetic impurity scattering in chiral superconductors. At low temperatures, thermally excited quasiparticles and phonons are dilute, therefore quasiparticles interact predominantly with quenched defects. For randomly distributed impurities, the self-energy is given by $\hat{\Sigma}_{\rm imp}(\hat{\mathbf{p}};\varepsilon) = n_{\rm imp}\hat{t}(\hat{\mathbf{p}},\hat{\mathbf{p}};\varepsilon)$, where $n_{\rm imp}$ is the mean impurity density and $\hat{t}(\hat{\mathbf{p}},\hat{\mathbf{p}};\varepsilon)$ is the forward scattering limit of the single-impurity t-matrix in the superconducting state. This t-matrix can be expressed in terms of the normal-state t-matrix, and the latter can be expressed in terms of scattering phase shifts for normal-state quasiparticle-impurity scattering,

$$\hat{t}^{R,A}(\hat{\mathbf{p}}',\hat{\mathbf{p}};\varepsilon) = \hat{t}_N^{R,A}(\hat{\mathbf{p}}',\hat{\mathbf{p}}) + N_f\langle \hat{t}_N^{R,A}(\hat{\mathbf{p}}',\hat{\mathbf{p}}'')\big[\hat{g}^{R,A}(\hat{\mathbf{p}}'';\varepsilon) - \hat{g}_N^{R,A}\big] \times \hat{t}^{R,A}(\hat{\mathbf{p}}'',\hat{\mathbf{p}};\varepsilon)\rangle_{\hat{\mathbf{p}}''}, \tag{26a}$$

$$\hat{t}^{K}(\hat{\mathbf{p}}',\hat{\mathbf{p}};\varepsilon) = N_f\langle \hat{t}^{R}(\hat{\mathbf{p}}',\hat{\mathbf{p}}'';\varepsilon)\hat{g}^{K}(\hat{\mathbf{p}}'';\varepsilon)\hat{t}^{A}(\hat{\mathbf{p}}'',\hat{\mathbf{p}};\varepsilon)\rangle_{\hat{\mathbf{p}}''}, \tag{26b}$$

where N_f is the normal-state density of states per spin at the Fermi surface and $\langle\ldots\rangle_{\hat{\mathbf{p}}}$ represents averaging over the Fermi-surface—for an isotropic 2D Fermi surface, $\langle\ldots\rangle_{\hat{\mathbf{p}}} = \int_0^{2\pi} d\phi_{\hat{\mathbf{p}}}/(2\pi)(\ldots)$. The superscripts denote three types of quasiclassical propagators: retarded (R), advanced (A) and Keldysh (K). In deriving Eq. 26, the bare electron-impurity interaction is eliminated in favor of the normal-state propagator, $\hat{g}_N = -\pi g_N\hat{\tau}_3$ with $g_N^R = (g_N^A)^\star = i$, and the normal-state t-matrix,

$$\hat{t}_N(\hat{\mathbf{p}}',\hat{\mathbf{p}}) = \frac{-1}{\pi N_f}\sum_{m=-\infty}^{+\infty}\frac{e^{im(\phi-\phi')}}{\cot\delta_m - g_N\hat{\tau}_3} \tag{27}$$

7 Results for heat and charge transport in zero field do not depend on the choice for the direction of $\hat{\mathbf{d}}$

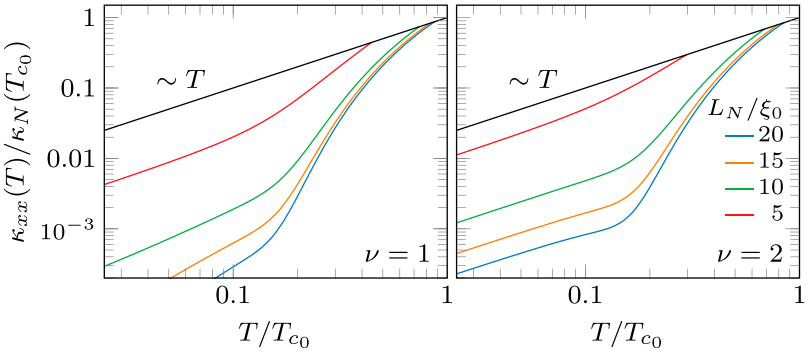

FIGURE 3
Longitudinal thermal conductivity *versus* temperature for chiral superconductors with $\nu = 1$ (left) and $\nu = 2$ (right), impurity radius $k_f R = 1$, and normal-state transport lengths listed in the legend. The normal-state thermal conductivity is shown in black. Figure reproduced from Ref. [52] with permission of the APS and the authors.

with δ_m the scattering phase shift in the m^{th} cylindrical harmonic.[8] Here and in the following, the directions $(\hat{\mathbf{p}}, \hat{\mathbf{p}}', \hat{\mathbf{p}}'', \ldots)$ on the Fermi surface and their corresponding azimuth angles $(\phi, \phi', \phi'', \ldots)$ are used interchangeably.

The mean field order parameter for unitary chiral states can be expressed in the following form, $\hat{\Delta}_S(\mathbf{p}) = \hat{U}_S \hat{\Delta}(\mathbf{p}) \hat{U}_S^\dagger$, where $\hat{U}_S$ is the unitary matrix for singlet $(S = 0)$ or triplet $(S = 1)$ pairing,

$$\hat{U}_0 = \begin{pmatrix} i\sigma_y & 0 \\ 0 & 1 \end{pmatrix}, \quad \hat{U}_1 = \begin{pmatrix} \hat{\mathbf{d}} \cdot i\boldsymbol{\sigma}\sigma_y & 0 \\ 0 & 1 \end{pmatrix}, \tag{28}$$

in which case $\hat{\Delta}(\mathbf{p})$ reduces to

$$\hat{\Delta}(\mathbf{p}) = \Delta\, e^{i\nu\phi_{\mathbf{p}}\hat{\tau}_3}(i\hat{\tau}_2) = \begin{pmatrix} 0 & \Delta\, e^{i\nu\phi_{\mathbf{p}}} \\ -\Delta\, e^{-i\nu\phi_{\mathbf{p}}} & 0 \end{pmatrix}, \tag{29}$$

for both $S = 0$ and $S = 1$. Thus, in the absence of external magnetic fields, magnetic impurities or spin-dependent perturbations, the spin structure of the order parameter can be transformed away by a unitary transformation, and as previously noted the quasiparticle excitation spectrum is doubly degenerate with respect to the quasiparticle spin.

This representation of the mean-field order parameter extends to the off-diagonal components of the impurity self energy. In Eq. 29 we chose Δ to be real. In this gauge the off-diagonal impurity self-energies reduce to

$$\hat{\Delta}^{R,A}_{\text{imp}}(\mathbf{p};\varepsilon) = \Delta^{R,A}_{\text{imp}}(\varepsilon)\, e^{i\nu\phi_{\mathbf{p}}\hat{\tau}_3}(i\hat{\tau}_2), \tag{30}$$

with the gauge condition, $\Delta^{R,A}_{\text{imp}}(\varepsilon) = \Delta^{R,A}_{\text{imp}}(-\varepsilon)^*$. The Nambu-matrix impurity self energy can then be expressed in terms of three functions

$$\hat{\Sigma}^{R,A}_{\text{imp}}(\mathbf{p};\varepsilon) = D^{R,A}_{\text{imp}}(\varepsilon)\hat{1} + \Sigma^{R,A}_{\text{imp}}(\varepsilon)\hat{\tau}_3 + \Delta^{R,A}_{\text{imp}}(\varepsilon)\, e^{i\nu\phi_{\mathbf{p}}\hat{\tau}_3}(i\hat{\tau}_2). \tag{31}$$

The term proportional to the unit Nambu matrix, $D^{R,A}_{\text{imp}}(\varepsilon)\hat{1}$, drops out of Eq. 23 for the equilibrium propagators, $\hat{g}^{R,A}$, and thus plays no role in determining the equilibrium properties of the superconductor. However, the unit-matrix term does contribute to the linear response of the superconductor, e.g., the a.c. conductivity [67].

The diagonal term proportional to $\hat{\tau}_3$ can be combined with the excitation energy and expressed as

$$\tilde{\varepsilon}^{R,A}(\varepsilon) = \varepsilon - \Sigma^{R,A}_{\text{imp}}(\varepsilon), \tag{32}$$

and similarly the impurity renormalized off-diagonal self energy is given by

$$\tilde{\Delta}^{R,A}(\varepsilon) = \Delta + \Delta^{R,A}_{\text{imp}}(\varepsilon) \tag{33}$$

Thus, for any of the chiral, unitary states described by Eq. 30, the equilibrium propagators that satisfy the transport equation and normalization condition, Eqs. 23, 24, are given by

$$g^{R,A}(\hat{\mathbf{p}};\varepsilon) = -\pi \frac{\tilde{\varepsilon}^{R,A}\hat{\tau}_3 - \tilde{\Delta}^{R,A}\, e^{i\nu\phi_{\mathbf{p}}\hat{\tau}_3}(i\hat{\tau}_2)}{\sqrt{\left(\tilde{\Delta}^{R,A}\right)^2 - \left(\tilde{\varepsilon}^{R,A}\right)^2}} \tag{34}$$

$$\equiv -\pi\left[g^{R,A}(\varepsilon)\hat{\tau}_3 + f^{R,A}(\varepsilon)\, e^{i\nu\phi_{\mathbf{p}}\hat{\tau}_3}(i\hat{\tau}_2)\right]. \tag{35}$$

Note that the functions $g^{R,A}$ and $f^{R,A}$ satisfy the symmetry relations: $g^A = (g^R)^*$ and $f^A = (f^R)^*$. In equilibrium, the Keldysh propagator is determined by the spectral functions for quasiparticles and Cooper pairs, and the thermal distribution of excitations,

$$\hat{g}^K(\mathbf{p};\varepsilon) = \left[\hat{g}^R(\mathbf{p};\varepsilon) - \hat{g}^A(\mathbf{p};\varepsilon)\right]\tanh\frac{\varepsilon}{2T}. \tag{36}$$

4.1.1 Gap equation: mean-field order parameter

The pairing interaction combined with the off-diagonal component of the Keldysh propagator determines the mean-field pairing self-energy for any of the unitary chiral states is given by the "gap equation,"

$$\Delta(\mathbf{p}) = \int d\mathbf{p}'\, \lambda(\mathbf{p},\mathbf{p}') \oint \frac{d\varepsilon'}{4\pi i}\, f^K(\mathbf{p}';\varepsilon') \tag{37}$$

8 The summation over m is truncated as a defect with characteristic radius R leads to rapidly decaying phase shifts for $|m| \gtrsim k_f R$.

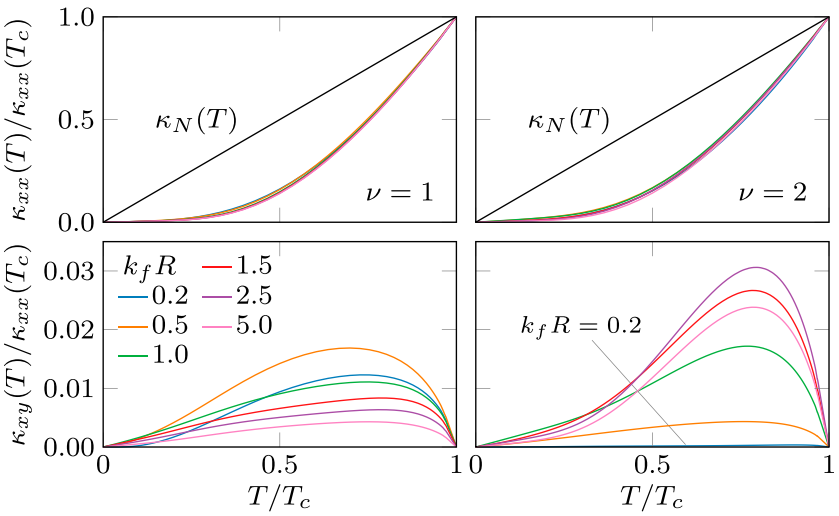

FIGURE 4
Longitudinal (top) and transverse (bottom) thermal conductivity vs. temperature for chiral order $\nu = 1$ (left) and $\nu = 2$ (right), normal-state transport length $L_N/\xi_0 = 7.5$, and various impurity radii (see legend). Normal-state thermal conductivity shown in black. Figure reproduced from Ref. [52] with permission of the APS and the authors.

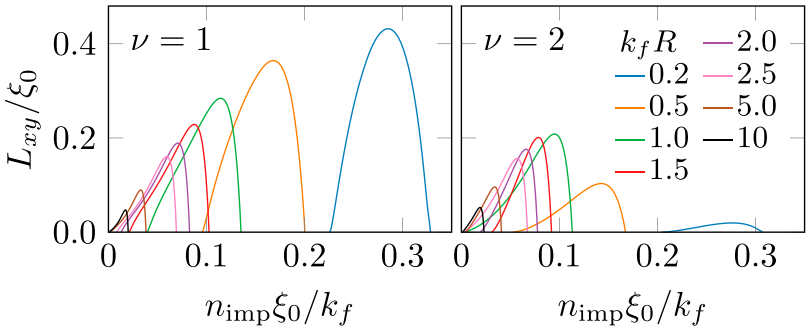

FIGURE 5
Thermal Hall transport length at $\varepsilon = 0$ for chiral order $\nu = 1$ (left) and $\nu = 2$ (right), and varying impurity radii (see legend). Low-temperature transport requires quasiparticles states at $\varepsilon = 0$, formed only with adequate impurity density. But high impurity density destroys superconductivity and thus rules out any anomalous Hall effects.

where the pairing interaction in any of the two-dimensional E-reps defined on a cylindrical Fermi surface has the form

$$\lambda(\mathbf{p},\mathbf{p}') = \lambda_{|\nu|}\left(e^{-i\nu\phi_{\mathbf{p}}}\, e^{+i\nu\phi_{\mathbf{p}'}} + e^{+i\nu\phi_{\mathbf{p}}}\, e^{-i\nu\phi_{\mathbf{p}'}}\right) = 2\lambda_{|\nu|}\cos\left[\nu\left(\phi_{\mathbf{p}} - \phi_{\mathbf{p}'}\right)\right]. \tag{38}$$

Thus, projecting out the amplitude of the chiral mean-field order parameter we obtain the gap equation,

$$\Delta = \lambda_{|\nu|}\oint \frac{d\varepsilon}{4\pi i}(\pi)\left[f^R(\varepsilon) - f^A(\varepsilon)\right]\tanh\frac{\varepsilon}{2T}. \tag{39}$$

In practice the pairing interaction strength $\lambda_{|\nu|}$ is eliminated in favor of the critical temperature.

The equilibrium retarded and advanced propagators are given by

$$\begin{aligned}\hat{g}^{R,A}(\hat{\mathbf{p}};\varepsilon) &= -\pi\frac{\tilde{\varepsilon}^{R,A}(\varepsilon)\hat{\tau}_3 - \tilde{\Delta}^{R,A}(\varepsilon)e^{i\hat{\tau}_3\nu\phi}(i\hat{\tau}_2)}{C^{R,A}(\varepsilon)} \\ &= -\pi\left[g(\varepsilon)\hat{\tau}_3 + f(\varepsilon)e^{i\hat{\tau}_3\nu\phi}(i\hat{\tau}_2)\right],\end{aligned} \tag{40}$$

where $g = \tilde{\varepsilon}/C$, $f = -\tilde{\Delta}/C$ and $C = [\tilde{\Delta}(\varepsilon)^2 - \tilde{\varepsilon}(\varepsilon)^2]^{1/2}$.[9] The equilibrium spectrum is renormalized by interactions with impurities, i.e., $\tilde{\varepsilon} = \varepsilon - \Sigma_{\rm imp}$ and $\tilde{\Delta} = \Delta + \Delta_{\rm imp}$, where Δ is the mean-field excitation gap from Eq. 39, and $\Sigma_{\rm imp}$ and $\Delta_{\rm imp}$ are the diagonal and off-diagonal terms in the impurity self energy, Eq. 31.[10] The self-energy is obtained from the equilibrium $\hat{t}$ matrix,

9 Hereafter the retarded (R) and advanced (A) superscripts are not shown for $g(\varepsilon)$, $f(\varepsilon)$ etc., but are implied.

10 Despite its absence from spectral renormalization, $D^{R,A}(\varepsilon)$ encodes particle-hole asymmetry, e.g. the difference in scattering lifetimes for particles and holes which could have implications for transport properties [68], especially in thermoelectric responses [70].

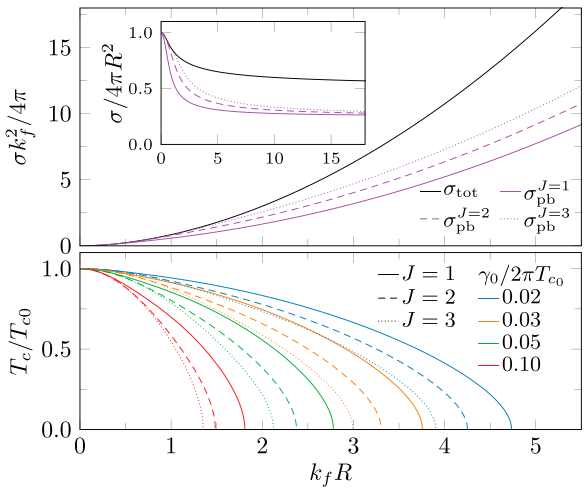

FIGURE 6
(Upper) Total cross section (black) and pair-breaking cross section (purple) *versus* hard-sphere radius for pairing with total angular momentum $J = 1$ (solid) $J = 2$ (dashed) and $J = 3$ (dotted). Note that the transport cross section is $\sigma_{\rm tr} = \sigma_{\rm pb}^{J=1}$. *Inset:* Scattering cross sections in units of $4\pi R^2$. (Lower) Critical temperature *versus* impurity radius for the same pairing states shown in the top panel for various impurity densities shown in the legend where $\gamma_0 = n_{\rm imp}/\pi N_f$.

$$\hat{t}(\hat{\mathbf{p}}',\hat{\mathbf{p}};\varepsilon) = \frac{-1}{\pi N_f}\begin{pmatrix} t(\hat{\mathbf{p}}',\hat{\mathbf{p}};\varepsilon) & a(\hat{\mathbf{p}}',\hat{\mathbf{p}};\varepsilon) \\ -\underline{a}(\hat{\mathbf{p}}',\hat{\mathbf{p}};\varepsilon) & \underline{t}(\hat{\mathbf{p}}',\hat{\mathbf{p}};\varepsilon)\end{pmatrix} = \frac{-1}{\pi N_f}\sum_m e^{im(\phi-\phi')}\begin{pmatrix} t_m(\varepsilon) & e^{i\nu\phi}a_{-m}(\varepsilon) \\ -e^{-i\nu\phi}\underline{a}_m(\varepsilon) & \underline{t}_{-m}(\varepsilon)\end{pmatrix}. \quad (41)$$

Upon solving Eq. 26, we obtain

$$\begin{Bmatrix} t_m(\varepsilon) \\ \underline{t}_m(\varepsilon)\end{Bmatrix} = \frac{\sin\delta_m\left[\cos\delta_{m+\nu} \pm g(\varepsilon)\sin\delta_{m+\nu}\right]}{\cos(\delta_m-\delta_{m+\nu}) \mp g(\varepsilon)\sin(\delta_m-\delta_{m+\nu})} \quad (42a)$$

$$\begin{Bmatrix} a_m(\varepsilon) \\ \underline{a}_m(\varepsilon)\end{Bmatrix} = \frac{f(\varepsilon)\sin\delta_m\sin\delta_{m-\nu}}{\cos(\delta_m-\delta_{m-\nu}) \mp g(\varepsilon)\sin(\delta_m-\delta_{m-\nu})}. \quad (42b)$$

The diagonal terms t_m and $\underline{t}_m$ are the amplitudes for quasi-particles and quasi-holes scattering off an impurity with relative angular momentum m. The off-diagonal terms, a_m and $\underline{a}_m$, are the amplitudes for branch conversion scattering in which a quasi-particle (quasi-hole) scatters off an impurity and also converts to a quasi-hole (quasi-particle). The branch conversion process is accompanied by the creation (destruction) of a Cooper pair. In a chiral superconductor the Cooper pairs have angular momentum $\nu\hbar$, and thus branch conversion scattering requires a corresponding change in the angular momentum of the scattered excitation, e.g., $m \to m - \nu$ for an incident quasi-particle scattering with relative angular momentum $m\hbar$ converting to a quasi-hole and a Cooper pair of angular momentum $\nu\hbar$. Thus, for branch conversion scattering to occur the quasiparticle-impurity potential must support amplitudes, a_m, and thus non-vanishing phase shifts δ_m with $|m| \in \{0, 1, \ldots, |\nu|\}$, as can be seen from Eq. 42b. A direct consequence is that isotropic impurity scattering from point-like impurities does not support branch conversion scattering in chiral superconductors since the incoming and outgoing scattering states are limited to the s-wave $(m = 0)$ scattering channel. As we show in what follows, the ionic radius of the impurity and branch conversion scattering are central in determining the magnitude and temperature dependence of anomalous Hall transport in chiral superconductors. Finally we note that the propagators, t-matrix and self-energies must be computed self-consistently with the gap equation, Eq. 39. In Section 4 we summarize results for thermal transport in 2D fully gapped chiral superconductors with a random distribution of finite size impurities.

4.2 3D chiral superconductors

Here we consider chiral superconductors in 3D belonging to the two-dimensional E-representations of the tetragonal (D_{4h}) and hexagonal (D_{6h}) point groups, both even- and odd-parity E_1 and E_2 representations. These groups describe the discrete point symmetries of Sr_2RuO_4 and UPt_3, respectively. See Table 1.

4.2.1 Symmetries of the order parameter

The mean-field pairing self-energy, after factoring the spin-structure using the unitary transformation in Eq. 28, has the structure,

$$\hat{\Delta}^{R,A}(\hat{\mathbf{p}}) = \begin{pmatrix} 0 & \Delta(\hat{\mathbf{p}}) \\ -\Delta(\hat{\mathbf{p}})^* & 0\end{pmatrix}. \quad (43)$$

The weak-coupling mean-field order parameter, "gap function", is independent of energy and related to the equilibrium Keldysh pair propagator by the BCS gap equation,

$$\Delta(\hat{\mathbf{p}}) = \oint \frac{d\varepsilon}{4\pi i}\langle\lambda(\hat{\mathbf{p}},\hat{\mathbf{p}}')f^K(\hat{\mathbf{p}}';\varepsilon)\rangle_{\hat{\mathbf{p}}'}, \quad (44)$$

where $\lambda(\hat{\mathbf{p}},\hat{\mathbf{p}}')$ provides the pairing interaction and the energy integral is over the bandwidth of attraction, ε_c, $\hat{\mathbf{p}}$ and $\hat{\mathbf{p}}'$ are the directions of the relative momentum of pairs of Fermions with zero total momentum, and $\langle\ldots\rangle_{\hat{\mathbf{p}}}$ is an average over the Fermi surface. The pairing interaction respects the maximal symmetry of the point group and can be expressed as a sum over bi-linear products of basis functions of the irreducible representations analogous to Eq. 18. We assume the irreducible representation, Γ, with the most attractive pairing interaction, λ_Γ, dominates, in which case we can ignore the sub-dominant pairing channels,

$$\lambda(\hat{\mathbf{p}},\hat{\mathbf{p}}') = \lambda_\Gamma\sum_\nu^{\dim\Gamma}\eta_{\Gamma,\nu}(\hat{\mathbf{p}})\eta_{\Gamma,\nu}(\hat{\mathbf{p}}')^*, \quad (45)$$

where the interaction amplitude λ_Γ determines the critical temperature and $\eta_{\Gamma,\nu}(\hat{\mathbf{p}})$ denotes the basis functions for the irreducible representation, Γ, of the relevant point group. Table 1 summarizes the basis functions, expressed in chiral basis, for the point groups D_{4h} and D_{6h}, and which are relevant for Sr_2RuO_4 and the heavy-fermion compound UPt_3, respectively.[11] For a chiral superconductor the order parameter is proportional to one of the chiral basis functions, e.g., $\Delta(\hat{\mathbf{p}}) \propto \eta_{\Gamma,\nu}(\hat{\mathbf{p}})$ for a chiral ground state

11 A comprehensive set of tables of basis functions for the tetragonal, hexagonal and cubic point groups is provided in Ref. [69]

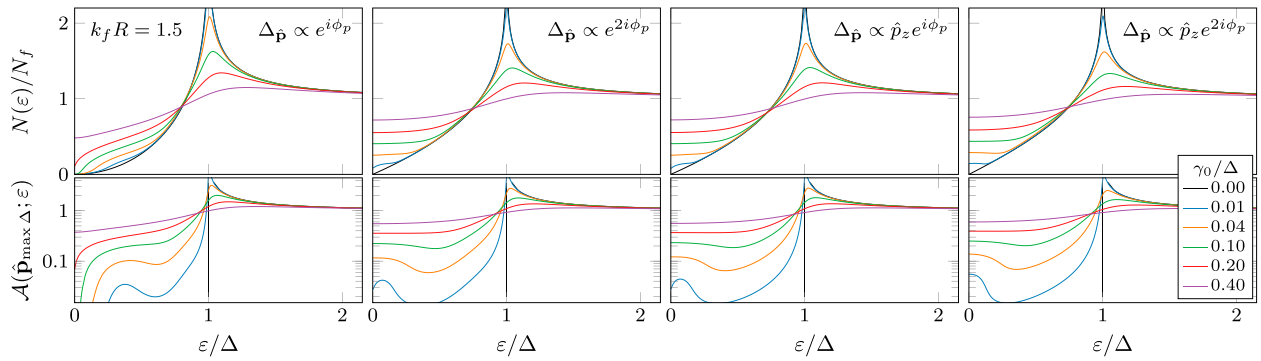

FIGURE 7
The quasiparticle density of states $N(\varepsilon)$ (top) and spectral function along the direction of gap maximum $\mathcal{A}(\hat{\mathbf{p}};\varepsilon)$ (bottom) are shown for hard-sphere impurities with radius, $k_f R = 1.5$, for impurity densities shown in the legend where $\gamma_0 = n_{\rm imp}/\pi N_f$. The four pairing states correspond to the chiral ground states of the irreducible representations E_{1u}, E_{2g}, E_{1g} and E_{2u} (left to right) of the hexagonal point group D_{6h}. Scattering resonances appears as impurity-induced sub-gap bands which depend on the topology of the order parameter and the structure of the scattering potential.

belonging to the irrep Γ with winding number ν. For the analysis to follow it is sufficient to consider pairing of states near a 3D spherical Fermi surface, in which case the mean-field pairing self-energy is proportional to the spherical harmonic, i.e., $\eta_{\Gamma,\nu}(\hat{\mathbf{p}}) = Y_l^\nu(\hat{\mathbf{p}})$, where l is the orbital angular momentum corresponding to the irrep Γ,

$$\Delta(\hat{\mathbf{p}}) = \Delta\, \tilde{Y}_l^\nu(\hat{\mathbf{p}}), \tag{46}$$

where Δ is the maximum value of the order parameter, and the normalized spherical harmonics are related to the standard spherical harmonics $Y_l^m(\hat{\mathbf{p}})$ via $\tilde{Y}_l^m(\hat{\mathbf{p}}) = Y_l^m(\hat{\mathbf{p}})/\max_{\hat{\mathbf{p}}}|Y_l^m(\hat{\mathbf{p}})|$.

4.2.2 Impurity self-energy

In the low temperature limit quasiparticle scattering from thermally excited quasiparticles and phonons is negligible compared to scattering off the random impurity potential. For a homogeneous uncorrelated random distribution of impurities the corresponding self-energy is a product of the mean impurity density $n_{\rm imp}$ and the forward scattering limit of the single impurity t-matrix,

$$\hat{\Sigma}^{R,A}_{\rm imp}(\hat{\mathbf{p}};\varepsilon) = n_{\rm imp}\hat{t}^{R,A}(\hat{\mathbf{p}},\hat{\mathbf{p}};\varepsilon), \tag{47}$$

where the t-matrices are obtained as a solution of the integral equation,

$$\hat{t}^{R,A}(\hat{\mathbf{p}}',\hat{\mathbf{p}}) = \hat{t}^{R,A}_N(\hat{\mathbf{p}}',\hat{\mathbf{p}}) + N_f\langle \hat{t}^{R,A}_N(\hat{\mathbf{p}}',\hat{\mathbf{p}}'')\big[\hat{g}^{R,A}(\hat{\mathbf{p}}'') - \hat{g}^{R,A}_N\big]\hat{t}^{R,A}(\hat{\mathbf{p}}'',\hat{\mathbf{p}})\rangle_{\hat{\mathbf{p}}''}. \tag{48}$$

The Keldysh component of the t-matrix then given by

$$\hat{t}^K(\hat{\mathbf{p}}',\hat{\mathbf{p}}) = N_f\langle \hat{t}^R(\hat{\mathbf{p}}',\hat{\mathbf{p}}'')\hat{g}^K(\hat{\mathbf{p}}'')\hat{t}^A(\hat{\mathbf{p}}'',\hat{\mathbf{p}})\rangle_{\hat{\mathbf{p}}''}. \tag{49}$$

Note that $\hat{t}^A$ can be obtained from the symmetry relation, $\hat{t}^A(\hat{\mathbf{p}}',\hat{\mathbf{p}}) = \hat{\tau}_3\hat{t}^R(\hat{\mathbf{p}},\hat{\mathbf{p}}')^\dagger\hat{\tau}_3$. In Eqs. 48, 49 we eliminated the electron-impurity matrix element, $\hat{u}$, in favor of the normal-state quasiparticle propagator, $\hat{g}_N = -\pi g_N\hat{\tau}_3$ with $g_N^R = (g_N^A)^\star = i$, and the normal-state t-matrix,

$$\hat{t}_N(\hat{\mathbf{p}}',\hat{\mathbf{p}}) = \frac{-1}{\pi N_f}\sum_{l\geq 0}\sum_{m=-l}^{+l}\frac{Y_l^m(\hat{\mathbf{p}}')Y_l^m(\hat{\mathbf{p}})^\star}{\cot\delta_l + \hat{g}_N/\pi}, \tag{50}$$

where δ_l is the phase shift in the relative angular momentum channel, l. The normalization of the spherical harmonics is given by

$$\langle Y_l^m(\hat{\mathbf{p}})^\star Y_{l'}^{m'}(\hat{\mathbf{p}})\rangle_{\hat{\mathbf{p}}} = \delta_{mm'}\delta_{ll'}. \tag{51}$$

An important feature of scattering theory by central force potentials, in this case the quasiparticle-impurity potential, is that the characteristic range R of the potential leads to phase shifts δ_l that decay rapidly to zero for $l \gtrsim k_f R$, effectively truncating the summations over m and l.

4.2.3 Equilibrium properties

Below we present the framework for determining the self-consistent equilibrium propagators. To highlight the effects of chiral phase winding we consider systems that are gauge-rotation invariant, i.e., invariant under a rotation around the chiral axis combined with a specific element of the U(1). As a result the diagonal equilibrium propagator depends on $\hat{\mathbf{p}}$ only through the polar angle θ_p measured from the chiral axis, $g(\hat{\mathbf{p}};\varepsilon) = g(\theta_p;\varepsilon)$. The azimuth angle ϕ_p appears only in the phase factor of the pair propagator, i.e., $f(\hat{\mathbf{p}};\varepsilon) = e^{i\nu\phi_p} f(\theta_p;\varepsilon)$, where ν is winding number of the chiral order parameter. Thus we parametrize the propagators as

$$\hat{g}^{R,A}(\hat{\mathbf{p}};\varepsilon) = -\pi\big[g^{R,A}\big(\theta_p;\varepsilon\big)\hat{\tau}_3 + f^{R,A}\big(\theta_p;\varepsilon\big)e^{i\nu\hat{\tau}_3\phi_p}(i\hat{\tau}_2)\big], \tag{52}$$

where the quasiparticle and pair propagators read

$$g^{R,A} = \frac{\tilde{\varepsilon}^{R,A}(\theta;\varepsilon)}{C^{R,A}(\theta;\varepsilon)} \quad \text{and} \quad f^{R,A} = -\frac{\tilde{\Delta}^{R,A}(\theta;\varepsilon)}{C^{R,A}(\theta;\varepsilon)}, \tag{53}$$

with

$$C^{R,A}(\theta;\varepsilon) = \sqrt{\tilde{\Delta}^{R,A}(\theta;\varepsilon)^2 - \tilde{\varepsilon}^{R,A}(\theta;\varepsilon)^2}. \tag{54}$$

The equilibrium Keldysh propagator is determined by $\hat{g}^{R,A}$ and the Fermi distribution function,

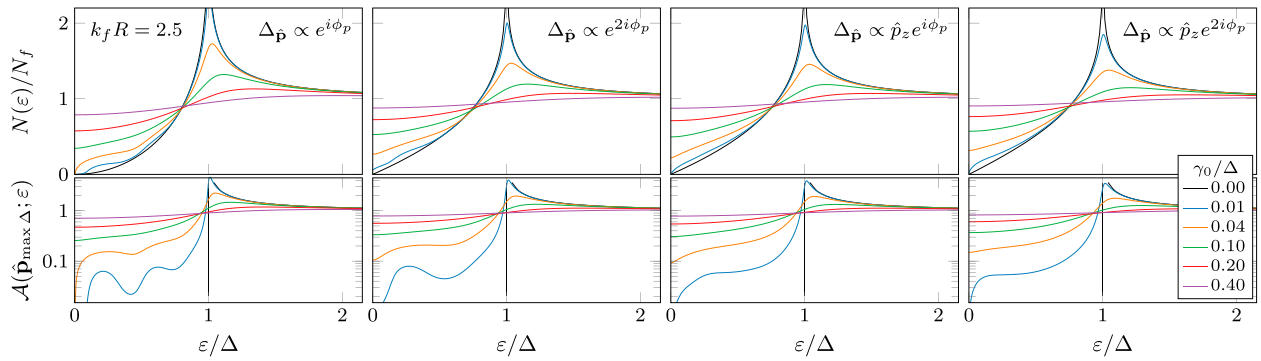

FIGURE 8
Same description as that in Figure 7, but for $k_f R = 2.5$.

$$\hat{g}^K = \left(\hat{g}^R - \hat{g}^A\right)\tanh\frac{\varepsilon}{2T}. \tag{55}$$

Note that the retarded and advanced propagators are related by the symmetry relation, $\hat{g}^A = \hat{\tau}_3(\hat{g}^R)^\dagger\hat{\tau}_3$. The excitation energy and order parameter are renormalized by impurity scattering through the impurity self-energies, $\Sigma_{\rm imp}$ and $\Delta_{\rm imp}$, via

$$\begin{aligned}\tilde{\varepsilon}^{R,A}(\theta;\varepsilon) &= \varepsilon - \Sigma^{R,A}_{\rm imp}(\theta;\varepsilon)\\ \tilde{\Delta}^{R,A}(\theta;\varepsilon) &= \Delta\,\tilde{\Theta}^\nu_l(\theta) + \Delta^{R,A}_{\rm imp}(\theta;\varepsilon),\end{aligned} \tag{56}$$

where $\tilde{\Theta}^\nu_l(\theta)$ is the polar-angle dependence of the normalized spherical harmonics. The functions $\Sigma_{\rm imp}$ and $\Delta_{\rm imp}$ are defined such that

$$\hat{\Sigma}^R_{\rm imp}(\hat{\mathbf{p}};\varepsilon) = D^R\left(\theta_p;\varepsilon\right)\hat{1} + \Sigma^R_{\rm imp}\left(\theta_p;\varepsilon\right)\hat{\tau}_3 + \Delta^R_{\rm imp}\left(\theta_p;\varepsilon\right)e^{i\hat{\tau}_3 w\phi_p}(i\hat{\tau}_2). \tag{57}$$

The function $D(\varepsilon)$ encodes the asymmetry in scattering rates for particles and holes, which has implications for the thermoelectric response of chiral superconductors [70].

Since the scattering potential is rotationally invariant we can expand the t-matrix Equation 48 into a set of decoupled equations for each cylindrical harmonic channel. Thus, we parametrize the t-matrix as follows

$$\hat{t}^R(\hat{\mathbf{p}}',\hat{\mathbf{p}}) = \sum_m e^{im\left(\phi_p-\phi_{p'}\right)}\left[\hat{t}^R_m\left(\theta_{p'},\theta_p\right) + e^{iv\hat{\tau}_3\phi_{p'}}\hat{a}^R_m\left(\theta_{p'},\theta_p\right)\right], \tag{58}$$

where the diagonal part of the t-matrix is given by

$$\hat{t}^R_m\left(\theta_{p'},\theta_p\right) = \begin{pmatrix} t^R_m\left(\theta_{p'},\theta_p\right) & 0\\ 0 & \underline{t}^R_m\left(\theta_{p'},\theta_p\right)\end{pmatrix}, \tag{59}$$

and the off-diagonal part is given by

$$\hat{a}^R_m\left(\theta_{p'},\theta_p\right) = \begin{pmatrix} 0 & a^R_m\left(\theta_{p'},\theta_p\right)\\ -\underline{a}^R_m\left(\theta_{p'},\theta_p\right) & 0\end{pmatrix}. \tag{60}$$

Thus, by factoring out the dependence on the azimuth angle as shown in Eq. 48, we obtain integral equations for the cylindrical harmonics of the t-matrix,

$$\begin{aligned}\hat{t}^R_m\left(\theta_{p'},\theta_p\right) = \hat{t}^R_{N,m}\left(\theta_{p'},\theta_p\right) + \langle\hat{t}^R_{N,m}\left(\theta_{p'},\theta_{p''}\right)\big[\left(g^R\left(\theta_{p''}\right) - g^R_N\right)\hat{\tau}_3\hat{t}^R_m\left(\theta_{p''},\theta_p\right)\\ + f^R\left(\theta_{p''}\right)(i\hat{\tau}_2)\,\hat{a}^R_m\left(\theta_{p''},\theta_p\right)\big]\rangle_{p''}\end{aligned} \tag{61}$$

$$\begin{aligned}\hat{a}^R_m\left(\theta_{p'},\theta_p\right) = \langle\hat{t}^R_{N,m-v\hat{\tau}_3}\left(\theta_{p'},\theta_{p''}\right)\big[f^R\left(\theta_{p''}\right)(i\hat{\tau}_2)\hat{t}^R_m\left(\theta_{p''},\theta_p\right)\\ + \left(g^R\left(\theta_{p''}\right) - g^R_N\right)\hat{\tau}_3\hat{a}^R_m\left(\theta_{p''},\theta_p\right)\big]\rangle_{p''},\end{aligned} \tag{62}$$

where $\hat{t}_{N,m-v\hat{\tau}_3} = \mathrm{Diag}\left(t_{N,m-v},\underline{t}_{N,m+v}\right)$. The off-diagonal t-matrix $\hat{a}_m$ describes Andreev scattering in which an incoming particle branch converts into an outgoing hole and *vice versa*. This process relies on the creation and destruction of a Cooper pair. For chiral pairing, the conservation of angular momentum implies that the cylindrical harmonics of incoming and outgoing scattering states must differ by the orbital angular momentum quantum number of a Cooper pair, hence the phase winding factor in front of $\hat{a}_m$ in Eq. 58. Since branch conversion scattering requires two distinct angular momentum channels, branch conversion scattering is absent for point-like impurities which support only s-wave ($l = 0$) scattering. Equations 61, 62 are solved for the 3D Fermi surface by expanding in the spherical harmonic basis functions, $\Theta^m_l(\theta)$. For cylindrical Fermi surfaces the dependence on θ drops out and the t-matrices are obtained by matrix inversion as described in Section 4.1.

5 Linear response theory

For small departures from equilibrium driven by a small temperature bias between different edges of the superconductor the heat current is proportional to the temperature gradient,

$$\mathbf{j}^{(q)} = -\overleftrightarrow{\kappa}\cdot\boldsymbol{\nabla}T, \tag{63}$$

where $\overleftrightarrow{\kappa}$ is the thermal conductivity tensor which is constrained by the chiral symmetry of the ground state. To obtain these transport coefficients, κ_{ij}, we determine the self-consistent, equilibrium propagators *and* their first-order non-equilibrium corrections to linear order in $\boldsymbol{\nabla}T$. The equilibrium propagators encode information about the bound and unbound quasiparticle pair spectrum, and are key inputs to the determination of the linear-response functions.

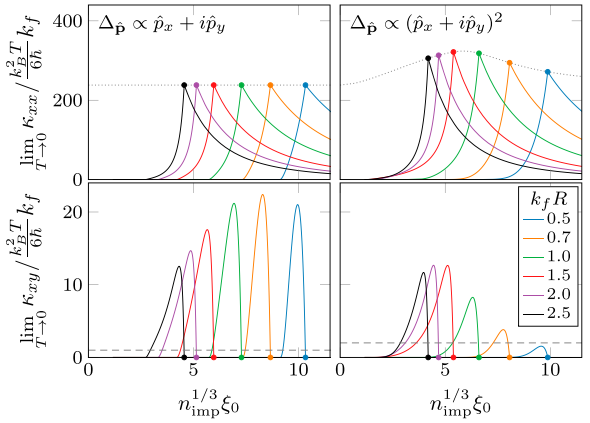

FIGURE 9
The components of the thermal conductivity tensor, κ_{xx} (top) and κ_{xy} (bottom), for $T \ll \gamma^*$ as a function of impurity density and hard-sphere radii (legend) for the pairing states, E_{1u} (left) and E_{2g} (right) of D_{6h}. The filled circles mark the critical impurity concentrations $n_{\rm imp}^c$ above which superconductivity breaks down. The dotted curves in the top panels trace the maximum value of κ_{xx}, while the dashed lines in the bottom panels show the Berry-phase contribution to the anomalous thermal Hall conductivity (Eq. 114). All results assume $k_f\xi_0 = 100$.

The heat current is computed from the non-equilibrium Keldysh propagator in Eq. 14.

Here we consider the linear response functions for a static and homogeneous thermal gradient. For convenience we separate the Keldysh response into a spectral and anomalous part. The anomalous response encodes information about the non-equilibrium distribution function and is defined by,

$$\delta\hat{x}^a(\varepsilon) = \delta\hat{x}^K(\varepsilon) - \tanh(\varepsilon/2T)\left[\delta\hat{x}^R(\varepsilon) - \delta\hat{x}^A(\varepsilon)\right], \quad (64)$$

where $\hat{x}$ stands for the propagator ($\hat{x} \to \hat{g}$) or self-energy ($\hat{x} \to \hat{\Sigma}$). We focus on the anomalous functions because the spectral response functions, $\delta\hat{x}^{R,A}$, do not contribute to the thermal conductivity tensor in linear response theory to leading order in the quasiclassical expansion parameters [64]. For a uniform thermal gradient the anomalous propagator is obtained from the solution of the linearized transport equations (see Ref. [64] for the general solution),

$$\delta\hat{g}^a = -\frac{C_+^a \hat{g}_{\rm eq}^R/\pi + D_-^a}{(C_+^a)^2 + (D_-^a)^2}\left[\left(\hat{g}_{\rm eq}^R - \hat{g}_{\rm eq}^A\right)(i\mathbf{v}_{\hat{\mathbf{p}}}\cdot\nabla\Phi) + \left(\hat{g}_{\rm eq}^R\delta\hat{\Sigma}^a - \delta\hat{\Sigma}^a\hat{g}_{\rm eq}^A\right)\right], \quad (65)$$

where $\nabla\Phi = \nabla\tanh[\varepsilon/2T(\mathbf{r})]$ is the gradient of the local equilibrium distribution function. We added the subscript "eq" to denote the equilibrium propagators. We also adopt the shorthand notation,

$$C_+^a = C^R + C^A \quad \text{and} \quad D_-^a = D^R - D^A, \quad (66)$$

with C and D defined in Eqs. 54, 57, respectively. It is also efficient to express the response functions as column vectors whose elements correspond to those of their corresponding matrices in particle-hole space,

$$|\delta g(\hat{\mathbf{p}};\varepsilon)\rangle = \left(\delta g(\hat{\mathbf{p}};\varepsilon), \delta\underline{g}(\hat{\mathbf{p}};\varepsilon), \delta f(\hat{\mathbf{p}};\varepsilon), \delta\underline{f}(\hat{\mathbf{p}};\varepsilon)\right)^T, \quad (67)$$

$$|\delta\Sigma(\hat{\mathbf{p}};\varepsilon)\rangle = \left(\delta\epsilon(\hat{\mathbf{p}};\varepsilon), \delta\underline{\epsilon}(\hat{\mathbf{p}};\varepsilon), \delta\Delta(\hat{\mathbf{p}};\varepsilon), \delta\underline{\Delta}(\hat{\mathbf{p}};\varepsilon)\right)^T. \quad (68)$$

The expression for the anomalous propagator (Eq. 65) can then be recast as

$$|\delta g^a(\hat{\mathbf{p}};\varepsilon)\rangle = \mathbb{L}^a(\hat{\mathbf{p}};\varepsilon)\left[|\psi^a(\hat{\mathbf{p}};\varepsilon)\rangle + |\delta\sigma^a(\hat{\mathbf{p}};\varepsilon)\rangle\right], \quad (69)$$

where the static thermal gradient leads to the perturbation,

$$|\psi(\hat{\mathbf{p}};\varepsilon)\rangle = i\mathbf{v}_{\hat{\mathbf{p}}}\cdot\nabla\Phi(1,1,\cdot,\cdot)^T \equiv \psi(\hat{\mathbf{p}};\varepsilon)(1,1,\cdot,\cdot)^T. \quad (70)$$

The linear-response matrix $\mathbb{L}(\hat{\mathbf{p}};\varepsilon)$ is defined in terms of the equilibrium propagators,

$$\mathbb{L}^a(\varepsilon) = -\mathcal{C}^a\begin{pmatrix} 1+|g|^2 & -|f|^2 & -g^Rf^A & -f^Rg^A \\ -|f|^2 & 1+|g|^2 & f^Rg^A & g^Rf^A \\ g^Rf^A & -f^Rg^A & 1-|g|^2 & -|f|^2 \\ f^Rg^A & -g^Rf^A & -|f|^2 & 1-|g|^2 \end{pmatrix} - \mathcal{D}^a\begin{pmatrix} g^R-g^A & \cdot & f^A & -f^R \\ \cdot & -g^R+g^A & -f^R & f^A \\ -f^A & f^R & g^R+g^A & \cdot \\ f^R & -f^A & \cdot & -g^R-g^A \end{pmatrix}, \quad (71)$$

where $|g|^2 = g^Rg^A$, $|f|^2 = f^Rf^A$ and

$$\{\mathcal{C}^a(\varepsilon), \mathcal{D}^a(\varepsilon)\} = \frac{1}{2}\frac{\{\mathrm{Re}\,C^R(\varepsilon), i\,\mathrm{Im}\,D^R(\varepsilon)\}}{[\mathrm{Re}\,C^R(\varepsilon)]^2 - [\mathrm{Im}\,D^R(\varepsilon)]^2}. \quad (72)$$

5.1 Self-energy—vertex corrections

The *r.h.s.* of Eq. 69 consists of two terms. The first is the contribution that is explicitly proportional to the external field, $\mathbf{v}_p\cdot\nabla T$. This term contributes only to the longitudinal thermal conductivity. Indeed the anomalous Hall conductivity arises solely from the non-equilibrium self-energy term. The self-energy corrections are the *vertex corrections* in the field-theoretical formulation based on Kubo response theory. These terms describe the response to perturbations by long-wavelength collective excitations of the interacting Fermi system [63]. In the context of the linear response theory developed for disordered chiral superconductors, the vertex corrections resulting from interactions of Bogoliubov quasiparticles with static impurities are obtained from the linear response corrections to the equilibrium t-matrix Eqs. 48, 49 obtained from the first-order non-equilibrium corrections to the full t-matrix Eqs. 21, 22. For the anomalous self-energy expressed in Nambu matrix form,

$$\delta\hat{\Sigma}_{\rm imp}^a(\hat{\mathbf{p}}) = n_{\rm imp}N_f\langle\hat{t}_{\rm eq}^R(\hat{\mathbf{p}},\hat{\mathbf{p}}')\delta\hat{g}^a(\hat{\mathbf{p}}')\hat{t}_{\rm eq}^A(\hat{\mathbf{p}}',\hat{\mathbf{p}})\rangle_{\hat{\mathbf{p}}'}, \quad (73)$$

can be recast in column vector form as defined by Eq. 68,

$$|\delta\Sigma^a(\hat{\mathbf{p}})\rangle = -\frac{n_{\rm imp}}{\pi N_f}\langle\mathbb{T}^a(\hat{\mathbf{p}},\hat{\mathbf{p}}')|\delta g^a(\hat{\mathbf{p}}')\rangle\rangle_{\hat{\mathbf{p}}'}, \quad (74)$$

where the impurity vertex-correction operator is given by

$$\mathbb{T}^a(\hat{\mathbf{p}},\hat{\mathbf{p}}') = \begin{pmatrix} t^Rt^A & -a^R\underline{a}^A & -t^R\underline{a}^A & -a^Rt^A \\ -\underline{a}^Ra^A & \underline{t}^R\underline{t}^A & -\underline{a}^R\underline{t}^A & -\underline{t}^Ra^A \\ t^Ra^A & a^R\underline{t}^A & t^R\underline{t}^A & -a^Ra^A \\ \underline{a}^Rt^A & \underline{t}^R\underline{a}^A & -\underline{a}^R\underline{a}^A & \underline{t}^Rt^A \end{pmatrix}. \quad (75)$$

The retarded [advanced] t-matrix elements are evaluated at $(\hat{\mathbf{p}}, \hat{\mathbf{p}}'; \varepsilon)$ $[(\hat{\mathbf{p}}', \hat{\mathbf{p}}; \varepsilon)]$, and the equilibrium t-matrix elements, t and a, are defined such that

$$\hat{t}^{R,A}_{\rm eq}(\hat{\mathbf{p}}', \hat{\mathbf{p}}) = \begin{pmatrix} t^{R,A}(\hat{\mathbf{p}}', \hat{\mathbf{p}}) & a^{R,A}(\hat{\mathbf{p}}', \hat{\mathbf{p}}) \\ -\underline{a}^{R,A}(\hat{\mathbf{p}}', \hat{\mathbf{p}}) & \underline{t}^{R,A}(\hat{\mathbf{p}}', \hat{\mathbf{p}}) \end{pmatrix}. \tag{76}$$

In general the mean-field pairing self-energy also contributes a vertex correction (i.e., $\delta\hat{\Sigma} = \delta\hat{\Delta} + \delta\hat{\Sigma}_{\rm imp}$). These terms play a central role in collective mode response of the condensate, however, in the present context they contribute only to the retarded and advanced self-energies. The vertex correction contributing to anomalous heat transport arises only from the impurity-induced self-energy.

For point-like impurities, the vertex correction, and thus the anomalous Hall current, vanishes in all but chiral p-wave states. This can be shown by noting that for isotropic impurity scattering the vertex correction from Eq. 73, $\delta\hat{\Sigma}(\varepsilon) \propto \langle \delta\hat{g}(\hat{\mathbf{p}}; \varepsilon)\rangle_{\hat{\mathbf{p}}}$, is obtained from the isotropic components of the anomalous propagator. The diagonal components of the equilibrium propagators are isotropic, and thus their contribution to the linear response function involves momentum dependence only from the perturbation, $\psi(\hat{\mathbf{p}}) \propto \mathbf{v}_{\hat{\mathbf{p}};\varepsilon} \cdot \boldsymbol{\nabla}\Phi$. This p-wave term vanishes when averaged over the Fermi-surface, and as a result does not contribute a vertex correction. On the other hand, the off-diagonal components of the equilibrium propagators acquire the phase factor $e^{\pm i\nu\phi}$, reflecting the angular momentum of the chiral Cooper pairs. The linear response functions from these terms include a phase factor $e^{i(\pm\nu+1)\phi}$, which contributes a vertex correction only when $|\nu| = 1$, i.e., for chiral p-wave pairing. This is a non-universal result specific to point-like impurities. For finite-size impurities vertex corrections and thus anomalous Hall effects result for chiral superconductors with $|\nu| > 1$ with results varying with the ionic radius of the impurity.

5.2 Cylindrical harmonic decomposition for 2D chiral superconductors

For chiral superconductors with cylindrically symmetric Fermi surfaces and pairing interactions we can parametrize the non-equilibrium corrections to the propagators and self-energies in terms of cylindrical harmonics,

$$\begin{aligned} \delta\hat{g}(\hat{\mathbf{p}}; \varepsilon) &= -\pi \sum_n e^{in\phi} \begin{pmatrix} \delta g_n(\varepsilon) & e^{i\nu\phi}\delta f_n(\varepsilon) \\ -e^{-i\nu\phi}\delta\underline{f}_n(\varepsilon) & \delta\underline{g}_n(\varepsilon) \end{pmatrix}, \\ \delta\hat{\Sigma}(\hat{\mathbf{p}}; \varepsilon) &= \sum_n e^{in\phi} \begin{pmatrix} \delta\epsilon_n(\varepsilon) & e^{i\nu\phi}\delta\Delta_n(\varepsilon) \\ -e^{-i\nu\phi}\delta\underline{\Delta}_n(\varepsilon) & \delta\underline{\epsilon}_n(\varepsilon) \end{pmatrix}. \end{aligned} \tag{77}$$

The response in different cylindrical harmonic channels can decoupled such that Eq. 69 reduces to

$$|\delta g^a_n(\varepsilon)\rangle = \mathbb{L}^a(\varepsilon)\big[|\psi^a_n(\varepsilon)\rangle + |\delta\Sigma^a_n(\varepsilon)\rangle\big], \tag{78}$$

where $|\delta g_n\rangle = (\delta g_n, \delta\underline{g}_n, \delta f_n, \delta\underline{f}_n)^T$, $|\delta\Sigma_n\rangle = (\delta\epsilon_n, \delta\underline{\epsilon}_n, \delta\Delta_n, \delta\underline{\Delta}_n)^T$, and the temperature gradient along the x-axis generates the perturbation

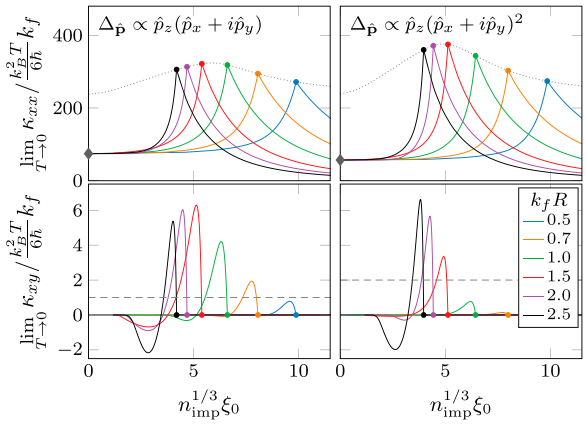

FIGURE 10
Same plots as Figure 9 but for the pairing states E_{1g} (left) and E_{2u} (right). The diamond symbols in the top panels show the values for the "universal limit" for the thermal conductivity in the point-like impurity model [64].

$$|\psi^a_n(\varepsilon)\rangle = \delta_{|n|,1}\psi^a_1(\varepsilon)(1, 1, \cdot, \cdot)^T \tag{79}$$

with $\psi^a_1(\varepsilon) = -i\frac{\varepsilon v_f}{4T^2}\mathrm{sech}^2\left(\frac{\varepsilon}{2T}\right)\partial_x T$. The impurity self-energy correction from Eq. 74 becomes

$$|\delta\Sigma^a_n(\varepsilon)\rangle = -\frac{n_{\rm imp}}{\pi N_f}\mathbb{T}^a_n(\varepsilon)|\delta g^a_n(\varepsilon)\rangle, \tag{80}$$

where the vertex-correction operators are given by

$$\mathbb{T}^a_n(\varepsilon) = \langle\langle \mathbb{Y}_n(\hat{\mathbf{p}})^\star \mathbb{T}^a(\hat{\mathbf{p}}, \hat{\mathbf{p}}'; \varepsilon)\mathbb{Y}_n(\hat{\mathbf{p}}')\rangle_{\hat{\mathbf{p}}}\rangle_{\hat{\mathbf{p}}'}, \tag{81}$$

with $\mathbb{Y}_n(\hat{\mathbf{p}}) = e^{in\phi}\mathrm{Diag}(1, 1, e^{i\nu\phi}, e^{-i\nu\phi})$. Substituting Eq. 80 into Eq. 78 results in a linear matrix equation for the cylindrical harmonics of the anomalous response.

5.3 Spherical harmonic decomposition for 3D chiral superconductors

To exploit the axial symmetry of the Fermi surface and chiral symmetry of the order parameter, we write the anomalous propagator $(\delta x \to \delta g)$ and self-energy $(\delta x \to \delta\Sigma)$ as a sum of spherical harmonic components

$$|\delta x(\hat{\mathbf{p}}; \varepsilon)\rangle = \sum_l \sum_m \mathbb{Y}^m_l(\hat{\mathbf{p}})|\delta x_{l;m}(\varepsilon)\rangle \tag{82}$$

with

$$\mathbb{Y}^l_m(\hat{\mathbf{p}}) \equiv \mathrm{Diag}\big[Y^m_l(\hat{\mathbf{p}}), Y^m_l(\hat{\mathbf{p}}), Y^{m+\nu}_l(\hat{\mathbf{p}}), Y^{m-\nu}_l(\hat{\mathbf{p}})\big]. \tag{83}$$

The spherical harmonic components are then given by

$$|\delta x_{l;m}(\varepsilon)\rangle = \langle \mathbb{Y}^m_l(\hat{\mathbf{p}})^* \big|\delta x(\hat{\mathbf{p}}; \varepsilon)\rangle\rangle_{\hat{\mathbf{p}}}. \tag{84}$$

The anomalous response in Eq. 69 can now be expressed in terms of solutions for each cylindrical harmonic component,

$$|\delta g^a_{l;m}(\varepsilon)\rangle = \sum_{l'} \mathbb{L}^a_{ll';m}(\varepsilon)\big[|\psi^a_{l';m}(\varepsilon)\rangle + |\delta\Sigma^a_{l';m}(\varepsilon)\rangle\big], \tag{85}$$

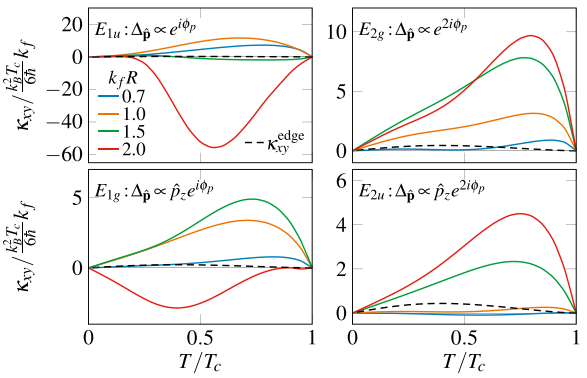

FIGURE 11
The anomalous thermal Hall conductivity *versus* temperature for hard-sphere radii $k_fR = 0.7, 1, 1.5, 2.0$, and for chiral order parameters belonging to the E_{1u}, E_{2g}, E_{1g} and E_{2u} irreducible representations of the hexagonal point group. The Berry phase contribution is shown for comparison (dashed curves). Results are shown for a transport mean free path is $L_N/\xi_0 = 7.5$ and coherence length of $\xi_0 = 100\,k_f^{-1}$. Figure reproduced from Ref. [52] with permission of the APS and the authors.

where the perturbation is

$$\left|\psi^a_{m;l}(\varepsilon)\right\rangle = \langle Y^m_l(\hat{\mathbf{p}})^*(i\mathbf{v}_{\hat{\mathbf{p}}}\cdot\nabla\Phi)\rangle_{\hat{\mathbf{p}}}(1,1,\cdot,\cdot)^T \tag{86}$$

and the linear response matrix is given by

$$\mathbb{L}^a_{ll';m}(\varepsilon) = \langle \mathbb{Y}^m_l(\hat{\mathbf{p}})^*\mathbb{L}^a(\hat{\mathbf{p}};\varepsilon)\mathbb{Y}^m_{l'}(\hat{\mathbf{p}})\rangle_{\hat{\mathbf{p}}}. \tag{87}$$

Similarly the vertex correction, Eq. 74, is recast as

$$\left|\delta\Sigma^a_{l;m},\right\rangle = -\frac{n_{\rm imp}}{\pi N_f}\sum_{l'}\mathbb{T}^a_{ll';m}\left|\delta g^a_{l';m}\right\rangle, \tag{88}$$

where

$$\mathbb{T}^a_{ll';m} = \langle\langle \mathbb{Y}^m_l(\hat{\mathbf{p}})^*\mathbb{T}^a(\hat{\mathbf{p}},\hat{\mathbf{p}}')\mathbb{Y}^m_{l'}(\hat{\mathbf{p}}')\rangle_{\hat{\mathbf{p}}}\rangle_{\hat{\mathbf{p}}'}. \tag{89}$$

Finally we use Eq. 88 to eliminate the self-energy term from Eq. 85, yielding

$$\sum_{l'}\left[\mathbb{1}\delta_{ll'} + \frac{n_{\rm imp}}{\pi N_f}\sum_k \mathbb{L}^a_{lk;m}\mathbb{T}^a_{kl';m}\right]\left|\delta g^a_{l';m}\right\rangle = \sum_{l'}\mathbb{L}^a_{ll';m}\left|\psi^a_{l';m}\right\rangle. \tag{90}$$

This equation is solved by matrix inversion.

6 Results for 2D chiral superconductors

To quantify the effects of finite-size impurities, we consider hard-disc scattering for which the scattering phase shifts are given by $\tan\delta_m = J_{|m|}(k_fR)/N_{|m|}(k_fR)$ [71], where R is the hard-disc radius and, $J_m(z)$ and $N_m(z)$ are Bessel functions of the first and second kind, respectively. Results presented in this section were reported in Ref. [52]. They are included here to highlight the effects of disorder on fully gapped topological chiral superconductors and to compare with new results for 3D nodal chiral superconductors. We start with the effects of impurities on the equilibrium properties and the sub-gap excitation spectrum.

6.1 Suppression of T_c and pair-breaking

For temperatures approaching the critical temperature, T_c, from below temperature the order parameter approaches zero continuously at the second order transition. The resulting linearized gap equation yields the transition temperature in terms of the pairing interaction, λ, bandwidth of attraction ("cutoff"), ε_c, and the pair-breaking effect of quasiparticle-impurity scattering. The pairing interaction and cutoff can be eliminated in favor of the clean-limit transition temperature, T_{c_0}, with the result being a transcendental equation for the suppression of T_c from quasiparticle scattering off the random distribution of impurities. The resulting critical temperature is given by.[12]

$$\ln\frac{T_{c_0}}{T_c} = \Psi\left(\frac{1}{2}+\frac{1}{2}\frac{\xi_0\sigma_{\rm pb}n_{\rm imp}}{T_c/T_{c_0}}\right) - \Psi\left(\frac{1}{2}\right), \tag{91}$$

where $\Psi(x)$ is the digamma function, T_{c_0} is the critical temperature and $\xi_0 = v_f/2\pi T_{c_0}$ is the coherence length in the clean limit. The effects of pair-breaking by impurity scattering is determined by the pair-breaking cross section

$$\sigma_{\rm pb} = \frac{2}{k_f}\sum_m \sin^2(\delta_m - \delta_{m+\nu}), \tag{92}$$

for a chiral order parameter with winding number ν. For s-wave pairing ($\nu = 0$), $\sigma_{\rm pb} = 0$ and consequently $T_c = T_{c_0}$ as expected from Anderson's theorem [72]. In Figure 1, we see that $\sigma_{\rm pb}$ is generally *different* from the total cross section $\sigma_{\rm tot} = (4/k_f)\sum_m \sin^2\delta_m$. The two cross sections approach one another only in the point-like impurity limit $k_fR \ll 1$. Furthermore, $\sigma_{\rm pb}$ and T_c both depend on the ionic radius and the winding number. A feature of the hard-disk scattering model is that $\sigma_{\rm pb}$ for $\nu = 2$ and $\nu = 1$ cross at $k_fR \approx 3.05$. For radii smaller (larger) than this value, pair breaking is stronger and T_c is lower for $\nu = 2$ ($\nu = 1$).

6.2 Density of states

The quasiparticle spectrum, $N(\varepsilon) = N_f\,\mathrm{Im}\,g^R(\varepsilon)$, also depends sensitively on the winding number, ν, as shown in Figure 2. Note the existence of multiple sub-gap impurity bound states, which are broadened into bands with increasing impurity density. These states are generated by the combination of potential scattering by impurities and multiple Andreev scattering by the chiral order parameter. As a result, the number of bound states and their sub-gap energies are determined by not only the impurity potential, e.g., the ionic radius, but also the winding number ν. The impurity-induced sub-gap spectrum has important implications for all quasiparticle transport processes. In the low-temperature limit, $T \ll |\Delta|$, the thermal conductivity is dominated by excitations at energies well below the clean limit gap edge. Diffusion within the lowest energy band of sub-gap states near the Fermi level determines the low temperature heat current as we discuss below.

12 Similar results were derived for the suppression of T_c by non-magnetic disorder in p-wave superconductors and superfluid ^{3}He in aerogel [73, 74].

6.3 Thermal conductivity and the anomalous Thermal Hall effect

In normal metals the thermal conductivity is limited by the transport mean free path for quasiparticles scattering off the random distribution of impurities, $\kappa_N = (\pi^2/3)N_f v_f L_N T$, where $L_N = 1/(\sigma_{\rm tr}\, n_{\rm imp})$ is determined by the transport cross-section.[13]

$$\sigma_{\rm tr} = \left(2/k_f\right)\sum_m \sin^2(\delta_m - \delta_{m+1}). \tag{93}$$

In the superconducting state the thermal conductivity depends on both the mean impurity density as well as the impurity cross-section via,

$$\kappa_{\left\{\begin{smallmatrix} xx \\ xy \end{smallmatrix}\right\}}(T) = N_f v_f \int d\varepsilon \left(\frac{\varepsilon}{2T}\,\mathrm{sech}\,\frac{\varepsilon}{2T}\right)^2 L_{\left\{\begin{smallmatrix} xx \\ xy \end{smallmatrix}\right\}}(\varepsilon), \tag{94}$$

where we define the thermal transport lengths for the longitudinal and transverse currents by

$$L_{xx}(\varepsilon) \equiv \mathrm{Re}\,\frac{v_f \delta g_1^a(\varepsilon)}{-2\psi_1^a(\varepsilon)} \quad \text{and} \quad L_{xy}(\varepsilon) \equiv \mathrm{Im}\,\frac{v_f \delta g_1^a(\varepsilon)}{-2\psi_1^a(\varepsilon)}. \tag{95}$$

Figure 3 shows the temperature dependence of longitudinal thermal conductivity for fully gapped chiral superconductors with $\nu = 1, 2$. Note that the presence of impurities generally enhances the low-temperature thermal conductivity through the formation of sub-gap states, but the enhancement depends on winding number of the chiral order. For impurities with $k_f R = 1$ note that a band of Andreev bound states with a finite density of states at $\varepsilon = 0$ develops for a chiral order parameter with $\nu = 2$, but not for $\nu = 1$ as shown in Figure 2. This is because the state with $\nu = 2$ has more phase space for scattering on the Fermi surface with a nearly perfect sign change that leads to maximal pairbreaking (i.e., scattering with $\delta\vartheta \approx \pm\,\pi/2$) compared to the state with $\nu = 1$ (scattering with $\delta\vartheta \approx \pi$). Thus, for $\nu = 2$ a gapless, diffusive, "metallic" band results in a low-temperature thermal conductivity which is linear in temperature as $T \to 0$, i.e., $\kappa_{xx}(T \to 0) \propto T$. We also note that for $\nu = 1$, such behavior only occurs for sufficiently large impurity densities where the impurity bands broaden to close the gap at $\varepsilon = 0$.

Figure 4 illustrates perhaps the most pronounced effects of finite-size impurities on transport properties. Although the longitudinal conductivity is relatively insensitive to the impurity size or the winding number, the Hall conductivity depends strongly on both R and ν. For point-like impurities with radii smaller than the Fermi wavelength, $k_f R \lesssim 1$, the thermal Hall conductivity is finite for $\nu = 1$, but is dramatically suppressed for chiral states with $|\nu| > 1$, as is clear in the comparison between $\nu = 1$ and $\nu = 2$ for $k_f R = 0.2$ shown in the lower two panels of Figure 4. This supports our previous argument that Hall currents vanish for point-like impurities, i.e., $k_f R \ll 1$, for all chiral winding numbers except $|\nu| = 1$. Also note that as we increase the radius of the impurities such that $k_f R \gtrsim 1$, the Hall conductivity for $\nu = 2$ increases dramatically and can be substantially larger than that for $\nu = 1$. Furthermore, for a fixed normal-state transport mean free path, the Hall conductivity exhibits a non-monotonic dependence on impurity size, reaching maximum at an intermediate radius. Thus, the details of the impurity potential, and thus the sub-gap spectrum, are of crucial importance for a quantitative understanding of anomalous Hall effects in chiral superconductors.

It is also instructive to compare the low-temperature limit of thermal Hall transport originating from the bulk topology in the form of chiral edge states with the bulk thermal Hall conductance from the random distribution of impurities embedded in the bulk of the superconductor. For chiral p-wave pairing the edge-state contribution to the thermal Hall conductance $K_{xy}^{\rm edge}/T = \pi k_B^2/6\hbar$ is universal [46, 75, 76]. By contrast the bulk impurity contribution to the low-temperature thermal Hall conductance can be expressed as $K_{xy}^{\rm bulk} = k_f L_{xy}^{\varepsilon=0} \times K_{xy}^{\rm edge}$ [see Eq. 94], where $L_{xy}^{\varepsilon=0}$ is the effective transport length, which is non-universal and depends on the impurity density and scattering cross-section. Furthermore, $L_{xy}^{\varepsilon=0}$ is finite in a finite range of impurity density for which there is a finite density of states at $\varepsilon = 0$, but not so disordered as to destroy superconductivity, as shown in Figure 5. At sufficiently low impurity density the spectrum is gapped at $\varepsilon = 0$ and so the edge contribution, which is linear in T can dominate at sufficiently low temperatures. While above a critical impurity density superconductivity is destroyed and with it the Hall transport. However, over a significant range of impurity density both the edge and bulk impurity contributions are present for all $T < T_c$.

To compare the edge and bulk contributions to K_{xy} when both are present we consider typical values of the coherence length to Fermi wavelength, $k_f \xi_0$, and the relative impurity size, $k_f R$. For example, taking $k_f \xi_0 = 100$, $\nu = 1$ and $k_f R = 0.5$ we find $K_{xy}^{\rm bulk} \approx 35 K_{xy}^{\rm edge}$ at the value of $n_{\rm imp}$ that maximizes L_{xy} as shown in Figure 5. In general we find that the bulk contribution to the anomalous thermal Hall conductivity is generally dominant over most of the temperature range.

7 Results for chiral superconductors in 3D

We have extended the analysis for chiral states in 2D to chiral states defined on closed 3D Fermi surfaces which often include symmetry enforced line and point nodes of the excitation gap. The results reported here include anomalous thermal Hall effects in candidates for 3D chiral superconductors belonging to tetragonal and hexagonal crystalline point groups, particularly the perovskite Sr_2RuO_4 and the heavy-fermion superconductor UPt_3. To investigate the effects of ionic radius and the dependence on the ionic cross-section, we use the hard-sphere impurity potential for which the scattering phase shifts are analytically given in terms of the hard-sphere radius, R, and the Fermi wavevector [77],

$$\tan\delta_l = \frac{j_l\left(k_f R\right)}{n_l\left(k_f R\right)}, \tag{96}$$

where $j_l(z)$ and $n_l(z)$ are spherical Bessel functions of the first and second kind, respectively [78].

7.1 Critical temperature

For 3D chiral superconductors we obtain a result of the same form as Eq. 91 for the suppression of T_c by disorder, but with a pair-

13 The transport and pair-breaking cross sections are different except for $|\nu| = 1$, c.f. Eq. (92).

breaking cross-section appropriate for scattering of a 3D Fermi surface with finite-size impurities in 3D,

$$\ln\frac{T_{c_0}}{T_c}=\Psi\left(\frac{1}{2}+\frac{n_{\rm imp}\xi_0\sigma_{\rm pb}}{2T_c/T_{c_0}}\right)-\Psi\left(\frac{1}{2}\right), \tag{97}$$

where the pair-breaking cross section is given by,

$$\sigma_{\rm pb}=\frac{4\pi}{k_f^2}\frac{1}{2}\sum_{ll'}\sin^2(\delta_l-\delta_{l'})\frac{(2l+1)(2l'+1)}{2J+1}\langle l,0;l',0|J,0\rangle^2, \tag{98}$$

with $\langle l,m;l',m'|L,M\rangle$ are Clebsch-Gordan coefficients and $J=|\nu|$ is the Cooper pair angular momentum quantum number. For s-wave pairing ($J=0$) the Clebsch-Gordan coefficient vanishes unless $l=l'$, and thus $\sigma_{\rm pb}=0$ and $T_c=T_{c_0}$, consistent with Anderson's theorem [72]. Note also that the pair-breaking cross-section is in general different from both the total cross-section and transport cross section, which are defined by

$$\sigma_{\rm tot}=\frac{4\pi}{k_f^2}\sum_l(2l+1)\sin^2\delta_l \tag{99}$$

$$\sigma_{\rm tr}=\frac{4\pi}{k_f^2}\sum_l(l+1)\sin^2(\delta_{l+1}-\delta_l)=\sigma_{\rm pb}^{J=1}, \tag{100}$$

which determine the quasiparticle scattering lifetime and transport mean-free path, respectively. For point-like impurities all of the above cross sections coincide except for pairing in the s-wave channel, in which case $\sigma_{\rm tot}=\sigma_{\rm tr}$, but $\sigma_{\rm pb}=0$.

In the limit $k_fR\ll1$ the total cross-section and pair-breaking cross-section both approach $\sigma_{\rm tot}=\sigma_{\rm pb}=4\pi R^2$, i.e., four times the geometric cross section of the hard sphere impurity. However, for $k_fR\gtrsim1$ the pair-breaking cross section is typically smaller than the total cross section as shown in Figure 6. In the limit $k_fR\gg1$ $\sigma_{\rm tr}$ and $\sigma_{\rm pb}^J$ approach the geometric limit, πR^2. However, in general the pair-breaking cross section is dependent on the topology of the order parameter. Chiral states with higher angular momentum are subject to stronger pair-breaking effects as we show for hard-sphere impurities. In the lower panel of Figure 6 we show the pair-breaking effects of impurity size and concentration on the critical temperature T_c as described by Eqs. 97, 98.

7.2 Quasiparticle spectrum

Central to the interplay between chiral symmetry, topology and disorder is the impact of impurity scattering on pair-breaking and the resulting sub-gap quasiparticle spectrum. Distinct from fully gapped 2D topological states, 3D chiral ground states support symmetry protected nodes of the order parameter which leads to quasiparticle states over the entire energy range from the maximum gap on the Fermi surface down to the Fermi energy. The quasiparticle spectral function defines the angle-resolved quasiparticle density of states is determined by the retarded diagonal propagator,

$$\mathcal{A}(\hat{\mathbf{p}};\varepsilon)=\mathrm{Im}\,g^R(\hat{\mathbf{p}};\varepsilon). \tag{101}$$

The local density of states is the Fermi-surface average of the spectral function,

$$N(\varepsilon)=N_f\langle\mathcal{A}(\hat{\mathbf{p}};\varepsilon)\rangle_{\hat{\mathbf{p}}}, \tag{102}$$

where N_f is the normal-state density of states at the Fermi level. Figures 7, 8 show the effects of impurity induced scattering on the quasiparticle spectrum. The coherence peak at the maximum gap edge is broadened by impurity scattering. The spectral weight is redistributed to sub-gap energies by the formation of sub-gap resonances. The formation of sub-gap impurity bands is clearly visible in the spectral function for positions on the Fermi surface corresponding to the maximum gap as shown in the bottom panel of Figures 7, 8. These resonances correspond to Andreev bound states that hybridize with continuum states near nodal regions of the order parameter (c.f. Ref. [8]). Impurity-induced sub-gap states are formed by multiple Andreev scattering from the combined potential scattering and branch-conversion scattering by the phase-winding of the order parameter on the Fermi surface. The spectrum depends on the structure of the scattering potential as well as the topological winding number of the order parameter. These impurity-induced sub-gap states play a central role in determining the magnitude and temperature dependence of the anomalous thermal Hall conductivity because these states couple to the chiral condensate is the source of broken time-reversal and mirror symmetries.

7.3 Thermal conductivity tensor for chiral superconductors

The heat current density in Eq. 14 for chiral ground states with embedded impurity disorder reduces to

$$j^{(q)}_{\left\{\begin{smallmatrix}x\\y\end{smallmatrix}\right\}}=\frac{\nu_fN_f}{\sqrt{6}}\left\{\begin{smallmatrix}\mathrm{Im}\\\mathrm{Re}\end{smallmatrix}\right\}\int d\varepsilon\,\varepsilon\,\delta g^a_{1;1}(\varepsilon), \tag{103}$$

where $\delta g^a_{l;m}(\varepsilon)$ is the spherical harmonic component of $g^K(\hat{\mathbf{p}};\varepsilon)^*=-g^K(\hat{\mathbf{p}};\varepsilon)$ with angular momentum quantum numbers l, m. In deriving this formula we used the symmetry relation $\delta g^a_{l;-m}(\varepsilon)=-(-1)^m\,\delta g^a_{l;m}(\varepsilon)^*$. We also note that in linear response theory a thermal gradient does not generate a spectral response, in which case the anomalous response is equal to the Keldysh propagator, $\delta g^a=\delta g^K$. From $\mathbf{j}^{(q)}=-\overleftrightarrow{\kappa}\cdot\nabla T$, we can express the longitudinal and transverse components of the thermal conductivity tensor as

$$\kappa_{\left\{\begin{smallmatrix}xx\\xy\end{smallmatrix}\right\}}=\frac{4}{3}N_f\nu_fT\int\frac{d\varepsilon}{2T}\left(\frac{\varepsilon}{2T}\mathrm{sech}\frac{\varepsilon}{2T}\right)^2L_{\left\{\begin{smallmatrix}xx\\xy\end{smallmatrix}\right\}}(\varepsilon), \tag{104}$$

where the spectral resolved transport mean free paths are defined by

$$L_{xx}(\varepsilon)\equiv\mathrm{Re}\frac{\nu_f\delta g^a_{1;1}(\varepsilon)}{-2\psi^a_{1;1}(\varepsilon)}\quad\text{and}\quad L_{xy}(\varepsilon)\equiv\mathrm{Im}\frac{\nu_f\delta g^a_{1;1}(\varepsilon)}{-2\psi^a_{1;1}(\varepsilon)} \tag{105}$$

with $\psi^a_{1;1}(\varepsilon)=\langle Y^1_1(\hat{\mathbf{p}})^*(i\mathbf{v}_{\hat{\mathbf{p}}}\cdot\nabla\Phi)\rangle_p$ and the thermal gradient is chosen to be along the x-axis, $\nabla\Phi=\hat{\mathbf{x}}\nabla_x\Phi$. In Eq. 104 the derivative of the Fermi distribution leads to the factor $(\varepsilon/2T)^2sech^2(\varepsilon/2T)$ which confines the quasiparticle contribution to the heat current to excitations with $|\varepsilon|\lesssim T$. Thus, if the transport mean free paths, $L_{xx,xy}(\varepsilon)$, vary with ε on a scale $\gamma^*\gg T$, then they may be approximated by $L_{xx,xy}(\varepsilon=0)$, in which case the integration over the spectrum and thermal distribution yields,

$$\kappa\left\{\begin{matrix} xx \\ xy \end{matrix}\right\}(T) \simeq \frac{2\pi^2}{9} N_f \nu_f L \left\{\begin{matrix} xx \\ xy \end{matrix}\right\}(\varepsilon = 0) \times T, \quad T \ll \gamma^\star. \tag{106}$$

In the normal state, $\gamma^\star \sim E_f \gg T$, and the above formula yields the well known result for the normal-state thermal conductivity with $L_{xx}(0)$ given by the transport mean-free path. In particular, in the normal state the matrices that determine the anomalous response and vertex corrections are

$$\begin{aligned} \mathbb{T}^a_{m;ll'} &= \mathbb{1}\delta_{ll'} \frac{k_f^2}{4\pi}(\sigma_{\rm tot} - \sigma_{\rm tr}) \\ \mathbb{L}^a_{m;ll'} &= \mathbb{1}\delta_{ll'} \frac{-2/\nu_f}{\sigma_{\rm tot} n_{\rm imp}}, \end{aligned} \tag{107}$$

where $\sigma_{\rm tot}$ and $\sigma_{\rm tr}$ given by Eqs. 99, 100. Then Eq. 90 yields the anomalous response function,

$$|\delta g^a_{m;l}\rangle = \delta_{l,1}\delta_{|m|,1} \frac{-2/\nu_f}{\sigma_{\rm tr} n_{\rm imp}} |\psi^a_{m;1}\rangle. \tag{108}$$

Combining Eqs. 105, 106 yields the normal-state thermal conductivity

$$\kappa_{xx} \equiv \kappa_N = \frac{2\pi^2}{9} N_f \nu_f L_N \times T, \tag{109}$$

$$\text{where} \quad L_{xx} \equiv L_N = \frac{1}{n_{\rm imp}\sigma_{\rm tr}}, \tag{110}$$

is the transport mean free path. Furthermore, the normal state does not break time-reversal and mirror symmetries and thus L_{xy} vanishes.

In the chiral superconducting phase, $\gamma^\star$ is a low energy scale set by the width of the impurity band at the Fermi level, $\varepsilon = 0$. When it exists a metallic-like band develops which at very low temperature in the superconducting state gives rise to diffusive heat transport that is again linear in temperature for $T < \gamma^\star$, now for both the longitudinal and Hall conductivities. This regime is shown in Figure 9 for both components of the conductivity tensor for the pairing states E_{1u} and E_{2g}, i.e., the states with $\Delta_{\hat{\mathbf{p}}} \propto e^{i\nu\phi_p}$ with $\nu = 1$ and 2, respectively. For these states, low-energy excitations are located around the point nodes at $\hat{\mathbf{p}} = \pm\,\hat{\mathbf{z}}$ (in the clean limit), and therefore do not contribute to low-temperature transport in the basal plane. Instead low-temperature transport relies on the impurity-induced sub-gap bands (see Figures 7, 8). The linear regime onsets for κ_{xx} and κ_{xy} at a threshold impurity density above which the impurity-induced resonances broaden sufficiently to generate a finite density of state at $\varepsilon = 0$. The longitudinal conductivity increases with the impurity density as more states become available at the Fermi level even as the impurity scattering rate goes up. This behavior is due to the fact that the total cross section, which characterizes spectral broadening, is greater than the transport cross section as seen in Figure 6. Above a critical impurity density, $n^c_{\rm imp} = e^{-\gamma_E}/(2\xi_0\sigma_{\rm pb})$, where $\gamma_E \approx 0.577$ is the Euler-Mascheroni constant, the number of available states no longer depends on impurity scattering, i.e., $N(\varepsilon = 0) = N_f$. Thus, increasing the density of impurities only decreases the thermal current by reducing the transport mean free path, $L_N = 1/n_{\rm imp}\sigma_{\rm tr}$, and thus $\kappa_N = L_N \times k_f^2 T/9$. At $n_{\rm imp} = n^c_{\rm imp}$ the zero-temperature limit of κ_{xx}/T is proportional to the ratio of the pair-breaking and transport cross sections, $\kappa^c_{xx}/T \propto \sigma_{\rm pb}/\sigma_{\rm tr}$. As a result the p-wave pairing state has a *universal upper bound* for κ_{xx}/T, i.e., independent of the structure of the impurity potential, because $\sigma_{\rm pb} = \sigma_{\rm tr}$ for $J = 1$ (Eq. 100),

$$\lim_{T\to 0} \frac{\kappa_{xx}}{T} \le \frac{2e^{\gamma_E} k_B^2}{9\hbar} k_f^2 \xi_0, \quad \text{for p} - \text{wave pairing}\,(E_{1u}). \tag{111}$$

The thermal Hall conductivity κ_{xy}/T also initially increases with the impurity concentration above the lower threshold density shown in Figure 9. However, κ_{xy}/T peaks below $n^c_{\rm imp}$ as the Hall response must vanish when disorder destroys the condensate and restores time-reversal and mirror symmetries. The thermal Hall conductivity also depends strongly on the topology of the order parameter *and* the structure of impurity potential. The latter is highlighted by the comparison between the thermal Hall currents for the E_{1u} and E_{2g} states with decreasing impurity size. The state with $\nu = 2$ is severely suppressed $k_f R < 1$. This behavior results from the suppression of branch-conversion scattering which couples impurity scattering to the order parameter of the chiral condensate. In the limit of pure s-wave impurity scattering *only* the chiral states with $\Delta_{\hat{\mathbf{p}}} \propto e^{\pm i\phi_p}$ can support a finite Hall conductivity (see Section 5.1).

Figure 10 shows the thermal conductivity in the zero-temperature limit for the states E_{1g} and E_{2u}, i.e., with $\Delta_{\hat{\mathbf{p}}} \propto \hat{p}_z e^{i\nu\phi_p}$ with $\nu = 1$ and 2, respectively. The presence of the line node at $\hat{p}_z = 0$ guarantees the availability of low-energy quasiparticles for transport in the basal (x, y) plane even in the clean limit. Consequently the low-temperature limit of κ_{xx}/T does not rely solely on impurity-induced sub-gap states at the Fermi level, and is finite even for $n_{\rm imp} \to 0$ as shown in the upper panels of Figure 10. Indeed κ_{xx}/T approaches universal values, identical to those obtained for point-like impurities by Ref. [64], shown as the diamond symbols in Figure 10. However, the thermal Hall conductivity, $\lim_{T\to 0}\kappa_{xy}/T$ does not onset at $n_{\rm imp} = 0$. A finite impurity density is still essential for a non-vanishing anomalous thermal Hall conductance, κ_{xy}/T, at low temperatures. The reason is that the transverse component of the heat current is generated by branch-conversion scattering induced by potential scattering off the distribution of impurities. For this process to generate a finite $\lim_{T\to 0}\kappa_{xy}/T$ the sub-gap Andreev resonances must be sufficiently broadened to generate a finite density of states at the Fermi level.

7.4 Comparison with the anomalous thermal Hall conductivity from Berry curvature

Anomalous Hall transport in ultra-clean topological superconductors with broken time-reversal and mirror symmetries was predicted by several authors [44, 46, 50]. In particular, anomalous Hall conductance originating from the gapless edge spectrum confined on the boundary of a topological chiral superconductor is predicted to be quantized, $\kappa_{xy}/k_B T = \frac{\pi}{12} k_B/\hbar$. This edge contribution to the anomalous thermal Hall conductance can be computed from the Berry curvature $\Omega^{(n)}_{k_x,k_y}$ via the formula [44, 50],

$$\kappa^{\rm edge}_{xy} = \frac{1}{VT} \sum_{n,\mathbf{k}} \Omega^{(n)}_{k_x,k_y}(\mathbf{k}) \int_{E_{\mathbf{k},n}}^{\infty} d\varepsilon \varepsilon^2 f'(\varepsilon), \tag{112}$$

where $f(\varepsilon) = \frac{1}{2}(1 - \tanh\frac{\varepsilon}{2T})$ denotes the Fermi-Dirac distribution, $E_{\mathbf{k},n}$, the quasiparticle spectrum with n being the band index and V the volume of the system. In the superconducting state energy eigenstates of the Bogoliubov Hamiltonian separates into two bands: above $(n = +1)$ and below $(n = -1)$ the Fermi level with eigenenergies $E_{\mathbf{k},\pm} = \pm\sqrt{\xi_{\mathbf{k}}^2 + |\Delta_{\mathbf{k}}|^2}$ where $\xi_{\mathbf{k}} = v_f(|\mathbf{k}| - k_f)$ is the normal-state excitation energy measured from the Fermi level. The Berry curvature reflects the topology of the order parameter, and thus decays rapidly away from the Fermi surface (c.f. Ref. [79]). In the limit $|\Delta| \ll E_f$ the Berry curvature confines the summation over $\mathbf{k}$ to the Fermi surface,

$$\lim_{|\Delta|/T\to 0} \Omega^{(\pm 1)}_{k_x,k_y}(\mathbf{k}) = \pm\,\nu k_f^{-1}\delta\big(|\mathbf{k}| - k_f\big), \tag{113}$$

where as before ν is the phase winding of the order parameter about the k_z-axis. The resulting Berry phase contribution to the anomalous thermal Hall conductance for isotropic Fermi surfaces in d dimensions is

$$\kappa_{xy}^{\rm edge} = -\frac{\nu}{2\pi\hbar T}\left(\frac{k_f}{\pi}\right)^{d-2}\left\langle\int_{-\Delta_{\hat{\mathbf{p}}}}^{+\Delta_{\hat{\mathbf{p}}}} d\varepsilon\,\varepsilon^2 f'(\varepsilon)\right\rangle_{\hat{\mathbf{p}}} = \nu\left(\frac{\pi k_B^2}{6\hbar}\right)\left(\frac{k_f}{\pi}\right)^{d-2} T, \tag{114}$$

in the low-temperature limit.

In Figures 9, 10 we compare the our results for the impurity-induced thermal Hall conductivity with the prediction of the edge contribution based on the Berry curvature in the low temperature limit $(T \to 0)$ for four different chiral ground states. The comparison is based on a typical coherence length scale $k_f\xi_0 = 100$. For all four chiral states the Berry phase contribution is dominant at impurity densities below the threshold for impurity-induced transverse transport in the limit $T \to 0$. However, above this threshold the impurity-induced Hall conductivity is comparable to or much larger than the Berry phase contribution. For example, for the chiral E_{1u} state (bottom left panel of Figure 9), the impurity-induced Hall effect yields transverse heat currents in the zero temperature limit which are approximately an order of magnitude larger than the Berry phase contribution for typical impurity dimensions.

Figure 11 depicts the zero-field thermal Hall conductivity as a function of temperature for chiral states belonging to the spin-triplet, odd-parity E_{1u} and E_{2u} representations and the spin-singlet, even-parity E_{1g} and E_{2g} representations of the hexagonal D_{6h} point group, and the E_u and, E_g representations of D_{4h}. Almost all proposed chiral superconductor candidates, including the perovskite Sr_2RuO_4 and the heavy-fermion superconductor UPt_3, belong to one of these representations. The results show that the impurity-induced anomalous Hall effect (solid lines) dominates the Berry curvature contribution [44, 50] (dashed lines) over the full temperature range in all four chiral pairing states for impurities with $k_f R \gtrsim 1.5$. In this context it is worth reiterating our earlier estimate of the magnitude of the impurity-induced anomalous thermal Hall conductivity for the chiral phase of UPt_3 [52]. Namely, for $k_f = 1\,\text{Å}^{-1}$, $\xi_0 = 100\,\text{Å}$ and $T_c = 0.5\,\text{K}$, representative of UPt_3 [38] we estimate $\kappa_{xy} > 3\times 10^{-3}\,\text{WK}^{-1}\text{m}^{-1}$ for $T \simeq 0.75\,T_c$ for the chiral E_{2u} state with $\nu = 2$ and impurity radius $k_f R = 1.5$ (Figure 11). Compared to the normal-state thermal conductivity at T_c, $\kappa_N(T_c)$, one needs sensitivity to transverse heat currents at the level of $0.01 - 0.03\,\kappa_N(T_c)$ as shown in Figure 4.

8 Summary and outlook

We presented the theoretical framework for understanding disorder-induced anomalous Hall transport in chiral superconductors, and we reported quantitative predictions for the thermal conductivity and the anomalous thermal Hall conductivity in superconductors with phase winding ν for chiral superconducting ground states belonging to the 2D irreducible representations of the hexagonal and tetragonal point groups. We highlight the role of quasiparticle-impurity scattering by *finite-size impurities*, i.e., $k_f R \gtrsim 1$. Our analysis demonstrates that an anomalous thermal Hall effect is obtained for chiral superconductors with winding ν, provided the ionic radius of the impurities satisfies $k_f R \gtrsim |\nu| - 1$. Thus, for point-like impurities with $k_f R \ll 1$ the anomalous thermal Hall current vanishes for all but chiral p-wave ground states. We also discussed the spectrum of impurity-induced Andreev bound states, which are formed via multiple Andreev scattering. The spectrum depends sensitively on the winding number of the chiral order parameter as well as the structure of the impurity potential. Our results also show that the impurity-induced anomalous thermal Hall transport dominates the edge state contribution by an order of magnitude or more over most of the temperature range below T_c. The impurity- and edge contributions to the thermal Hall effect both depend on broken time-reversal and mirror symmetries. Thus, they are equally good signatures of chiral superconductivity. The bulk impurity effect is likely more accessible experimentally; it produces larger Hall currents, and it is insensitive to the quality of the surfaces of a sample. In summary this work provides the theoretical framework for computing and analyzing experiments seeking to identify broken time-reversal and mirror symmetries, as well as non-trivial topology of chiral superconductors, from bulk transport measurements.

8.1 Outlook

There are a number of candidates for chiral superconductivity that have been proposed theoretically and pursued experimentally. The chiral phase of ^{3}He was proven to be chiral p-wave based on the observation of anomalous Hall transport of electrons embedded in superfluid ^{3}He-A [7, 8]. The heavy electron metal UPt_3 shows evidence of broken time-reversal symmetry based on Kerr rotation [33], Josephson interferometry [3], μSR [31] and SANS studies of diffraction by the vortex lattice [6]. Observation of an anomalous thermal Hall effect onsetting at the A to B transition would provide a definitive bulk signature of broken time-reversal and mirror symmetries in UPt_3. Analysis of the temperature- and impurity-dependences of the Hall conductivity could provide new and quantitative experimental constraints on the symmetry class of E-rep of UPt_3. For a number of proposed candidates for chiral superconductivity, e.g., Sr_2RuO_4, doped graphene, SrPtAs, etc., observation of an anomalous thermal Hall effect would provide confirmation of broken time-reversal and mirror symmetry by the superconducting order parameter. NMR experiments revealed the existence of new superfluid phases of liquid ^{3}He when it is infused into low density, anisotropic, random solids - "aerogels" [80] - or confined into sub-micron cavities [81]. Analysis based on

Ginzburg–Landau theory predicts that the ground state of ^{3}He under anisotropic confinement is a chiral phase [82]. Thus, experiments designed to measure the transverse heat current could provide a definitive test of the theory for the ground state of superfluid ^{3}He infused into anisotropic aerogels [83], and similarly for ^{3}He confined in sub-micron cavities [84].

Data availability statement

The original contributions presented in the study are included in the article/supplementary material, further inquiries can be directed to the corresponding author.

Author contributions

VN: Writing–original draft, Writing–review and editing. JS: Writing–original draft, Writing–review and editing.

Funding

The author(s) declare that financial support was received for the research, authorship, and/or publication of this article. The research of VN was supported through the Center for Applied Physics and Superconducting Technologies at Northwestern University and Fermi National Accelerator Laboratory. The research of JS was supported in part by the National Science Foundation (Grant DMR-1508730), "Nonequilibrium States of Topological Quantum Fluids and Unconventional Superconductors," and by the U.S. Department of Energy, Office of Science, National Quantum Information Science Research Centers, Superconducting Quantum Materials and Systems Center (SQMS) under contract number DE-AC02-07CH11359.

Conflict of interest

The authors declare that the research was conducted in the absence of any commercial or financial relationships that could be construed as a potential conflict of interest.

The author(s) declared that they were an editorial board member of Frontiers, at the time of submission. This had no impact on the peer review process and the final decision.

Publisher's note

References

1. Kycia JB, Hong JI, Graf MJ, Sauls JA, Seidman DN, Halperin WP. Suppression of superconductivity in UPt_3 single crystals. *Phys Rev B* (1998) 58:R603–6. doi:10.1103/physrevb.58.r603

2. Mackenzie AP, Maeno Y. The superconductivity of Sr_2RuO_4 and the physics of spin-triplet pairing. *Rev Mod Phys* (2003) 75:657–712. doi:10.1103/revmodphys.75.657

3. Strand JD, Van Harlingen DJ, Kycia JB, Halperin WP. Evidence for complex superconducting order parameter symmetry in the low-temperature phase of UPt_3 from josephson interferometry. *Phys Rev Lett* (2009) 103:197002. doi:10.1103/physrevlett.103.197002

4. Maeno Y, Kittaka S, Nomura T, Yonezawa S, Ishida K. Evaluation of spin-triplet superconductivity in Sr_2RuO_4. *J Phys Soc Jpn* (2012) 81:011009. doi:10.1143/jpsj.81.011009

5. Gannon WJ, Halperin WP, Rastovski C, Schlesinger KJ, Hlevyack J, Eskildsen MR, et al. Nodal gap structure and order parameter symmetry of the unconventional superconductor UPt_3. *New J Phys* (2015) 17:023041. doi:10.1088/1367-2630/17/2/023041

6. Avers KE, Gannon WJ, Kuhn SJ, Halperin WP, Sauls JA, DeBeer-Schmitt L, et al. Broken time-reversal symmetry in the topological superconductor UPt_3. *Nat Phys* (2020) 16:531–5. doi:10.1038/s41567-020-0822-z

7. Ikegami H, Tsutsumi Y, Kono K. Chiral symmetry in superfluid ^{3}He-A. *Science* (2013) 341:59–62. doi:10.1126/science.1236509

8. Shevtsov O, Sauls JA. Electron bubbles and Weyl fermions in chiral superfluid ^{3}He-A. *Phys Rev B* (2016) 94:064511. doi:10.1103/physrevb.94.064511

9. Nandkishore R, Levitov LS, Chubukov AV. Chiral superconductivity from repulsive interactions in doped graphene. *Nat Phys* (2012) 8:158–63. doi:10.1038/nphys2208

10. Black-Schaffer AM, Le Hur K. Topological superconductivity in two dimensions with mixed chirality. *Phys Rev B* (2015) 92:140503. doi:10.1103/physrevb.92.140503

11. Yuan NFQ, Kin FM, Law KT. Possible topological superconducting phases of MoS_2. *Phys Rev Lett* (2014) 113:097001. doi:10.1103/physrevlett.113.097001

12. Biswas PK, Luetkens H, Neupert T, Stürzer T, Baines C, Pascua G, et al. Evidence for superconductivity with broken time-reversal symmetry in locally noncentrosymmetric SrPtAs. *Phys Rev B* (2013) 87:180503. doi:10.1103/physrevb.87.180503

13. Fischer MH, Neupert T, Platt C, Schnyder AP, Werner H, Goryo J, et al. Chiral *d*-wave superconductivity in SrPtAs. *Phys Rev B* (2014) 89:020509. doi:10.1103/physrevb.89.020509

14. Biswas PK, Ghosh SK, Zhao JZ, Mayoh DA, Zhigadlo ND, Xu X, et al. Chiral singlet superconductivity in the weakly correlated metal $LaPt_3P$. *Nat Comm* (2021) 12:2504. doi:10.1038/s41467-021-22807-8

15. Rice TM, Sigrist M. Sr_2RuO_4: an electronic analogue of ^{3}He? *J Phys Cond Mat* (1995) 7:L643–8. doi:10.1088/0953-8984/7/47/002

16. Kallin C. Chiral p-wave order in Sr_2RuO_4. *Rep Prog Phys* (2012) 75:042501. doi:10.1088/0034-4885/75/4/042501

17. Luke GM, Fudamoto Y, Kojima KM, Larkin MI, Merrin J, Nachumi B, et al. Time-reversal symmetry breaking superconductivity in Sr_2RuO_4. *Nature* (1998) 394:558–61. doi:10.1038/29038

18. Xia J, Maeno Y, Peter B, Fejer M, Kapitulnik A. High resolution polar Kerr effect measurements of Sr_2RuO_4: evidence for broken time-reversal symmetry in the superconducting state. *Phys Rev Lett* (2006) 97:167002. doi:10.1103/physrevlett.97.167002

19. Matsumoto M, Sigrist M. Quasiparticle states near the surface and the domain wall in a $p_x + ip_y$ wave superconductor. *J Phys Soc Jpn* (1999) 68:994–1007. doi:10.1143/jpsj.68.994

20. Kirtley JR, Kallin C, Hicks CW, Kim E-A, Liu Y, Moler KA, et al. Upper limit on spontaneous supercurrents in Sr_2RuO_4. *Phys Rev B* (2007) 76:014526. doi:10.1103/physrevb.76.014526

21. Hicks CW, Kirtley JR, Lippman TM, Koshnick NC, Huber ME, Maeno Y, et al. Limits on superconductivity-related magnetization in Sr_2RuO_4 and $PrOs_4Sb_{12}$ from scanning SQUID microscopy. *Phys Rev B* (2010) 81:214501. doi:10.1103/physrevb.81.214501

22. Curran PJ, Bending SJ, Desoky WM, Gibbs AS, Lee SL, Mackenzie AP. Search for spontaneous edge currents and vortex imaging in Sr_2RuO_4 mesostructures. *Phys Rev B* (2014) 89:144504. doi:10.1103/physrevb.89.144504

23. Hicks CW, Brodsky DO, Yelland EA, Alexandra SG, Edkins SD, Nishimura K, et al. Strong increase of T_c of Sr_2RuO_4 under both tensile and compressive strain. *Science* (2014) 344:283–5. doi:10.1126/science.1248292

24. Hassinger E, Bourgeois-Hope P, Taniguchi H, René de Cotret S, Grissonnanche G, Anwar MS, et al. Vertical line nodes in the superconducting gap structure of Sr_2RuO_4. *Phys Rev X* (2017) 7:011032. doi:10.1103/physrevx.7.011032

25. Graf MJ, Balatsky AV. Identifying the pairing symmetry in the Sr_2RuO_4 superconductor. *Phys Rev B* (2000) 62:9697–702. doi:10.1103/physrevb.62.9697

26. Mackenzie AP, Scaffidi T, Hicks CW, Maeno Y. Even odder after twenty-three years: the superconducting order parameter puzzle of Sr_2RuO_4. *npj Quan Mater* (2017) 2:40. doi:10.1038/s41535-017-0045-4

27. Kashiwaya S, Saitoh K, Kashiwaya H, Koyanagi M, Sato M, Yada K, et al. Time-reversal invariant superconductivity of Sr_2RuO_4 revealed by josephson effects. *Phys Rev B* (2019) 100:094530. doi:10.1103/physrevb.100.094530

28. Pustogow A, Luo Y, Chronister A, Su YS, Sokolov DA, Jerzembeck F, et al. Constraints on the superconducting order parameter in Sr_2RuO_4 from oxygen-17 nuclear magnetic resonance. *Nature* (2019) 574:72–5. doi:10.1038/s41586-019-1596-2

29. Sharma R, Edkins SD, Wang Z, Kostin A, Chanchal Sow Maeno Y, et al. Momentum-resolved superconducting energy gaps of Sr_2RuO_4 from quasiparticle interference imaging. *Proc Nat Acad Sci* (2020) 117:5222–7. doi:10.1073/pnas.1916463117

30. Chronister A, Pustogow A, Kikugawa N, Sokolov DA, Jerzembeck F, Hicks CW, et al. Evidence for even parity unconventional superconductivity in Sr_2RuO_4. *Proc Nat Acad Sci* (2021) 118:e2025313118. doi:10.1073/pnas.2025313118

31. Luke GM, Keren A, Le LP, Wu WD, Uemura YJ, Bonn DA, et al. Muon spin relaxation in UPt_3. *Phys Rev Lett* (1993) 71:1466–9. doi:10.1103/physrevlett.71.1466

32. Hess DW, Tokuyasu TA, Sauls JA. Broken symmetry in an unconventional superconductor: a model for the double transition in UPt_3. *J Phys Cond Matt* (1989) 1:8135–45. doi:10.1088/0953-8984/1/43/014

33. Schemm ER, Gannon WJ, Wishne CM, Halperin WP, Kapitulnik A. Observation of broken time-reversal symmetry in the heavy-fermion superconductor UPt_3. *Science* (2014) 345:190–3. doi:10.1126/science.1248552

34. Machida K, Ozaki M. Splitting of superconducting transitions in UPt_3. *J Phys Soc Jpn* (1989) 58:2244–7. doi:10.1143/jpsj.58.2244

35. Huxley A, Rodiere P, Paul DMK, Niels van Dijk Cubitt R, Flouquet J. Re-alignment of the flux-line lattice by a change in the symmetry of superconductivity in UPt_3. *Nature* (2000) 406:160–4. doi:10.1038/35018020

36. Strand JD, Bahr DJ, Van Harlingen DJ, Davis JP, Gannon WJ, Halperin WP. The transition between real and complex superconducting order parameter phases in UPt_3. *Science* (2010) 328:1368–9. doi:10.1126/science.1187943

37. Sauls JA. The order parameter for the superconducting phases of UPt_3. *Adv Phys* (1994) 43:113–41. doi:10.1080/00018739400101475

38. Joynt R, Taillefer L. The superconducting phases of UPt_3. *Rev Mod Phys* (2002) 74:235–94. doi:10.1103/revmodphys.74.235

39. Choi CH, Sauls JA. Identification of odd-parity superconductivity in UPt_3 based on paramagnetic limiting of the upper critical field. *Phys Rev Lett* (1991) 66:484–7. doi:10.1103/physrevlett.66.484

40. Choi CH, Sauls JA. Anisotropy of the upper critical field in a heavy-fermion superconductor. *Phys Rev B* (1993) 48:13684–90. doi:10.1103/physrevb.48.13684

41. Graf MJ, Yip S-K, Sauls JA. Thermal conductivity of UPt_3 at low temperatures. *J Low Temp Phys* (1996) 102:367–79. (E) 106, 727 (1997). doi:10.1007/bf00755120

42. Graf MJ, Yip S-K, Sauls JA. Thermal conductivity of the accidental degeneracy and enlarged symmetry group models for superconducting UPt_3. *J Low Temp Phys* (1999) 114:257–73. doi:10.1023/a:1021814206687

43. Matthias J, Graf S-KY, Sauls JA. Identification of the orbital pairing symmetry in UPt_3. *Phys Rev B* (2000) 62:14393–402. doi:10.1103/PhysRevB.62.14393

44. Goswami P, Andriy H. Nevidomskyy, Topological Weyl superconductor to diffusive thermal Hall metal crossover in the B phase of UPt_3. *Phys Rev B* (2015) 92:214504. doi:10.1103/physrevb.92.214504

45. Tsutsumi Y, Machida K. Edge mass current and the role of Majorana fermions in A-phase superfluid ^{3}He. *Phys Rev B* (2012) 85:100506. doi:10.1103/physrevb.85.100506

46. Read N, Green D. Paired states of Fermions in two dimensions with breaking of parity and time-reversal symmetries and the fractional quantum Hall effect. *Phys Rev B* (2000) 61:10267–97. doi:10.1103/physrevb.61.10267

47. Stone M, Roy R. Edge modes, edge currents, and gauge invariance in $p_x + ip_y$ superfluids and superconductors. *Phys Rev B* (2004) 69:184511. doi:10.1103/physrevb.69.184511

48. Sauls JA. Surface states, edge currents, and the angular momentum of chiral *p*-wave superfluids. *Phys Rev B* (2011) 84:214509. doi:10.1103/physrevb.84.214509

49. Sumiyoshi H, Fujimoto S. Quantum thermal Hall effect in a time-reversal-symmetry-broken topological superconductor in two dimensions: approach from bulk calculations. *J Phys Soc Jpn* (2013) 82:023602. doi:10.7566/jpsj.82.023602

50. Qin T, Niu Q, Shi J. Energy magnetization and the thermal Hall effect. *Phys Rev Lett* (2011) 107:236601. doi:10.1103/physrevlett.107.236601

51. Scaffidi T, Simon SH. Large chern number and edge currents in Sr_2RuO_4. *Phys Rev Lett* (2015) 115:087003. doi:10.1103/physrevlett.115.087003

52. Ngampruetikorn V, Sauls JA. Impurity-induced anomalous thermal hall effect in chiral superconductors. *Phys Rev Lett* (2020) 124:157002. doi:10.1103/physrevlett.124.157002

53. Arfi B, Bahlouli H, Pethick CJ, Pines D. Unusual transport effects in anisotropic superconductors. *Phys Rev Lett* (1988) 60:2206–9. doi:10.1103/physrevlett.60.2206

54. Li S, Andreev AV, Spivak BZ. Anomalous transport phenomena in $p_x + ip_y$ superconductors. *Phys Rev B* (2015) 92:100506. doi:10.1103/physrevb.92.100506

55. Yip S. Low temperature thermal hall conductivity of a nodal chiral superconductor. *Supercond Sci Technol* (2016) 29:085006. doi:10.1088/0953-2048/29/8/085006

56. Keldysh LV. Diagram technique for nonequilibrium processes. *Zh Eskp Teor Fiz* (1965) 47:1515. Sov. Phys. JETP, 20, 1018 (1965).

57. Eilenberger G. Transformation of gorkov's equation for type II superconductors into transport-like equations. *Zeit F Physik* (1968) 214:195–213. doi:10.1007/bf01379803

58. Larkin AI, Ovchinnikov YN. Quasiclassical method in the theory of superconductivity. *Sov Phys JETP* (1969) 28:1200–5.

59. Larkin AI, Ovchinnikov YN. Nonlinear conductivity of superconductors in the mixed state. *Sov Phys JETP* (1975) 41:960.

60. Stanev V, Tešanović Z. Three-band superconductivity and the order parameter that breaks time-reversal symmetry. *Phys Rev B* (2010) 81:134522. doi:10.1103/physrevb.81.134522

61. Serene JW, Rainer D. The quasiclassical approach to ^{3}*He*. *Phys Rep* (1983) 101:221–311. doi:10.1016/0370-1573(83)90051-0

62. Larkin AI, Ovchinnikov YN. Nonequilibrium superconductivity. In: Langenberg D, Larkin A, editors. *Modern problems in condensed matter Physics*. Amsterdam: Elsevier Science Publishers (1986).

63. Rainer D, Sauls JA. Strong-coupling theory of superconductivity. In: *Superconductivity: from basic Physics to new developments*. Singapore: World Scientific (1994). p. 45–78. arXiv. Available at: https://arxiv.org/abs/1809.05264.

64. Graf MJ, Yip S-K, Sauls JA, Rainer D. Electronic thermal conductivity and the wiedemann-franz law for unconventional superconductors. *Phys Rev B* (1996) 53:15147–61. doi:10.1103/physrevb.53.15147

65. Rainer D. Principles of *ab initio* calculations of superconducting transition temperatures. In: *Progress in low temperature Physics*, 10. Amsterdam: Elsevier Science Publishers B.V. (1986). p. 371–424.

66. Ambegaokar V, Mermin ND. Thermal anomalies of ^{3}He pairing in a magnetic field. *Phys Rev Lett* (1973) 30:81–4. doi:10.1103/physrevlett.30.81

67. Graf MJ, Palumbo M, Rainer D, Sauls JA. Infrared conductivity in layered d-wave superconductors. *Phys Rev B* (1995) 52:10588–600. doi:10.1103/physrevb.52.10588

68. Arfi B, Bahlouli H, Pethick CJ. Transport properties of anisotropic superconductors: influence of arbitrary electron-impurity phase shifts. *Phys Rev B* (1989) 39:8959–83. doi:10.1103/physrevb.39.8959

69. Mineev VP, Samokhin K. *Introduction to unconventional superconductivity*. Amsterdam: Gordon and Breach Science Publishers (1999).

70. Löfwander T, Fogelström M. Large thermoelectric effects in unconventional superconductors. *Phys Rev B* (2004) 70:024515. doi:10.1103/physrevb.70.024515

71. Richard Lapidus I. Scattering by two-dimensional circular barrier, hard circle, and delta function ring potentials. *Am J Phys* (1986) 54:459–61. doi:10.1119/1.14585

72. Anderson PW. Theory of dirty superconductors. *J Phys Chem Sol* (1959) 11:26–30. doi:10.1016/0022-3697(59)90036-8

73. Larkin AI. Vector paring in superconductors in small dimensions. *Sov Phys JETP Lett* (1965) 2:130–2.

74. Thuneberg EV, Yip S-K, Fogelström M, Sauls JA. Scattering models for superfluid ^{3}He in aerogel. *Phys Rev Lett* (1998) 80:2861–4. cond-mat/9601148v2. doi:10.1103/physrevlett.80.2861

75. Senthil T, Marston JB, Fisher MPA. Spin quantum hall effect in unconventional superconductors. *Phys Rev B* (1999) 60:4245–54. doi:10.1103/physrevb.60.4245

76. Sumiyoshi H, Fujimoto S. Quantum thermal hall effect in a time-reversal-symmetry-broken topological superconductor in two dimensions: approach

from bulk calculations. *J Phys Soc Jpn* (2013) 82:023602. doi:10.7566/JPSJ.82.023602

77. Albert M. *Quantum mechanics*, I. North-Holland (1958).

78. Abramowitz M, Stegun IA. *Handbook of mathematical functions*. New York: Dover (1970).

79. Andreas PS, Brydon PMR. Topological surface states in nodal superconductors. *J Phys Cond Matt* (2015) 27:243201. doi:10.1088/0953-8984/27/24/243201

80. Pollanen J, Li JIA, Collett CA, Gannon WJ, Halperin WP, Sauls JA. New chiral phases of superfluid ^{3}He stabilized by anisotropic silica aerogel. *Nat Phys* (2012) 8:317–20. doi:10.1038/nphys2220

81. Levitin LV, Bennett RG, Casey A, Cowan B, Saunders J, Drung D, et al. Phase diagram of the topological superfluid ^{3}He confined in a nano-scale slab geometry. *Science* (2013) 340:841–4. doi:10.1126/science.1233621

82. Sauls JA. Chiral phases of superfluid ^{3}He in an anisotropic medium. *Phys Rev B* (2013) 88:214503. doi:10.1103/physrevb.88.214503

83. Sharma P, Sauls JA. Anomalous thermal Hall effect in chiral phases of ^{3}He-aerogel. *J Low Temp Phys* (2022) 208:341–55. doi:10.1007/s10909-021-02657-w

84. Sharma P, Vorontsov A, Sauls JA. Disorder induced anomalous thermal Hall effect in chiral phases of superfluid ^{3}He. *JPS Conf Proc* (2023) 38:011002. Proc. of LT29, Hokkaido, Japan, 2209.04004. doi:10.7566/JPSCP.38.011002

frontiers | Frontiers in Physics

TYPE Original Research
PUBLISHED 13 May 2024
DOI 10.3389/fphy.2024.1396463

OPEN ACCESS

EDITED BY
Vladimir Dobrosavljevic,
Florida State University, United States

REVIEWED BY
Mario Cuoco,
National Research Council (CNR), Italy
Takeshi Egami,
The University of Tennessee, United States

*CORRESPONDENCE
N. E. Hussey,
n.e.hussey@bristol.ac.uk

RECEIVED 05 March 2024
ACCEPTED 24 April 2024
PUBLISHED 13 May 2024

CITATION
Juskus D, Ayres J, Nicholls R and Hussey NE (2024), Insensitivity of T_c to the residual resistivity in high-T_c cuprates and the tale of two domes.
Front. Phys. 12:1396463.
doi: 10.3389/fphy.2024.1396463

Insensitivity of T_c to the residual resistivity in high-T_c cuprates and the tale of two domes

D. Juskus[1], J. Ayres[1], R. Nicholls[1] and N. E. Hussey[1,2]*

[1]H. H. Wills Physics Laboratory, University of Bristol, Bristol, United Kingdom, [2]High Field Magnet Laboratory (HFML-FELIX) and Institute for Molecules and Materials, Radboud University, Nijmegen, Netherlands

One of the few undisputed facts about hole-doped high-T_c cuprates is that their superconducting gap Δ has *d*-wave symmetry. According to 'dirty' *d*-wave BCS theory, even structural (non-magnetic) disorder can suppress Δ, the transition temperature T_c and the superfluid density ρ_s. The degree to which the latter is affected by disorder depends on the nature of the scattering. By contrast, T_c is only sensitive to the total elastic scattering rate (as estimated from the residual resistivity ρ_0) and should follow the Abrikosov-Gor'kov pair-breaking formula. Here, we report a remarkable robustness of T_c in a set of Bi2201 single crystals to large variations in ρ_0. We also survey an extended body of data, both recent and historical, on the LSCO family which challenge key predictions from dirty *d*-wave theory. We discuss the possible causes of these discrepancies, and argue that either we do not understand the nature of disorder in cuprates, or that the dirty *d*-wave scenario is not an appropriate framework. Finally, we present an alternative (non-BCS) scenario that may account for the fact that the superconducting dome in Tl2201 extends beyond that seen in Bi2201 and LSCO and suggest ways to test the validity of such a scenario.

KEYWORDS

superconductivity, cuprates, charge transport, dirty d-wave theory, disorder

1 Introduction

Over the past decade or so, overdoped (OD) cuprates, i.e., those with a carrier density beyond optimal doping, have become the central focus of efforts to elucidate the origin of high-T_c superconductivity. This shift of focus has emerged from two seemingly contradictory standpoints. The first is the perceived simplicity of the nature of the OD regime; the normal state pseudogap (on the hole-doped side) having been suppressed and with it, many of the associated ordering tendencies [1]. The second is the realization that this region of the cuprate phase diagram also hosts its own highly anomalous properties, both in the normal and superconducting (SC) states [2–14]. Chief among these is the report of a robust linear-in-T dependence of the superfluid stiffness ρ_s as $T_c \to 0$ on the overdoped side [5]. Prior to this discovery, the observed reduction in T_c and ρ_s with overdoping had been attributed to a combination of a diminishing pairing interaction and the pair-breaking effects of impurities treated within a 'dirty *d*-wave' extension of BCS theory. The robustness of the T-linear form of $\rho_s(T)$, a hallmark of clean *d*-wave superconductivity, was inconsistent with theoretical predictions and thus presented a challenge to the pre-existing consensus of what drives the reduction of T_c and ρ_s with overdoping.

In response to this challenge, a thorough examination of the viability of the dirty *d*-wave scenario was carried out on two very different OD cuprates–$La_{2-x}Sr_xCuO_4$ (LSCO) and

$Tl_2Ba_2CuO_{6+\delta}$ (Tl2201)–using realistic parameterisations of their respective electronic structures and treating the scattering potentials generated by out-of-plane defects with *ab initio* DFT calculations [15–19]. The conclusions of this work were that many facets of the SC state in both families, including the dependence of ρ_s on T and p [5], the THz optical conductivity (in LSCO) [7], the residual specific heat [20, 21] and the residual thermal conductivity [22–25] could be successfully captured within the existing framework. In order to account for the robustness of the T-linearity of $\rho_s(T)$ down to low-T, the total scattering potential was argued to consist almost exclusively of weak (Born) scatterers–due to the out-of-plane defects–combined with a small amount of strong (unitarity-limit) scatterers located within the CuO_2 plane (see also Ref. [26]).

Within the same picture, the suppression of T_c from its disorder-free value T_{c0} does not depend on the nature of the scatterer, only on the absolute magnitude of the normal-state scattering rate Γ_n, as described by the Abrikosov-Gorkov pair-breaking formula [27]. In the work of Broun, Hirschfeld and co-workers [15–19], estimates for Γ_n were deduced from the residual resistivity ρ_0 (essentially an extrapolation of the normal-state in-plane resistivity $\rho_{ab}(T)$ down to zero temperature). These estimates for Γ_n (≈20 K in OD Tl2201 and ≈55 K in OD LSCO) were then found to generate $T_c(p)$ domes with realistic values for the maximum T_c (T_c^{max}) as well as the doping level (p_{sc}) at which superconductivity vanishes in both families. Initially, these $T_c(p)$ domes were derived from a single $T_{c0}(p)$ dome [17]. The later, more refined *ab initio* treatment required two $T_{c0}(p)$ domes to reproduce the experimental results though the difference between them was only slight [18].

One of the most consequential aspects of dirty *d*-wave theory, largely overlooked until now, is the strong dependence of T_c on Γ_n, irrespective of the nature of the scattering potential. As a rough guide, an increase in ρ_0 by 10 $\mu\Omega$cm corresponds to a decrease in both Γ_n and T_c of order 10 K. (More details of this correspondence will be presented later). Such modest variations in ρ_0 are not uncommon in samples from different growth batches or in samples synthesized in different laboratories and thus one might expect a notable variation in reported T_c values. Yet, throughout almost 4 decades of cuprate research, the SC domes reported in the literature for a particular cuprate family have been, to all intents and purposes, identical, both in terms of their T_c^{max} values and the doping extent of the dome itself.

The aim of this article is to highlight this insensitivity of T_c to changes in ρ_0 in different OD cuprates through a combination of new measurements and analysis of existing data. The article itself is divided into three parts. The first is an in-house transport study of one of the most inhomogeneous cuprate families–Pb/La-doped $Bi_2Sr_2CuO_{6+\delta}$ (Bi2201)–that exhibits a remarkable robustness of T_c to marked changes in ρ_0. The second is a survey of recent transport data on LSCO crystals and films which, when combined with multiple reports of the $T_c(x)$ dome in LSCO spanning several decades, represent a notable challenge to the applicability of dirty *d*-wave BCS theory to OD cuprates. In the final section, we present a simple (two-fluid) scenario for OD cuprates which offers an alternative explanation as to why p_{sc} (Tl2201) > p_{sc}(Bi2201/LSCO). While incorporating disorder-induced pair-breaking in some capacity, this scenario considers the strange metallic nature of OD cuprates [28] as its defining feature. The corollary of this study is that either we do not understand the nature of disorder in cuprates, or that the dirty *d*-wave scenario, at least in its present guise, is not an appropriate framework to describe the suppression of superconductivity in OD cuprates as $p \rightarrow p_{sc}$.

2 Results and discussion

2.1 Robustness of T_c to variations of ρ_0 in Bi2201

Large single crystals of Pb/La-doped Bi2201 were taken from boules grown independently at two sites via the floating-zone technique. The doping level of the crystals used in this study ($p = 0.215 \pm 0.005$) was estimated from the measured T_c using the Presland relation $1 - T_c/T_c^{max} = 82.6\,(p - 0.16)^2$ [29], with $T_c^{max} = 36$ K. Recently, it was shown that when using this relation, normalized $\rho_{ab}(T)$ curves for Bi2201 and LSCO single crystals of the same p (or T_c) value collapse on top of one another [30]. The crystals were cleaved along the *ab*-plane and cut into shape along the *c*-axis using a wire saw which leaves no burring of the edges. Typical sample dimensions were approximately $1{,}000 \times 200 \times 8$–$40\ \mu m^3$ (the thicknesses having been determined by a scanning electron microscope).

For the resistivity measurements, electrical contacts were made using 25 μm Au wire and fixed using Dupont 6838 paint before being annealed in flowing oxygen for 10 min at 450°C. Typical contact resistances were between 1 and 10 Ω. All samples were cooled using a ^{4}He flow cryostat and their in-plane resistivity measured using a standard four-point ac lock-in detection technique. While the dimensions of the samples could be determined to a high degree of accuracy, the absolute magnitudes of $\rho_{ab}(T)$ were subject to an uncertainty of ±25% due to the uncertainty in estimating the distance between the voltage electrodes. Complementary magnetization measurements were carried out in a commercial SQUID magnetometer.

Figure 1 shows $\rho_{ab}(T)$ curves for 6 Pb/La-doped Bi2201 crystals grown in Amsterdam (top panel) and Sendai (bottom panel). For both sets of crystals $T_c \simeq 27$ K and $p \simeq 0.20$. According to a recent combined transport and angle-resolved photoemission spectroscopy (ARPES) study [30], this doping level lies very close to the doping level $p^\star$ at which the pseudogap regime terminates in Bi2201. Correspondingly, all $\rho_{ab}(T)$ curves display a quasi-T-linear dependence from room temperature down to T_c albeit shifted with respect to each other due to the difference in their respective ρ_0 values.

In certain crystals (labelled ♯1B and ♯1C in Figure 1A), $\rho_{ab}(T)$ displays a small upward deviation from T-linearity below around 75 K. One possible origin for this upward deviation is contamination of the signal from *c*-axis mixing, whereby a proportion of the current flows between the CuO_2 planes. The anisotropy in the resistivity ρ_c/ρ_{ab} is extremely large in Bi2201 (≈10^5–10^6) [31] and $\rho_c(T)$ is known to exhibit only weakly metallic behaviour in the OD regime. Hence, any *c*-axis mixing would lead to a marked increase in the absolute value of the as-measured resistivity relative to the intrinsic *ab*-plane response as well as a different T-dependence. In order to minimise this possibility, each sample was mounted in a 'floating' configuration, i.e., elevated above the substrate with the silver paint fully extending across the sample thickness, in order to isolate the in-plane current response and avoid any contamination from current along the *c*-axis. Using only samples in which the resistivities on opposite sides of the crystal were

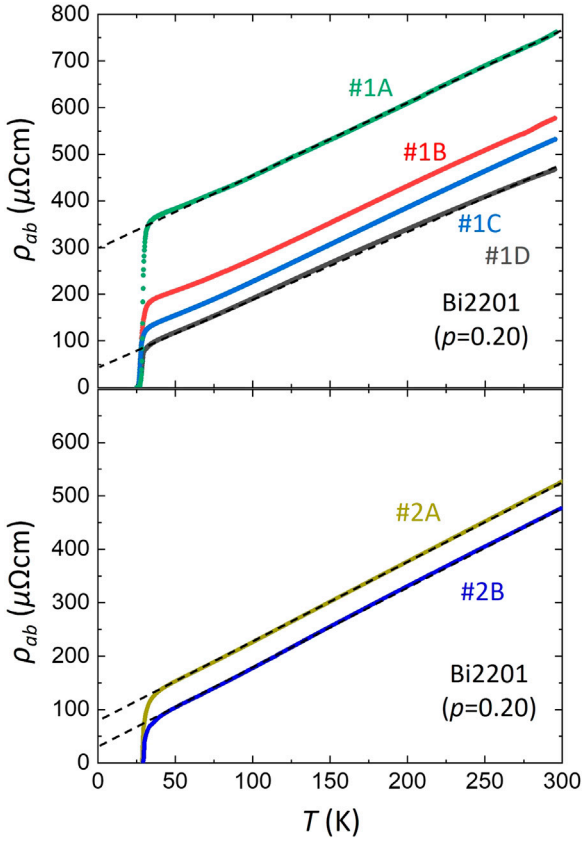

FIGURE 1
In-plane resistivity *versus* temperature $\rho_{ab}(T)$ for several Bi2201 single crystals with a doping level $p \approx 0.20$. The crystals in the two panels were grown at two distinct sites: those labeled #1 (top panel) were grown in Amsterdam, while those labeled #2 (bottom panel) were grown in Sendai. The dashed lines are extrapolations of a fit to $\rho_{ab}(T)$ between 50 and 150 K to allow a better estimate of the residual resistivity (ρ_0) values for each crystal. Note that the $\rho_{ab}(T)$ curves have been normalised such that their high-T T-linear slopes are equivalent. The adjustments required to normalise these slopes were of the order of the geometrical uncertainty (±25%) in each panel.

identical, we obtained a series of $\rho_{ab}(T)$ curves that exhibit the same T-linear slope between 75 K and 300 K (to within our geometrical uncertainty), suggesting that c-axis mixing is indeed negligible in these crystals.

The most striking feature of Figure 1 is the invariance of T_c (= 27 ± 1 K), irrespective of the magnitude of ρ_0, that itself varies by over 250 $\mu\Omega$cm. (For each crystal, ρ_0 is obtained by extrapolating a fit to $\rho_{ab}(T)$ between 50 K and 150 K). Moreover, any small variations in the value of T_c do not appear to be correlated with ρ_0. As we will discuss in the following section, this level of impurity scattering should be enough to destroy superconductivity many times over. Such robustness is contrary to expectations within dirty d-wave theory in which changes in T_c and ρ_0 are strongly correlated (via Γ_n).

2.2 Comparison with dirty *d*-wave theory

Dirty d-wave theory, as applied to cuprate superconductivity, is an extension of an original treatment of paramagnetic impurities in a conventional (s-wave) BCS superconductor [27]. Due to the sign change of the SC order parameter Δ occurring at the nodes, even non-magnetic impurities can induce pair breaking in a d-wave superconductor. This in turn leads to a residual density of zero-energy states and a suppression of both T_c and the superfluid density n_s. More quantitatively, Δ closes at a T_c value that is reduced in the presence of disorder from its optimal value T_{c0} according to the Abrikosov-Gor'kov (AG) equation:

$$\ln\frac{T_{c0}}{T_c} = \psi_0\left(\frac{1}{2}+\frac{\hbar\Gamma_n}{2\pi k_B T_c}\right) - \psi_0\left(\frac{1}{2}\right), \quad (1)$$

where ψ_0 is the usual digamma function, Γ_n is the normal-state impurity scattering rate, and $\hbar$ and k_B are the reduced Planck constant and Boltzmann constant, respectively.

As mentioned in the Introduction, a recent series of studies based on the self-consistent T-matrix approximation (SCTMA) have indicated that a number of experimental observations in LSCO and Tl2201 can be successfully accounted for by carefully treating the scattering potentials arising from different types of out-of-plane disorder within the dirty d-wave formalism [15–19]. Within their picture, the momentum relaxation rate is assumed to be the same as the single-particle scattering rate, as deduced, for example, from ARPES. Accordingly, Γ_n can be estimated from the Drude expression for the (residual) dc resistivity:

$$\rho_0 = \frac{m^\star}{ne^2}\Gamma_n. \quad (2)$$

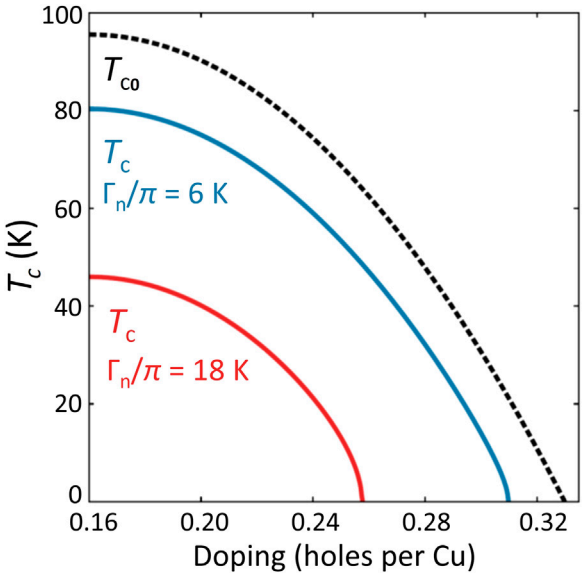

FIGURE 2
Predictions of dirty *d*-wave theory. For a single parabolic doping dependence of the underlying $T_{c0}(p)$, different choices of Γ_n result in superconducting domes $T_c(p)$ reminiscent of Tl2201 and LSCO. The quoted values of $\Gamma_n = 6\pi$ (18π) K correspond to ρ_0 values of 6 (20) $\mu\Omega$cm for Tl2201 (LSCO), respectively. For Bi2201, ρ_0 = 50 $\mu\Omega$cm corresponds to $\Gamma_n \sim 90$ K or 30π K. Reproduced with kind permission from Ref. [17].

Here m^* is the effective mass, n is the carrier density and e is the electronic charge. Within the SCTMA, Born and unitarity scattering contribute additively to Γ_n and thus, from the perspective of Eq. 1, the suppression of T_c is largely independent of the impurity phase shift. Note too that the above expression does not take into account the effects of small-angle scattering, which can cause the momentum relaxation rate to be substantially smaller than the single-particle scattering rate. Hence, the estimate of Γ_n from Eq. 2 is in fact a lower bound for input into Eq. 1.

Figure 2 reproduced from Ref. [17]–shows how different $T_c(p)$ domes for LSCO (red line) and Tl2201 (blue line) can be derived from a singular form of $T_{c0}(p)$ using estimates for Γ_n that are consistent with experimental observations. The quoted values of $\Gamma_n = 6\pi$ (18π) K correspond to ρ_0 = 6 (20) $\mu\Omega$cm for Tl2201 (LSCO), respectively. (As mentioned above, in a subsequent study [18], slightly modified $T_{c0}(p)$ domes for Tl2201 and LSCO were incorporated into the model, though the differences were only minor.) The essential feature of Figure 2 is that the reduction in T_c of ~ 20 K (60 K) from its inferred T_{c0} value in optimally doped Tl2201 (LSCO) is attributed to a normal state scattering rate of approximately the same magnitude. At the same time, the extent of the SC dome in LSCO (on the overdoped side) is reduced by $\Delta p \approx 0.06$ for the same level of impurity scattering.

In order to link these estimates for Γ_n to ρ_0, we must also derive estimates for m^* and $n = (1 + p)/V_{\text{cell}}$ into Eq. 1, where V_{cell} is the volume of the unit cell. First, let us consider LSCO. For $p = x = 0.20$, we obtain $m^* \sim 10\ m_e$ (the bare electron mass) from the electronic specific heat [32] and $n = 1.3 \times 10^{28}$ m^{-3} (using $1 + p$ instead of p). Hence, Γ_n = 55 K corresponds to $\rho_0 \sim 20$ $\mu\Omega$cm, as quoted above. Similarly for Tl2201 ($p = 0.27$), $m^* \sim 5\ m_e$ [33, 34], $n = 7.4 \times 10^{27}$ m^{-3} and Γ_n = 18 K, giving $\rho_0 \sim 6$ $\mu\Omega$cm.

2.3 Application of dirty *d*-wave theory to Bi2201

For Bi2201, m* ~ 7–10 m_e for $p \sim 0.23$ (T_c = 18 K) [35] and $n = 7.0 \times 10^{27}$ m^{-3}. Hence, the spread in ρ_0 shown in Figure 1 (40–290 $\mu\Omega$cm) corresponds to 70 K $\lesssim \Gamma_n \lesssim$ 500 K. In other words, while the impurity scattering rate deduced from ρ_0 varies on the scale of 500 K, the superconducting transition temperature is found to be constant to within 1 K. Such extreme inequality is clearly at odds with expectations from dirty *d*-wave theory but is likely, at least in part, to reflect the presence of some form of defect that contributes to an enhanced ρ_0 while creating, by itself, little or no pair-breaking. Before addressing the viability of the BCS pair-breaking picture, therefore, let us first consider alternative explanations for this surprising finding. (Recall that we have already dismissed *c*-axis mixing in the current flow as a possible cause of this variation in ρ_0.)

In this present study, T_c values are quoted based on $\rho_{ab}(T)$ measurements. Resistivity is effectively a one-dimensional probe of superconductivity, in the sense that a transition to zero resistivity requires only a single, filamentary SC path to be realized. Hence, if a sliver of nominally pristine Bi2201 (i.e., with minimal disorder) permeates each crystal, the apparent robustness of T_c may be illusory. In the normal state, by contrast, the current distribution will be sensitive to all regions of the sample and indeed, if the SC filament is sufficiently thin, it will be dominated by those non-SC regions with higher ρ_0. Such a scenario may help explain why T_c is so insensitive to marked variations in ρ_0.

Simulations presented in Supplementary Appendix SA indicate that for such a scenario to be applicable, the SC region must occupy ~ 1% of the total volume of the sample; otherwise the T-dependence of $\rho_{ab}(T)$ will visibly deviate downwards from its intrinsic (T-linear)

behaviour, which is not observed. In order to estimate the SC volume fraction of our crystals, we measured the dc magnetisation of two of them (with ρ_0 values of 80 $\mu\Omega cm$ (ρ(T) data not shown) and 300 $\mu\Omega cm$ (Sample #1A in Figure 1), respectively) using a SQUID magnetometer with the magnetic field applied parallel to the *ab*-plane (where the demagnetisation factor is minimised). The results are shown in Supplementary Appendix SB and reveal an estimated volume fraction in both crystals of ~ 100%. Thus, it seems unlikely that the presence of a filamentary SC path (which would have to be very similar in form in all crystals studied) can account for the observed robustness of the SC transition.

A more plausible origin of this insensitivity of T_c on ρ_0 is the presence of specific (extended) forms of microstructural defects (e.g., dislocations, columnar defects, grain boundaries, etc., . . .) that adversely affect ρ_0 while contributing minimally to pair breaking. An example of such extended defects having a profound effect on $\rho_{ab}(T)$ but a minimal effect on T_c can be found in the infinite-layer nickelates [36, 37]. Structural and electronic nanoscale inhomogeneity is a well-known feature of Bi-based cuprates [14, 38], but this inhomogeneity tends to be more point-like than extended and as such, should also have a similar effect on both T_c and ρ_0. Larger defects, such as microcracks, could also cause an increased resistivity though in this case, one might expect to see Arrhenius-type behaviour ($\rho(T) \propto \exp(-\Delta/k_BT)$) due to tunneling across the crack, as one finds in polycrystalline samples with multiple grain boundaries. While we noted earlier that there were small upturns observed in the $\rho_{ab}(T)$ curves of some of our Bi2201 crystals, there did not appear to be any correlation between the value of ρ_0 and the presence of an upturn.

A dedicated transmission electron microscopy (TEM) study is currently underway to look for evidence for the type of defect that might cause this dichotomy between T_c and ρ_0, the results of which will be published elsewhere. Although we cannot rule out the presence of such extended defects affecting ρ_0 without impacting T_c, in the following section we present a body of evidence on the LSCO family that provides arguably a greater challenge to the viability of the dirty *d*-wave scenario to cuprates within the strange metal regime.

2.4 Review of T_c dependence on ρ_0 in LSCO

It is well known that superconductivity in cuprates is strongly suppressed upon Zn substitution on the planar Cu site. In LSCO, for example, 4% Zn substitution can destroy superconductivity entirely while at the same time raising ρ_0 by ~ 50 $\mu\Omega$cm [39]. The origin of this suppression is not entirely clear. Despite being a non-magnetic impurity, Zn dopants appear to influence strongly the magnetic environment within the CuO_2 plane as well as act as unitarity-limit scatterers [39].

Mahmood *et al.* [40] recently reported a study on OD LSCO thin films irradiated using 1 MeV oxygen ions. Ion irradiation is believed to create narrow columnar defect tracks throughout the film. Figure 3A shows a series of $\rho_{ab}(T)$ curves obtained on an optimally doped LSCO film exposed to different fluences using a flux gradient to produce a spread in defect density. Irradiation leads to a maximal increase in ρ_0 of 36–40 $\mu\Omega$cm without the *T*-dependence or the slope of the $\rho_{ab}(T)$ curves changing. Such adherence to Matthiessen's rule, coupled with accompanying measurements of the low-frequency Drude response, suggests that the irradiation is simply creating additional elastic scattering centres. According to the calculations in Section 2.2, the magnitude of $\Delta\rho_0$ corresponds to $\Delta\Gamma_n > 100$ K, and given that Eqs 1, 2 predict a ~ 1 K drop in T_c for every 1 K increase in Γ_n, clearly such a level of disorder should be sufficient to remove all vestiges of superconductivity in the film. Yet T_c itself is found to drop by less than 5 K.

One expects that an optimally doped film will possess a more robust SC state than those at a higher doping level with a lower T_c. In reality, Mahmood *et al.* observed the opposite trend. As shown in Figure 3B, for a pristine film with T_c ~ 10 K, there was no discernible change in T_c for the same level of fluence that induced a ~ 5 K reduction in T_c in the optimally-doped film. It seems that the more overdoped the pristine film is and the lower its initial superfluid density, the more robust is the superconductivity to similar levels of irradiation.

Two further examples of the insensitivity of T_c to changes in ρ_0 in OD LSCO are shown in Panels C and D of Figure 3. Panel C shows $\rho_{ab}(T)$ curves for two single crystals ($x = 0.24$) whose ρ_0 values differ by ~ 35 $\mu\Omega$cm, corresponding to $\Delta\Gamma_n$ ~ 100 K [41], yet the difference in T_c in the two crystals is less than 2 K. Panel D shows $\rho_{ab}(T)$ for a single crystal [2] and thin film [42] with $x = 0.23$. Note that the form of $\rho_{ab}(T)$, as well as their derivatives [43], are the same, implying that their doping levels are essentially equivalent. The difference in ρ_0 of the two samples (after normalising their slopes [43]) is such that $\Delta\Gamma_n$ ~ 85 K, but yet again, their T_c values are almost indistinguishable.

In the previous section, we discussed the possibility that in Bi2201, the insensitivity of T_c on ρ_0 reflects the fact that elastic scattering is dominated by extended defects that contribute largely to ρ_0 but do not, by themselves, break pairs and thereby cause a suppression in T_c. In the study by Mahmood *et al.*, extended (columnar) defects were found to cause an increase in scattering, as deduced from the width of the Drude conductivity peak. We note too that the superfluid density also decreased, implying that such defects do indeed cause pair breaking, yet T_c itself remained remarkably robust.

According to Figure 2 and the corresponding relation between Γ_n and ρ_0, dirty *d*-wave theory predicts that for every 1 $\mu\Omega$cm increase in ρ_0, T_c in optimally doped LSCO should decrease by around 2.5 K [17], irrespective of the phase shift of the dominant scattering process. At the same time, the full extent of the SC dome diminishes by Δp ~ 0.0075 per 1 $\mu\Omega$cm increase in ρ_0. This extreme sensitivity of the $T_c(p)$ dome to small changes in ρ_0 represents arguably the greatest challenge to the theory's applicability. Indeed, one of the most striking and largely overlooked features of cuprate research is the immutability of the $T_c(p)$ dome.

The six panels in Figure 4 reproduce full $T_c(p)$ domes for bulk LSCO reported over a period of 2 decades (1989–2009) [44–49]. The samples in question are both poly- and single crystalline and were prepared by various techniques, including flux and travelling-solvent floating-zone growth of single crystals and spray-drying or powder-mixing procedures for the ceramic powders. Note that all T_c values, bar those in panel (E), were determined by magnetisation or susceptibility measurements. The dashed green line in each panel represents the Presland formula [29] with $T_c^{\max} = 38$ K and assuming

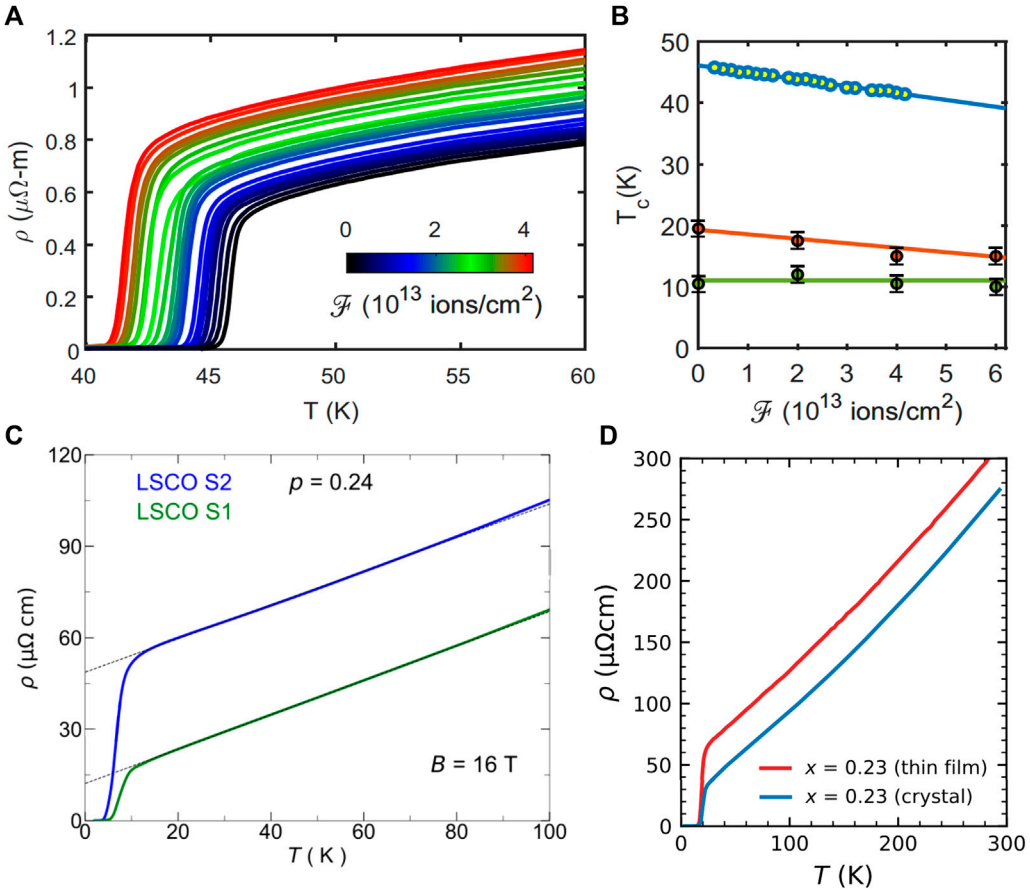

FIGURE 3
Examples of the robustness of T_c to changes in ρ_0 in LSCO. **(A)** $\rho_{ab}(T)$ of an optimally doped LSCO thin film (x = 0.16) irradiated with 1 MeV oxygen ions, but with a total fluence that varies across the devices between 0 and 4 × 10^{13} ions/cm^2, as indicated by the inset color bar. Reproduced with kind permission from Ref. [40]. **(B)** T_c as a function of irradiation fluence $\mathcal{F}$ for an optimally doped film (blue dots) and two overdoped LSCO films with different initial T_c values (red and green dots). Solid lines are guides to the eye. Reproduced with kind permission from Ref. [40]. **(C)** $\rho_{ab}(T)$ of two different crystals of LSCO (x = 0.24) with ρ_0 values differing by 36 $\mu\Omega$cm, corresponding to $\Delta\Gamma_n \sim 100$ K. Despite this large value of $\Delta\Gamma_n$, the respective T_c values differ by only 1.5 K (Note that these $\rho_{ab}(T)$ curves were obtained in a magnetic field of 16 T applied perpendicular to the CuO_2 planes). Reproduced with kind permission from Ref. [41]. **(D)** Comparison of $\rho_{ab}(T)$ of a LSCO single crystal (x = 0.23, blue curve) and a LSCO thin film (x = 0.23, red curve). Reproduced from Ref. [43]. The $\rho_{ab}(T)$ data for the thin film has been divided by two in order to normalize the slopes. The corresponding ρ_0 values are 20 and 50 $\mu\Omega$cm respectively, corresponding to $\Delta\Gamma_n \sim 85$ K.

$p = x$ (the Sr content). The consistent overlap between the dashed lines and the data indicates that the $T_c(p)$ dome in bulk, as-grown LSCO is invariant, independent of the quality of the starting materials or the way in which the samples have been synthesized. Moreover, as highlighted by the single horizontal line spanning all six panels, T_c^{max} is the same for all series of samples to within 1 K. For such consistency to be accounted for within the dirty d-wave scenario, ρ_0 would have to be identical to within 0.4 $\mu\Omega$cm ($< 2\%$) for every sample at every single doping level.

Such extreme levels of reproducibility are clearly beyond all reasonable expectations (requiring as it does that all LSCO samples have identical values of Γ_n to within 1 K) and highlight a key feature of the superconductivity in LSCO that remains unresolved. It appears that the $T_c(p)$ dome in bulk LSCO is not, as has been argued [15], set by the level of disorder in the material, but by some other driving mechanism, such as the strength of next-nearest hopping [50, 51]. Certainly, it would be remarkable if the drop from $T_{c0}(p)$ to $T_c(p)$ for LSCO in Figure 2 were due to a scattering rate Γ_n whose magnitude is fixed and commensurate with a ρ_0 value equivalent to 20 $\mu\Omega$cm and that all other contributions to ρ_0, e.g., flux or crucible inclusions, were extraneous and had no further pair-breaking effect. A similar fundamental limit to ρ_0 would also have to exist for Bi2201, despite the fact that Bi2201 may contain multiple elements (e.g., Bi/Pb, La/Sr) in its formula unit.

Although a number of SC properties of OD LSCO and Tl2201 have been successfully modeled by considering the differences in the impurity potential, its phase shift and its location relative to the CuO_2 plane [15–19], the relation between T_c and Γ_n is, by and large, independent of these details and as such, should be a robust test of the theory's applicability. The inability of dirty d-wave theory to account for the remarkable insensitivity of T_c to changes in ρ_0–highlighted in Figures 1, 4 – thus implies that either we do not understand the true causes of residual resistivity in cuprates (i.e., that the correspondence between Γ_n and ρ_0 is somehow lost), or that the basis of the theory is not the right

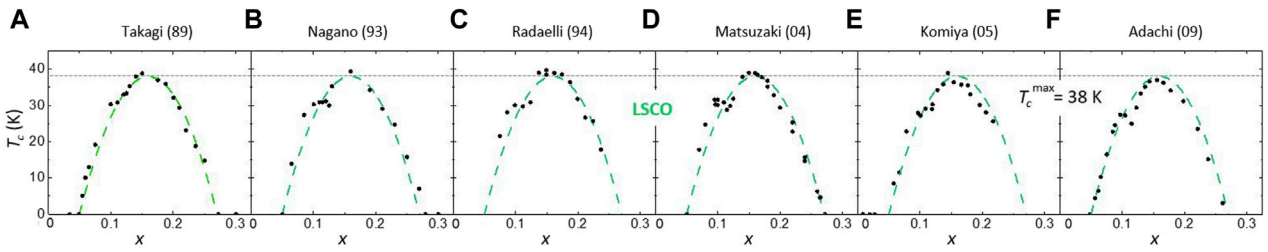

FIGURE 4
Superconducting domes in LSCO over the decades. $T_c(x)$ as measured on **(A–C)** polycrystalline pellets grown via various techniques [44–46]; **(D)** flux-grown single crystals [47]; **(E,F)** travelling-solvent floating-zone crystals [48, 49]. For all panels except (E), T_c was determined from the onset of the Meissner (diamagnetic) signal. For panel **(E)**, T_c was determined from the onset of zero resistivity. The dashed line in each panel is the Presland formula $T_c = T_c^{max}(1–82.6\ (x - 0.16)^2)$ with T_c^{max} = 38 K. All $T_c(x)$ domes appear to follow the same trajectory with the same T_c^{max} value (±1 K) and most remarkably, the same beginning (x = 0.05) and end (x = 0.27) points.

framework to describe the transition from strange metal to superconductor.

Motivated by these findings, we present below an alternative (non-BCS) scenario for the robust $T_c(p)$ domes in OD cuprates in which the non-FL nature of the cuprate strange-metal plays a central role. In the process, we offer an alternative explanation as to why the SC dome in cleaner Tl2201 extends to a higher p-value than in Bi2201 and LSCO and suggest ways to test the validity of such a scenario.

2.5 A tale of two domes

In the previous section, we highlighted various types of extended defects that could, in principle, enhance ρ_0 without necessarily inducing substantial pair breaking within the CuO_2 plane. In order to investigate whether such defects are indeed the root cause of this behaviour, more detailed microstructural studies of each of the relevant cuprate families are strongly advocated. Certainly, it is something that has been largely overlooked by the community. Until such time, however, it is worthwhile to at least consider alternative explanations for the demise of superconductivity on the overdoped side.

Franz et al. [52] have argued that the predicted drop in T_c with disorder is higher than observed experimentally due to the fact that within AG theory, the order parameter is spatially averaged, an assumption that may not be applicable to high-T_c cuprates by virtue of their short coherence lengths. Allowing for the spatial variation of the order parameter within a Bogoliubov-de Gennes formalism leads to a suppression of T_c that is indeed weaker than that predicted by the AG theory, but only by a factor of 2. Moreover, naively, one would expect the coherence length to diverge as $p \rightarrow p_{sc}$, yet according to the study of Mahmood et al., T_c becomes even more robust at higher doping levels [40].

The SCTMA used by Lee-Hone et al. [15] treats disorder using an effective medium theory in which the SC state is also assumed to be homogeneous. Other treatments, however, have considered inhomogeneity or granularity in the SC state [53, 54]. When the Cooper pair coherence length becomes comparable to the correlation length of the disorder potential, the order parameter is found to vary spatially while the superconductor segregates into regions of high and low superfluid density, that in turn enhances the propensity for SC phase fluctuations. Indeed, evidence has emerged for both granular superconductivity [14, 55] and enhanced SC phase fluctuations [56] in OD cuprates.

While the granular model described in Ref. [54] captures a number of key observations, it cannot be the complete picture. What this model–and indeed the majority of disorder models that consider this problem–assumes it that the OD cuprates are essentially Fermi-liquids that transition into a BCS superconductor (homogeneous or otherwise) below T_c. Yet, as stressed elsewhere, there is now mounting evidence that OD cuprates are in fact strange metals, with a dominant non-FL T-linear resistivity extending over the entire doping region [2]. Moreover, this strange metal is claimed to exhibit dual character [9, 10] with coexisting but spatially separated regions with FL and non-FL character, respectively [57].

The natural question that arises is whether the non-FL sector possesses the necessary qualities to preserve the size of the pairing amplitude in the presence of disorder. While there is currently no microscopic picture that addresses this, we consider here a simple ‘patchwork’ model for OD cuprates in which intrinsic superconductivity emerges uniquely from the non-FL sector and is resilient to large changes in Γ_n. Figure 5A shows a schematic of such a patchwork cuprate comprising distinct regions of non-FL (in blue) and FL (in red). In a related article [59], we applied both effective medium theory and random resistor networks to a binary mixture of FL and non-FL patches to capture the evolution of the low-T resistivity from purely T^2 at high dopings to T-linear near p^* (≈0.19) with an increasing fraction f of non-FL sector. The same model also explains the correlation between the T-linear resistivity coefficient and the slope of the H-linear magnetoresistance [59]. In Figure 5A, the doping level is set such that there is no percolation path available for the non-FL component. Supercurrent could, in principle, flow through the FL regions via the proximity effect and thus maintain the SC state. In inhomogeneous systems like LSCO and Bi2201, however, the FL sector will be susceptible to strong pair-breaking effects due to scattering off such inhomogeneities, thereby inhibiting the flow of supercurrent between the SC patches. Hence, as soon as the percolation limit is exceeded, the zero-resistance state is lost. For LSCO and Bi2201, this percolation limit is assumed to coincide with the end of the SC dome at p_{sc} = 0.27.

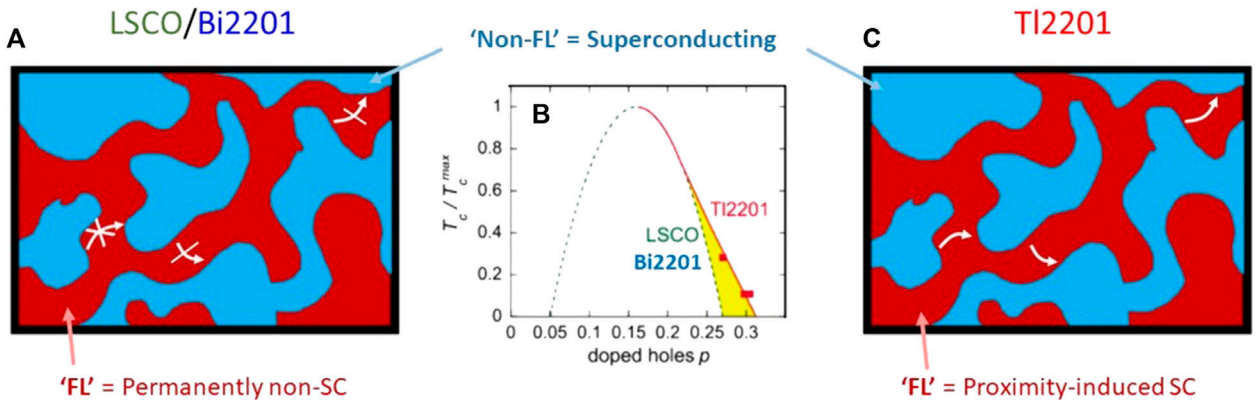

FIGURE 5
A tale of two superconducting domes. **(A)** Patchwork model for a hole-doped cuprate comprising distinct regions of non-FL (in blue) and FL (in red). Here, the doping level is such that there is no percolation path available for the non-FL sector. In LSCO and Bi2201, supercurrent could, in principle, flow through the FL sectors via the proximity effect (and thus maintain superconductivity. Due to the presence of strong inhomogeneities, however, pair-breaking effects inhibit the formation of proximity-induced superconductivity within the FL sectors. **(B)** Normalized $T_c(p)$ domes for LSCO and Bi2201 (dashed line) and Tl2201 (solid line and squares). Reproduced from Ref. [58]. The yellow shaded area represents the proposed region of suppressed superconductivity in OD LSCO and Bi2201. **(C)** Patchwork model for Tl2201 with the same concentration (and distribution) of non-FL sectors. Due to its lower levels of disorder, superconductivity can survive beyond the percolation limit because the supercurrent is now able flow through the FL sectors via the proximity effect. Once the non-FL sector vanishes at p = 0.31, however, then all traces of superconductivity are lost.

According to Pelc et al., percolation emerges when the fraction of SC patches reaches a critical value of 0.3 (assuming SC and non-SC patches of equivalent size) [60]. Related to this, α_1–the coefficient of the low-T T-linear resistivity in OD cuprates–is found to grow linearly from p = 0.31 up to its maximum value α_1^{max} at $p^\star$ ~ 0.20 where the pseudogap opens. Thus, at p = 0.27, α_1/α_1^{max} ~ 0.35. In a recent high-field transport study [59], we argued that α_1/α_1^{max} is a measure of the fraction of Planckian carriers that are present at a particular doping. If these carriers, and only these carriers, form the superfluid condensate in LSCO and Bi2201, then the reason for the onset of superconductivity at $p = p_{sc}$ becomes self-evident–it is the point at which the supercurrent can travel percolatively between adjacent patches.

Figure 5B compares the normalised T_c dome for LSCO and Bi2201 (dashed line) with that of Tl2201 (solid line and squares). The yellow shaded area in Figure 5B represents the region of the phase diagram where the superconductivity in Tl2201 is enhanced relative to that seen in LSCO and Bi2201. (This extended region of superconductivity is essentially the same as that shown in Figure 2.) Tl2201 is known to be more homogeneous than LSCO and Bi2201 and possess longer mean-free-paths (as manifest in lower ρ_0 values) [34]. According to the above picture, the level of disorder scattering in Tl2201 is low enough to allow supercurrent to traverse the FL sectors via the proximity effect (see Figure 5C) and for superconductivity to persist beyond the percolation limit. Once the non-FL sector vanishes at p = 0.31, however, then all traces of superconductivity are lost.

This picture represents a marked departure from the extended BCS description for a disordered d-wave superconductor, yet is clearly nothing more than a toy model at present. Before closing, therefore, let us consider some of the consequences of the proposed picture and how it might be tested experimentally. One such consequence may in fact have been tested already. In an earlier electron irradiation study on OD Tl2201 (T_c = 31 K) [61], an increase in ρ_0 by 70 $\mu\Omega$cm was found to cause a reduction of 20 K in T_c. Using the values quoted in Section 2.2, we find that $\Delta\Gamma_n$ ~ 210 K > 10 ΔT_c. Despite this level of T_c reduction being far smaller than expected by modified AG theory ($\Delta T_c = -(\pi/4)\Gamma_n$ [61]), it is still more than is seen in LSCO or in Bi2201. (In Ref. [61], the authors used p, rather than 1 + p, for the carrier density, making the agreement with their expectations from AG theory appear reasonable.). If superconductivity within the FL sector is susceptible to disorder (in accordance with dirty d-wave theory) but is resilient within the non-FL sector, electron radiation might induce pair-breaking predominantly or uniquely within the FL sector. Moreover, if the doping level sits close to the percolation threshold, superconductivity will be appreciably suppressed. Further irradiation, on the other hand, would not cause a further deterioration in T_c due to the resilience of the superfluid residing the non-FL sector. A more dedicated irradiation study, over a range of dopings and to higher fluences, could thus serve as a robust test of the validity of this proposal.

The other corollary of this picture is the presence of SC droplets beyond p_{sc} = 0.27. According to Ref. [59], signatures of superconductivity are intimately tied to the existence of the T-linear component in $\rho(T)$ that itself indicates the fraction of carriers that are not standard Landau quasiparticles. Hence, for 0.27 $\leq p \leq$ 0.31, one expects SC patches to survive, fluctuating or otherwise. A recent STM study [14] observed gap features persisting in nominally non-SC Bi2201, albeit with a low filling fraction, consistent with this picture. In order to test this idea more rigorously, however, one would need to track the evolution of these features in combination with $\rho(T)$ measurements up to p = 0.31 and beyond.

3 Conclusion

The measurements, reproductions and analysis presented in this article serve to highlight serious shortcomings in our understanding of the normal and SC properties of overdoped cuprates. The fundamental problem can be expressed as follows; either we do not understand the relation between Γ_n and ρ_0 and the origins of residual resistivity in OD cuprates, or dirty *d*-wave theory, at least in its present guise, is not the appropriate framework to describe OD cuprates. The reality is probably a combination of the two. The robustness of the $T_c(p)$ domes in LSCO is particularly challenging for scenarios based on standard pair-breaking effects in *d*-wave superconductors. At the same time, there clearly needs to be a more concerted effort to understand the nature of defects and their contribution to pair-breaking and to ρ_0.

In the absence of a consistent picture, we have introduced here an alternative explanation for the robustness of T_c in different OD cuprates, based on a 'patchwork' model that recognises the dual character and non-FL nature of the strange metal regime and the importance of the latter for pair condensation. Within this model, dirty *d*-wave theory is still found to play some role, accounting for difference in the extent of the $T_c(p)$ domes in LSCO, Bi2201 and Tl2201. Further irradiation studies on samples located at the edge of the SC dome may allow us to differentiate between the different explanations for these striking effects.

Data availability statement

The raw data supporting the conclusion of this article will be made available by the authors, without undue reservation.

Author contributions

DJ: Conceptualization, Data curation, Formal Analysis, Investigation, Methodology, Writing–original draft, Writing–review and editing. JA: Data curation, Investigation, Validation, Writing–review and editing, Writing–original draft. RN: Data curation, Investigation, Validation, Writing–review and editing. NH: Conceptualization, Formal Analysis, Funding acquisition, Methodology, Project administration, Resources, Supervision, Writing–original draft, Writing–review and editing.

Funding

The author(s) declare that financial support was received for the research, authorship, and/or publication of this article. This work was supported by the Netherlands Organisation for Scientific Research (NWO) Grant No. 16METL01 "Strange Metals" (MB), the European Research Council (ERC) under the European Union's Horizon 2020 research and innovation programme (Grant Agreement No. 835279-Catch-22) (DJ, JA and NH) and the Engineering and Physical Sciences Research Council (United Kingdom) grant EP/V02986X/1 (NEH). JA acknowledges the support of a Leverhulme Trust Early Career Fellowship.

Acknowledgments

We acknowledge stimulating discussions with W. A. Atkinson, A. Carrington, C. Duffy, P. Chudzinski, A. Ghosh and M. Grüning. We also acknowledge T. Kondo, T. Takeuchi and Y. Huang for synthesising the Bi2201 single crystals used in this study, as well as M. Berben for preparation of some of the single crystals for transport measurements.

Conflict of interest

The authors declare that the research was conducted in the absence of any commercial or financial relationships that could be construed as a potential conflict of interest.

Publisher's note

Supplementary material

The Supplementary Material for this article can be found online at: https://www.frontiersin.org/articles/10.3389/fphy.2024.1396463/full#supplementary-material

References

1. Keimer B, Kivelson SA, Norman MR, Uchida S, Zaanen J. From quantum matter to high-temperature superconductivity in copper oxides. *Nature* (2015) 518:179–86. doi:10.1038/nature14165

2. Cooper RA, Wang Y, Vignolle B, Lipscombe OJ, Hayden SM, Tanabe Y, et al. Anomalous criticality in the electrical resistivity of $La_{2-x}Sr_xCuO_4$. *Science* (2009) 323: 603–7. doi:10.1126/science.1165015

3. Jin K, Butch NP, Kirshenbaum K, Paglione J, Greene RL. Link between spin fluctuations and electron pairing in copper oxide superconductors. *Nature* (2011) 476: 73–5. doi:10.1038/nature10308

4. Chang J, Månsson M, Pailhes S, Claesson T, Lipscombe OJ, Hayden SM, et al. Anisotropic breakdown of Fermi-liquid quasiparticle excitations in overdoped $La_{2-x}Sr_xCuO_4$. *Nat Commun* (2015) 4:2559. doi:10.1038/ncomms3559

5. Božović I, He X, Wu J, Bollinger AT. Dependence of the critical temperature in overdoped copper oxides on superfluid density. *Nature* (2016) 510:309–11. doi:10.1038/nature19061

6. Giraldo-Gallo P, Galvis JA, Stegen Z, Modic KA, Balakirev FF, Betts JB, et al. Scale-invariant magnetoresistance in a cuprate superconductor. *Science* (2018) 361:479–81. doi:10.1126/science.aan3178

7. Mahmood F, He X, Božović I, Armitage NP. Locating the missing superconducting electrons in the overdoped cuprates $La_{2-x}Sr_xCuO_4$. *Phys Rev Lett* (2019) 122:027003. doi:10.1103/PhysRevLett.122.027003

8. Legros A, Benhabib S, Tabis W, Laliberté F, Dion M, Lizaire M, et al. Universal *T*-linear resistivity and Planckian dissipation in overdoped cuprates. *Nat Phys* (2019) 15:142–7. doi:10.1038/s41567-018-0334-2

9. Putzke C, Benhabib S, Tabis W, Ayres J, Wang Z, Malone L, et al. Reduced Hall carrier density in the overdoped strange metal regime of cuprate superconductors. *Nat Phys* (2021) 17:826–31. doi:10.1038/s41567-021-01197-0

10. Ayres J, Berben M, Čulo M, Hsu YT, van Heumen E, Huang Y, et al. Incoherent transport across the strange-metal regime of overdoped cuprates. *Nature* (2021) 595: 661–6. doi:10.1038/s41586-021-03622-z

11. Grissonnanche G, Fang Y, Legros A, Verret S, Laliberté F, Collignon C, et al. Linear-in temperature resistivity from an isotropic Planckian scattering rate. *Nature* (2021) 595:667–72. doi:10.1038/s41586-021-03697-8

12. Smit S, Mauri E, Bawden L, Heringa F, Gerritsen F, van Heumen E, et al. *Momentum-dependent scaling exponents of nodal self-energies measured in strange metal cuprates and modelled using semi-holography* (2021). arXiv:2112.06576 [cond-mat].

13. Yuan J, Chen Q, Jiang K, Feng Z, Lin Z, Yu H, et al. Scaling of the strange-metal scattering in unconventional superconductors. *Nature* (2022) 602:431–6. doi:10.1038/s41586-021-04305-5

14. Tromp WO, Benschop T, Ge JF, Battisti I, Bastiaans KM, Chatzopoulos D, et al. Puddle formation, persistent gaps, and non-mean-field breakdown of superconductivity in overdoped $(Pb,Bi)_2Sr_2CuO_{6+\delta}$. *Nat Mater* (2023) 22:703–9. doi:10.1038/s41563-023-01497-1

15. Lee-Hone NR, Dodge JS, Broun DM. Disorder and superfluid density in overdoped cuprate superconductors. *Phys Rev B* (2017) 96:024501. doi:10.1103/PhysRevB.96.024501

16. Lee-Hone NR, Mishra V, Broun DM, Hirschfeld PJ. Optical conductivity of overdoped cuprate superconductors: application to $La_{2-x}Sr_xCuO_4$. *Phys Rev B* (2018) 98:054506. doi:10.1103/PhysRevB.98.054506

17. Lee-Hone NR, Özdemir HU, Mishra V, Broun DM, Hirschfeld PJ. Low energy phenomenology of the overdoped cuprates: viability of the Landau-BCS paradigm. *Phys Rev Res* (2020) 2:013228. doi:10.1103/PhysRevResearch.2.013228

18. Özdemir HU, Mishra V, Lee-Hone NR, Kong X, Berlijn T, Broun DM, et al. Effect of realistic out-of-plane dopant potentials on the superfluid density of overdoped cuprates. *Phys Rev B* (2022) 106:184510. doi:10.1103/PhysRevB.106.184510

19. Broun DM, Özdemir HU, Mishra V, Lee-Hone NR, Kong X, Berlijn T, et al. *Optical conductivity of overdoped cuprates from* ab initio *out-of-plane impurity potentials* (2023). arXiv:2312.16632 [cond-mat].

20. Loram JW, Mirza KA, Wade JM, Cooper JR, Liang WY. The electronic specific heat of cuprate superconductors. *Physica C* (1994) 235–240:134–7. doi:10.1016/0921-4534(94)91331-5

21. Wang Y, Yan J, Shan L, Wen HH, Tanabe Y, Adachi T, et al. Weak-coupling *d*-wave BCS superconductivity and unpaired electrons in overdoped $La_{2-x}Sr_xCuO_4$ single crystals. *Phys Rev B* (2007) 76:064512. doi:10.1103/PhysRevB.76.064512

22. Takeya J, Ando Y, Komiya S, Sun XF. Low-temperature electronic heat transport in $La_{2-x}Sr_xCuO_4$ single crystals: unusual low-energy physics in the normal and superconducting states. *Phys Rev Lett* (2002) 88:077001. doi:10.1103/physrevlett.88.077001

23. Sutherland M, Hawthorn DG, Hill RW, Ronning F, Wakimoto S, Zhang H, et al. Thermal conductivity across the phase diagram of cuprates: low-energy quasiparticles and doping dependence of the superconducting gap. *Phys Rev B* (2003) 67:174520. doi:10.1103/PhysRevB.67.174520

24. Proust C, Boaknin E, Hill RW, Taillefer L, Mackenzie AP. Heat transport in a strongly overdoped cuprate: Fermi liquid and a pure *d*-wave BCS superconductor. *Phys Rev Lett* (2002) 89:147003. doi:10.1103/PhysRevLett.89.147003

25. Hawthorn DG, Li SY, Sutherland M, Boaknin E, Hill RW, Proust C, et al. Doping dependence of the superconducting gap in $Tl_2Ba_2CuO_{6+\delta}$ from heat transport. *Phys Rev B* (2007) 75:104518. doi:10.1103/PhysRevB.75.104518

26. Wang D, Xu JQ, Zhang HJ, Wang QH. Anisotropic scattering caused by apical oxygen vacancies in thin films of overdoped high-temperature cuprate superconductors. *Phys Rev Lett* (2022) 128:137001. doi:10.1103/PhysRevLett.128.137001

27. Abrikosov AA, Gor'kov LP *Methods of quantum field theory in statistical physics*. New York, NY: Dover (1975).

28. Hussey NE, Licciardello S, Buhot J. A tale of two metals: contrasting criticalities in the pnictides and hole-doped cuprates. *Rep Prog Phys* (2018) 81:052501. doi:10.1088/1361-6633/aaa97c

29. Presland MR, Tallon JL, Buckley RG, Liu RS, Flower NE. General trends in oxygen stoichiometry effects on T_c in Bi and Tl superconductors. *Physica C* (1991) 176:95–105. doi:10.1016/0921-4534(91)90700-9

30. Berben M, Smit S, Duffy C, Hsu YT, Bawden L, Heringa F, et al. Superconducting dome and pseudogap endpoint in Bi2201. *Phys Rev Mater* (2022) 6:044804. doi:10.1103/PhysRevMaterials.6.044804

31. Ono S, Ando Y. Evolution of the resistivity anisotropy in $Bi_2Sr_{2-x}La_xCuO_{6+\delta}$ single crystals for a wide range of hole doping. *Phys Rev B* (2003) 67:104512. doi:10.1103/PhysRevB.67.104512

32. Momono N, Matsuzaki T, Oda M, Ido M. Superconducting condensation energy and pseudogap formation in $La_{2-x}Sr_xCuO_4$: new energy scale for superconductivity. *J Phys Soc Jpn* (2002) 71:2832–5. doi:10.1143/JPSJ.71.2832

33. Wade JM, Loram JW, Mirza KA, Cooper JR, Tallon JL. Electronic specific heat of $Tl_2Ba_2CuO_{6+\delta}$ from 2 K to 300 K for $0 \leq \delta \leq 0.1$. *J Supercond* (1994) 7:261–4. doi:10.1007/BF00730408

34. Rourke PMC, Bangura AF, Benseman TM, Matusiak M, Cooper JR, Carrington A, et al. A detailed de Haas–van Alphen effect study of the overdoped cuprate $Tl_2Ba_2CuO_{6+\delta}$. *New J Phys* (2010) 12:105009. doi:10.1088/1367-2630/12/10/105009

35. Girod C, LeBoeuf D, Demuer A, Seyfarth G, Imajo YSamd K, Kohama Y, et al. Normal state specific heat in the cuprate superconductors $La_{2x}Sr_xCuO_4$ and $Bi_{2+y}Sr_{2-x-y}La_xCuO_{6+\delta}$ near the critical point of the pseudogap phase. *Phys Rev B* (2022) 103:214506. doi:10.1103/PhysRevB.103.214506

36. Lee K, Goodge BH, Li D, Osada M, Wang BY, Cui Y, et al. Aspects of the synthesis of thin film superconducting infinite-layer nickelates. *APL Mater* (2020) 8:041107. doi:10.1063/5.0005103

37. Lee K, Wang BY, Osada M, Goodge BH, Wang TC, Lee Y, et al. Linear-in-temperature resistivity for optimally superconducting $(Nd,Sr)NiO_2$. *Nature* (2023) 619: 288–92. doi:10.1038/s41586-023-06129-x

38. Pan SH, O'Neal JP, Badzey RL, Chamon C, Ding H, Engelbrecht JR, et al. Microscopic electronic inhomogeneity in the high-T_c superconductor $Bi_2Sr_2CaCu_2O_{8+x}$. *Nature* (2001) 413:282–5. doi:10.1038/35095012

39. Fukuzumi Y, Mizuhashi K, Takenaka K, Uchida S. Universal superconductor-insulator transition and T_c depression in Zn-substituted high-T_c cuprates in the underdoped regime. *Phys Rev Lett* (1996) 76:684–7. doi:10.1103/PhysRevLett.76.684

40. Mahmood F, Ingram D, He X, Clayhold JA, Božović I, Armitage NP. Effect of radiation-induced defects on the superfluid density and optical conductivity of overdoped $La_{2-x}Sr_xCuO_4$. *Phys Rev B* (2022) 105:174501. doi:10.1103/PhysRevB.105.174501

41. Ataei A, Gourgout A, Grissonnanche G, Chen L, Baglo J, Boulanger ME, et al. Electrons with Planckian scattering obey standard orbital motion in a magnetic field. *Nat Phys* (2022) 18:1420–4. doi:10.1038/s41567-022-01763-0

42. Ando Y, Boebinger GS, Passner A, Wang NL, Geibel C, Steglich F, et al. Normal-state Hall effect and the insulating resistivity of high-T_c cuprates at low temperatures. *Phys Rev B* (1997) 56:R8530–4. doi:10.1103/PhysRevB.56.R8530

43. Čulo M, Duffy C, Ayres J, Berben M, Hsu YT, Hinlopen RDH, et al. (2021) Possible superconductivity from incoherent carriers in overdoped cuprates, *Scipost Phys* 11:012. doi:10.21468/SciPostPhys.11.1.012

44. Takagi H, Ido T, Ishibashi S, Uota M, Uchida S, Tokura Y. Superconductor-to-nonsuperconductor transition in $La_{2-x}Sr_xCuO_4$ as investigated by transport and magnetic measurements. *Phys Rev B* (1989) 40:2254–61. doi:10.1103/PhysRevB.40.2254

45. Nagano T, Tomioka Y, Nakayama Y, Kishio K, Kitazawa K. Bulk superconductivity in both tetragonal and orthorhombic solid solutions of $La_{2-x}Sr_xCuO_4$. *Phys Rev B* (1993) 48:9689–96. doi:10.1103/PhysRevB.48.9689

46. Radaelli PG, Hinks DG, Mitchell AW, Hunter BA, Wagner JL, Dabrowski B, et al. Structural and superconducting properties of $La_{2-x}Sr_xCuO_4$ as a function of sr content. *Phys Rev B* (1994) 49:4163–75. doi:10.1103/PhysRevB.49.4163

47. Matsuzaki T, Momono N, Oda M, Ido M. Electronic specific heat of $La_{2-x}Sr_xCuO_4$: pseudogap formation and reduction of the superconducting condensation energy. *J Phys Soc Jpn* (2004) 73:2232–8. doi:10.1143/JPSJ.73.2232

48. Komiya S, Chen HD, Zhang SC, Ando Y. Magic doping fractions for high-temperature superconductors. *Phys Rev Lett* (2005) 94:207004. doi:10.1103/PhysRevLett.94.207004

49. Adachi T, Omori K, Tanabe Y, Koike Y. Magnetic-susceptibility and specific-heat studies on the inhomogeneity of superconductivity in the underdoped $La_{2-x}Sr_xCuO_4$. *J Phys Soc Jpn* (2009) 78:114707. doi:10.1143/JPSJ.78.114707

50. Pavarini E, Dasgupta I, Saha-Dasgupta T, Jepsen O, Andersen OK. Band-structure trend in hole-doped cuprates and correlation with T_c^{max}. *Phys Rev Lett* (2001) 87: 047003. doi:10.1103/PhysRevLett.87.047003

51. Eberlein A, Metzner W. Superconductivity in the two-dimensional $t - t'$-Hubbard model. *Phys Rev B* (2014) 89:035126. doi:10.1103/PhysRevB.89.035126

52. Franz M, Kallin C, Berlinsky AJ, Salkola MI. Critical temperature and superfluid density suppression in disordered high-T_c cuprate superconductors. *Phys Rev B* (1997) 56:7882–5. doi:10.1103/PhysRevB.56.7882

53. Atkinson WA, Hirschfeld PJ, MacDonald AH. Gap inhomogeneities and the density of states in disordered *d*-wave superconductors. *Phys Rev Lett* (2000) 85:3922–5. doi:10.1103/PhysRevLett.85.3922

54. Li ZX, Kivelson SA, Lee DH. Superconductor-to-metal transition in overdoped cuprates. *npj Quant Mater* (2021) 6:36. doi:10.1038/s41535-021-00335-4

55. Li Y, Sapkota A, Lozano PM, Du Z, Li H, Wu Z, et al. Strongly overdoped $La_{2-x}Sr_xCuO_4$: evidence for Josephson-coupled grains of strongly correlated superconductor. *Phys Rev B* (2022) 106:224515. doi:10.1103/PhysRevB.106.224515

56. Rourke PMC, Mouzopoulou I, Xu XF, Panagopoulos C, Wang Y, Vignolle B, et al. Phase-fluctuating superconductivity in overdoped $La_{2-x}Sr_xCuO_4$. *Nat Phys* (2011) 7: 455–8. doi:10.1038/nphys1945

57. Ayres J, Katsnelson MI, Hussey NE. Superfluid density and two-component conductivity in hole-doped cuprates. *Front Phys* (2022) 10:1021462. doi:10.3389/fphy.2022.1021462

58. Bangura AF, Rourke PMC, Benseman TM, Matusiak M, Cooper JR, Hussey NE, et al. Fermi surface and electronic homogeneity of the overdoped cuprate superconductor $Tl_2Ba_2CuO_{\{6+\delta\}}$ as revealed by quantum oscillations. *Phys Rev B* (2010) 82:140501. doi:10.1103/PhysRevB.82.140501

59. Ayres J, Berben M, Duffy C, Hinlopen RDH, Hsu YT, Cuoghi A, et al. *Universal correlation between* H-*linear magnetoresistance and* T-*linear resistivity in high-temperature superconductors* (2023). Submitted.

60. Pelc D, Vučković M, Grbić MS, Požek M, Yu G, Sasagawa T, et al. Emergence of superconductivity in the cuprates via a universal percolation process. *Nat Commun* (2018) 9:4327. doi:10.1038/s41467-018-06707-y

61. Rullier-Albenque F, Vieillefond PA, Alloul H, Tyler AW, Lejay P, Marucco JF. Universal T_c depression by irradiation defects in underdoped and overdoped cuprates? *Europhys Lett* (2000) 50:81–7. doi:10.1209/epl/i2000-00238-x

frontiers | Frontiers in Physics

TYPE Review
PUBLISHED 20 May 2024
DOI 10.3389/fphy.2024.1353425

OPEN ACCESS

EDITED BY
Matt Beekman,
California Polytechnic State University,
United States

REVIEWED BY
Mario Cuoco,
National Research Council (CNR), Italy
Shyam Sundar,
Universidade Federal do ABC, Brazil
Vivek Kumar Anand,
University of Stavanger, Norway

*CORRESPONDENCE
Brian M. Andersen,
bma@nbi.ku.dk

RECEIVED 10 December 2023
ACCEPTED 15 April 2024
PUBLISHED 20 May 2024

CITATION
Andersen BM, Kreisel A and Hirschfeld PJ (2024), Spontaneous time-reversal symmetry breaking by disorder in superconductors. *Front. Phys.* 12:1353425.
doi: 10.3389/fphy.2024.1353425

Spontaneous time-reversal symmetry breaking by disorder in superconductors

Brian M. Andersen[1]*, Andreas Kreisel[1] and P. J. Hirschfeld[2]

[1]Niels Bohr Institute, University of Copenhagen, Copenhagen, Denmark, [2]Department of Physics, University of Florida, Gainesville, FL, United States

A growing number of superconducting materials display evidence for spontaneous time-reversal symmetry breaking (TRSB) below their critical transition temperatures. Precisely what this implies for the nature of the superconducting ground state of such materials, however, is often not straightforward to infer. We review the experimental status and survey different theoretical mechanisms for the generation of TRSB in superconductors. In cases where a TRSB complex combination of two superconducting order parameter components is realized, defects, dislocations and sample edges may generate superflow patterns that can be picked up by magnetic probes. However, even single-component condensates that do not break time-reversal symmetry in their pure bulk phases can also support signatures of magnetism inside the superconducting state. This includes, for example, the generation of localized orbital current patterns or spin-polarization near atomic-scale impurities, twin boundaries and other defects. Signals of TRSB may also arise from a superconductivity-enhanced Ruderman-Kittel-Kasuya-Yosida exchange coupling between magnetic impurity moments present in the normal state. We discuss the relevance of these different mechanisms for TRSB in light of recent experiments on superconducting materials of current interest.

KEYWORDS

time-reversal symmetry breaking, superconductivity, disorder, condensed matter theory, quantum materials

1 Introduction

Several superconducting materials have been discovered to manifest evidence of spontaneous time-reversal symmetry breaking (TRSB) that appears only below their critical superconducting transition temperatures T_c [1–4]. Evidence for such TRSB originates mainly from an enhanced muon-spin relaxation (μSR) and/or polar Kerr effect measurements finding a change in the optical polar Kerr angle below T_c. Additional probes able to detect breaking of time-reversal symmetry in the superconducting phase include Josephson interferometry [5], superconducting quantum interference device (SQUID) magnetometry [6], and polarized and small-angle neutron scattering [7]. These experimental methods detect the internal magnetic fields spontaneously generated in the superconducting state. Explanations for the occurrence of such fields from the perspective of clean (homogeneous) physical effects are either in terms of a TRSB non-unitary spin-triplet pairing state or in terms of multi-component superconducting condensates entering a complex TRSB superposition of two superconducting order parameter components. The latter option is particularly natural for superconducting instabilities condensing in two-dimensional (2D) irreducible representations of the associated crystal point group. Complex superpositions of two

symmetry-distinct order parameters break TRSB, and generate persistent supercurrent patterns at material edges, dislocations, or around various defect sites, which produce magnetic fields that may not average to zero locally. Such a multi-component scenario for the origin of TRSB below T_c has been extensively discussed for e.g., Sr_2RuO_4 [4, 8–12], UPt_3 [13, 14], URu_2Si_2 [15], UTe_2 [16, 17], SrPtAs [18], Re [19], Zr_3Ir [20], $LaNiC_2$ [21], $LaNiGa_2$ [22], $PrOs_4Sb_{12}$ [23, 24], $Ba_{1-x}K_xFe_2As_2$ [25, 26], $FeSe_{1-x}S_x$ [27], and more recently also for the kagome superconductors AV_3Sb_5 (A: K, Rb, Cs) [28–30], 4Hb-TaS_2 [31], $CaPd_2Ge_2$ [32], skutterudites [33, 34] and $Na_2Cr_3As_3$ [35]. For most of the compounds listed here, the evidence for TRSB originates from μSR experiments. For further materials displaying TRSB in their superconducting phases, and other types of evidence, we refer to Refs. [1–4].

At present, the status of the precise superconducting ground state remains controversial for many of the materials listed above. This is the case, for example, for the two materials Sr_2RuO_4 and UTe_2, where specific heat data features only a single thermodynamic transition that does not split under uniaxial strain, casting considerable doubt on the multi-component nature of their superconducting condensates [36–39]. Therefore, it appears timely and important to pursue other possibilities for the origin of TRSB detected solely inside the superconducting phase. This motivates the question of what mechanisms there are for TRSB of superconducting condensates composed of a single component order parameter? Barring non-unitary TRSB spin-triplet order, the answer to this question naturally leads to a study of different forms of spatial inhomogeneities and their influence on the local properties of superconductivity. For example, it is known that some superconductors generate magnetic moments below T_c due to an interplay between the gap structure and electronic correlations [40–46]. As mentioned above, another possibility for TRSB appearing only below T_c includes the generation of localized orbital loops of supercurrents near impurities. The latter is well-known to arise near nonmagnetic disorder sites in complex TRSB multi-component condensates [47–54], but was recently shown to be also present in the strongly disordered regime of single-component superconductors [55, 56]. Likewise, one might expect dislocations and grain boundaries to similarly operate as seeds of localized supercurrents producing sizable internal magnetic fields. Recently, the latter scenario was studied in Refs. [57, 58] as a possible explanation for reconciling the existence of TRSB and a single specific heat transition in Sr_2RuO_4. Indeed for this material, edge dislocations are known to be prevalent in many samples [59]. Finally, one might also envision that time-reversal symmetry is already broken above T_c through the existence of small magnetic regions that are either too dilute or rapidly fluctuating to be picked up by most probes. Only through a superconductivity-enhanced coupling, or a sufficient slowing-down of such preexisting magnetism below T_c, can it be detected, e.g., by entering the muon relaxation time window.

Here, motivated by the above-mentioned developments we survey a number of different mechanisms for *inhomogeneity-induced* TRSB in superconductors. Our discussion of disorder-induced TRSB refers both to cases where TRSB exists only locally near inhomogeneity sites and where TRS is broken globally, but manifested via induced currents near disorder sites. We discuss these both in view of recent theoretical and experimental developments of unconventional superconductivity.

2 Mechanisms of TRSB from disorder in superconductors

In this section we discuss three different mechanisms for disorder-generated TRSB in spin-singlet superconductors. Section 2.1 reviews the generation of magnetic fields from disorder in superconducting phases with TRSB in the bulk or generated near spatial inhomogeneities. Section 2.2 discusses another case where disorder in conjunction with electronic interactions and appropriate superconducting gap structures lead to the generation of static magnetic moments. Due to the required gapping of states for these moments to form, this mechanism is tied to the superconducting phase. Finally, Sec. 2.3 surveys a third case where preexisting magnetic local order (fluctuation moments) in the normal state get enhanced (slowed-down) by superconductivity. Clearly these mechanisms do not exhaust the options for disorder-induced TRSB in superconductors where e.g., cases with substantial spin-orbit coupling may also be of interest [60, 61]. We focus on these three options given recent research along similar lines and for their relevance for some of the superconducting materials mentioned above. For a discussion of the possibility of TRSB in homogeneous superconductors originating from conventional electron-phonon coupling, we refer to the review [3] and the references therein. A theoretical proposal for a mechanism has been proposed in Ref. [62] and recent experimental evidence for TRSB in materials where superconductivity is believed to originate from electron-phonon coupling is reported in Refs. [32–34, 63].

2.1 Complex combinations of two superconducting condensates

Entering the superconducting state is associated with a breaking of the symmetry of the normal state symmetry group composed of a direct product of crystalline symmetries, gauge symmetry and the time reversal operation [70–72]. For non-magnetic normal states, the allowed solutions of the gap equation can be characterized by the irreducible representations (irreps) of the associated point group. The leading instability is found from the linearized BCS gap equation as the solution with the largest eigenvalue and thereby also the highest T_c [73–76]. Broken time-reversal symmetry can arise from a complex combination of superconducting condensates or the breaking of the spin-rotational invariance in non-unitary triplet states. Whenever the preferred superconducting instability corresponds to a two-dimensional (2D) irrep, the system may take advantage of the degeneracy between the representations. From a perspective of the minimization of the Ginzburg–Landau free energy, there is the possibility to either form a real combination thereby breaking a crystal symmetry or to form complex superpositions [3, 12, 71]. The latter often maximizes the condensation energy by forming a fully-gapped state and can be shown to be the ground state for a single band setting within a loop expansion [77]. We will not elaborate further on the possibility of real superpositions, but focus instead on complex linear combinations with standard examples as $p_x + ip_y$ ($p + ip$) chiral order (E_u) in tetragonal systems and $d_{xy} + id_{x^2-y^2}$ ($d + id$) ordered superconductivity (E_2) in hexagonal lattices. Note that by "chiral", we refer to a particular subclass of TRSB superconducting

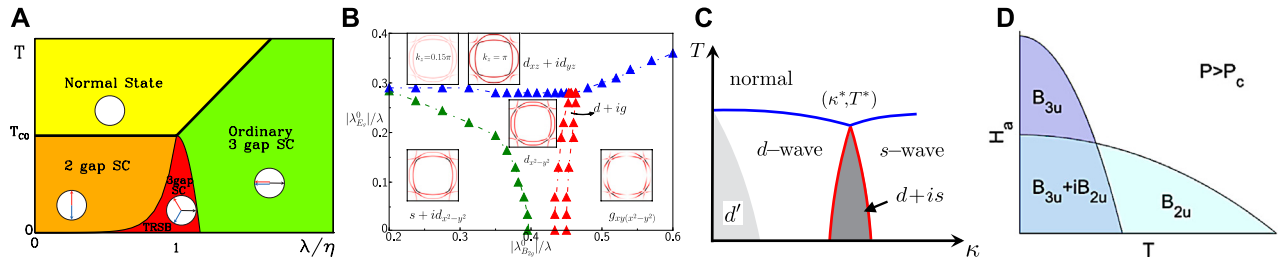

FIGURE 1
Selection of theoretical proposals for phase diagrams exhibiting TRSB in homogeneous superconducting phases. **(A)** Frustrated multiband superconductor which exhibits, as a function of frustration parameter, a state with complex order parameters of $s + is$ type. The three order parameters are symbolized as arrows in the white circles where the magnitude is the arrow length while the direction indicates phase in the complex plane [64–66]. **(B)** Phase diagram relevant for Sr_2RuO_4 exhibiting a TRSB phase of degenerate solutions $d_{xz} + id_{yz}$ [67]. **(C)** Phase diagram calculated for Fe-based systems with only electron pockets which support d-wave instabilities and s-wave states; if these become degenerate (almost degenerate) as a function of a tuning parameter κ, a TRSB superconducting state is stabilized at and below T_c [68]. **(D)** Qualitative magnetic field-temperature phase diagram proposed for UTe_2 where accidentally degenerate (nearly degenerate) triplet states produce a TRSB state at T_c (below T_c) [69]. **(A)** Reprinted figure with permission from [64], Copyright 2010 by the American Physical Society. **(B)** Reproduced from [67]. CC BY 4.0. **(C)** Reprinted figure with permission from [68], Copyright 2012 by the American Physical Society. **(D)** Reprinted figure with permission from [69], Copyright 2021 by the American Physical Society.

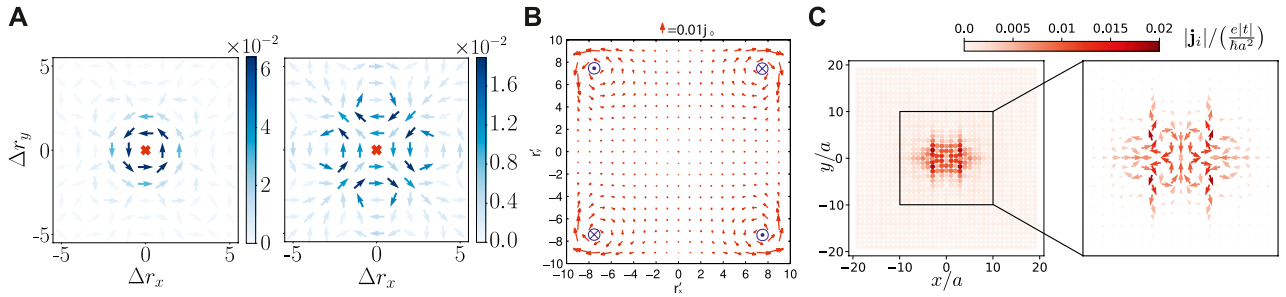

FIGURE 2
Examples of static supercurrent patterns induced by spatial perturbations in TRSB superconductors. **(A)** Induced supercurrents from a single point-like nonmagnetic impurity for the cases of $d_{x^2-y^2} + id_{xy}$ (left) and $d_{x^2-y^2} + ig_{xy(x^2-y^2)}$ (right) order parameters obtained from selfconsistent studies of the extended one-band Hubbard model [53]. **(B)** Supercurrent distribution of a square system with chiral corner loop currents in an $s + id_{x^2-y^2}$ state [47]. **(C)** Spontaneous supercurrents induced near a dislocation modelled by five missing atoms. In this case the bulk superconductor is a pure $d_{x^2-y^2}$ state, yet the dislocation is able to locally stabilize nontrivial phase gradients with associated current patterns [58]. **(A)** Reprinted figure with permission from [53], Copyright 2022 by the American Physical Society. **(B)** Reprinted figure with permission from [47], Copyright 2009 by the American Physical Society. **(C)** Reprinted figure with permission from [58], Copyright 2023 by the American Physical Society.

condensates exhibiting phase winding that breaks mirror symmetries. Along the same lines, solutions of one-dimensional (1D) irreps that are accidentally degenerate may also form such complex superpositions. Such cases are fine tuned, but Fermi surfaces with competing nesting tendencies, for example, are prone to near-degeneracy between several symmetry-distinct superconducting instabilities and may therefore more naturally feature such accidental degenerate superpositions. Examples of these include $d + is$ and $d + ig$ as discussed in the context of iron-based superconductors and Sr_2RuO_4 (see Figures 1B,C), or the so-called $s + is$ state with nontrivial phases on different bands as displayed in the phase diagram in Figure 1A, which also arises as a result of frustrated pairing interactions which are discussed in view of Fe-based superconductors [64–66] and other multiband materials [78]. More recently, accidental degeneracies are also explored for UTe_2 where candidate states include complex spin-triplet superpositions of the form e.g., $A_u + iB_{3u}$, $B_{1u} + iB_{3u}$ or $B_{3u} + iB_{2u}$ now expressed directly in terms of the 1D irreps, see Figure 1D. All the complex superpositions mentioned above break time-reversal symmetry, as evident e.g., from the chosen directionality of the orbital motion of the Cooper pairs.

Even though the above homogeneous superconducting condensates spontaneously break time-reversal symmetry, their unambiguous detection in actual materials is challenging experimentally since the internal magnetic fields produced in these states are suppressed due to the condensate of overlapping Cooper pairs and Meissner screening. However, defects, edges, dislocations, twin boundary interfaces, and other spatial inhomogeneities are known to produce persistent current patterns with associated magnetic fields that do not average to zero [47–53, 57, 58, 79–86]. In Figure 2 we show several examples of disorder- and dislocation-induced current patterns in TRSB superconducting phases. The examples include cases where the homogeneous superconducting phase breaks time-reversal symmetry (Figure 2A, B), and a case (Figure 2C) where TRSB is only induced locally due to the dislocation, whereas the clean homogeneous superconducting phase preserves time-reversal symmetry, see also Ref. [87]. Naturally, a remaining important question is whether

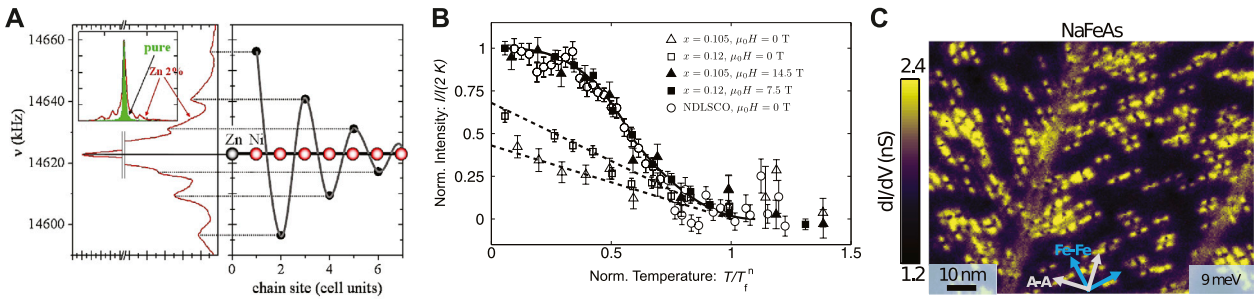

FIGURE 3
(A) Zn impurity on 1D inorganic chain YBa_2NiO_5 [96]. NMR satellite lines (left) indicate different Ni nuclei at different distances from the Zn. Polarization (right) on each site oscillates in sign with distance [88]; **(B)** Elastic neutron scattering data on underdoped LSCO showing the intensity at the incommensurate Bragg peaks near (π, π) vs. temperature T [97]. While a magnetic field induces SDW order, significant incommensurate magnetism is present already in zero field. This effect is enhanced with Zn substitution [98]; **(C)** Highly anisotropic electronic states induced by strain near a NaFeAs grain boundary, interpreted as magnetic stripes along the Fe-Fe directions (blue arrows) [99]. **(A)** Reprinted figure with permission from [88], Copyright 2009 by the American Physical Society. **(B)** Reprinted figure with permission from [97], Copyright 2008 by the American Physical Society. **(C)** Reprinted from [99].

induced fields from this mechanism exhibit the required amplitudes and are voluminous enough to explain experiments of specific materials, or one needs to resort to other explanations for the TRSB signal. We return to this discussion in the final section of the paper.

2.2 Disorder and superconductivity-induced quasi-ordered magnetism

2.2.1 Magnetic droplets from impurities

Nonmagnetic disorder has been known for many years to give rise to magnetic bound states and magnetic glassy behavior in correlated electron systems [88]. In superconductors, the opening up of a gap promotes the existence of these bound states. For fixed correlation and gap size, increasing disorder "freezes" the spin fluctuations present in the system [46], transferring the spectral weight to low frequencies and creating static configurations of localized spins that can break time-reversal symmetry. There are several models that exhibit these phenomena in a qualitative sense, and many somewhat mysterious aspects of the phenomenology of underdoped cuprates can be explained on this basis [88]. The approach has been to begin with the study of simple, localized and isolated defects in model Fermi systems with strong antiferromagnetic correlations, like Hubbard, $t-J$, and Anderson models, combined as needed with BCS pairing interactions [40–45, 89–92]. The magnetic response generally takes the form of a "droplet" of magnetic correlations around a defect, whose effective size corresponds to the antiferromagnetic correlation length ξ_{AF} of the pure host. If the correlations and/or defect potentials are sufficiently strong, this droplet is spontaneously nucleated, carries net spin 1/2 and may be considered as a localized moment, but also displays a staggered magnetic behavior over ξ_{AF} [40–45]. If correlations or the impurity potential are weaker, the correlated spin response is still present, but must be induced by an applied magnetic field [45, 93]. This is a mean-field picture of the freezing of spin fluctuations present in the host, which needs to be supplemented by a description of dynamics, a complete version of which is still lacking. In the quantum critical regime, some aspects simplify, and the basic qualitative features have been discussed in Refs. [94, 95].

Away from the quantum critical point, the droplet picture has been extensively confirmed for dilute, intentionally substituted defects, primarily by NMR and μSR experiments in quasi-1D inorganic chain and ladder compounds (see Figure 3A) [96], as well as in some quasi-2D cuprate materials where impurity substitution into quite clean hosts can be adequately controlled [88]. On the other hand, there is no reason why similar physics should not take place when defects occur naturally in the crystal or film growth process, which is characteristic of many complex oxides, particularly chemically doped ones. The question then naturally arises as to what happens when the inter-defect spacing becomes comparable to the AF correlation length ξ_{AF}. In calculations for a 2D Hubbard model with disorder and d-wave pairing correlations, the overlap of the magnetic droplets in the correlated state leads to interference processes which tend to align the droplets in a state which displays quasi-long range AF order [44, 46, 100–102]. It seems likely that the results of many experiments which are attributed to "stripe order" in underdoped cuprates may in fact be explained by the quasi-long range order arising from interacting droplets [89, 103]. The creation of 1D structures to lower the kinetic energy via 1D rivers of mobile charge while maintaining some correlation energy is clearly an attractive and simple picture. But creation of such structures also raises the energy of the state around a single impurity, which would prefer to be more globular in shape. One can, within Hubbard-type models on square lattices, answer the question about which mechanism enables the system to lower its energy more efficiently in which situation. This clearly depends on a variety of factors, including doping, correlations, and disorder. By performing simulations, one can - without prejudicing the system - determine which part of the generalized phase diagram corresponds to 1D stripe-like structures, and which to other ground states [89, 104, 105].

Experimentally, manifestations of this physics have been observed in a wide variety of contexts. In Figure 3A, we show the well-established oscillations in the Y NMR line in a 1D inorganic chain due to the modulation of the magnetic response locally by a Zn

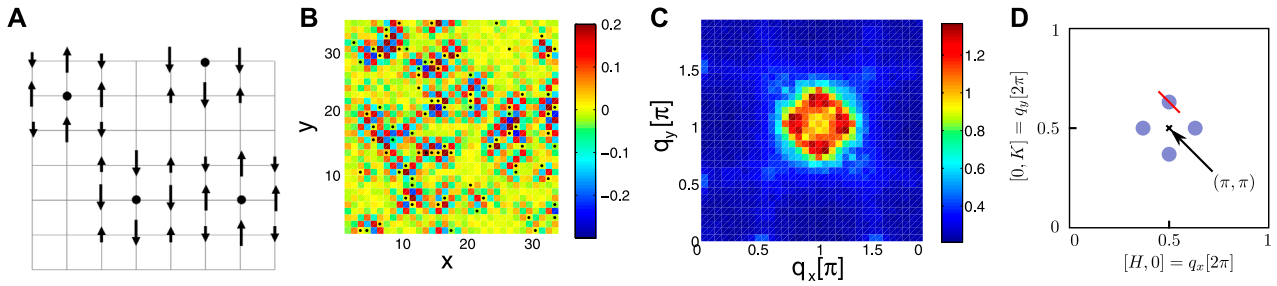

FIGURE 4
(A) Schematic of magnetic droplets created around individual nonmagnetic impurities in a correlated system, which interact via an effective collective exchange, which may be understood by the need to maintain Néel coherence among the different droplets. **(B)**, typical magnetization map $M(\mathbf{r})$ of a disordered superconductor is shown for $U = 3.2t$ [44]. **(C)** the Fourier transform of $M(\mathbf{r})$ yields the structure factor $S(\mathbf{q})$. **(D)** Sketch of the expected intensities (light blue dots) away from (π, π) (black cross) as measured in neutron scattering experiments by taking data along line cuts (red line) [106]. **(A,B, C)** Reprinted figure with permission from [44], Copyright 2007 by the American Physical Society.

impurity. Figure 3B shows data from an elastic neutron study [97] (see also [106–108]) with frozen magnetic order in a disordered cuprate in zero field, enhanced further by application of a field. The order is apparently quasi-long-ranged since it appears in the neutron scattering intensity near wave vector (π, π), yet it occurs in a part of the cuprate phase diagram where true long-range order has disappeared. Finally, in Figure 3C, STM reveals in an Fe-based superconductor a spatially modulated density of states pattern due to strain near a twin boundary with a wave vector close the $(\pi, 0)$ magnetic ordering vector, indicating local impurity-induced magnetism.

2.2.2 Quasi-long range magnetic order from disorder

Quasi long-range antiferromagnetic order has been reported in many cuprate samples whose T_c or nominal doping puts them outside the long-range AF phase, particularly in the superconducting state at low temperatures, e.g., in LSCO [97, 98, 106, 107, 109–112]. Characteristic dynamical features of spin glasses have occasionally been observed, but even if these are not always found, the term "spin glass" has become commonplace in cuprates to describe the existence of a phase of short-range frozen magnetism. The size of the spin-glass phase varies significantly with material [112]; whereas in LSCO it extends in zero field out to 15% doping, it is confined to very low doping in the much cleaner YBCO system [113, 114], and BSCCO is in-between [112]. Moreover, disorder due to Zn substitution on the Cu sites enhances the size of the spin-glass phase [98]. These empirical facts suggest strongly the picture of disorder-induced short-range magnetism described above. Quasi-long range order occurs when these droplets begin to overlap [44], which can occur without frustration on a square lattice, as shown in Figure 4A. This lack of frustration has important implications not only for the quasi-long range (π, π) magnetic order, but may also carry a macroscopic net magnetic moment. Since each droplet of *staggered* order is dominated by the NN spins, it carries a net spin 1/2 [41], and the droplets overlap coherently. While the net moments associated with each droplet do not align ferromagnetically, a fluctuating magnetic state with both short range and longer range (inter-impurity distance) is created (Figure 4B). The final magnetization profile appears as a clear peak in the structure factor, as seen in Figure 4C, compared to the Lake et al. experiment on underdoped LSCO where intensity at the incommensurate positions is found [106], as shown schematically in Figure 4D. It is this disorder-induced random magnetic landscape that is relevant to our current study as a possible mechanism of TRSB in superconductors.

Thus far we have said little about why such a TRSB signal might arise only below T_c, as observed in many unconventional superconductors. Here the proposal is that the gapping of the low-energy density of states enhances the probability of creating an impurity bound state carrying the spin-1/2 moment. Figure 5A shows the selfconsistently obtained magnetization in the presence of a nonmagnetic point-like impurity at $T = 0$ *versus* Hubbard U. As seen, before entering the bulk SDW phase, a regime exists where the superconductor prefers a local impurity-induced magnetic droplet as discussed above. What is the origin of this local magnetic structure? In Figure 5B, we show the local density of states of the tight-binding model with band parameters suitable for a cuprate superconductor. Addition of a strong impurity does not produce a bound state resonance due to the fact that the impurity state is embedded in the continuum. Addition of correlations does not change this qualitative picture. On the other hand, when a superconducting gap is created, as in the d-wave case shown in Figure 5C, the expected in-gap resonance is clearly visible (compare, e.g., with Zn impurity in BSCCO [115]). In the presence of correlations, the bound state splits to lower the overall energy including magnetism, creating in the process the localized spin-1/2 state with maximal polarization typically on nearest neighbor sites. Creating such a state depends both on the impurity potential V_{imp} and on the strength of the correlations U, as shown in the "phase diagram" of Figure 6A. The explicit evolution of the 1-impurity local magnetic state for increasing correlation strength is shown in Figure 6B: it is stabilized in a range of U just below the critical U corresponding to creation of true long-range order in the Hartree-Fock approximation. Even if the magnetic bound states are not formed spontaneously, i.e., one is in the $S = 0$ part of the phase diagram shown in 6 A, it is important to recall that the system is still highly correlated as indicated by the response of many impurities for small but nonzero U to a weak magnetic field, as seen from Figure 6C.

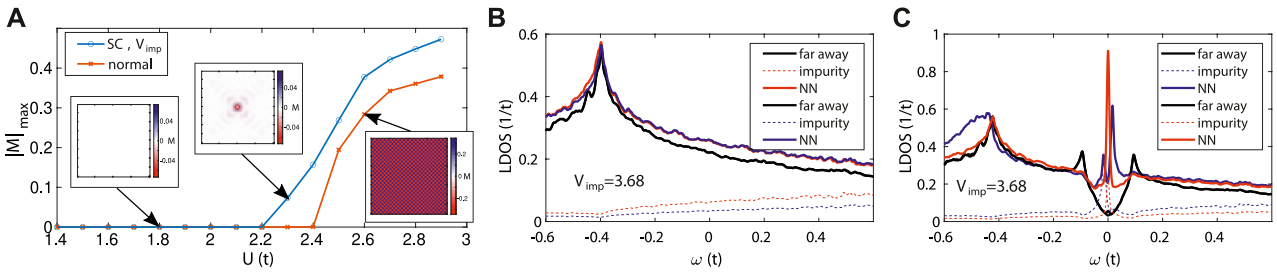

FIGURE 5
(A) Magnetic phase diagram for a superconductor including a nonmagnetic impurity and a normal correlated metal. **(B)** Density of states of a normal metal including a nonmagnetic impurity with correlations (blue curves, $U = 2.3t$) and without correlations (red curves, $U = 0$). **(C)** Density of states of a *d*-wave superconductor including a nonmagnetic impurity with and without correlations.

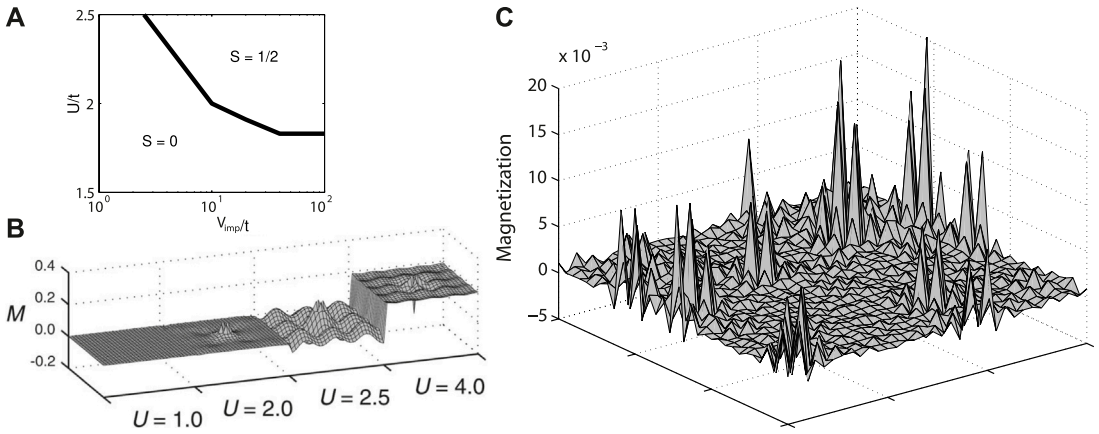

FIGURE 6
(A) phase diagram for single impurity in *d*-wave superconductors. *U* is the Hubbard interaction, treated in Hartree-Fock approximation, and V_{imp} is the impurity potential. **(B)** staggered magnetization near a strong impurity for increasing correlation strength *U*. **(C)** magnetization landscape induced by a weak magnetic field in the presence of many impurities without spontaneous spin freezing. From Ref. [45]. **(A,B,C)** Reprinted figure with permission from [45], Copyright 2007 by the American Physical Society.

Similar phenomena have been observed in many other correlated superconductors. Most recently, magnetic clustering was reported by μSR in samples of UTe_2 grown by chemical vapor transport with T_c's of order 1.6K [116], whereas no magnetic signal was reported in cleaner molten-salt flux grown crystals with T_c's of order 2.1K [117].

To summarize this section, simulations of a *d*-wave superconductor in the presence of local Coulomb interactions and nonmagnetic disorder [44, 89, 101, 103] are compatible with the experiments on relatively disordered cuprates like LSCO and BSCCO where a spin-glass phase is observed at low doping in the SC state [112]. These studies explain as well why such a phase is *not* seen in the cleanest YBCO samples, why in LSCO and BSCCO the spin-glass phase is more robust at underdoping, and why it is enhanced by addition of further disorder. The order-from-disorder many-impurity magnetic state is favored to appear only below T_c when the gap opens. Similar phenomena have been observed in other correlated superconductors [91, 118–120].

2.2.3 TRSB from disorder-induced loop currents

Recently, a Bogoliubov-de Gennes study of a disordered *d*-wave superconductor without magnetic correlations [55] reported local TRSB current loops for sufficiently high disorder levels, see Figure 7A. Since a pure *d*-wave superconducting state does not break time-reversal symmetry, and parameters are chosen to place the pure system far from TRSB mixed-symmetry states ($d + is$), it is surprising that such persistent currents can arise purely from nonmagnetic disorder. In addition, the possible emergence of an effective granular *d*-wave description was proposed by Li et al. [55]. In this picture, cuprates consist of intrinsically inhomogeneous *d*-wave regions of roughly constant phase, weakly coupled by Josephson tunneling. For example, such behavior has been claimed experimentally from STM, magnetization and transport measurements on certain overdoped LSCO samples [121]. Such a proposal, if correct, would have profound implications for the disappearance of superconductivity on the overdoped side of the superconducting dome, since phase fluctuations, rather than pair interaction weakening (as due, for example, to the weakening of spin fluctuations and disorder [122]) would determine T_c.

However, detailed theoretical investigations of the disorder-induced orbital currents in the same model framework were performed in Ref. [56], showing that the occurrence of such currents can be traced to local extended *s*-wave pairing out of

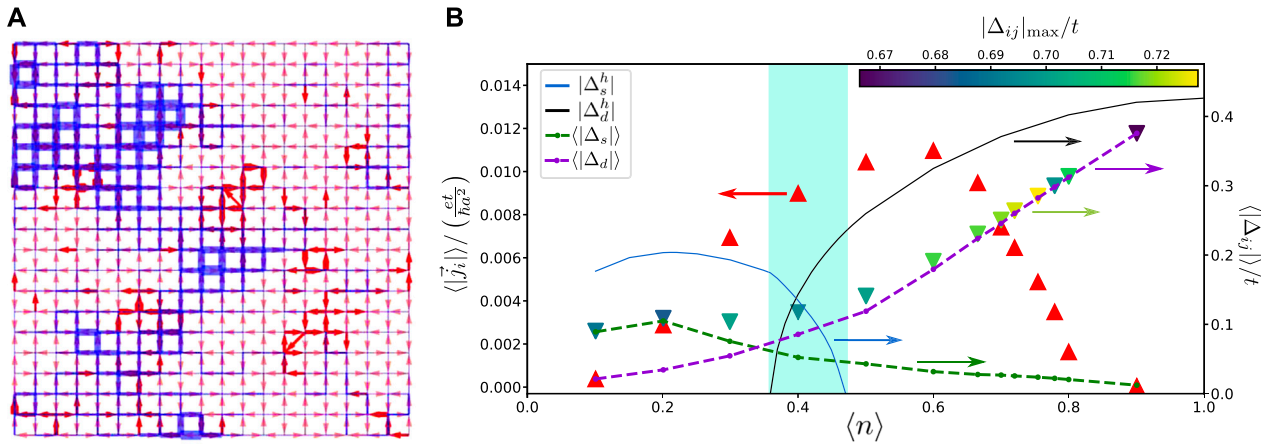

FIGURE 7
(A) Spontaneous current pattern in a *d*-wave superconductor with large disorder [55]. **(B)** Zero temperature phase diagram indicating average current (red triangles, left scale) vs. doping. Also indicated are *s*- and *d*-wave order parameter amplitudes, respectively (solid lines). The shaded region marks the range of doping where a mixed state $s + id$ is stable in the homogeneous case. Dashed lines show the average *d*-wave (purple) and *s*-wave (green) order parameter components (see main text) with random distributions of impurities [56]. **(A)** Reproduced from [55]. CC BY 4.0. **(B)** Reprinted figure with permission from [56], Copyright 2007 by the American Physical S.ociety.

phase with *d*-wave order, despite the fact that the effect occurs far from the homogeneous $s + id$ phase (see Figure 7B). The system does not appear to spontaneously phase separate into granular regions. Instead, the energetics leading to regions of *local* $s \pm id$ order are driven by inhomogeneous density modulations.

2.3 Enhanced RKKY exchange coupling and slowing-down of magnetic fluctuations by superconductivity

While the previous sections addressed the case where superconductivity is a necessary ingredient for orbital currents or moment formation, here we focus on different scenarios where disorder and superconductivity interact to either slow down magnetic fluctuations or enhance the mutual coupling between magnetic regions/moments existing already in the normal state. This section serves to suggest alternative mechanisms for observing TRSB below T_c. We focus on the physical picture and outline several options whereas a quantitative study is left for future research. We consider the following possibilities:

- (A) Time-reversal symmetry is preserved in the normal state, but disorder pins or slows down fluctuations in the superconducting state to either break time-reversal symmetry or bring the system closer to local magnetism.
- (B) The normal state contains significant amounts of magnetic moments, but time-reversal symmetry remains preserved in the normal state. The magnetic moments get resonantly coupled in the superconducting state thereby breaking time-reversal symmetry or bringing the system closer to static magnetism.
- (C) Time-reversal symmetry is broken already in the normal state, yet too weak or dilute to be detected by standard experimental probes. Superconductivity enhances the magnetic volume fraction and/or increases the coupling between magnetic regions.

The first **scenario (A)** was largely discussed in Sec. 2.2, there exemplified through models relevant for cuprates, i.e., $d_{x^2-y^2}$-wave superconductivity in the presence of nonmagnetic impurities and electronic correlations. This mechanism is likely much more broadly applicable since most unconventional superconductors allow for in-gap bound states from nonmagnetic disorder [90, 123, 124]. This causes enhanced local spin susceptibilities and associated tendency to slow down magnetic fluctuations locally or even pin magnetic moments [88]. This mechanism may well also be at play near e.g., sample edges or various forms of dislocations [57, 58, 125, 126]. A related property may happen near sample edges when zero-energy Andreev bound states generated by sign-changes of the gap function split by spontaneous generation of edge supercurrents [82, 84, 86].

Regarding **scenario (B)**, consider the case of a normal metal with a concentration of magnetic moments. Due to quantum fluctuations, time-reversal symmetry is preserved in the normal state. We assume additionally a low Kondo temperature, $T_K < T_c$, i.e., unscreened spins. We return briefly to the opposite case with $T_K > T_c$ further below. The magnetic moments couple via the indirect Ruderman-Kittel-Kasuya-Yosida (RKKY) interaction, i.e., via a partial spin polarization of the conduction electrons, causing the well-known oscillatory RKKY exchange interaction [127–129]. The detailed behavior of the RKKY coupling in the superconducting phase depends on dimensionality, the normal state bandstructure, and the superconducting pairing symmetry, and is generally a complex matter that requires thorough investigation [130–133]. Typically, however, for spin-singlet superconductivity the RKKY coupling is weakened by the singlet formation of the conduction electrons. More specifically, for the standard RKKY interaction *s*-wave superconductivity contributes a weak

antiferromagnetic correction when the inter-moment distance R is smaller than the coherence length ξ. For $R > \xi$, the RKKY coupling becomes purely antiferromagnetic from the anomalous (superconducting) part of the spin susceptibility, but is exponentially suppressed in R [130]. These are consequences of the typical suppressed spin susceptibility in the superconducting phase. It is important to emphasize that these properties apply to the perturbative RKKY expression calculated in the Born approximation, only in the case of *s*-wave spin-singlet superconductivity.

It is known, however, that another contribution to the exchange coupling arises from the Yu-Shiba-Rusinov (YSR) bound states produced by magnetic impurities [123, 134–137]. The overlap of the YSR bound state wavefunctions leads to a resonant-like contribution to the energy with a singular dependence of the exchange coupling on the YSR bound state energy [137]. Thus, in some superconductors where the average distance between the magnetic moments is lower than ξ, it is conceivable (though somewhat fine-tuned due to the requirement of very low-lying YSR states [137, 138]) that the RKKY coupling gets enhanced in the superconducting phase, thereby boosting the tendency for magnetism and the detection of a TRSB signal only below T_c. In fact, this mechanism may also be at play for the mechanism discussed in Sec. 2.2 where magnetic moments are generated only by electronic interactions and superconducting bound states from nonmagnetic impurity potentials. To the best of our knowledge, the resonant-like YSR energy contribution has not been thoroughly investigated for other superconducting pairing symmetries, but presumably nodal gaps or triplet order can drive even stronger, directional-dependent couplings [131]. Quantum corrections to the classical YSR picture can also in principle lead to TRSB enhancement in the superconducting state, if in the case $T_K \gtrsim T_c$, spin-singlet superconducting gap formation unscreens the moments. In that case, if the moments couple and generate a weak magnetic state, it may be picked up by e.g., μSR similarly to the scenario discussed in Sec. 2.2.

Finally we discuss **scenario (C)** where a distribution of disordered static magnetic moments are already present in the normal state. Thus in this case, strictly speaking, TRSB is not restricted to the superconducting phase below Tc. We do not discuss in detail the origin of such moments, but they could simply arise from weakly coupled magnetic impurities, or small spin-polarized regions that have crossed into a nearby magnetic phase due to chemical disorder. It might also be due to the mechanism discussed in Sec. 2.2 if the "normal state" exhibits pseudo-gap behavior. We assume that the magnetism in the normal state is too weak to be detected by standard probes, for example, due to a tiny volume fraction and/or short-range nature. A TRSB signal may be detected, however, in cases where the volume fraction grows and/or the moments couple more strongly, and the magnetic quasi-order becomes longer ranged as a result upon entering the superconducting phase [139, 116]. The latter may arise from the mechanism discussed under (B). It might also take place via new "stepping stone" magnetic islands produced by nonmagnetic disorder in the superconducting state via the mechanism discussed in Sec. 2.2. An enhanced volume fraction can take place in cases where another competing order is in the game. If local disorder-induced magnetism is limited by orbital order or a CDW phase, for example, then superconductivity may suppress these competing orders and thereby alleviate the magnetism. Clearly, these are merely possibilities for observing TRSB below T_c, and need further detailed investigations for specific materials.

3 Experimental consequences

In this section we discuss the main current experimental techniques to directly probe TRSB in superconductors, and mention subtleties in the interpretation of experimental results. Many unconventional superconductors are investigated using the muon spin relaxation (μSR) technique where a beam of spin-polarized muons with given energy is directed to the sample [140]. Muons are stopped in the material, implanted at preferred positions in the crystal structure and can be used to detect the magnetic field locally at their positions. Within the lifetime of the muons, their spins precess in the local field. Once the muon decays into a positron and two neutrinos, the direction of the magnetic moment fixes the probability distribution of emitted positrons. The counting rates of the latter in the forward and backward directions of the (original) polarization of the muon beam yield the asymmetry $A(t)$, which is recorded as a function of time.

The Fourier transform of $A(t)$ for measurements on superconductors in a finite field (in the vortex state) is directly related to the magnetic field distribution of the sample and can be used to deduce the temperature dependence of the penetration depth [140–142]. In a zero field experiment, the information about the field distribution is also contained in the asymmetry function, but typically full oscillations are not observed in superconductors because of the smallness of the internal field. Still, an increased relaxation as a function of temperature is taken as signature of the occurrence of an additional internal field that collectively depolarizes the implanted muons. Average fields that are static on the time scale of the muon decay can then be detected down to the scale of μT [140]. From the shape of the asymmetry $A(t)$ at low temperature (when there is evidence for TRSB), it is possible to estimate the average field by the reduction at largest measuring times. A quick initial reduction and no further deviation as a function of time are indications of few muons getting depolarized in a large field. By contrast, an initial weak difference of the depolarization rates that behaves quadratically in time indicates an almost uniform field distribution. Fitting to such behavior can give bounds on the fraction of the sample exhibiting TRSB. Such bounds may be further benchmarked against scanning SQUID microscopy measurement [6, 143, 144]. Depending on the initial energy of the muons, implantation happens on length scales of 10 nm–100 nm from the surface, such that the technique can be considered as bulk-like. By varying the initial energy of the muons, the stopping profiles allow deductions of the TRSB as function of distance from the surface [139]. The μSR technique has been used to claim TRSB in a number of superconductors; for a list see Ref. [3].

Knowledge from *ab initio* methods about the preferred position within the elementary cell where muons are implanted [145, 146] can facilitate the interpretation of the results, i.e., help decipher whether the positive charge of the muons might cause a perturbation large enough to self-generate a TRSB signal. In addition, the position of the stopping site and the associated form factor can be important for a quantitative description of the relaxation, e.g., in cases where the muon locations may feature enhanced or reduced field effects from purely geometric reasons. The typical magnitude of the internal field at the muon site for a generic interstitial position in the unit cell may be estimated; in the vicinity of local spin-1/2 droplets (Sec. 2.2) or impurity-induced localized orbital currents are of order 1 G [3, 147], which is of the same order as fields reported in experiments.

The second main probe of TRSB is the polar Kerr effect, where the polarization plane of light incident on a sample is rotated upon reflection. The classic example is reflection from a ferromagnetic surface, but in recent years the technique has been employed to detect TRSB in unconventional superconductors [1, 2, 148–151]. The angle θ_K, which is related to the Hall conductivity, can be expressed as

$$\theta_K(\omega) = \frac{4\pi}{\omega}\mathrm{Im}\left(\frac{\sigma_H(\omega)}{n(n^2-1)}\right),$$

where n is the complex, frequency-dependent index of refraction, and $\sigma_H(\omega)$ is the Hall conductivity. For the experimental identification of a polar Kerr effect arising from the superconducting state, it needs to be checked that the rotation onsets at T_c, the sign and magnitude of the signals vary after each cool-down in the absence of an external magnetic field, a small training field saturates the rotation angle (but with sign given by the direction of the field), and the temperature dependence of the Kerr angle follows mean-field-like order parameter behavior [148].

From a theoretical point of view, a finite Kerr angle is directly related to a nonzero Hall conductivity, which requires time-reversal symmetry breaking and breaking of mirror symmetries about all planes parallel to the incident wave vector [152]. Therefore, the order parameter has to be chiral and not simply break TRSB. For example, a pure $s + id$ superconductor is nonchiral and will not generate an intrinsic Kerr signal. By contrast, a one-band $p + ip$ superconductor will produce a weak intrinsic Kerr effect with θ_K arising only from the collective modes of the order parameter [153]. This effect is many orders of magnitude smaller than typical measured rotation angles θ_K of order tens of nanoradians. The intrinsic effect in a chiral *multiband* superconductor, arising from contributions to σ_H from interband transitions, is larger at optical frequencies (but still difficult to definitively quantify) [154]. On the other hand, if the state is nonchiral, there will be no intrinsic Kerr signal at all.

It is important to note that chirality can occur for complex linear combinations of 1D irreps of the point group, and not necessarily only those states corresponding to 2D irreps that have been traditionally discussed, like $p_x + ip_y$ in tetragonal and $d_{xy} + id_{x^2-y^2}$ in hexagonal symmetries. For example, in tetragonal symmetry, $d_{x^2-y^2}$ and d_{xy} are distinct 1D irreps, but may occur in an accidental linear combination $a \cdot d_{xy} + ib \cdot d_{x^2-y^2}$. Such states should also give rise to an intrinsic polar Kerr effect, but nonchiral TRSB combinations like $s + id$ will not.

One of the problems with the interpretation of Kerr measurements is that the size of an intrinsic signal is very hard to estimate, and the size of an extrinsic one may in principle be in fact much larger, but depend on the type of disorder and the nature of the ground state. For example, the division between chiral and non-chiral states with regard to their polar Kerr signals is muddied somewhat by disorder. In $p + ip$ states, an extrinsic Kerr rotation angle orders of magnitude larger than the intrinsic effect may result from the skew-scattering of chiral Cooper pairs from impurities [155, 156], but for $d + id$ and higher order angular momentum states, the contribution is of higher order in (nV_{imp}^2) where V_{imp} is the impurity potential of point-like impurities with density n [1, 155]. Estimates in both cases are model dependent and require disorder averaging. Impurities in nonchiral TRSB states will also give rise to small signals from induced currents, but after averaging such signals should be substantially smaller, while for chiral $d + id$ states the signal is small but remains finite upon impurity averaging [157]. A similar contribution should therefore be provided by local spatially fluctuating magnetic moments. Whether or not a Kerr signal is observed, and its size, depends on how much averaging of the fluctuations takes place over the laser spot. In both these cases, some kind of ability to "train" the state with an external magnetic field should be observed [148]. Finally, we mention some recent calculations showing that local currents can be created near dislocations, which induce $d + ig$ or $s + id$ states [57, 58]. The Kerr effect arising from these local states has not been properly explored.

4 Summary and outlook

In the above we focused on different theoretical mechanisms where magnetism in various guises appear only below the superconducting critical transition temperature T_c and is generated by disorder or other spatial inhomogeneities. This included discussions of localized defect-induced orbital supercurrents, magnetic moment generation from superconductivity and electronic correlations, and the possibility of enhanced RKKY exchange coupling by superconductivity.

Naturally an important question relates to the relevance of these mechanisms to the observation of TRSB below T_c in currently discussed unconventional superconducting materials. In the above, we provided a detailed discussion of the cuprates and the possibility of superconductivity-enhanced spin-polarization. Two other materials of significant current interest are UTe_2 and Sr_2RuO_4. For these compounds, two-component condensates are widely discussed, but inconsistent with specific heat measurements, also under uniaxial strain featuring no signs of double transitions [36–39]. This points to single-component superconductivity which has received recent support from a number of other probes as well [117, 150, 158, 159], but leaves open the question of what causes a TRSB signal in some measurements. We have surveyed several possible answers to this question from the perspective of induced fields within the superconducting state from spatial inhomogeneity.

Resolving the detailed nature of TRSB in superconductors is important since the resolution will have profound implications for our general understanding of unconventional superconductivity. Therefore, we hope that future collective research efforts will

continue to be devoted to this task. This includes both improved experiments and better theoretical descriptions, the latter including material-specific studies of the interplay between unconventional pairing states and realistic models for the relevant sources of spatial inhomogeneity. μSR and Kerr experiments on systematically disordered samples, e.g., with strong chemical impurities or Frenkel defects created by electron irradiation, can help to distinguish the extrinsic TRSB effects described here from intrinsic effects, and from each other.

Author contributions

BA: Writing–original draft. AK: Writing–original draft. PH: Writing–original draft.

Funding

The author(s) declare financial support was received for the research, authorship, and/or publication of this article. AK acknowledges support by the Danish National Committee for Research Infrastructure (NUFI) through the ESS-Lighthouse Q-MAT. PH acknowledges support from NSF-DMR-2231821.

Acknowledgments

We acknowledge useful discussions with C. N. Breiø, M. H. Christensen, P. Hedegård, C. Hicks, M. Roig, H. Røising, A. T. Rømer, and J. Schmalian. We thank M. Pal for assistance with calculations for Figure 5.

Conflict of interest

The authors declare that the research was conducted in the absence of any commercial or financial relationships that could be construed as a potential conflict of interest.

Publisher's note

References

1. Kallin C, Berlinsky J. Chiral superconductors. *Rep Prog Phys* (2016) 79:054502. doi:10.1088/0034-4885/79/5/054502

2. Wysokiński KI. Time reversal symmetry breaking superconductors: Sr_2RuO_4 and beyond. *Condensed Matter* (2019) 4:47. doi:10.3390/condmat4020047

3. Ghosh SK, Smidman M, Shang T, Annett JF, Hillier AD, Quintanilla J, et al. Recent progress on superconductors with time-reversal symmetry breaking. *J Phys Condens Matter* (2021) 33:033001. doi:10.1088/1361-648x/abaa06

4. Røising HS, Wagner G, Roig M, Rømer AT, Andersen BM. Heat capacity double transitions in time-reversal symmetry broken superconductors. *Phys Rev B* (2022) 106:174518. doi:10.1103/PhysRevB.106.174518

5. Strand JD, Van Harlingen DJ, Kycia JB, Halperin WP. Evidence for complex superconducting order parameter symmetry in the low-temperature phase of UPt_3 from Josephson interferometry. *Phys Rev Lett* (2009) 103:197002. doi:10.1103/PhysRevLett.103.197002

6. Hicks CW, Kirtley JR, Lippman TM, Koshnick NC, Huber ME, Maeno Y, et al. Limits on superconductivity-related magnetization in Sr_2RuO_4 and $PrOs_4Sb_{12}$ from scanning SQUID microscopy. *Phys Rev B* (2010) 81:214501. doi:10.1103/PhysRevB.81.214501

7. Avers KE, Gannon WJ, Kuhn SJ, Halperin WP, Sauls JA, DeBeer-Schmitt L, et al. Broken time-reversal symmetry in the topological superconductor UPt_3. *Nat Phys* (2020) 16:531–5. doi:10.1038/s41567-020-0822-z

8. Maeno Y, Hashimoto H, Yoshida K, Nishizaki S, Fujita T, Bednorz JG, et al. Superconductivity in a layered perovskite without copper. *Nature (London)* (1994) 372:532–4. doi:10.1038/372532a0

9. Mackenzie AP, Scaffidi T, Hicks CW, Maeno Y. Even odder after twenty-three years: the superconducting order parameter puzzle of Sr_2RuO_4. *Npj Quan Mater.* (2017) 2:40. doi:10.1038/s41535-017-0045-4

10. Rømer AT, Scherer DD, Eremin IM, Hirschfeld PJ, Andersen BM. Knight shift and leading superconducting instability from spin fluctuations in Sr_2RuO_4. *Phys Rev Lett* (2019) 123:247001. doi:10.1103/PhysRevLett.123.247001

11. Rømer AT, Hirschfeld PJ, Andersen BM. Superconducting state of Sr_2RuO_4 in the presence of longer-range Coulomb interactions. *Phys Rev B* (2021) 104:064507. doi:10.1103/PhysRevB.104.064507

12. Kivelson SA, Yuan AC, Ramshaw BJ, Thomale R. A proposal for reconciling diverse experiments on the superconducting state in Sr_2RuO_4. *Npj Quan Mater.* (2020) 5:43. doi:10.1038/s41535-020-0245-1

13. Stewart GR. Heavy-fermion systems. *Rev Mod Phys* (1984) 56:755–87. doi:10.1103/RevModPhys.56.755

14. Joynt R, Taillefer L. The superconducting phases of UPt_3. *Rev Mod Phys* (2002) 74:235–94. doi:10.1103/RevModPhys.74.235

15. Kawasaki I, Watanabe I, Hillier A, Aoki D. Time-reversal symmetry in the hidden order and superconducting states of URu_2Si_2. *J Phys Soc Jpn* (2014) 83:094720. doi:10.7566/JPSJ.83.094720

16. Ran S, Eckberg C, Ding QP, Furukawa Y, Metz T, Saha SR, et al. Nearly ferromagnetic spin-triplet superconductivity. *Science* (2019) 365:684–7. doi:10.1126/science.aav8645

17. Aoki D, Brison JP, Flouquet J, Ishida K, Knebel G, Tokunaga Y, et al. Unconventional superconductivity in UTe_2. *J Phys Condens Matter* (2022) 34:243002. doi:10.1088/1361-648x/ac5863

18. Biswas PK, Luetkens H, Neupert T, Stürzer T, Baines C, Pascua G, et al. Evidence for superconductivity with broken time-reversal symmetry in locally noncentrosymmetric SrPtAs. *Phys Rev B* (2013) 87:180503. doi:10.1103/PhysRevB.87.180503

19. Shang T, Smidman M, Ghosh SK, Baines C, Chang LJ, Gawryluk DJ, et al. Time-reversal symmetry breaking in Re-based superconductors. *Phys Rev Lett* (2018) 121:257002. doi:10.1103/PhysRevLett.121.257002

20. Shang T, Ghosh SK, Zhao JZ, Chang LJ, Baines C, Lee MK, et al. Time-reversal symmetry breaking in the noncentrosymmetric Zr_3Ir superconductor. *Phys Rev B* (2020) 102:020503. doi:10.1103/PhysRevB.102.020503

21. Hillier AD, Quintanilla J, Cywinski R. Evidence for time-reversal symmetry breaking in the noncentrosymmetric superconductor $LaNiC_2$. *Phys Rev Lett* (2009) 102:117007. doi:10.1103/PhysRevLett.102.117007

22. Hillier AD, Quintanilla J, Mazidian B, Annett JF, Cywinski R. Nonunitary triplet pairing in the centrosymmetric superconductor $LaNiGa_2$. *Phys Rev Lett* (2012) 109:097001. doi:10.1103/PhysRevLett.109.097001

23. Bauer ED, Frederick NA, Ho PC, Zapf VS, Maple MB. Superconductivity and heavy fermion behavior in $PrOs_4Sb_{12}$. *Phys Rev B* (2002) 65:100506. doi:10.1103/PhysRevB.65.100506

24. Aoki Y, Tsuchiya A, Kanayama T, Saha SR, Sugawara H, Sato H, et al. Time-reversal symmetry-breaking superconductivity in heavy-fermion $PrOs_4Sb_{12}$ detected by muon-spin relaxation. *Phys Rev Lett* (2003) 91:067003. doi:10.1103/PhysRevLett.91.067003

25. Rotter M, Tegel M, Johrendt D. Superconductivity at 38 K in the iron arsenide $(Ba_{1-x}K_x)Fe_2As_2$. *Phys Rev Lett* (2008) 101:107006. doi:10.1103/PhysRevLett.101.107006

26. Böker J, Volkov PA, Efetov KB, Eremin I. *s + is* superconductivity with incipient bands: doping dependence and STM signatures. *Phys Rev B* (2017) 96:014517. doi:10.1103/PhysRevB.96.014517

27. Matsuura K, Roppongi M, Qiu M, Sheng Q, Cai Y, Yamakawa K, et al. Two superconducting states with broken time-reversal symmetry in $FeSe_{1-x}S_x$. *Proc Natl Acad Sci* (2023) 120:e2208276120. doi:10.1073/pnas.2208276120

28. Guguchia Z, Mielke C, Das D, Gupta R, Yin JX, Liu H, et al. Tunable unconventional kagome superconductivity in charge ordered RbV_3Sb_5 and KV_3Sb_5. *Nat Commun* (2023) 14:153. doi:10.1038/s41467-022-35718-z

29. Mielke C, Das D, Yin JX, Liu H, Gupta R, Jiang YX, et al. Time-reversal symmetry-breaking charge order in a kagome superconductor. *Nature* (2022) 602:245–50. doi:10.1038/s41586-021-04327-z

30. Rømer AT, Bhattacharyya S, Valenti R, Christensen MH, Andersen BM. Superconductivity from repulsive interactions on the kagome lattice. *Phys Rev B* (2022) 106:174514. doi:10.1103/PhysRevB.106.174514

31. Ribak A, Skiff RM, Mograbi M, Rout PK, Fischer MH, Ruhman J, et al. Chiral superconductivity in the alternate stacking compound 4Hb-TaS_2. *Sci Adv* (2020) 6: eaax9480. doi:10.1126/sciadv.aax9480

32. Anand VK, Bhattacharyya A, Adroja DT, Panda K, Biswas PK, Hillier AD, et al. Time-reversal symmetry breaking and *s*-wave superconductivity in $CaPd_2Ge_2$: a μSR study. *Phys Rev B* (2023) 108:224519. doi:10.1103/PhysRevB.108.224519

33. Kataria A, Verezhak JAT, Prakash O, Kushwaha RK, Thamizhavel A, Ramakrishnan S, et al. Time-reversal symmetry breaking in the superconducting low carrier density quasiskutterudite $Lu_3Os_4Ge_{13}$. *Phys Rev B* (2023) 107:L100506. doi:10.1103/PhysRevB.107.L100506

34. Kataria A, Verezhak JAT, Prakash O, Kushwaha RK, Thamizhavel A, Ramakrishnan S, et al. Broken time-reversal symmetry in the cubic skutterudite-like superconductor $Y_3Ru_4Ge_{13}$. *Phys Rev B* (2023) 108:214512. doi:10.1103/PhysRevB.108.214512

35. Bhattacharyya A, Adroja D, Feng Y, Das D, Biswas PK, Das T, et al. μSR study of unconventional pairing symmetry in the quasi-1D $Na_2Cr_3As_3$ superconductor. *Magnetochemistry* (2023) 9:70. doi:10.3390/magnetochemistry9030070

36. Steppke A, Zhao L, Barber ME, Scaffidi T, Jerzembeck F, Rosner H, et al. Strong peak in T_c of Sr_2RuO_4 under uniaxial pressure. *Science* (2017) 355:eaaf9398. doi:10.1126/science.aaf9398

37. Li YS, Kikugawa N, Sokolov DA, Jerzembeck F, Gibbs AS, Maeno Y, et al. High-sensitivity heat-capacity measurements on Sr_2RuO_4 under uniaxial pressure. *Proc Natl Acad Sci USA* (2021) 118:e2020492118. doi:10.1073/pnas.2020492118

38. Rosa PFS, Weiland A, Fender SS, Scott BL, Ronning F, Thompson JD, et al. Single thermodynamic transition at 2 K in superconducting UTe_2 single crystals. *Commun Mater* (2022) 3:33. doi:10.1038/s43246-022-00254-2

39. Girod C, Stevens CR, Huxley A, Bauer ED, Santos FB, Thompson JD, et al. Thermodynamic and electrical transport properties of UTe_2 under uniaxial stress. *Phys Rev B* (2022) 106:L121101. doi:10.1103/PhysRevB.106.L121101

40. Tsuchiura H, Tanaka Y, Ogata M, Kashiwaya S. Local magnetic moments around a nonmagnetic impurity in the two-dimensional $t-J$ model. *Phys Rev B* (2001) 64: 140501. doi:10.1103/PhysRevB.64.140501

41. Wang Z, Lee PA. Local moment formation in the superconducting state of a doped Mott insulator. *Phys Rev Lett* (2002) 89:217002. doi:10.1103/PhysRevLett.89.217002

42. Zhu JX, Martin I, Bishop AR. Spin and charge order around vortices and impurities in high-T_c superconductors. *Phys Rev Lett* (2002) 89:067003. doi:10.1103/PhysRevLett.89.067003

43. Chen Y, Ting CS. States of local moment induced by nonmagnetic impurities in cuprate superconductors. *Phys Rev Lett* (2004) 92:077203. doi:10.1103/PhysRevLett.92.077203

44. Andersen BM, Hirschfeld PJ, Kampf AP, Schmid M. Disorder-induced static antiferromagnetism in cuprate superconductors. *Phys Rev Lett* (2007) 99:147002. doi:10.1103/PhysRevLett.99.147002

45. Harter JW, Andersen BM, Bobroff J, Gabay M, Hirschfeld PJ. Antiferromagnetic correlations and impurity broadening of NMR linewidths in cuprate superconductors. *Phys Rev B* (2007) 75:054520. doi:10.1103/PhysRevB.75.054520

46. Andersen BM, Graser S, Hirschfeld PJ. Disorder-induced freezing of dynamical spin fluctuations in underdoped cuprate superconductors. *Phys Rev Lett* (2010) 105: 147002. doi:10.1103/PhysRevLett.105.147002

47. Lee WC, Zhang SC, Wu C. Pairing state with a time-reversal symmetry breaking in FeAs-based superconductors. *Phys Rev Lett* (2009) 102:217002. doi:10.1103/PhysRevLett.102.217002

48. Garaud J, Babaev E. Domain walls and their experimental signatures in $s+is$ superconductors. *Phys Rev Lett* (2014) 112:017003. doi:10.1103/PhysRevLett.112.017003

49. Maiti S, Sigrist M, Chubukov A. Spontaneous currents in a superconductor with $s+is$ symmetry. *Phys Rev B* (2015) 91:161102. doi:10.1103/PhysRevB.91.161102

50. Lin SZ, Maiti S, Chubukov A. Distinguishing between $s+id$ and $s+is$ pairing symmetries in multiband superconductors through spontaneous magnetization pattern induced by a defect. *Phys Rev B* (2016) 94:064519. doi:10.1103/PhysRevB.94.064519

51. Garaud J, Silaev M, Babaev E. Thermoelectric signatures of time-reversal symmetry breaking states in multiband superconductors. *Phys Rev Lett* (2016) 116: 097002. doi:10.1103/PhysRevLett.116.097002

52. Benfenati A, Barkman M, Winyard T, Wormald A, Speight M, Babaev E. Magnetic signatures of domain walls in $s+is$ and $s+id$ superconductors: observability and what that can tell us about the superconducting order parameter. *Phys Rev B* (2020) 101: 054507. doi:10.1103/PhysRevB.101.054507

53. Roig M, Rømer AT, Hirschfeld PJ, Andersen BM. Revisiting superconductivity in the extended one-band Hubbard model: pairing via spin and charge fluctuations. *Phys Rev B* (2022) 106:214530. doi:10.1103/PhysRevB.106.214530

54. Yerin Y, Drechsler SL, Cuoco M, Petrillo C. Magneto-topological transitions in multicomponent superconductors. *Phys Rev B* (2022) 106:054517. doi:10.1103/PhysRevB.106.054517

55. Li ZX, Kivelson SA, Lee DH. Superconductor-to-metal transition in overdoped cuprates. *npj Quan Mater* (2021) 6:36. doi:10.1038/s41535-021-00335-4

56. Breiø CN, Hirschfeld PJ, Andersen BM. Supercurrents and spontaneous time-reversal symmetry breaking by nonmagnetic disorder in unconventional superconductors. *Phys Rev B* (2022) 105:014504. doi:10.1103/PhysRevB.105.014504

57. Willa R, Hecker M, Fernandes RM, Schmalian J. Inhomogeneous time-reversal symmetry breaking in Sr_2RuO_4. *Phys Rev B* (2021) 104:024511. doi:10.1103/PhysRevB.104.024511

58. Breiø CN, Kreisel A, Roig M, Hirschfeld PJ, Andersen BM. Time-reversal symmetry breaking from lattice dislocations in superconductors. *Phys Rev B* (2024) 109:014505. doi:10.1103/PhysRevB.109.014505

59. Ying YA, Staley NE, Xin Y, Sun K, Cai X, Fobes D, et al. Enhanced spin-triplet superconductivity near dislocations in Sr_2RuO_4. *Nat Commun* (2013) 4:2596. doi:10.1038/ncomms3596

60. Graf MJ, Balatsky AV. Identifying the pairing symmetry in the Sr_2RuO_4 superconductor. *Phys Rev B* (2000) 62:9697–702. doi:10.1103/PhysRevB.62.9697

61. Kotetes P, Sura HOM, Andersen BM. Anatomy of spin and current generation from magnetization gradients in topological insulators and Rashba metals. *Phys Rev B* (2023) 108:155310. doi:10.1103/PhysRevB.108.155310

62. Agterberg DF, Barzykin V, Gor'kov LP. Conventional mechanisms for exotic superconductivity. *Phys Rev B* (1999) 60:14868–71. doi:10.1103/PhysRevB.60.14868

63. Bhattacharyya A, Lees MR, Panda K, Ferreira PP, Dorini TT, Gaudry E, et al. Nodeless time-reversal symmetry breaking in the centrosymmetric superconductor $Sc_5Co_4Si_{10}$ probed by muon-spin spectroscopy. *Phys Rev Mater* (2022) 6:064802. doi:10.1103/PhysRevMaterials.6.064802

64. Stanev V, Tešanović Z. Three-band superconductivity and the order parameter that breaks time-reversal symmetry. *Phys Rev B* (2010) 81:134522. doi:10.1103/PhysRevB.81.134522

65. Carlström J, Garaud J, Babaev E. Length scales, collective modes, and type-1.5 regimes in three-band superconductors. *Phys Rev B* (2011) 84:134518. doi:10.1103/PhysRevB.84.134518

66. Maiti S, Chubukov AV. $s+is$ state with broken time-reversal symmetry in Fe-based superconductors. *Phys Rev B* (2013) 87:144511. doi:10.1103/PhysRevB.87.144511

67. Clepkens J, Lindquist AW, Kee HY. Shadowed triplet pairings in Hund's metals with spin-orbit coupling. *Phys Rev Res* (2021) 3:013001. doi:10.1103/PhysRevResearch.3.013001

68. Khodas M, Chubukov AV. Interpocket pairing and gap symmetry in Fe-based superconductors with only electron pockets. *Phys Rev Lett* (2012) 108:247003. doi:10.1103/PhysRevLett.108.247003

69. Shishidou T, Suh HG, Brydon PMR, Weinert M, Agterberg DF. Topological band and superconductivity in UTe_2. *Phys Rev B* (2021) 103:104504. doi:10.1103/PhysRevB.103.104504

70. Volovik G, Gor'kov L. Superconducting classes in heavy-fermion systems. *Eksp Teor Fiz* (1985) 88:1412.

71. Annett JF. Symmetry of the order parameter for high-temperature superconductivity. *Adv Phys* (1990) 39:83–126. doi:10.1080/00018739000101481

72. Sigrist M, Ueda K. Phenomenological theory of unconventional superconductivity. *Rev Mod Phys* (1991) 63:239–311. doi:10.1103/RevModPhys.63.239

73. Graser S, Maier TA, Hirschfeld PJ, Scalapino DJ. Near-degeneracy of several pairing channels in multiorbital models for the Fe pnictides. *New J Phys* (2009) 11: 025016. doi:10.1088/1367-2630/11/2/025016

74. Rømer AT, Kreisel A, Eremin I, Malakhov MA, Maier TA, Hirschfeld PJ, et al. Pairing symmetry of the one-band Hubbard model in the paramagnetic weak-coupling limit: a numerical RPA study. *Phys Rev B* (2015) 92:104505. doi:10.1103/PhysRevB.92.104505

75. Rømer AT, Maier TA, Kreisel A, Eremin I, Hirschfeld PJ, Andersen BM. Pairing in the two-dimensional Hubbard model from weak to strong coupling. *Phys Rev Res* (2020) 2:013108. doi:10.1103/PhysRevResearch.2.013108

76. Kreisel A, Hirschfeld PJ, Andersen BM. On the remarkable superconductivity of FeSe and its close cousins. *Symmetry* (2020) 12:1402. doi:10.3390/sym12091402

77. Røising HS, Geier M, Kreisel A, Andersen BM. Thermodynamic transitions and topology of spin-triplet superconductivity: application to UTe_2. *Phys Rev B* (2024) 109: 054521. doi:10.1103/PhysRevB.109.054521

78. Mandal M, Kataria A, Patra C, Singh D, Biswas PK, Hillier AD, et al. Time-reversal symmetry breaking in frustrated superconductor Re_2Hf. *Phys Rev B* (2022) 105:094513. doi:10.1103/PhysRevB.105.094513

79. Matsumoto M, Sigrist M. Quasiparticle states near the surface and the domain wall in a $p_x \pm ip_y$-wave superconductor. *J Phys Soc Jpn* (1999) 68:994–1007. doi:10.1143/JPSJ.68.994

80. Stone M, Roy R. Edge modes, edge currents, and gauge invariance in p_x+ip_y superfluids and superconductors. *Phys Rev B* (2004) 69:184511. doi:10.1103/PhysRevB.69.184511

81. Watashige T, Tsutsumi Y, Hanaguri T, Kohsaka Y, Kasahara S, Furusaki A, et al. Evidence for time-reversal symmetry breaking of the superconducting state near twin-boundary interfaces in FeSe revealed by scanning tunneling spectroscopy. *Phys Rev X* (2015) 5:031022. doi:10.1103/PhysRevX.5.031022

82. Håkansson M, Löfwander T, Fogelström M. Spontaneously broken time-reversal symmetry in high-temperature superconductors. *Nat Phys* (2015) 11:755–60. doi:10.1038/nphys3383

83. Silaev M, Garaud J, Babaev E. Phase diagram of dirty two-band superconductors and observability of impurity-induced *s* + *is* state. *Phys Rev B* (2017) 95:024517. doi:10.1103/PhysRevB.95.024517

84. Holmvall P, Vorontsov AB, Fogelström M, Löfwander T. Broken translational symmetry at edges of high-temperature superconductors. *Nat Commun* (2018) 9:2190. doi:10.1038/s41467-018-04531-y

85. Song SY, Martiny JHJ, Kreisel A, Andersen BM, Seo J. Visualization of local magnetic moments emerging from impurities in hund's metal states of FeSe. *Phys Rev Lett* (2020) 124:117001. doi:10.1103/PhysRevLett.124.117001

86. Wennerdal NW, Ask A, Holmvall P, Löfwander T, Fogelström M. Breaking time-reversal and translational symmetry at edges of *d*-wave superconductors: microscopic theory and comparison with quasiclassical theory. *Phys Rev Res* (2020) 2:043198. doi:10.1103/PhysRevResearch.2.043198

87. Stanev V, Koshelev AE. Complex state induced by impurities in multiband superconductors. *Phys Rev B* (2014) 89:100505. doi:10.1103/PhysRevB.89.100505

88. Alloul H, Bobroff J, Gabay M, Hirschfeld PJ. Defects in correlated metals and superconductors. *Rev Mod Phys* (2009) 81:45–108. doi:10.1103/RevModPhys.81.45

89. Schmid M, Andersen BM, Kampf AP, Hirschfeld PJ. d-Wave superconductivity as a catalyst for antiferromagnetism in underdoped cuprates. *New J Phys* (2010) 12:053043. doi:10.1088/1367-2630/12/5/053043

90. Gastiasoro MN, Hirschfeld PJ, Andersen BM. Impurity states and cooperative magnetic order in Fe-based superconductors. *Phys Rev B* (2013) 88:220509. doi:10.1103/PhysRevB.88.220509

91. Martiny JHJ, Gastiasoro MN, Vekhter I, Andersen BM. Impurity-induced antiferromagnetic order in Pauli-limited nodal superconductors: application to heavy-fermion $CeCoIn_5$. *Phys Rev B* (2015) 92:224510. doi:10.1103/PhysRevB.92.224510

92. Martiny JHJ, Kreisel A, Andersen BM. Theoretical study of impurity-induced magnetism in FeSe. *Phys Rev B* (2019) 99:014509. doi:10.1103/PhysRevB.99.014509

93. Chen W, Andersen BM, Hirschfeld PJ. Theory of resistivity upturns in metallic cuprates. *Phys Rev B* (2009) 80:134518. doi:10.1103/PhysRevB.80.134518

94. Castro Neto AH, Castilla G, Jones BA. Non-fermi liquid behavior and griffiths phase in *f* -electron compounds. *Phys Rev Lett* (1998) 81:3531–4. doi:10.1103/PhysRevLett.81.3531

95. Millis AJ, Morr DK, Schmalian J. Local defect in metallic quantum critical systems. *Phys Rev Lett* (2001) 87:167202. doi:10.1103/PhysRevLett.87.167202

96. Das J, Mahajan AV, Bobroff J, Alloul H, Alet F, Sørensen ES. Comparison of *S* = 0 and S=1/2 impurities in the Haldane chain compound Y_2BaNiO_5. *Phys Rev B* (2004) 69:144404. doi:10.1103/PhysRevB.69.144404

97. Chang J, Niedermayer C, Gilardi R, Christensen NB, Rønnow HM, McMorrow DF, et al. Tuning competing orders in $La_{2-x}Sr_xCuO_4$ cuprate superconductors by the application of an external magnetic field. *Phys Rev B* (2008) 78:104525. doi:10.1103/PhysRevB.78.104525

98. Kimura H, Kofu M, Matsumoto Y, Hirota K. Novel in-gap spin state in Zn-doped $La_{1.85}Sr_{0.15}CuO_4$. *Phys Rev Lett* (2003) 91:067002. doi:10.1103/PhysRevLett.91.067002

99. Rosenthal EP. *Visualizing nematicity in the pnictides with scanning tunneling spectroscopy*. Columbia University (2015). Ph.D. thesis. doi:10.7916/D8N29W34

100. Shender EF, Kivelson SA. Dilution-induced order in quasi-one-dimensional quantum antiferromagnets. *Phys Rev Lett* (1991) 66:2384–7. doi:10.1103/PhysRevLett.66.2384

101. Andersen BM, Hirschfeld PJ. Breakdown of universal transport in correlated *d*-wave superconductors. *Phys Rev Lett* (2008) 100:257003. doi:10.1103/PhysRevLett.100.257003

102. Christensen RB, Hirschfeld PJ, Andersen BM. Two routes to magnetic order by disorder in underdoped cuprates. *Phys Rev B* (2011) 84:184511. doi:10.1103/PhysRevB.84.184511

103. Schmid M, Loder F, Kampf AP, Kopp T. Disorder induced stripes in d-wave superconductors. *New J Phys* (2013) 15:073049. doi:10.1088/1367-2630/15/7/073049

104. Kivelson SA, Bindloss IP, Fradkin E, Oganesyan V, Tranquada JM, Kapitulnik A, et al. How to detect fluctuating stripes in the high-temperature superconductors. *Rev Mod Phys* (2003) 75:1201–41. doi:10.1103/RevModPhys.75.1201

105. Vojta M. Lattice symmetry breaking in cuprate superconductors: stripes, nematics, and superconductivity. *Adv Phys* (2009) 58:699–820. doi:10.1080/00018730903122242

106. Lake B, Rønnow HM, Christensen NB, Aeppli G, Lefmann K, McMorrow DF, et al. Antiferromagnetic order induced by an applied magnetic field in a high-temperature superconductor. *Nature* (2002) 415:299–302. doi:10.1038/415299a

107. Khaykovich B, Lee YS, Erwin RW, Lee SH, Wakimoto S, Thomas KJ, et al. Enhancement of long-range magnetic order by magnetic field in superconducting La_2CuO_{4+y}. *Phys Rev B* (2002) 66:014528. doi:10.1103/PhysRevB.66.014528

108. Rømer AT, Chang J, Christensen NB, Andersen BM, Lefmann K, Mähler L, et al. Glassy low-energy spin fluctuations and anisotropy gap in $La_{1.88}Sr_{0.12}CuO_4$. *Phys Rev B* (2013) 87:144513. doi:10.1103/PhysRevB.87.144513

109. Watanabe I, Adachi T, Takahashi K, Yairi S, Koike Y, Nagamine K. Muon-spin-relaxation study of the effect of nonmagnetic impurities on the Cu-spin fluctuations in $La_{2-x}Sr_xCu_{1-y}Zn_yO_4$ around $x = 0.115$. *Phys Rev B* (2002) 65:180516. doi:10.1103/PhysRevB.65.180516

110. Khaykovich B, Wakimoto S, Birgeneau RJ, Kastner MA, Lee YS, Smeibidl P, et al. Field-induced transition between magnetically disordered and ordered phases in underdoped $La_{2-x}Sr_xCuO_4$. *Phys Rev B* (2005) 71:220508. doi:10.1103/PhysRevB.71.220508

111. Niedermayer C, Bernhard C, Blasius T, Golnik A, Moodenbaugh A, Budnick JI. Common phase diagram for antiferromagnetism in $la_{2-x}Sr_xCuO_4$ and $Y_{1-x}Ca_xBa_2Cu_3O_6$ as seen by muon spin rotation. *Phys Rev Lett* (1998) 80:3843–6. doi:10.1103/PhysRevLett.80.3843

112. Panagopoulos C, Tallon JL, Rainford BD, Xiang T, Cooper JR, Scott CA. Evidence for a generic quantum transition in high-T_c cuprates. *Phys Rev B* (2002) 66:064501. doi:10.1103/PhysRevB.66.064501

113. Miller RI, Kiefl RF, Brewer JH, Callaghan FD, Sonier JE, Liang R, et al. Coexistence of magnetism and superconductivity in ultraclean underdoped $YBa_2Cu_3O_{6.37}$. *Phys Rev B* (2006) 73:144509. doi:10.1103/PhysRevB.73.144509

114. Haug D, Hinkov V, Suchaneck A, Inosov DS, Christensen NB, Niedermayer C, et al. Magnetic-field-enhanced incommensurate magnetic order in the underdoped high-temperature superconductor $YBa_2Cu_3O_{6.45}$. *Phys Rev Lett* (2009) 103:017001. doi:10.1103/PhysRevLett.103.017001

115. Pan SH, Hudson EW, Lang KM, Eisaki H, Uchida S, Davis JC. Imaging the effects of individual zinc impurity atoms on superconductivity in $Bi_2Sr_2CaCu_2O_{8\delta}$. *Nature* (2000) 403:746–50. doi:10.1038/35001534

116. Sundar S, Azari N, Goeks MR, Gheidi S, Abedi M, Yakovlev M, et al. Ubiquitous spin freezing in the superconducting state of UTe_2. *Comm Phys* (2023) 6:24. doi:10.1038/s42005-023-01146-8

117. Azari N, Yakovlev M, Rye N, Dunsiger SR, Sundar S, Bordelon MM, et al. Absence of spontaneous magnetic fields due to time-reversal symmetry breaking in bulk superconducting UTe_2. *Phys Rev Lett* (2023) 131:226504. doi:10.1103/PhysRevLett.131.226504

118. Inosov DS, Friemel G, Park JT, Walters AC, Texier Y, Laplace Y, et al. Possible realization of an antiferromagnetic Griffiths phase in $Ba(Fe_{1-x}Mn_x)_2As_2$. *Phys Rev B* (2013) 87:224425. doi:10.1103/PhysRevB.87.224425

119. Gastiasoro MN, Andersen BM. Enhancement of magnetic stripe order in iron-pnictide superconductors from the interaction between conduction electrons and magnetic impurities. *Phys Rev Lett* (2014) 113:067002. doi:10.1103/PhysRevLett.113.067002

120. Urbano RR, Young BL, Curro NJ, Thompson JD, Pham LD, Fisk Z. Interacting antiferromagnetic droplets in quantum critical $CeCoIn_5$. *Phys Rev Lett* (2007) 99:146402. doi:10.1103/PhysRevLett.99.146402

121. Li Y, Sapkota A, Lozano PM, Du Z, Li H, Wu Z, et al. Strongly overdoped $La_{2-x}Sr_xCuO_4$: evidence for Josephson-coupled grains of strongly correlated superconductor. *Phys Rev B* (2022) 106:224515. doi:10.1103/PhysRevB.106.224515

122. Maier TA, Karakuzu S, Scalapino DJ. Overdoped end of the cuprate phase diagram. *Phys Rev Res* (2020) 2:033132. doi:10.1103/PhysRevResearch.2.033132

123. Balatsky AV, Vekhter I, Zhu JX. Impurity-induced states in conventional and unconventional superconductors. *Rev Mod Phys* (2006) 78:373–433. doi:10.1103/RevModPhys.78.373

124. Holbæk SC, Christensen MH, Kreisel A, Andersen BM. Unconventional superconductivity protected from disorder on the kagome lattice. *Phys Rev B* (2023) 108:144508. doi:10.1103/PhysRevB.108.144508

125. Pal M, Bettmann L, Kreisel A, Hirschfeld PJ. Magnetic anisotropy from strain-induced dislocations in correlated electron systems. *Phys. Rev. B* (2021) 103:245132. doi:10.1103/PhysRevB.103.245132

126. Pal M, Kreisel A, Hirschfeld PJ. Topological superconductivity driven by correlations and linear defects in multiband superconductors. *Phys. Rev. B* (2023) 107:134503. doi:10.1103/PhysRevB.107.134503

127. Ruderman MA, Kittel C. Indirect exchange coupling of nuclear magnetic moments by conduction electrons. *Phys Rev* (1954) 96:99–102. doi:10.1103/PhysRev.96.99

128. Kasuya T. A theory of metallic ferro- and antiferromagnetism on zener's model. *Prog Theor Phys* (1956) 16:45–57. doi:10.1143/PTP.16.45

129. Yosida K. Magnetic properties of Cu-Mn alloys. *Phys Rev* (1957) 106:893–8. doi:10.1103/PhysRev.106.893

130. Abrikosov A. (1988).*Fundamentals of the theory of metals*. Fundamentals of the Theory of Metals (North-Holland

131. Aristov DN, Maleyev SV, Yashenkin AG. RKKY interaction in layered superconductors with anisotropic pairing. *Z für Physik B Condensed Matter* (1997) 102:467–71. doi:10.1007/s002570050313

132. Galitski VM, Larkin AI. Spin glass versus superconductivity. *Phys Rev B* (2002) 66:064526. doi:10.1103/PhysRevB.66.064526

133. Schecter M, Flensberg K, Christensen MH, Andersen BM, Paaske J. Self-organized topological superconductivity in a Yu-Shiba-Rusinov chain. *Phys Rev B* (2016) 93:140503. doi:10.1103/PhysRevB.93.140503

134. Yu L. Bound state in superconductors with paramagnetic impurities. *Acta Physica Sinica* (1965) 21:75–91. doi:10.7498/aps.21.75

135. Shiba H. Classical spins in superconductors. *Prog Theor Phys* (1968) 40:435–51. doi:10.1143/PTP.40.435

136. Rusinov A. Theory of gapless superconductivity in alloys containing paramagnetic impurities. *Sov Phys JETP* (1969) 29:1101–6.

137. Yao NY, Glazman LI, Demler EA, Lukin MD, Sau JD. Enhanced antiferromagnetic exchange between magnetic impurities in a superconducting host. *Phys Rev Lett* (2014) 113:087202. doi:10.1103/PhysRevLett.113.087202

138. Hoffman S, Klinovaja J, Meng T, Loss D. Impurity-induced quantum phase transitions and magnetic order in conventional superconductors: competition between bound and quasiparticle states. *Phys Rev B* (2015) 92:125422. doi:10.1103/PhysRevB.92.125422

139. Fittipaldi R, Hartmann R, Mercaldo MT, Komori S, Bjørlig A, Kyung W, et al. Unveiling unconventional magnetism at the surface of Sr_2RuO_4. *Nat Commun* (2021) 12:5792. doi:10.1038/s41467-021-26020-5

140. Blundell S, De Renzi R, Lancaster T, Pratt F. *Muon spectroscopy: an introduction*. Oxford University Press (2022).

141. Sonier JE, Brewer JH, Kiefl RF. μSR studies of the vortex state in type-II superconductors. *Rev Mod Phys* (2000) 72:769–811. doi:10.1103/RevModPhys.72.769

142. Khasanov R, Guguchia Z. Probing the multi gap behavior within '11' and '122' families of iron based superconductors: the muon-spin rotation studies. *Superconductor Sci Technol* (2015) 28:034003. doi:10.1088/0953-2048/28/3/034003

143. Curran PJ, Bending SJ, Gibbs AS, Mackenzie AP. The search for spontaneous edge currents in Sr_2RuO_4 mesa structures with controlled geometrical shapes. *Scientific Rep* (2023) 13:12652. doi:10.1038/s41598-023-39590-9

144. Mueller E, Iguchi Y, Watson C, Hicks CW, Maeno Y, Moler KA. Constraints on a split superconducting transition under uniaxial strain in Sr_2RuO_4 from scanning SQUID microscopy. *Phys Rev B* (2023) 108:144501. doi:10.1103/PhysRevB.108.144501

145. Huddart BM, Onuorah IJ, Isah MM, Bonfà P, Blundell SJ, Clark SJ, et al. Intrinsic nature of spontaneous magnetic fields in superconductors with time-reversal symmetry breaking. *Phys Rev Lett* (2021) 127:237002. doi:10.1103/PhysRevLett.127.237002

146. Blundell SJ, Lancaster T. DFT + μ: density functional theory for muon site determination. *Appl Phys Rev* (2023) 10:021316. doi:10.1063/5.0149080

147. Miyake K, Tsuruta A. Theory for intrinsic magnetic field in chiral superconductor measured by muSR: case of Sr_2RuO_4. arXiv e-prints (2017) 1709.09388. doi:10.48550/arXiv.1709.09388

148. Schemm E, Levenson-Falk E, Kapitulnik A. Polar Kerr effect studies of time reversal symmetry breaking states in heavy fermion superconductors. *Physica C: Superconductivity its Appl* (2017) 535:13–9. doi:10.1016/j.physc.2016.11.012

149. Hayes IM, Wei DS, Metz T, Zhang J, Eo YS, Ran S, et al. Multicomponent superconducting order parameter in UTe_2. *Science* (2021) 373:797–801. doi:10.1126/science.abb0272

150. Ajeesh MO, Bordelon M, Girod C, Mishra S, Ronning F, Bauer ED, et al. Fate of time-reversal symmetry breaking in UTe_2. *Phys Rev X* (2023) 13:041019. doi:10.1103/PhysRevX.13.041019

151. Xia J, Maeno Y, Beyersdorf PT, Fejer MM, Kapitulnik A. High resolution polar Kerr effect measurements of Sr_2RuO_4: evidence for broken time-reversal symmetry in the superconducting state. *Phys Rev Lett* (2006) 97:167002. doi:10.1103/PhysRevLett.97.167002

152. Cho W, Kivelson SA. Necessity of time-reversal symmetry breaking for the polar Kerr effect in linear response. *Phys Rev Lett* (2016) 116:093903. doi:10.1103/PhysRevLett.116.093903

153. Yip SK, Sauls JA. Circular dichroism and birefringence in unconventional superconductors. *J Low Temperature Phys* (1992) 86:257–90. doi:10.1007/BF01151804

154. Taylor E, Kallin C. Intrinsic Hall effect in a multiband chiral superconductor in the absence of an external magnetic field. *Phys Rev Lett* (2012) 108:157001. doi:10.1103/PhysRevLett.108.157001

155. Goryo J. Impurity-induced polar Kerr effect in a chiral *p*-wave superconductor. *Phys Rev B* (2008) 78:060501. doi:10.1103/PhysRevB.78.060501

156. Lutchyn RM, Nagornykh P, Yakovenko VM. Frequency and temperature dependence of the anomalous ac Hall conductivity in a chiral $p_x + ip_y$ superconductor with impurities. *Phys Rev B* (2009) 80:104508. doi:10.1103/PhysRevB.80.104508

157. Liu HT, Chen W, Huang W. Impact of random impurities on the anomalous Hall effect in chiral superconductors. *Phys Rev B* (2023) 107:224517. doi:10.1103/PhysRevB.107.224517

158. Palle G, Hicks C, Valenti R, Hu Z, Li YS, Rost A, et al. Constraints on the superconducting state of Sr_2RuO_4 from elastocaloric measurements. *Phys Rev B* (2023) 108:094516. doi:10.1103/PhysRevB.108.094516

159. Theuss F, Shragai A, Grissonnanche G, Hayes IM, Saha SR, Eo YS, et al. Single-component superconductivity in UTe_2 at ambient pressure. *arXiv e-prints* (2023):10938. doi:10.48550/arXiv.2307.10938

frontiers | Frontiers in Physics

TYPE Original Research
PUBLISHED 04 June 2024
DOI 10.3389/fphy.2024.1393229

OPEN ACCESS

EDITED BY
James Avery Sauls,
Louisiana State University, United States

REVIEWED BY
William Paul Halperin,
Northwestern University, United States
Vesna Mitrovic,
Brown University, United States

*CORRESPONDENCE
N. J. Curro,
njcurro@ucdavis.edu

RECEIVED 28 February 2024
ACCEPTED 13 May 2024
PUBLISHED 04 June 2024

CITATION
Nian Y-H, Vinograd I, Chaffey C, Li Y, Zic MP, Massat P, Singh RRP, Fisher IR and Curro NJ (2024), Nuclear magnetic resonance studies in a model transverse field Ising system.
Front. Phys. 12:1393229.
doi: 10.3389/fphy.2024.1393229

Nuclear magnetic resonance studies in a model transverse field Ising system

Y.-H. Nian[1], I. Vinograd[1], C. Chaffey[1], Y. Li[2], M. P. Zic[3,4], P. Massat[2], R. R. P. Singh[1], I. R. Fisher[2] and N. J. Curro[1]*

[1]Department of Physics and Astronomy, University of California Davis, Davis, CA, United States, [2]Geballe Laboratory for Advanced Materials and Department of Applied Physics, Stanford University, Stanford, CA, United States, [3]Geballe Laboratory for Advanced Materials, Stanford University, Stanford, CA, United States, [4]Department of Physics, Stanford University, Stanford, CA, United States

The suppression of ferroquadrupolar order in $TmVO_4$ in a magnetic field is well-described by the transverse field Ising model, enabling detailed studies of critical dynamics near the quantum phase transition. We describe nuclear magnetic resonance measurements in pure and Y-doped single crystals. The non-Kramers nature of the ground state doublet leads to a unique form of the hyperfine coupling that exclusively probes the transverse field susceptibility. Our results show that this quantity diverges at the critical field, in contrast to the mean-field prediction. Furthermore, we find evidence for quantum critical fluctuations present near Tm-rich regions in Y-doped crystals at levels beyond which long-range order is suppressed, suggesting the presence of quantum Griffiths phases.

KEYWORDS

nuclear magnetic resonance, quantum criticality, transverse field Ising model, Griffiths phases, hyperfine coupling, quantum fidelity

1 Introduction

Unconventional superconductivity tends to emerge in the vicinity of a quantum critical point (QCP), where some form of long-range ordered state is continually suppressed to $T = 0$ [1–9]. This observation suggests that there may be an important relationship between the superconducting pairing mechanism and the strong quantum fluctuations associated with the QCP, however there are major challenges to understanding the fundamental physics at play in these systems. In practice various approaches can be utilized to tune the ordered state to the QCP. Hydrostatic pressure or magnetic field are thermodynamic variables that are homogeneous throughout the material and can be varied continuously. Doping, on the other hand, offers a convenient method to apply "chemical pressure" or introduce charge carriers, but can introduce electronic heterogeneity at the nanoscale which can complicate interpretation [10, 11]. In such cases it can be difficult to disentangle what experimental observations to ascribe to fundamental properties of a quantum phase transition versus extrinsic effects arising from the long-range effects of the dopants.

In order to better understand the influence of doping in strongly interacting system near a quantum phase transition, it is valuable to study a model system in the absence of superconductivity. $TmVO_4$ is as material that has attracted interest recently because its low temperature properties are well-described by the transverse field Ising model (TFIM), an archetype of quantum criticality [12, 13]. $TmVO_4$ exhibits long-range ferroquadrupolar order in which the Tm $4f$ orbitals spontaneously align in the same direction, as illustrated in Figure 1. The Tm^{3+} ions ($4f^{12}$ with $L = 5$, $S = 1$, $J = 6$) experience a tetragonal crystal field

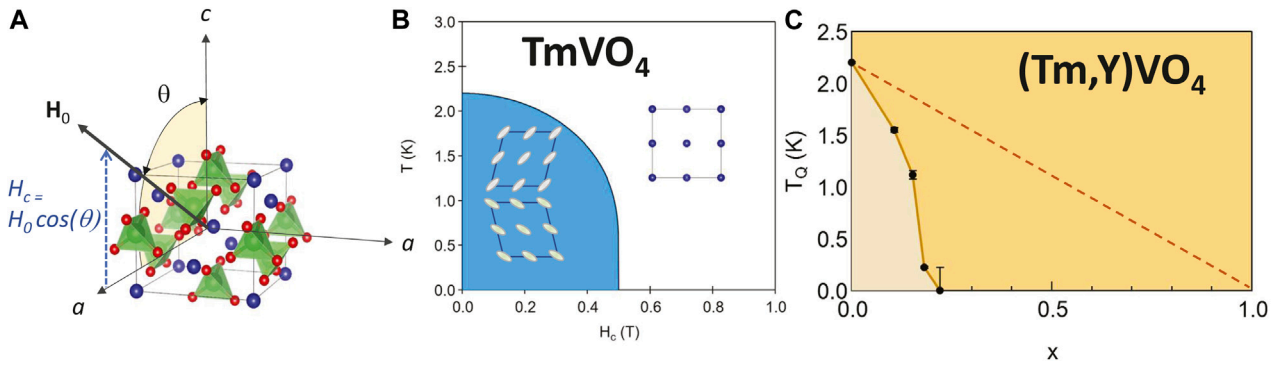

FIGURE 1
(A) Crystal structure of $TmVO_4$ (*I*41/*amd*) with Tm atoms in blue, V atoms lie at the center of green tetrahedra, and oxygen atoms in red. For the studies discussed here, the magnetic field, $\mathbf{H}_0$, was rotated in the *ac*-plane, with an angle θ between $\mathbf{H}_0$ and the *c* axis. The projection of the field along the *c*-axis is $H_0 \cos\theta$. **(B)** Schematic phase diagram of $TmVO_4$ as a function of magnetic field H_c along the *c*-axis, illustrating the B_{2g} orthorhombic distortion in the ferroquadrupolar state. **(C)** Phase diagram for $Tm_{1-x}Y_xVO_4$, reproduced from [14]. The dashed line represents the mean-field result expected purely from dilution.

interaction, and the ground state is well separated by a gap of ~ 77 K to the lowest excited state [15, 16]. The ground state is a non-Kramers doublet, so the first order Zeeman interaction vanishes for in-plane fields (i.e., $g_c \sim 10$ while $g_a = g_b = 0$). This doublet can be described by a spin-1/2 pseudospin in which one component, σ_z, corresponds to a magnetic dipole moment oriented along the *c*-axis, while the other two components σ_x and σ_y correspond to electric quadrupole moments with B_{2g} (xy) and B_{1g} ($x^2 - y^2$) symmetry, respectively [17]. The two quadrupole moments couple bilinearly to lattice strains $\varepsilon_{xx} - \varepsilon_{yy}$ and ε_{xy}, which gives rise to an effective interaction between the moments and leads to a cooperative Jahn-Teller distortion at a temperature, T_Q [18]. $TmVO_4$ spontaneously undergoes a tetragonal to orthorhombic distortion with B_{2g} symmetry below $T_Q = 2.15$ K with orthorhombicity $\delta \approx 0.01$, as illustrated in Figure 1B. Because there are two distinct orientations of the quadrupolar moments, the ferroquadrupolar order has Ising symmetry that can be described as a coupling between neighboring pseudospins. On the other hand, a magnetic field oriented along the *c*-axis couples to the pseudospin in a direction that is transverse to the ferroquadrupolar order [19]. This field mixes the two degenerate ground state quadrupolar states, enhancing the fluctuations of the pseudospins and suppressing T_Q at a quantum phase transition with critical field $H_c^* \approx 0.5$ T [12]. This interpretation has been strengthened by the recent observation of a quantum critical fan emerging from the QCP that extends to temperatures above T_Q [20].

$LiHoF_4$ is another important material whose physics is well described by the TFIM [21]. There are important differences, however, between $LiHoF_4$ and $TmVO_4$. Although the physics of both systems derives from non-Kramers doublets, the former is a ferromagnet with Ho moments ordering along the *c*-axis, whereas the latter has ferroquadrupolar order with quadrupolar moments ordering in the plane. As a result, the transverse field direction for $LiHoF_4$ is perpendicular to the *c*-axis, whereas in $TmVO_4$ the transverse field direction is parallel to *c*. This fact is crucial for $TmVO_4$ because it also has profound consequences for the hyperfine coupling to neighboring nuclear spins and enables unique measurements of the quantum fluctuations directly. Moreover, since the quadrupolar moments couple to strain fields, long-range order in $TmVO_4$ is particularly sensitive to dopants. Therefore substituting with Y in $TmVO_4$ offers a unique opportunity to investigate how the quantum phase transition changes in response to the disorder and random fields introduced by the dopant atoms.

2 Couplings to non-Kramers doublet

2.1 Lattice interaction

2.1.1 Ground state wavefunctions

The ground state wavefunctions of the Tm in the D_{4h} point group symmetry of the $TmVO_4$ lattice are given by:

$$|\psi_{1,2}\rangle = \alpha_1|\pm 5\rangle + \alpha_2|\pm 1\rangle + \alpha_3|\mp 3\rangle$$

in the $|J_z\rangle$ basis, where the α_i coefficients are determined by the details of the crystal field Hamiltonian [16, 19]. Is is straightforward to show that $J_{x,y}$ operators vanish in the subspace spanned by these states. On the other hand, there are three other operators that do not vanish:

$$J_x^2 - J_y^2 \sim \sigma_x, \quad J_xJ_y + J_yJ_x \sim \sigma_y, \quad \text{and } J_z \sim \sigma_z,$$

where the σ_α are the Pauli matrices. Physically, the first two operators represent quadrupolar moments with B_{1g} and B_{2g} symmetries, respectively, and the third represents a magnetic moment along the *z* direction. The conjugate fields to these moments are strain $\epsilon_{B1g} = \epsilon_{xx} - \epsilon_{yy}$, $\epsilon_{B2g} = \epsilon_{xy}$, and magnetic field H_z, respectively. Here the strain tensor is defined as $\epsilon_{ij} = (\partial u_i/\partial x_j - \partial u_j/\partial x_i)/2$, where $\mathbf{u}(\mathbf{x})$ is the displacement from the equilibrium lattice positions.

2.1.2 Cooperative Jahn-Teller effect

Because the quadrupolar moments have non-uniform charge distributions, they can interact with a strained lattice via a bilinear coupling of the form $-\eta_i\varepsilon_i\sigma_i$, where η_i is an electron-lattice coupling constant. This coupling renormalizes the elastic constant, leading to

a softening in both the B_{1g} and B_{2g} channels, but is strongest for the B_{2g} channel for $TmVO_4$. It can be shown that this leads to an effective coupling between the quadrupolar moments:

$$\mathcal{H}_{ex} = \sum_{l \neq l'} J(l - l')\sigma_y(l)\sigma_y(l') \quad (1)$$

where the sum is over the lattice sites, and $J(l - l')$ is an Ising interaction between the Tm quadrupolar moments [17, 18]. The coupling depends on the details of the lattice, and because it is mediated by strain fields, it can extend well beyond just nearest neighbor sites. This interaction leads to long-range order in the three-dimensional $TmVO_4$ lattice below a temperature $T_Q = 2.15$ K, with finite expectation values of $\pm\langle\sigma_y\rangle$. This ferroquadrupolar order is accompanied by a B_{2g} lattice distortion as illustrated in Figure 1B [22].

2.2 Zeeman interaction

The interaction between a non-Kramers doublet in a tetragonal environment and a magnetic field is given by:

$$\mathcal{H}_Z = g_z\mu_B H_z\sigma_z + \frac{1}{2}(g_J\mu_B)^2 b\left[\left(H_x^2 - H_y^2\right)\sigma_x + 2H_xH_y\sigma_y\right], \quad (2)$$

where $H_{x,y}$ is a magnetic field along the (x, y) direction, $g_J = 7/6$ for Tm^{3+} and g_c and b depend on the crystal field Hamiltonian [23]. These parameters have been measured for $TmVO_4$ to be $g_c = 10.21$ and $b/k_B = 0.082\ K^{-1}$ [16]. Note that **H** couples quadratically in the x and y directions, rather than linearly for a Kramers doublet. A field in the z direction splits the doublet linearly, and acts as a *transverse* field for the Ising interaction in Eq. 1.

2.2.1 Induced moments for perpendicular fields

The Zeeman interaction can also be written as $\mathcal{H}_Z = \mu \cdot \mathbf{H}$, where the magnetic moment along z is $\mu_z = g_{\|}\mu_B\sigma_z$, and the perpendicular fields $H_{x,y}$ can couple with quadrupolar moments giving rise to effective magnetic moments:

$$\mu_{x,y} = \frac{1}{2}(g_J\mu_B)^2 b\left(H_x\sigma_{y,x} \pm H_y\sigma_{x,y}\right).$$

For sufficiently low perpendicular fields, $H_{x,y} \leq 3$ T, the second order Zeeman interaction in the perpendicular direction will be less than $0.1k_BT_Q$, and can be safely ignored. At higher fields, H_x and H_y can also act as either longitudinal or transverse fields for the Ising order, and can in fact be used to detwin the ferroquadrupolar order [24].

2.3 Transverse field Ising model for ferroquadrupolar order

The low temperature degrees of the Tm electronic degrees of freedom are thus captured by the sum $\mathcal{H}_{ex} + \mathcal{H}_Z$, which maps directly to the TFIM:

$$\mathcal{H}_{Tm} = \sum_{l \neq l'} J(l - l')\sigma_y(l)\sigma_y(l') + g_z\mu_B H_c \sum_l \sigma_z(l), \quad (3)$$

where the sum is over the Tm lattice sites. Here we have ignored the small contribution from the perpendicular component of the magnetic field. Mean field theory predicts a QCP for a c-axis field of $T_Q/g_c\mu_B \approx 0.3$ T, which is close to the experimental value of $H_c^* = 0.5$ T. Note that if there is a perpendicular field oriented such that H_x or H_y is zero, the system can still be described by the TFIM, because $\mathcal{H}_Z$ does not couple to the longitudinal order in pseudospin space (σ_y). Rather, there is an effective transverse field in the x-z plane of pseudospin space leading to a different value of the critical field [24].

2.4 Coupling to nuclear spins

2.4.1 Hyperfine coupling to ^{51}V

In most insulators the hyperfine coupling between a localized electron spin and a nearby nucleus arises due to the direct dipolar interaction and can be described as $\mathcal{H}_{hyp} = \mathbf{I} \cdot \mathbb{A} \cdot \mathbf{J}$, where **I** is the nuclear spin, **A** is the (traceless) hyperfine tensor, and **J** is the electron spin. For temperatures well below the crystal field excitations, **J** should be replaced by the ground state pseudospin operators and $\mathbb{A}$ should be renormalized. For a non-Kramers doublet, there can be no coupling along the x or y directions because the magnetic field of the nucleus does not interact with the doublet. Rather, the hyperfine coupling has the form:

$$\mathcal{H}_{hyp} = A_{zz}I_z\sigma_z + C\left(H_xI_x - H_yI_y\right)\sigma_x + C\left(H_xI_y + H_yI_x\right)\sigma_y, \quad (4)$$

where A_{zz} and C are constants [23]. In the absence of magnetic field, there is only a coupling along the z direction, corresponding to the transverse field direction. To determine the values of the coupling C, note that Eq. 4 can be re-written in terms of the effective magnetic moments:

$$\begin{aligned}\mathcal{H}_{hyp} &= \frac{2C}{(g_J\mu_B)^2 b}\left(I_x\mu_x + I_y\mu_y\right) + \frac{A_{zz}}{g_z\mu_B}I_z\mu_z \\ &= \gamma\hbar\left(h_xI_x + h_yI_y + h_zI_z\right),\end{aligned} \quad (5)$$

where h_α are the hyperfine fields at the nucleus created by the Tm moments. Using the measured values of $h_x/\mu_x = -0.0336$ T/μ_B and $h_z/\mu_z = 0.0671$ T/μ_B obtained by comparing the Knight shift versus susceptibility, we can then identify:

$$C = \frac{1}{2}\gamma\hbar(g_J\mu_B)^2 b\left(\frac{h_x}{\mu_x}\right) \approx -0.37\mu\text{K}\Big/\text{T}$$

$$A_{zz} = \gamma\hbar g_z\mu_B\left(\frac{h_z}{\mu_z}\right) \approx 368\mu\text{K}.$$

these values of the hyperfine fields were obtained via direct Knight shift measurements, but agree well with the calculated direct dipolar fields in the $TmVO_4$ lattice [25].

2.4.2 Quadrupolar coupling to ^{51}V

^{51}V has spin $I = 7/2$ and a nuclear quadrupolar moment $Q = 0.052$ barns. Note that this moment is several orders of magnitude smaller than the electronic quadrupolar moment of the Tm 4f orbitals that undergo the ferroquadrupolar ordering at T_Q. Nevertheless, the extended charge distribution of the latter can contribute to the electric field gradient (EFG) tensor at the V nuclear site, which in turn couples to Q. As a result, the nuclear

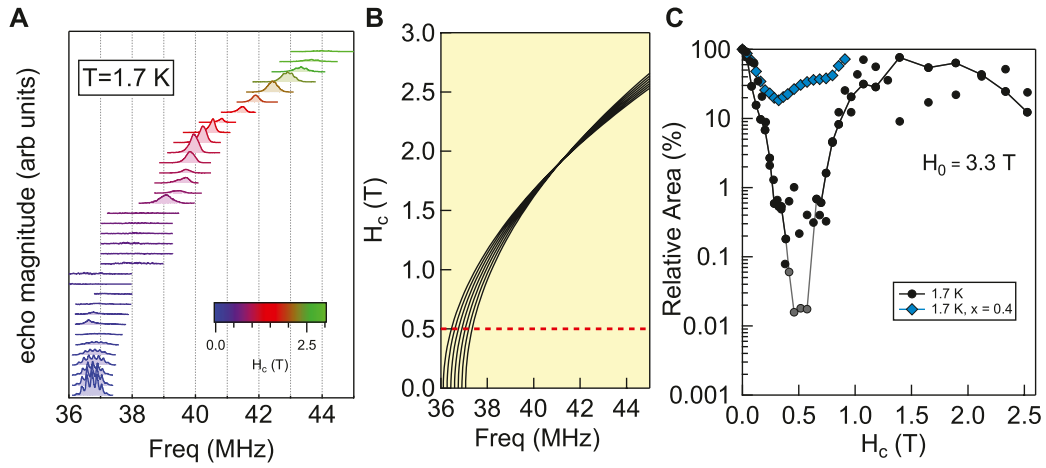

FIGURE 2
(A) Spectra of ^{51}V for several different values of H_c as the crystal is rotated (see Figure 1A). **(B)** Calculated frequencies of the seven transitions as a function of H_c. The transitions merge at the magic angle, and then separate at higher values of H_c. The dashed red line corresponds to the critical field, H_c^*. **(C)** The spectral area versus H_c for several different values of temperature. The blue diamonds correspond to $Tm_{1-x}Y_xVO_4$ with $x = 0.4$.

spins can couple to the pseudospin via the nuclear quadrupolar interaction [23]:

$$\mathcal{H}_Q = B_1\left(I_x^2 - I_y^2\right)\sigma_x + B_2\left(I_xI_y + I_yI_x\right)\sigma_y + P\left[3I_z^2 - I(I+1)\right]\mathbf{1}.$$

Note that $B_2 = B_1$, and corresponds to a 45° rotation of the principal axes of the EFG. The last term, P, is determined by the local charge distribution in the VO_4 tetrahedra, and is independent of the 4f orbitals. The EFG asymmetry parameter is given by $B_1\langle\sigma_x\rangle/P$, and can be measured through detailed spectral measurements as a function of angle in the ordered state. We estimate $P \approx 15\,\mu$K and $B_1 = B_2 \approx 0.22\,\mu$K [24].

Of all the terms in $\mathcal{H}_{hyp} + \mathcal{H}_Q$, A_{zz} is several orders of magnitude larger than any other, even for perpendicular fields of several tesla. Thus the coupling between the ^{51}V and the Tm 4f orbitals is essentially only along the transverse field direction.

2.4.3 Hyperfine coupling to ^{169}Tm

^{169}Tm has a spin of $I = 1/2$, and experiences a hyperfine coupling but no quadrupolar interaction. By symmetry, the form of the hyperfine coupling must also be described by Eq. 5. In this case, however, the coupling $A_{zz} \approx 160$ mK is nearly three orders of magnitude larger than that for the ^{51}V due to the on-site coupling [26]. As a result, the spin lattice relaxation rate in the paramagnetic state is so fast that the ^{169}Tm resonance has not been observed. On the other hand, Bleaney and Wells reported ^{169}Tm in the ferroquadrupolar state, where they found a large shift of the resonance frequency for fields applied in the perpendicular direction [16]. In this case, the shift is due to the induced moments from the ordered Tm quadrupoles. The shift exhibited a two-fold rotation symmetry as the field was rotated in the perpendicular direction, which they attributed to the second order Zeeman interaction and the induced magnetization. The two-fold rotation reflects the orthorhombic crystal structure in the ferroquadrupolar state.

3 Nuclear magnetic resonance studies

Recently several studies have been conducted of the ^{51}V NMR in $TmVO_4$ in order to better understand the nature of the quantum phase transition [19, 24, 25]. In principle, one could perform zero-field NMR (or nuclear quadrupolar resonance, NQR) and gradually apply a c-axis field to investigate the behavior as the field is tuned to the QCP. In this case, the NMR resonance frequency is given by $|\gamma H + n\nu_{zz}|$, where $\gamma = 11.193$ MHz/T is the gyromagnetic ratio, $\nu_{zz} = 0.33$ MHz, and $n = -3, \ldots, +3$. Thus the highest transition frequency at $H = 0$ is only 1 MHz, but experiments below 1 MHz are difficult because the signal-to-noise ratio varies as $f^{3/2}$, where f is frequency [27]. To overcome this challenge, a perpendicular field of 3.3 T was applied along the [100] direction of the crystal (corresponding to the x or y directions in Eq. 2), and the crystal was rotated to project a small component along the c-axis, as illustrated in Figure 1A.

Spectra for several different values of H_c are shown in Figure 2A. For $H_c = 0$, the spectra consist of seven transitions separated by a quadrupolar interaction $P \sim 300$ kHz, as seen in Figure 2A. As H_c increases, the anisotropic Knight shift and EFG tensors alter the frequencies of the various quadrupolar satellites in a well-controlled fashion, shown in Figure 2B. The separation between the seven peaks gradually reduces and vanishes at the magic angle (where $H_c = H_0/\sqrt{3} \approx 1.8$ T), and all the peaks shift to higher frequency, reflecting the strong magnetic anisotropy. Surprisingly, the integrated area of the spectra is dramatically suppressed in the vicinity of the QCP, as shown in Figure 2C. This suppression of intensity has been interpreted as evidence for quantum critical fluctuations of the transverse field, due to an increase in T_2^{-1}, the decoherence rate of the nuclear spins [20]. The relative area shown in the figure is proportional to signal size $L(t) \sim e^{-t/T_2}$, which depends on the time evolved, t, since the nuclear spins are prepared in their initial superposition state. In this experiment t is a fixed quantity determined by the pulse spacing in the experiment. An increase in T_2^{-1} thus drives a suppression of the

area. If $L(t)$ decays faster than the minimum time to perform an experiment, then the signal intensity will be suppressed, or "wiped out." The data in Figure 2C suggests that T_2^{-1} reaches a maximum at the QCP.

3.1 Transverse field susceptibility

The decoherence of an NMR signal can often be extended by applying refocusing pulses [28]. The simplest such pulse sequence consists of a spin echo, in which a single π pulse at time $t/2$ reverses the direction of precession and refocuses static field inhomogeneities. Noise fluctuations at time scales shorter than $t/2$, however, will lead to decoherence and loss of signal. In general, the decay envelope, $L(t)$, of a spin-echo can be related to the noise fluctuations of the environment. In $TmVO_4$, this quantity can be written as:

$$\log[L(t)/L(0)] = -\frac{A_{zz}^2}{\hbar^2}\int_0^\infty S_{zz}(\omega)\frac{F(\omega t)}{\pi\omega^2}d\omega,$$

where S_{zz} is the dynamical structure factor for the transverse field fluctuations:

$$S_{zz}(\omega) = \int_0^\infty \langle\sigma_z(\tau)\sigma_z(0)\rangle e^{i\omega\tau}d\tau,$$

and $F(x) = 8\sin^4(x/4)$ is a filter function for the spin echo pulse sequence, which takes into account the refocusing nature of the spin echo π pulse [29, 30]. The spectral area, shown in Figure 2C, is proportional to $L(t)$ at fixed t corresponding to the pulse spacing in the spin echo experiment. Because the hyperfine coupling in $TmVO_4$ is solely along the *transverse field* direction, the nuclei are invisible to the longitudinal degrees of freedom. Only $S_{zz}(\omega)$, the noise spectrum in the transverse direction, contributes to the decoherence of the nuclear spins. This anisotropic coupling is highly unusual, but it enables us to probe the transverse fluctuations without any contamination from the longitudinal fluctuations, which diverge strongly at the QCP. The filter function acts to remove the static or low frequency ($\omega \leq 10^5$ Hz) components of the fluctuations, which are dominated by thermal fluctuations [19, 31]. The remaining contributions to $S_{zz}(\omega)$, and hence to the decay of $L(t)$, is from quantum fluctuations, which exist at finite frequency. This is because they arise from the intrinsic time evolution due to the many-body Hamiltonian, which has a finite gap except at the QCP. The fact that $L(t)$ reaches a minimum at the QCP indicates that these quantum fluctuations are largest here. Importantly, these extend to finite temperature, even exceeding T_Q. These results thus imply that there is a broad region of phase space, a "quantum critical fan," where quantum fluctuations are present.

An open question is how does the *transverse* susceptibility behave in the vicinity of the quantum phase transition? In mean-field theory at $T = 0$, χ_{zz} remains constant in the ordered state, and vanishes for $H_c > H_c^*$, as shown in Figure 3A. The NMR data are inconsistent with the mean field picture, since the relative area under the spectra decreases dramatically at the QCP, indicating that χ_{zz} must be strongly field-dependent in this range. Numerical calculations that are based on high and low field series expansions indicate that χ_{zz} diverges logarithmically on both sides of the QCP for various 3D lattices [32]. At $T = 0$ the enhancement is in a very narrow region but it should widen into a quantum critical fan at finite temperatures. Indeed we find significant differences between numerical calculations for small finite clusters and mean field theory at finite temperatures with enhancement in the general vicinity of the QCP, as seen in Figure 3B. We expect the differences to be much larger and centered at the critical point in the thermodynamic limit. These calculations, however, assume only a nearest neighbor interaction [e.g., $J(l = l') = 0$ if l, l' are not nearest neighbors in Eq. 3]. The interaction is expected to be long-range in $TmVO_4$, which could tend to stabilize mean-field behavior.

3.2 Fidelity susceptibility

Understanding the mechanisms of decoherence is a key problem for quantum computing, and the behavior of a central spin coupled to a well-controlled environment is an important theoretical model that has been studied extensively [31, 33]. In the case where the central spin (or qubit) is coupled to a 1D TFIM via a hyperfine coupling along the transverse field direction, the decoherence of the qubit can be elegantly expressed in terms of the overlap of the wavefunction of the environment at different times and values of the transverse field. In fact, the ^{51}V spins coupled to the ferroquadrupolar ordering in $TmVO_4$ maps well to this model, but with a 3D lattice for the environment. Although the central spin model was originally developed for a single spin coupled to an environment, it is straightforward to generalize to an ensemble of nuclear spins in a lattice, each with its own identical coupling [20]. Thus, $TmVO_4$ offers a unique opportunity to experimentally study this model.

Importantly, this connection offers a new approach to understanding NMR decoherence in terms of the quantum fidelity of the environment, which is defined as the modulus of the overlap between two states: $F = |\langle\Psi'|\Psi\rangle|$. In the case of the central spin model, the two states are $\Psi_\lambda'(t = 0)$ and $\Psi_{\lambda+\epsilon}(t)$, where λ corresponds to the transverse field, and ϵ corresponds to the small hyperfine field. Two ground states of the TFIM at different values of the transverse field may initially be very similar, but will evolve strongly away from one another in the vicinity of the QCP. At $T = 0$, the intensity of the NMR free induction decay is proportional to F^2, thus the qubit experiences a strong decoherence as the transverse field approaches the critical value. This tendency can be captured by the fidelity susceptibility: $\chi_F = -\partial^2 F/\partial\epsilon^2$. At finite temperatures, the fidelity can be expressed in terms of the density matrix [31]. A related quantity is the Quantum Fisher Information which quantifies the sensitivity of density matrices to small changes in parameters [34]. Because the fidelity susceptibility tends to diverge at a QCP, this quantity has been exploited theoretically to identify quantum and topological phase transitions [35, 36].

On the surface, this picture differs from the conventional NMR picture in which decoherence arises due to the presence of stochastic fluctuations of the hyperfine field, which can be quantitatively measured via Bloch-Wangsness-Redfield theory: $T_2^{-1} = A_{zz}^2 S_{zz}(\omega = 0)/2\hbar^2$ [28, 37, 38]. However, χ_F in fact can be related to the transverse field susceptibility, $\chi_{zz} = S_{zz}/k_BT$ [39]. This remarkable connection offers new insights and connections between NMR and quantum information theory. For example,

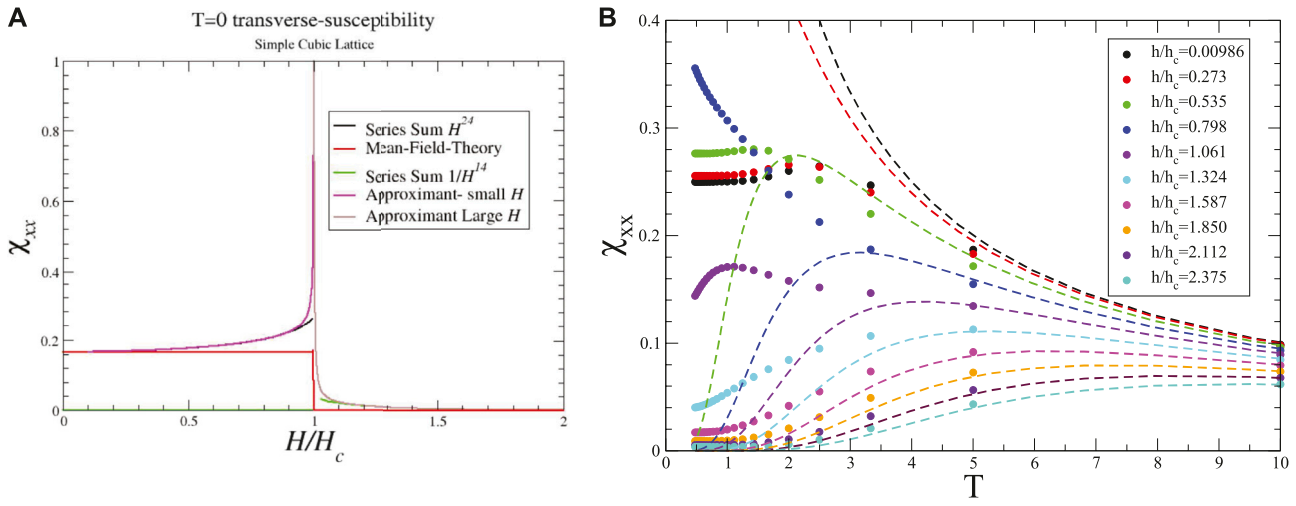

FIGURE 3
(A) Transverse susceptibility as a function of field for a simple cubic lattice at $T = 0$ in mean-field theory and in 3D short-range models. **(B)** Temperature dependence of the transverse field susceptibility at several different values of the transverse field calculated numerically for small periodic clusters of the square-lattice. The dashed lines are the mean field result, and the solid points of the same color are the results of numerical calculations.

NMR wipeout is ubiquitous in strongly correlated systems, and has been observed in the high temperature superconducting cuprates and the iron based superconductors [40–44]. In these cases, this phenomenon has been attributed to electronic inhomogeneity introduced because of the dopant atoms. However, the behavior in $TmVO_4$ suggests that it might be valuable to considering the wipeout in these other systems as a consequence of their proximity to a QCP.

4 NMR studies of Y substitution

Replacing Tm with Y suppresses the long range ferroquadrupolar order in $Tm_{1-x}Y_xVO_4$ to zero at $x_c \approx 0.22$, as illustrated in Figure 1C [14]. Y has no 4*f* electrons and thus lacks any magnetic or quadrupolar moments, so it acts to dilute the interactions between the Tm quadrupolar moments. The rapid suppression with doping is surprising because mean-field theory predicts a much weaker doping dependence: $T_Q \sim 1 - x$. Y doping also suppresses ferromagnetic order in $LiHoF_4$, however in this case long-range order persists until $x = 0.95$ [45]. The reason for the difference between the $TmVO_4$ and $LiHoF_4$ is that the Y creates strain fields that couple to the ferroquadrupolar order in the former. Y is slightly larger than Tm, thus it creates local distortions in the lattice that couple to the Tm quadrupolar moments [14]. This behavior is similar to that of a random field Ising model (RFIM), and causes T_Q to be suppressed much faster with Y doping [46]. The local strain fields may have components with B_{1g} symmetry, which couples to σ_x and is a transverse field, as well as fields with B_{2g} symmetry, which couples to σ_y and is a longitudinal field.

Y substitution offers an opportunity to test whether the decoherence observed in the pure $TmVO_4$ is due to quantum critical fluctuations. Figure 2C shows that for $x = 0.40$, which has no long-range ferroquadruplar order, the relative spectral area does not change significantly at H_c^*, in contrast to $x = 0$. This observation indicates that the quantum fluctuations are suppressed in the $x = 0.40$ sample.

4.1 NMR spectra

NMR spectra in doped systems are generally broader than in undoped materials because the dopants often give rise to inhomogeneity. As seen in Figure 4A, the spectra of the pure $TmVO_4$ and YVO_4 consist of seven clear resonances with small linewidths, but these resonances grow progressively broader with doping. Each of the seven resonances broadens equally between $0 \leq x \leq 0.1$. This behavior indicates that the broadening mechanism is not quadrupolar inhomogeneity, but rather a Knight shift inhomogeneity. The red dotted lines in Figure 4A are fits to the spectra, and the data in panel (e) show how the Gaussian width, σ, varies with doping for the spectra that can be clearly fit. It is surprising that even though random strain fields are clearly present and rapidly suppressing T_Q, they apparently do not significantly alter the local EFG at the V sites. In many other strongly-correlated systems, doping usually causes significant quadrupolar broadening [47–50]. In $Tm_{1-x}Y_xVO_4$, the larger Y atoms slightly displace the O and V in their vicinity [14]. On the other hand, it is possible that the VO_4 tetrahedra may not be significantly distorted upon Y substitution. Also, there are two main contributions to the EFG: a lattice term arising from the arrangement of charges, and an on-site term that is determined by the electronic configuration of the local electronic orbitals [28]. It is reasonable that the latter term dominates the EFG at the V, and that the electronic configuration of the V and O orbitals remain relatively unperturbed by Y doping.

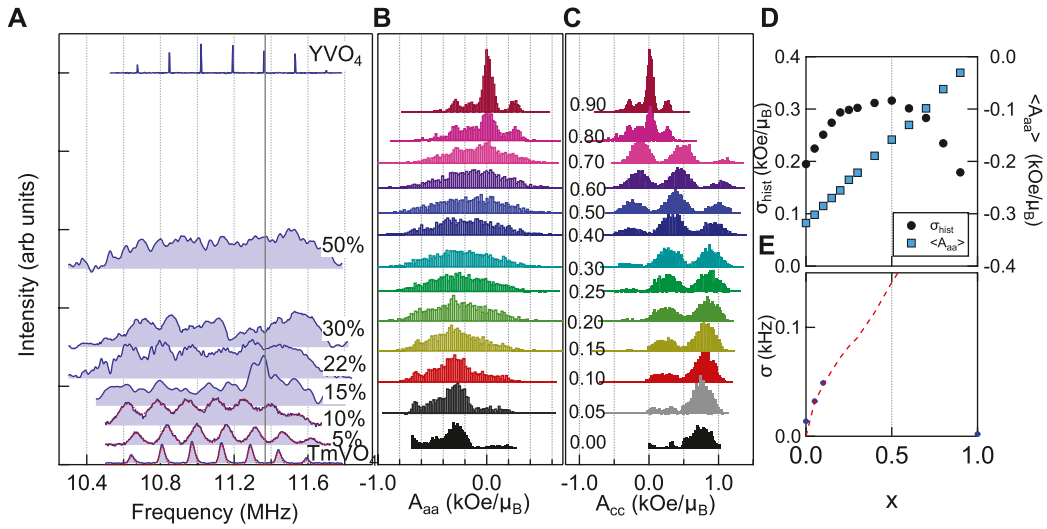

FIGURE 4
(A) Spectra for several values of x measured in an external field H_0 = 1 T oriented perpendicular to the c-axis at 1.8 K for all but the x = 1 case. For YVO_4 the spectrum was measured at 4.5 T and 10 K, but has been shifted to lower frequency by $\gamma\Delta H$ (ΔH = 3.9 T) to coincide with the other spectra. The red dotted lines are fits as described in the text. **(B,C)** Histograms of the hyperfine coupling constants, A_{aa} and A_{cc}, respectively, for a series of Y dopings for simulations as described in the text. **(D)** Average $\langle A_{aa}\rangle$ and standard deviation, σ, of the distributions shown in **(B)** as a function of Y doping, x. **(E)** The measured Gaussian linewidth of the spectra shown in **(A)** as a function of Y doping. The dashed red line was calculated using the computed standard deviation, as discussed in the text.

4.1.1 Numerical simulations

To investigate the inhomogeneity of the magnetic environments, we computed the direct dipolar hyperfine couplings, A_{aa} and A_{cc}, to the V sites in a 9 × 9 × 9 superlattice in which a fraction of the Tm sites are randomly removed. Histograms of these couplings are shown in Figures 4B, C for different Y concentrations. The sum is dominated by the two nearest neighbor Tm sites along the c-axis direction (see Figure 1A). The distribution for the perpendicular direction (A_{aa}) broadens with doping, but does not exhibit any structure. Figure 4D shows how the mean, $\langle A_{aa}\rangle$, and standard deviation, σ_{hist}, of the histograms vary with Y concentration. The standard deviation increases linearly with doping, which agrees with the experimental observation of the linewidth. The dashed red line in Figure 4E represents the expected magnetic linewidth in a field of H_0 = 1 T, as in the experiment. This quantity is given by $\sigma(x)|K|\gamma H_0/\langle A_{aa}\rangle$, where K = −0.66%. Here we have subtracted (in quadrature) the standard deviation of the histogram of the pure $TmVO_4$ case, which includes boundary effects: $\sigma(x) = \sqrt{\sigma_{hist}^2(x) - \sigma_{hist}(0)^2}$. The simulated linewidth agrees well with the measured linewidth, indicating that for low Y concentrations the magnetic environment of the remaining Tm is not significantly altered, despite the presence of the strain fields surrounding the Y sites. At higher doping levels, the magnetic broadening becomes comparable to the quadrupolar splitting, and the spectra become too broad to extract any information.

4.1.2 Effect of *c*-axis field

Figure 5A shows how the spectra for the x = 0.40 sample vary as the crystal is rotated in a fixed field, similar to the data shown in Figure 2A for the x = 0 case. As H_c increases, there is no significant wipeout at $H_c^\star$, as expected since there is no long range order at this doping level and therefore no quantum critical behavior. The integrated area for these spectra are shown in Figure 2C as a function of H_c. However, there are three peaks that emerge as H_c increases beyond ~ 1.5 T, labelled A, B, and C, that are not present in the undoped sample. In fact, these extra peaks are consistent with the simulated histograms of the c-axis hyperfine couplings shown in Figure 4C. The three peaks correspond to V sites with 0, 1 or 2 nearest neighbor Tm atoms, respectively.

As seen in Figure 4B these different V sites should not be discernible for a field $H_0 \perp c$. On the other hand, as $\mathbf{H}_0$ rotates towards the c-axis, three distinct peaks should emerge. This behavior is demonstrated in Figure 5B, which displays the histograms of the Knight shift, $K(\theta) = A_{aa}\chi_{aa}\sin^2\theta + A_{cc}\chi_{cc}\cos^2\theta$, for several different values of $H_c = H_0\cos\theta$. Here $\chi_{\alpha\alpha}$ is the static susceptibility, and we assume χ_{cc}/χ_{aa} = 3 for concreteness. The three sites are indeed discernible for sufficiently large H_c, which agrees well with the observations shown in panel (a). Moreover, the relative intensity of the peaks (A: B: C = 0.32 : 0.49: 0.18) also agrees well with the observed spectra (0.33 ± 0.01 : 0.51 ± 0.01 : 0.16 ± 0.01). We therefore conclude that site A corresponds to V with 2 n.n. Tm, site B with 1 n.n. Tm, and site C with 0 n.n. Tm. This property enables us to learn about the electronic inhomogeneity by measuring the relaxation at the different sites.

4.2 Spin lattice relaxation rate

Figure 6A displays $(T_1T)^{-1}$ versus temperature for several different doping levels, measured for field perpendicular to the c-axis. Note that for this field orientation the resonance frequencies of sites A, B, and C overlap, and thus we are unable to discern if these spin fluctuations are spatially inhomogeneous. We do not see any evidence for stretched relaxation for x < 0.1, which would indicate the presence of inhomogeneity. In this range the different quadrupolar satellites are

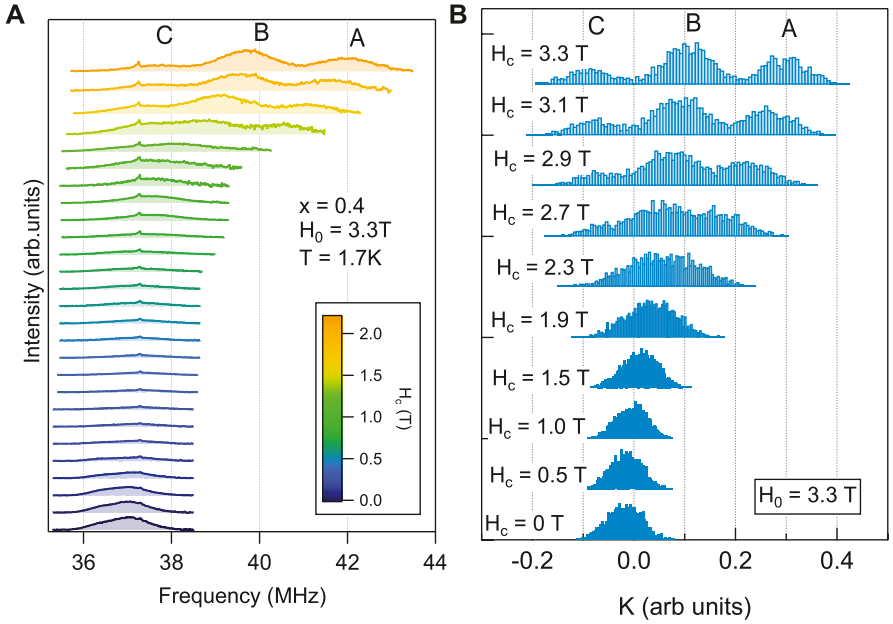

FIGURE 5
(A) Spectra of $Tm_{1-x}Y_xVO_4$ with $x = 0.40$ for several different values of H_c. For $H_c \gtrsim 1.5$ T, three peaks are discernable, *A*, *B*, and *C*. **(B)** Computed spectra based on the histograms of hyperfine couplings shown in Figures 4B, C for several different values of H_c for $x = 0.40$.

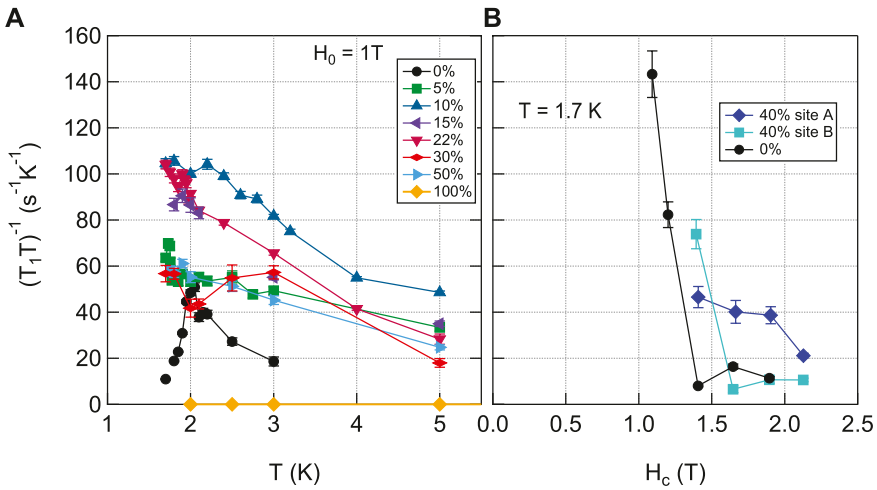

FIGURE 6
(A) $(T_1T)^{-1}$ versus temperature for several different Y doping levels, measured at $H_0 = 1$ T (except for the 100%, measured at 4.5 T), for $\theta = 90^\circ$. In this case, all three sites overlap. This data corresponds to the magnetic relaxation channel, as described in [51]. **(B)** $(T_1T)^{-1}$ versus the c-axis field component, H_c, for the pure $TmVO_4$, and for the *A* and *B* sites in the 40% sample.

clearly resolved, and the relaxation was measured at all transitions to extract both the magnetic and quadrupolar relaxation channels, although just the magnetic contribution is shown [24]. For higher doping levels where the spectra no longer show any structure, we are unable to determine if there is any stretched relaxation behavior. There is a clear peak for the pure $TmVO_4$ at T_Q reflecting the critical slowing down at the thermal phase transition. As the doping level increases this peak is suppressed to lower temperatures, yet $(T_1T)^{-1}$ increases and reaches a broad maximum around $x \approx 0.10$. In fact, the spin fluctuations appear to be enhanced near the vicinity of the critical doping level, x_c, possibly reflecting quantum critical fluctuations at this doping. At higher doping levels, the fluctuations gradually are suppressed and eventually disappear. For the pure YVO_4, there are no magnetic moments present anymore, and $(T_1T)^{-1}$ is several orders of magnitude smaller.

Sites *A*, *B* and *C* can be discerned when there is a finite H_c component present. Figure 6B compares $(T_1T)^{-1}$ versus H_c in pure $TmVO_4$ with $Tm_{0.6}Y_{0.4}VO_4$ for the *A* and *B* sites. The strong field

dependence of the pure system reflects the growth of the gap as the system is tuned away from the QCP at $H_c^\star$: $(T_1T)^{-1} \sim \exp(-\Delta(H_c)/T)$ [20]. As H_c is tuned beyond the QCP, the gap increases and $(T_1T)^{-1}$ decreases. It is surprising that in the $x = 0.40$ sample, which has no long range order, the *A* and *B* sites exhibit behavior that is qualitatively similar to that in the pure system. In other words, they each increase with decreasing field as H_c approaches the critical value. This behavior suggests that there are still localized clusters of Tm which continue to exhibit behavior reminiscent of the undoped lattice. Statistically there are regions of the disordered lattice with connected Tm atoms, and these may continue to exhibit correlations despite the absence of long-range order, giving rise to Griffiths phases [52]. An interesting open question is how such disconnected clusters may be affected by the presence of random strain fields.

Inhomogeneous dynamics in the disordered lattice may also explain the fact that the spectra in Figure 5A appear to exhibit an increasing intensity for $H_c \gtrsim 1.5$ T once the *A* and *B* peaks emerge. If local clusters of Tm continue to exhibit quantum critical fluctuations at these sites, then T_2^{-1} will be large, suppressing the signal from these sites. In other words, the *A* and *B* sites may experience partial wipeout in the vicinity of $H_c^\star$. Overall these sites contribute 84% of the total area, and the relative area under the spectra decreases by approximately the same value near $H_c^\star$ in Figure 2C. These observations further support the argument that the *A* and *B* sites are locally unperturbed by the Y dopants, and may exhibit behavior consistent with quantum Griffiths phases.

5 Conclusion

$TmVO_4$ offers a unique new experimental platform to investigate quantum critical phenomena and the effects of doping. The unique properties of the non-Kramers doublet in this system not only gives rise to the unusual Ising ferroquadrupolar order, but also ensures that the nuclear spins in this system only couple to the transverse field degrees of freedom. Studies of the $Tm_{1-x}Y_xVO_4$ uncovered several unexpected results. First, despite the presence of random strain fields, the EFG at the V sites remains unperturbed, at least for low doping concentrations. As the doping level increases and the long range ferroquadrupolar order vanishes, the spin lattice relaxation rate for the V sites is enhanced, before decreasing for doping levels that exceed the critical concentration. However, we find evidence that quantum critical fluctuations remain present for V sites that belong to Tm-rich clusters, even beyond the critical doping level, suggesting the presence of quantum Griffiths phases in the Y-doped system. It is unclear whether such isolated Tm clusters also experience random transverse or longitudinal strain fields. Further studies of this doped system will shed important light on how quantum fluctuations are destroyed by disorder.

Data availability statement

The raw data supporting the conclusion of this article will be made available by the authors, without undue reservation.

Author contributions

Y-HN: Data curation, Investigation, Writing–review and editing. IV: Data curation, Investigation, Writing–review and editing. CC: Investigation, Writing–review and editing. YL: Resources, Writing–review and editing. MZ: Resources, Writing–review and editing. PM: Resources, Writing–review and editing. RS: Conceptualization, Formal Analysis, Investigation, Writing–review and editing. IF: Conceptualization, Resources, Writing–review and editing. NC: Conceptualization, Writing–original draft, Writing–review and editing.

Funding

The authors declare financial support was received for the research, authorship, and/or publication of this article. Work at UC Davis was supported by the NSF under Grants No. DMR-1807889 and DMR-2210613, as well as the UC Laboratory Fees Research Program ID LFR-20-653926. Crystal growth performed at Stanford University was supported by the Air Force Office of Scientific Research under award number FA9550-20-1-0252.

Acknowledgments

We thank P. Klavins for support with cryogenic operations at UC Davis, and A. Albrecht and R. Fernandes for enlightening discussions.

Conflict of interest

The authors declare that the research was conducted in the absence of any commercial or financial relationships that could be construed as a potential conflict of interest.

Publisher's note

References

1. Balakirev FF, Betts JB, Migliori A, Ono S, Ando Y, Boebinger GS. Signature of optimal doping in Hall-effect measurements on a high-temperature superconductor. *Nature* (2003) 424:912–5. doi:10.1038/nature01890

2. Coleman P, Schofield AJ. Quantum criticality. *Nature* (2005) 433:226–9. doi:10.1038/nature03279

3. Park T, Ronning F, Yuan HQ, Salamon MB, Movshovich R, Sarrao JL, et al. Hidden magnetism and quantum criticality in the heavy fermion superconductor $CeRhIn_5$. *Nature* (2006) 440:65–8. doi:10.1038/nature04571

4. Park T, Sidorov VA, Ronning F, Zhu JX, Tokiwa Y, Lee H, et al. Isotropic quantum scattering and unconventional superconductivity. *Nature* (2008) 456:366–8. doi:10.1038/nature07431

5. Shibauchi T, Carrington A, Matsuda Y. A quantum critical point lying beneath the superconducting dome in iron pnictides. *Annu Rev Condens Matter Phys* (2014) 5: 113–35. doi:10.1146/annurev-conmatphys-031113-133921

6. Kuo HH, Chu JH, Palmstrom JC, Kivelson SA, Fisher IR. Ubiquitous signatures of nematic quantum criticality in optimally doped Fe-based superconductors. *Science* (2016) 352:958–62. doi:10.1126/science.aab0103

7. Lederer S, Schattner Y, Berg E, Kivelson SA. Enhancement of superconductivity near a nematic quantum critical point. *Phys Rev Lett* (2015) 114:097001. doi:10.1103/PhysRevLett.114.097001

8. Schuberth E, Tippmann M, Steinke L, Lausberg S, Steppke A, Brando M, et al. Emergence of superconductivity in the canonical heavy-electron metal $YbRh_2Si_2$. *Science* (2016) 351:485–8. doi:10.1126/science.aaa9733

9. Paschen S, Si Q. Quantum phases driven by strong correlations. *Nat Rev Phys* (2020) 3:9–26. doi:10.1038/s42254-020-00262-6

10. Alloul H, Bobroff J, Gabay M, Hirschfeld PJ. Defects in correlated metals and superconductors. *Rev Mod Phys* (2009) 81:45–108. doi:10.1103/RevModPhys.81.45

11. Seo S, Lu X, Zhu JX, Urbano RR, Curro N, Bauer ED, et al. Disorder in quantum critical superconductors. *Nat Phys* (2014) 10:120–5. doi:10.1038/nphys2820

12. Massat P, Wen J, Jiang JM, Hristov AT, Liu Y, Smaha RW, et al. Field-tuned ferroquadrupolar quantum phase transition in the insulator $TmVO_4$. *Proc Natl Acad Sci* (2022) 119:e2119942119. doi:10.1073/pnas.2119942119

13. Sachdev S *Quantum phase transitions*. Cambridge University Press (2001).

14. Li Y, Zic MP, Ye L, Meese WJ, Massat P, Zhu Y, et al. *Disorder-induced local strain distribution in Y-doped $TmVO_4$* (2024). doi:10.48550/ARXIV.2402.17049

15. Knoll KD. Absorption and fluorescence spectra of Tm^{3+} in YVO_4 and YPO_4. *Physica Status Solidi (B)* (1971) 45:553–9. doi:10.1002/pssb.2220450218

16. Bleaney B, Wells MR. Radiofrequency studies of $TmVO_4$. *Proc R Soc Lond Ser A, Math Phys Sci* (1980) 370:131–53.

17. Melcher RL *The anomalous elastic properties of materials undergoing cooperative Jahn Teller phase transisions (Elsevier), chap. The anomalous elastic properties of materials undergoing cooperative Jahn Teller phase transisions* (1976). p. 1–77. doi:10.1016/B978-0-12-477912-9.50006-0

18. Gehring GA, Gehring KA. Co-operative Jahn-Teller effects. *Rep Prog Phys* (1975) 38:1–89. doi:10.1088/0034-4885/38/1/001

19. Maharaj AV, Rosenberg EW, Hristov AT, Berg E, Fernandes RM, Fisher IR, et al. Transverse fields to tune an Ising-nematic quantum phase transition. *Proc Natl Acad Sci* (2017) 114:13430–4. doi:10.1073/pnas.1712533114

20. Nian YH, Vinograd I, Green T, Chaffey C, Massat P, Singh RRP, et al. Spin-echo and quantum versus classical critical fluctuations in $TmVO_4$. *Phys. Rev. Lett* (2024) 132: 216502. doi:10.1103/PhysRevLett.132.216502

21. Bitko D, Rosenbaum TF, Aeppli G. Quantum critical behavior for a model magnet. *Phys Rev Lett* (1996) 77:940–3. doi:10.1103/PhysRevLett.77.940

22. Melcher RL, Pytte E, Scott BA. Phonon instabilities in $TmVO_4$. *Phys Rev Lett* (1973) 31:307–10. doi:10.1103/PhysRevLett.31.307

23. Washimiya S, Shinagawa K, Sugano S. Effective Hamiltonian for non-Kramers doublets. *Phys Rev B* (1970) 1:2976–85. doi:10.1103/physrevb.1.2976

24. Vinograd I, Shirer KR, Massat P, Wang Z, Kissikov T, Garcia D, et al. Second order Zeeman interaction and ferroquadrupolar order in $TmVO_4$. *npj Quan Mater* (2022) 7: 68. doi:10.1038/s41535-022-00475-1

25. Wang Z, Vinograd I, Mei Z, Menegasso P, Garcia D, Massat P, et al. Anisotropic nematic fluctuations above the ferroquadrupolar transition in $TmVO_4$. *Phys Rev B* (2021) 104:205137. doi:10.1103/PhysRevB.104.205137

26. Schwab G, Hillmer W. Epr of non-kramers rare-earth ions in tetragonal crystals. *physica status solidi (b)* (1975) 70:237–44. doi:10.1002/pssb.2220700122

27. Hoult D, Richards R. The signal-to-noise ratio of the nuclear magnetic resonance experiment. *J Magn Reson (1969)* (1976) 24:71–85. doi:10.1016/0022-2364(76)90233-x

28. Slichter CP *Principles of nuclear magnetic resonance*. 3rd ed. Springer-Verlag (1992).

29. Cywiński Ł, Lutchyn RM, Nave CP, Sarma SD. How to enhance dephasing time in superconducting qubits. *Phys Rev B* (2008) 77:174509. doi:10.1103/physrevb.77.174509

30. Yang W, Ma WL, Liu RB. Quantum many-body theory for electron spin decoherence in nanoscale nuclear spin baths. *Rep Prog Phys* (2016) 80:016001. doi:10.1088/0034-4885/80/1/016001

31. Chen SW, Jiang ZF, Liu RB. Quantum criticality at high temperature revealed by spin echo. *New J Phys* (2013) 15:043032. doi:10.1088/1367-2630/15/4/043032

32. Weihong Z, Oitmaa J, Hamer CJ. Series expansions for the 3D transverse Ising model at T=0. *J Phys A: Math Gen* (1994) 27:5425–44. doi:10.1088/0305-4470/27/16/010

33. Quan HT, Song Z, Liu XF, Zanardi P, Sun CP. Decay of Loschmidt echo enhanced by quantum criticality. *Phys Rev Lett* (2006) 96:140604. doi:10.1103/physrevlett.96.140604

34. Hauke P, Heyl M, Tagliacozzo L, Zoller P. Measuring multipartite entanglement through dynamic susceptibilities. *Nat Phys* (2016) 12:778–82. doi:10.1038/nphys3700

35. König EJ, Levchenko A, Sedlmayr N. Universal fidelity near quantum and topological phase transitions in finite one-dimensional systems. *Phys Rev B* (2016) 93:235160. doi:10.1103/PhysRevB.93.235160

36. Tang HK, Marashli MA, Yu WC. Unveiling quantum phase transitions by fidelity mapping. *Phys Rev B* (2021) 104:075142. doi:10.1103/PhysRevB.104.075142

37. Wangsness RK, Bloch F. The dynamical theory of nuclear induction. *Phys Rev* (1953) 89:728–39. doi:10.1103/PhysRev.89.728

38. Redfield AG. On the theory of relaxation processes. *IBM J Res Dev* (1957) 1:19–31. doi:10.1147/rd.11.0019

39. Gu SJ. Fidelity approach to quantum phase transitions. *Int J Mod Phys B* (2010) 24: 4371–458. doi:10.1142/S0217979210056335

40. Curro N, Hammel P. The Cu NMR echo decay in stripe ordered $La_{1.65}Eu_{0.2}Sr_{0.15}CuO_4$. *Phys C* (2000) 341:1797–8. doi:10.1016/S0921-4534(00)01084-4

41. Curro N, Hammel P, Suh B, Hücker M, Büchner B, Ammerahl U, et al. Inhomogeneous low frequency spin dynamics in $La_{1.65}Eu_{0.2}Sr_{0.15}CuO_4$. *Phys Rev Lett* (2000) 85:642–5. doi:10.1103/PhysRevLett.85.642

42. Hunt A, Singer P, Thurber K, Imai T. ^{63}Cu NQR measurement of stripe order parameter in $La_{2-x}Sr_xCuO_4$. *Phys Rev Lett* (1999) 82:4300–3. doi:10.1103/PhysRevLett.82.4300

43. Julien MH, Campana A, Rigamonti A, Carretta P, Borsa F, Kuhns P, et al. Glassy spin freezing and NMR wipeout effect in the high-T_c superconductor $La_{1.90}Sr_{0.10}CuO_4$ critical discussion of the role of stripes. *Phys Rev B* (2001) 63:144508. doi:10.1103/PhysRevB.63.144508

44. Dioguardi AP, Crocker J, Shockley AC, Lin CH, Shirer KR, Nisson DM, et al. Coexistence of cluster spin glass and superconductivity in $Ba(Fe_{1-x}Co_x)_2As_2$ for $0.060 \leq x \leq 0.071$. *Phys Rev Lett* (2013) 111:207201. doi:10.1103/PhysRevLett.111.207201

45. Babkevich P, Nikseresht N, Kovacevic I, Piatek JO, Dalla Piazza B, Kraemer C, et al. Phase diagram of diluted Ising ferromagnet $LiHo_xy_{1-x}f_4$. *Phys Rev B* (2016) 94: 174443. doi:10.1103/PhysRevB.94.174443

46. Nattermann T *Theory of the random field ising model (world scientific)* (1997). p. 277–98. doi:10.1142/9789812819437_0009

47. Imai T, Slichter CP, Yoshimura K, Kosuge K. Low frequency spin dynamics in undoped and Sr-doped La_2CuO_4. *Phys Rev Lett* (1993) 70:1002–5. doi:10.1103/PhysRevLett.70.1002

48. Lang G, Grafe HJ, Paar D, Hammerath F, Manthey K, Behr G, et al. Nanoscale electronic order in iron pnictides. *Phys Rev Lett* (2010) 104:097001. doi:10.1103/PhysRevLett.104.097001

49. Kissikov T, Dioguardi AP, Timmons EI, Tanatar MA, Prozorov R, Bud'ko SL, et al. NMR study of nematic spin fluctuations in a detwinned single crystal of underdoped $Ba(Fe_{2-x}Co_x)_2As_2$. *Phys Rev B* (2016) 94:165123. doi:10.1103/PhysRevB.94.165123

50. Menegasso P, Souza JC, Vinograd I, Wang Z, Edwards SP, Pagliuso PG, et al. Hyperfine couplings as a probe of orbital anisotropy in heavy-fermion materials. *Phys Rev B* (2021) 104:035154. doi:10.1103/physrevb.104.035154

51. Vinograd I, Edwards SP, Wang Z, Kissikov T, Byland JK, Badger JR, et al. Inhomogeneous Knight shift in vortex cores of superconducting FeSe. *Phys Rev B* (2021) 104:014502. doi:10.1103/physrevb.104.014502

52. Vojta T. Disorder in quantum many-body systems. *Annu Rev Conden Ma P* (2019) 10:233–52. doi:10.1146/annurev-conmatphys-031218-013433

frontiers | Frontiers in Physics

TYPE Original Research
PUBLISHED 19 June 2024
DOI 10.3389/fphy.2024.1397524

OPEN ACCESS

EDITED BY
Dimosthenis Stamopoulos,
National and Kapodistrian University of Athens, Greece

REVIEWED BY
Övgü Ceyda Yelgel,
Recep Tayyip Erdoğan University, Türkiye
Panagiotis Kotetes,
Chinese Academy of Sciences (CAS), China
Yi-feng Yang,
Chinese Academy of Sciences (CAS), China

*CORRESPONDENCE
Vivek Mishra,
vivekm.phys@gmail.com
P. J. Hirschfeld,
pjh@phys.ufl.edu

RECEIVED 07 March 2024
ACCEPTED 22 April 2024
PUBLISHED 19 June 2024

CITATION
Mishra V, Wang G and Hirschfeld PJ (2024), Thermal conductivity of nonunitary triplet superconductors: application to UTe_2. *Front. Phys.* 12:1397524. doi: 10.3389/fphy.2024.1397524

Thermal conductivity of nonunitary triplet superconductors: application to UTe_2

Vivek Mishra*, Ge Wang and P. J. Hirschfeld*

Department of Physics, University of Florida, Gainesville, FL, United States

Considerable evidence shows that the heavy fermion material UTe_2 is a spin-triplet superconductor, possibly manifesting time-reversal symmetry breaking, as measured by Kerr effect below the critical temperature, in some samples. Such signals can arise due to a chiral orbital state or possible nonunitary pairing. Although experiments at low temperatures appear to be consistent with point nodes in the spectral gap, the detailed form of the order parameter and even the nodal positions are not yet determined. Thermal conductivity measurements can extend to quite low temperatures, and varying the heat current direction should be able to provide information on the order parameter structure. Here, we derive a general expression for the thermal conductivity of a spin-triplet superconductor and use it to compare the low-temperature behavior of various states proposed for UTe_2.

KEYWORDS

triplet superconductors, thermal transport, impurity scattering, nonunitary pairing, unitary pairing

1 Introduction

The uranium-based superconductor UTe_2 has stimulated a large number of experimental and theoretical studies, initially because of its apparent role as a paramagnetic end point of a family of ferromagnetic superconductors [1–3] and later as evidence for spin-triplet superconductivity accumulated. The nuclear magnetic resonance (NMR) Knight shift measurements on the earlier samples did not show any change in the superconducting state [4], although recent Knight shift measurements on high-quality samples show a small reduction along all three axes [5]. Both measurements support spin–triplet pairing; however, the spin structure of Cooper pairs remains unclear. Another piece of evidence that indicates spin–triplet pairing is the size of the upper critical field H_{c2} that exceeds the Pauli limit for all field directions [1, 6]. Measured power–law temperature dependence in NMR relaxation, specific heat [1], and thermal conductivity [7, 8] was found to be consistent with point nodes, as expected for a triplet superconductor in a system with strong spin–orbit coupling (SOC) [9–11]. Finally, a reentrant superconducting phase was shown to be stabilized at high magnetic fields [12].

A second set of measurements relevant to the nature of the superconducting state purports to exhibit evidence for time-reversal symmetry breaking (TRSB) below T_c, suggesting that UTe_2 may support the long-sought chiral p-wave state that may serve as a quantum computing platform [13–17]. Initially, the polar Kerr effect [18] experiments suggested that TRSB occurred in the superconductor, implying the existence of a

multicomponent spin-triplet order parameter. According to group theoretical classifications of the one-dimensional (1D) irreducible representations (irreps) allowed in orthorhombic symmetry, order parameters corresponding to single irreps must be unitary triplet states, meaning that any TRSB must arise from a nonunitary multicomponent state. Such combinations of 1D representations were discussed intensively, particularly because a double specific heat transition was sometimes observed in early samples, recalling the specific heat experiments in multicomponent UPt_3.

More recently, measurements of a new generation of high-quality UTe_2 crystals grown in molten salt flux have challenged this characterization of UTe_2 as a chiral triplet state breaking time-reversal symmetry (TRS). The Kerr effect was observed in a sample showing two specific heat jumps, but as the quality of the samples improved, only a single transition was observed [19, 20]. A recent investigation of the Kerr effect on both the old- and new-generation UTe_2 single crystals displaying a single specific heat jump found no evidence for TRSB superconductivity [21]. Similarly, muon spin relaxation (μSR) measurements of the molten salt flux-grown samples found no evidence of TRSB [22]. Finally, sound velocity changes across T_c [23] and recent NMR Knight shift measurements on similar samples [5] both point to a single-component, odd parity-order parameter, i.e., inconsistent with the previous hypothesis of nonunitary pairing.

The thermal conductivity $\kappa(T)$ is an important probe of the gap structure of unconventional superconductors, reflecting the ability of the superconductor to carry heat current in various directions. The theory of thermal conductivity in *unitary* triplet superconductors is quite similar to the well-known theory developed for singlet superconductors [24, 25]. Most of the popular model triplet states in the literature, including the ^{3}He-A phase, belong to this class. In that case, the triplet quasiparticle energies are $E_{\mathbf{k}} = \sqrt{\xi_{\mathbf{k}}^2 + |\mathbf{d}(\mathbf{k})|^2}$, where $\mathbf{d}(\mathbf{k})$ is the triplet-order parameter vector defining its structure in spin space via $\Delta_{\sigma\sigma'} = [\mathbf{d}(\mathbf{k}) \cdot \boldsymbol{\sigma}(i\sigma_y)]_{\sigma\sigma'}$. Here, $\boldsymbol{\sigma}$ is the Pauli vector in the spin space spanned by the Pauli matrices σ_x, σ_y, and σ_z. Since the thermal current response depends only on the quasiparticle energies, the same expressions can be used for triplet superconductors [26–28] with $|\Delta(\mathbf{k})|^2$ replaced by $|\mathbf{d}(\mathbf{k})|^2$. As shown below, however, in the nonunitary state, additional terms involving the spin moment $\mathbf{q} \equiv i\mathbf{d}(\mathbf{k}) \times \mathbf{d}^*(\mathbf{k})$ carried by quasiparticles of momentum $\mathbf{k}$ occur in both the quasiparticle energies and the weights of scattering processes. Furthermore, in nonunitary triplet superconductors, the zeros of $|\mathbf{d}(\mathbf{k})|^2$ differ from those of $E_{\mathbf{k}}$, even when $\mathbf{k}$ is on the Fermi surface ("spectral nodes"). This distinction may be important; it was suggested by Ishihara et al. [29] that in UTe_2, complex linear combinations of 1D irreducible representations could support spectral nodes pointing in generic directions in the orthorhombic Brillouin zone and thereby explain early experiments exhibiting TRSB and relative isotropy of the low-temperature penetration depth. On the other hand, order parameters corresponding to a single 1D irrep must be real, with nodes along high-symmetry axes.

In this paper, we derive a general form of the thermal conductivity of a triplet superconductor in the presence of nonmagnetic pointlike impurities and evaluate it for various types of triplet states that have been proposed for UTe_2. The aim is to see whether there are qualitative distinctions between the thermal conductivity temperature and heat current direction dependence of unitary and nonunitary states and whether or not predictions of low-temperature behavior can be used, by comparison with experiments, to identify the ground state of UTe_2.

TABLE 1 List of possible spin-triplet superconducting states for an orthorhombic crystal with strong spin–orbit coupling. Here, $p_{i=1,..,3}$ are constants, and $\forall p_i \in \mathbb{R}$.

Γ	Gap function d(k)	Nodes
A_{1u}	(p_1k_x, p_2k_y, p_3k_z)	Accidental
B_{1u}	$(p_1k_y, p_2k_x, p_3k_xk_yk_z)$	z-axis
B_{2u}	$(p_1k_z, p_2k_xk_yk_z, p_3k_x)$	y-axis
B_{3u}	$(p_1k_xk_yk_z, p_2k_z, p_3k_y)$	x-axis

2 Model and formalism

2.1 Superconducting state

In a general triplet superconductor, the spin structure of the superconducting order parameter is constrained by the underlying crystal symmetries. The structure of the UTe_2 crystals corresponds to the orthorhombic point group D_{2h}, and the symmetry of the odd-parity pairing states can be deduced according to the irreducible representations of the D_{2h} point group [30–32]. Table 1 shows the odd-parity triplet superconducting states considered in this article. Here, we do not consider the even-parity states for the D_{2h} point group, and we further assume strong SOC due to heavy atoms like U and Te. Due to strong SOC, orbital and spin degrees of freedom do not transform independently; instead, each space group rotation involves a rotation in spin and spatial spaces of the order parameter. In the weak SOC limit, the odd-parity states for the D_{2h} point group come with line nodes that are not consistent with experimental measurements.

The **d**-vector is real for the superconducting states listed in Table 1; hence, these states preserve TRS. These states are unitary triplet states, i.e., $\hat{\Delta}^\dagger\hat{\Delta} \propto \hat{\mathbb{1}}$. We denote a 2×2 matrix in the spin space with $\hat{\square}$ and a 4×4 matrix in the Nambu-spin space with $\check{\square}$. A TRSB state is not possible with a single-component order parameter, noting that the D_{2h} group has only one-dimensional irreducible representations. We construct the TRSB superconducting state with a combination of two irreducible representations, and all such possible combinations are shown in Table 2. In principle, a combination of two different irreducible representations involves six real constants; however, we introduce a single-parameter model for the TRSB states. The effective **d**-vector is $(\mathbf{d}_1 + ir\mathbf{d}_2)/\sqrt{1+r^2}$, where r is the mixing parameter that determines the relative strength of the individual order parameter. The individual **d**-vectors are listed in Table 1 with all the coefficients $p_{i=1,2..3}$ set to unity.

In the Nambu-spin basis, the mean field Hamiltonian reads

$$\check{\mathbf{H}} = \begin{pmatrix} \xi_{\mathbf{k}}\sigma_0 & i\Delta_0(\mathbf{d}\cdot\boldsymbol{\sigma})\sigma_y \\ -i\Delta_0\sigma_y(\mathbf{d}^*\cdot\boldsymbol{\sigma}) & -\xi_{\mathbf{k}}\sigma_0 \end{pmatrix}, \tag{1}$$

where $\xi_{\mathbf{k}}$ is the electronic dispersion, Δ_0 is the superconducting gap energy scale, and σ_0 is the identity matrix in the spin space. We adopt a model where the electronic dispersion reads

TABLE 2 Six possible mixed IR states.

Classification	d(k)	Cylindrical FS		Spherical FS	
		r	N_{nodes}	r	N_{nodes}
Antiferromagnetic nonunitary	$A_{1u} + irB_{1u}$	$r < 1$	0	$r < 1$	0
		$r = 1$	4 (xy-plane)	$r = 1$	4 (xy-plane)
		$1 < r \leq \sqrt{2}$	8 (xz- and yz-planes)	$r > 1$	8 (xz- and yz-planes)
		$r > \sqrt{2}$	0		
	$A_{1u} + irB_{2u}$	$r < 1$	0	$r < 1$	0
		$r = 1$	2 (x-axis)	$r = 1$	4 (xz-plane)
		$1 < r \leq \sqrt{2}$	4 (xy-plane)	$r > 1$	8 (xy- and yz-planes)
		$r > \sqrt{2}$	8 (xy- and yz-planes)		
	$A_{1u} + irB_{3u}$	$r < 1$	0	$r < 1$	0
		$r = 1$	2 (y-axis)	$r = 1$	4 (yz-plane)
		$1 < r \leq \sqrt{2}$	4 (xy-plane)	$r > 1$	8 (xy- and xz-planes)
		$r > \sqrt{2}$	8 (xy- and xz-planes)		
Ferromagnetic nonunitary	$B_{1u} + irB_{2u}$ ($\hat{x}$ spin moment)	$r < \frac{1}{\sqrt{2}}$	0	$r < 1$	4 (xz-plane)
		$\frac{1}{\sqrt{2}} \leq r < 1$	4 (xz-plane)	$r = 1$	2 (x-axis)
		$r = 1$	2 x-axis	$r > 1$	4 (xy-plane)
		$r > 1$	4 (xy-plane)		
	$B_{1u} + irB_{3u}$ ($\hat{y}$ spin moment)	$r < \frac{1}{\sqrt{2}}$	0	$r < 1$	4 (yz-plane)
		$\frac{1}{\sqrt{2}} \leq r < 1$	4 (yz-plane)	$r = 1$	2 (y-axis)
		$r = 1$	2 (y-axis)	$r > 1$	4 (xy-plane)
		$r > 1$	4 (xy-plane)		
	$B_{2u} + irB_{3u}$ ($\hat{z}$ spin moment)	$r \leq \frac{1}{\sqrt{2}}$	4 (yz-plane)	$r < 1$	4 (yz-plane)
		$\frac{1}{\sqrt{2}} < r < \sqrt{2}$	0	$r = 1$	2 (z-axis)
		$r \geq \sqrt{2}$	4 (xz-plane)	$r > 1$	4 (xz-plane)

$$\xi_{\mathbf{k}} = \frac{\hbar^2 k_x^2}{2m_a} + \frac{\hbar^2 k_y^2}{2m_b} - \mu - 2t_\perp \cos k_z, \tag{2}$$

where $m_{a/b}$ is the effective masses along $\hat{x}/\hat{y}$ directions, $t_\perp$ is the hopping energy that controls the $\hat{z}$ velocity, and μ is the chemical potential. We further assume that $t_\perp \ll \mu$. An alternate dispersion with a closed Fermi surface is considered in the Supplementary Material. The bare Green's function is

$$\check{G}_0 = \left(\check{\mathbb{1}}\omega - \check{\mathbf{H}}\right)^{-1} = \begin{pmatrix} \hat{G}_{11} & \hat{G}_{12} \\ \hat{G}_{21} & \hat{G}_{22} \end{pmatrix}. \tag{3}$$

Here, ω is the quasiparticle energy. The Matsubara Green's function can be obtained by $\omega \to i\omega_n$. The 2×2 matrices in the spin space are

$$\hat{G}_{11} = \frac{(\omega + \xi)}{D}\left[\left(\omega^2 - \xi^2 - \Delta_0^2|\mathbf{d}|^2\right)\sigma_0 + \Delta_0^2 \mathbf{q}\cdot\boldsymbol{\sigma}\right], \tag{4}$$

$$\hat{G}_{12} = \left[\left(\omega^2 - \xi^2 - \Delta_0^2|\mathbf{d}|^2\right)\sigma_0 + \Delta_0^2 \mathbf{q}\cdot\boldsymbol{\sigma}\right]\frac{i\Delta_0(\mathbf{d}\cdot\boldsymbol{\sigma})\sigma_y}{D}, \tag{5}$$

$$\hat{G}_{21} = -\left[\left(\omega^2 - \xi^2 - \Delta_0^2|\mathbf{d}|^2\right)\sigma_0 + \Delta_0^2 \mathbf{q}\cdot\boldsymbol{\sigma}^T\right]\frac{\Delta_0 i\sigma_y(\mathbf{d}^*\cdot\boldsymbol{\sigma})}{D}, \tag{6}$$

$$\hat{G}_{22} = \frac{(\omega - \xi)}{D}\left[\left(\omega^2 - \xi^2 - \Delta_0^2|\mathbf{d}|^2\right)\sigma_0 + \Delta_0^2 \mathbf{q}\cdot\boldsymbol{\sigma}^T\right]. \tag{7}$$

Here, $\mathbf{q} = i\,(\mathbf{d} \times \mathbf{d}^*)$, and the denominator D is

$$D = \left(\omega^2 - \xi^2 - \Delta_0^2|\mathbf{d}|^2\right)^2 - \Delta_0^4|\mathbf{q}|^2 = \left(\xi^2 - \omega^2 + \Delta_+^2\right)\left(\xi^2 - \omega^2 + \Delta_-^2\right). \tag{8}$$

Here, we introduce $\Delta_\pm^2 = \Delta_0^2\left(|\mathbf{d}|^2 \pm |\mathbf{q}|\right)$. For the unitary case, $\mathbf{q} = 0$; therefore, there is only a single energy scale. In contrast, for the TRSB nonunitary states, $\mathbf{q} \neq 0$, which leads to non-degenerate excitation energies. For single-component order parameters, $\mathbf{q}$ vanishes. However, for a mixture of multiple irreducible representations, $\mathbf{q}$ remains finite, and it can be interpreted as the spin moment of the Cooper pairs. The average of $\mathbf{q}$ over the Fermi surface may or may not vanish. The nonunitary states can therefore be further divided into antiferromagnetic (AF) and ferromagnetic (FM) states, where the

average of **q** vanishes over the Fermi surface for the former and remains finite for the latter [9]. The six possible nonunitary states are shown in Table 2, with the possibility of nodes on a spherical or a cylindrical Fermi surface open along the $\hat{z}$ axis. For a cylindrical Fermi surface, we adopt cylindrical coordinates with k_z dependence of the gap functions replaced with sin $(k_z d/2)$, where d is the z-axis. The factor of 1/2 is added to ensure only a single pair of point nodes in the first Brillouin zone in the unitary limit. However, this does not have any qualitative effect on our results.

2.2 Impurity scattering and thermal transport

In order to calculate the thermal conductivity, we need to include the effect of impurity scattering that dominates all other relaxation mechanisms at low temperatures. We consider elastic impurity scattering due to pointlike defects and include its effect through a disorder-averaged self-energy. The impurity self-energy is calculated within the self-consistent T-matrix approximation. The momentum-integrated Green's function $\hat{g}$ has both vector and scalar components for the normal Green's functions:

$$\hat{g}_{11} = \pi N_0 (g_0 + \mathbf{g}\cdot\boldsymbol{\sigma}), \tag{9}$$

$$\hat{g}_{22} = \pi N_0 (g_0 + \mathbf{g}\cdot\boldsymbol{\sigma}^T), \tag{10}$$

and the anomalous Green's functions $\hat{g}_{12}$ and $\hat{g}_{21}$ vanish because the odd-parity order parameter averages to 0. In Eqs 9, 10, **g** is directly related to the Fermi surface average of the spin moment **q** and remains finite for the chiral nonunitary states, only. Using these integrated Green's functions, we can write the T-matrix self-energy for the non-magnetic impurities as

$$\check{\Sigma} = \check{\tau}_3 \cdot \begin{pmatrix} \Sigma_3 + \boldsymbol{\Sigma_3}\cdot\boldsymbol{\sigma} & 0 \\ 0 & \Sigma_3 + \boldsymbol{\Sigma_3}\cdot\boldsymbol{\sigma}^T \end{pmatrix} + \check{\tau}_0 \cdot \begin{pmatrix} \Sigma_0 + \boldsymbol{\Sigma}\cdot\boldsymbol{\sigma} & 0 \\ 0 & \Sigma_0 + \boldsymbol{\Sigma}\cdot\boldsymbol{\sigma}^T \end{pmatrix}, \tag{11}$$

$$\Sigma_3 = \Gamma_u \frac{\cot\delta_s\left[\cot^2\delta_s - \left(g_0^2 + \mathbf{g}\cdot\mathbf{g}\right)\right]}{D_{imp}}, \tag{12}$$

$$\boldsymbol{\Sigma_3} = \Gamma_u \frac{2\cot\delta_s g_0 \mathbf{g}}{D_{imp}}, \tag{13}$$

$$\Sigma_0 = \Gamma_u \frac{g_0\left[\cot^2\delta_s - \left(g_0^2 - \mathbf{g}\cdot\mathbf{g}\right)\right]}{D_{imp}}, \tag{14}$$

$$\boldsymbol{\Sigma} = \Gamma_u \frac{\mathbf{g}\left[\cot^2\delta_s + \left(g_0^2 - \mathbf{g}\cdot\mathbf{g}\right)\right]}{D_{imp}}, \tag{15}$$

$$D_{imp} = \cot^4\delta_s - 2\cot^2\delta_s\left(g_0^2 + \mathbf{g}\cdot\mathbf{g}\right) + \left(g_0^2 - \mathbf{g}\cdot\mathbf{g}\right)^2, \tag{16}$$

where $\delta_s \equiv \tan^{-1}(\pi N_0 V_{imp})$ is the s-wave scattering phase shift; $\Gamma_u = n_{imp}/(\pi N_0)$; and n_{imp} and V_{imp} are the impurity concentration and impurity potential, respectively. Here, $\check{\tau}_3$ is the Pauli matrix in the Nambu space. The τ_3 component of the self-energy that renormalizes the electronic dispersion is ignored. It can be absorbed in the chemical potential. The impurity-dressed Green's function reads

$$\check{\mathbf{G}}^{-1} = \check{G}_0^{-1} - \check{\Sigma} = \begin{pmatrix} \tilde{\omega} - \xi\sigma_0 - \Sigma\cdot\boldsymbol{\sigma} & -\hat{\Delta} \\ -\hat{\Delta}^\dagger & \tilde{\omega} + \xi\sigma_0 - \Sigma\cdot\boldsymbol{\sigma}^T \end{pmatrix}, \quad \check{\mathbf{G}} = \begin{pmatrix} \hat{\mathbf{G}}_{11} & \hat{\mathbf{G}}_{12} \\ \hat{\mathbf{G}}_{21} & \hat{\mathbf{G}}_{22} \end{pmatrix}. \tag{17}$$

Here, impurity-renormalized $\tilde{\omega} = \omega - \Sigma_0$, which is obtained self-consistently. Unlike unitary superconductors, the impurity-dressed nonunitary Green's function acquires a different structure from that of the bare Green's function, in particular the structure in spin space for the normal component. The individual components of the Green's function $\check{\mathbf{G}}$ are

$$\hat{\mathbf{G}}_{11} = \frac{L_0 + \mathbf{L}_1\cdot\boldsymbol{\sigma}}{\tilde{\mathbf{D}}}, \tag{18}$$

$$\hat{\mathbf{G}}_{22} = \frac{L_0(\xi\to-\xi) + \mathbf{L}_1(\xi\to-\xi)\cdot\boldsymbol{\sigma}^T}{\tilde{\mathbf{D}}}, \tag{19}$$

$$\hat{\mathbf{G}}_{12} = \Big[2\xi(\boldsymbol{\Sigma}\cdot\mathbf{d}) + \left(\tilde{\omega}^2 - \xi^2 - \Delta_0^2|\mathbf{d}|^2 + \boldsymbol{\Sigma}\cdot\boldsymbol{\Sigma}\right)\mathbf{d}\cdot\boldsymbol{\sigma} + i\Delta_0^2(\mathbf{q}\times\mathbf{d})\cdot\boldsymbol{\sigma} - 2(\boldsymbol{\Sigma}\cdot\mathbf{d})\boldsymbol{\Sigma}\cdot\boldsymbol{\sigma} + 2i\tilde{\omega}(\boldsymbol{\Sigma}\times\mathbf{d})\cdot\boldsymbol{\sigma}\Big]\frac{i\sigma_y\Delta_0}{\tilde{\mathbf{D}}}, \tag{20}$$

$$\hat{\mathbf{G}}_{21} = \Big[-2\xi\boldsymbol{\Sigma}\cdot\mathbf{d}^\star + \left(\tilde{\omega}^2 - \xi^2 - \Delta_0^2|\mathbf{d}|^2 + \boldsymbol{\Sigma}\cdot\boldsymbol{\Sigma}\right)\mathbf{d}^\star\cdot\boldsymbol{\sigma}^T - i\Delta_0^2(\mathbf{q}\times\mathbf{d}^\star)\cdot\boldsymbol{\sigma}^T - 2\boldsymbol{\Sigma}\cdot\mathbf{d}^\star\boldsymbol{\Sigma}\cdot\boldsymbol{\sigma}^T - 2i\tilde{\omega}(\boldsymbol{\Sigma}\times\mathbf{d}^\star)\cdot\boldsymbol{\sigma}^T\Big]\frac{i\sigma_y\Delta_0}{\tilde{\mathbf{D}}}, \tag{21}$$

where

$$L_0 = X_0 a_0 - \Delta_0^2 b_0|\mathbf{d}|^2 - \Delta_0^2\mathbf{q}\cdot\boldsymbol{\Sigma}, \tag{22}$$

$$\mathbf{L}_1 = \left(X_0 + \Delta_0^2|\mathbf{d}|^2\right)\boldsymbol{\Sigma} + \Delta_0^2 b_0\mathbf{q} - \Delta_0^2\boldsymbol{\Sigma}\cdot\mathbf{d}\mathbf{d}^\star - \Delta_0^2\boldsymbol{\Sigma}\cdot\mathbf{d}^\star\mathbf{d}. \tag{23}$$

Here, $a_0/b_0 = \tilde{\omega} \mp \xi$, $X_0 = b_0^2 - \boldsymbol{\Sigma}\cdot\boldsymbol{\Sigma}$, and the denominator $\tilde{\mathbf{D}} = (\xi^2 + \tilde{Q}_+^2)(\xi^2 + \tilde{Q}_-^2)$, where $\tilde{Q}_\pm$ is

$$\tilde{Q}_\pm^2 = \Delta_0^2|\mathbf{d}|^2 - \tilde{\omega}^2 - \boldsymbol{\Sigma}\cdot\boldsymbol{\Sigma} \pm \sqrt{\Delta_0^4\mathbf{q}\cdot\mathbf{q} + 4\tilde{\omega}^2\boldsymbol{\Sigma}\cdot\boldsymbol{\Sigma} + 4\Delta_0^2\tilde{\omega}\mathbf{q}\cdot\boldsymbol{\Sigma} - 4\Delta_0^2(\boldsymbol{\Sigma}\cdot\mathbf{d})(\boldsymbol{\Sigma}\cdot\mathbf{d}^\star)}. \tag{24}$$

For the unitary states, the nodes are symmetry-imposed, and for the nonunitary states, nodes may shift away from the high-symmetry directions, and their positions remain protected against disorder as long as the $\boldsymbol{\Sigma}$ component of the impurity self-energy vanishes. $\boldsymbol{\Sigma}$ can be interpreted as impurity-induced magnetization. For the chiral states, this term remains finite and gives rise to non-degenerate quasiparticle spin density and, in principle, can change the nodal positions. Here, the nodes do not refer to the zeros of the gap or the order parameter; instead, they are the zeros in the quasiparticle spectrum on the Fermi surface. In the unitary states, the gap nodes and the spectral nodes are same, unlike the nonunitary states. There are some additional triplet terms $\boldsymbol{\Sigma}\cdot\boldsymbol{\sigma}$ and $(\boldsymbol{\Sigma}\times\mathbf{d})\cdot\boldsymbol{\sigma}$ in Eq. 20, which reflect the impurity-induced modification of the spin structure of the Cooper pairs. It is worth mentioning that there is an impurity-induced odd-frequency pairing for the chiral nonunitary states, which is spin singlet and odd parity in nature.

After obtaining the impurity-dressed Green's function, we calculate the electronic thermal conductivity κ using the Kubo formula that relates the thermal conductivity to the

heat–current response [24]. We ignore the vertex corrections and restrict ourselves to the bare thermal–current response function. The vertex corrections are small in the strong scattering limit that is focused on in this article [33]. The diagonal thermal conductivity for a general triplet superconductor reads

$$\frac{\kappa_{ii}}{T} = \int_{-\infty}^{\infty} d\omega \frac{\omega^2}{T^2}\left(-\frac{dn_F(\omega)}{d\omega}\right)$$

$$\left\langle N_0 v_{Fi}^2 \frac{(-c_1c_4 + c_2c_3) + c_3b_1 + c_1b_2 + b_3(-c_3 + c_1c_2)/c_4}{(c_3^2 + c_1^2c_4 - c_1c_2c_3)}\right\rangle_{FS}. \quad (25)$$

Here, $c_1 = -2\mathrm{Re}(\tilde{Q}_+ + \tilde{Q}_-)$, $c_2 = |\tilde{Q}_+|^2 + |\tilde{Q}_-|^2 + 4\mathrm{Re}(\tilde{Q}_+)\mathrm{Re}(\tilde{Q}_-)$, $c_3 = -2|\tilde{Q}_+|^2\mathrm{Re}(\tilde{Q}_-) - 2|\tilde{Q}_-|^2\mathrm{Re}(\tilde{Q}_+)$, and $c_4 = |\tilde{Q}_+|^2|\tilde{Q}_-|^2$, and the coefficients $b_{i=1,.,3}$ are

$$b_1 = \left(|\tilde{\omega}|^2 - \Delta_0^2|\mathbf{d}|^2 + |\mathbf{\Sigma}|^2\right) + \mathrm{Re}\left[\tilde{Q}_+^2 + \tilde{Q}_-^2\right], \quad (26)$$

$$\begin{aligned} b_2 = {} & \frac{1}{4}|\tilde{Q}_+^2 + \tilde{Q}_-^2|^2 + \left(|\tilde{\omega}|^2 + |\mathbf{\Sigma}|^2 - \Delta_0^2|\mathbf{d}|^2\right)\mathrm{Re}\left[\tilde{Q}_+^2 + \tilde{Q}_-^2\right] + 3\Delta_0^4\mathbf{q}\cdot\mathbf{q} \\ & + 4|\mathbf{\Sigma}|^2\left(|\tilde{\omega}|^2 + \mathrm{Re}[\tilde{\omega}^2]\right) \\ & - 4\Delta_0^2\left(|\mathbf{\Sigma}\cdot\mathbf{d}|^2 + |\mathbf{\Sigma}\cdot\mathbf{d}^*|^2 + \mathrm{Re}[(\mathbf{\Sigma}\cdot\mathbf{d})(\mathbf{\Sigma}\cdot\mathbf{d}^*)]\right) \\ & + 4|\tilde{\omega}|^2\mathrm{Re}[\mathbf{\Sigma}\cdot\mathbf{\Sigma}] + 4\Delta_0^2\mathrm{Re}\left[\tilde{\omega}\mathbf{q}\cdot\mathbf{\Sigma}^* + 2\tilde{\omega}\mathbf{q}\cdot\mathbf{\Sigma}\right], \end{aligned} \quad (27)$$

$$b_3 = \left(|\tilde{\omega}|^2 - \Delta_0^2|\mathbf{d}|^2\right)\left[|\alpha_+|^2 + \Delta_0^4\mathbf{q}\cdot\mathbf{q}\right] - 2\Delta_0^4\mathbf{q}\cdot\mathbf{q}\mathrm{Re}[\alpha_+] + \mathcal{Y}(\mathbf{\Sigma}), \quad (28)$$

$$\begin{aligned} \mathcal{Y}(\mathbf{\Sigma}) = {} & \left\{\left|\left(\tilde{\omega}^2 + \Delta_0^2|\mathbf{d}|^2 - \mathbf{\Sigma}\cdot\mathbf{\Sigma}\right)\right|^2 - \Delta_0^4\mathbf{q}\cdot\mathbf{q}\right\}|\mathbf{\Sigma}|^2 \\ & - 2\Delta_0^2\mathrm{Re}\left[(\alpha_- - \alpha_-^*)\tilde{\omega}\mathbf{q}\cdot\mathbf{\Sigma}^*\right] \\ & - 4\Delta_0^2\left(|\tilde{\omega}|^2 + |\mathbf{\Sigma}|^2 - \Delta_0^2|\mathbf{d}|^2\right)\mathrm{Re}\left[\tilde{\omega}\mathbf{q}\cdot\mathbf{\Sigma}^*\right] \\ & + 2\Delta_0^4\mathrm{Re}\left[|\mathbf{q}\cdot\mathbf{\Sigma}|^2 - (\mathbf{q}\cdot\mathbf{\Sigma})^2 + \mathbf{\Sigma}\cdot\mathbf{\Sigma}\mathbf{q}\cdot\mathbf{q}\right] \\ & + 2\Delta_0^2\mathrm{Re}\left[\left(|\tilde{\omega}|^2 - \tilde{\omega}^2\right) - \left(|\mathbf{\Sigma}|^2 - \mathbf{\Sigma}\cdot\mathbf{\Sigma}\right)\right]\left(|\mathbf{\Sigma}\cdot\mathbf{d}|^2 + |\mathbf{\Sigma}\cdot\mathbf{d}^*|^2\right) \\ & - 4\Delta_0^2|\mathbf{d}|^2|\tilde{\omega}|^2|\mathbf{\Sigma}|^2 \quad + 4\Delta_0^2\mathrm{Re}\left[\alpha_+(\mathbf{\Sigma}^*\cdot\mathbf{d}^*)(\mathbf{\Sigma}^*\cdot\mathbf{d})\right] \\ & - 4\Delta_0^2\mathrm{Re}\left[\left(\tilde{\omega}^2 - \Delta_0^2|\mathbf{d}|^2\right)\mathbf{\Sigma}^*\cdot\mathbf{\Sigma}^*\right], \end{aligned} \quad (29)$$

where $\alpha_\pm = \tilde{\omega}^2 - \Delta_0^2|\mathbf{d}|^2 \pm \mathbf{\Sigma}\cdot\mathbf{\Sigma}$. The derivation of thermal conductivity is provided in Supplementary Material. We calculate the full temperature dependence of thermal conductivity using the self-consistently determined superconducting gap using an effective pairing potential to obtain a single transition temperature (see Supplementary Material).

3 Results and discussion

3.1 $T = 0$ limit of the density of states and thermal conductivity

We start with the single-component states based on four irreducible representations of the D_{2h} point group symmetry. The basis functions for these four states are listed in Table 1, where the A_{1u} state remains gapped unless the coefficient of one of the basis functions is set to zero. We exclude that possibility and choose the same coefficients for all three basis functions, and this choice of coefficients is adopted for the other states as well, which is a reasonable choice for a qualitative understanding of the low-energy properties. In principle, it is also possible to generate line nodes with an appropriate choice of basis function coefficients, but those possibilities are excluded considering the recent experimental results on UTe_2. Apart from the A_{1u} state, the B_{1u} state also remains gapped because the open Fermi surface along the $\hat{z}$-axis forbids the nodes for this state. For the B_{2u} and B_{3u} states, a pair of point nodes exists along the $\hat{y}$-axis and $\hat{x}$-axis, respectively. Figures 1A–D show the disorder dependence of the thermal conductivity normalized to the normal state value at the transition as a function of relative reduction in the transition temperature $\delta t_c \equiv = 1 - T_c/T_{c0}$, where T_{c0} is the transition temperature in the clean limit. For a clean system, $\delta t_c = 0$, and δt_c reaches unity as the impurity scattering kills superconductivity. The normalized residual thermal conductivity $\kappa T_c/\kappa_N T$ in the zero-temperature limit remains 0 up to a threshold value of disorder Γ_{th} for all four states; this Γ_{th} corresponds to a threshold level of T_c suppression δt_c^{th}. This threshold value of disorder depends on the superconducting gap structure and the strength of the impurity potential [27]. For the gapped states A_{1u} and B_{1u}, the residual thermal conductivity remains 0 for slightly higher values of disorder compared to the other two states B_{2u} and B_{3u} as expected due to the presence of impurity-induced quasiparticle states near the nodes. The normalized thermal conductivity remains very isotropic for the A_{1u} and B_{1u} states. However, for the nodal states, the residual thermal conductivity is enhanced for thermal current along the nodal directions. This trend in anisotropy in thermal conductivity continues even at finite temperatures, as shown in the temperature evolution of $\kappa T_c/\kappa_N T$ for the four single-component states in Figures 1E–H for $\tan\theta_s = 2$ and in Figures 1I–L for $\tan\theta_s = 5$, which represents the stronger scatterers. For both impurity strengths, δt_c is 0.02. In the presence of the point nodes, the thermal conductivity shows a weak maximum at very low temperature along the nodal direction for the weak scatterers, which disappears as the scattering rate increases. This is a known behavior for the superconducting states with point nodes [28], which is not present for the stronger impurity potentials.

It is useful to examine the density of states (DOS) and the structure of the low-energy quasiparticle states before discussing the thermal transport for the nonunitary states. We first report the average density of states per spin for the nonunitary states on a cylindrical Fermi surface that is open along the $\hat{z}$-axis. Figure 2A shows the DOS for the $A_{1u} + irB_{2u}$ state, which is a chiral state, and Figures 2B–D show Δ_- for this state. In the gapped phase ($r < 1$), this state has minima near the $\hat{x}$-axis, and a small gap is visible in the DOS. For $r = 1$, a pair of point nodes appear along the $\hat{x}$-axis, and the low-energy DOS shows ω^2 behavior that is expected for linear point nodes. Here, and in subsequent discussions, a "node" refers to spectral nodes, not the gap nodes. However, in contrast to a unitary state, the low-energy quadratic behavior remains confined to a very low energy scale, as compared to the unitary B_{3u} state. For $r > 1$, the nodes move away

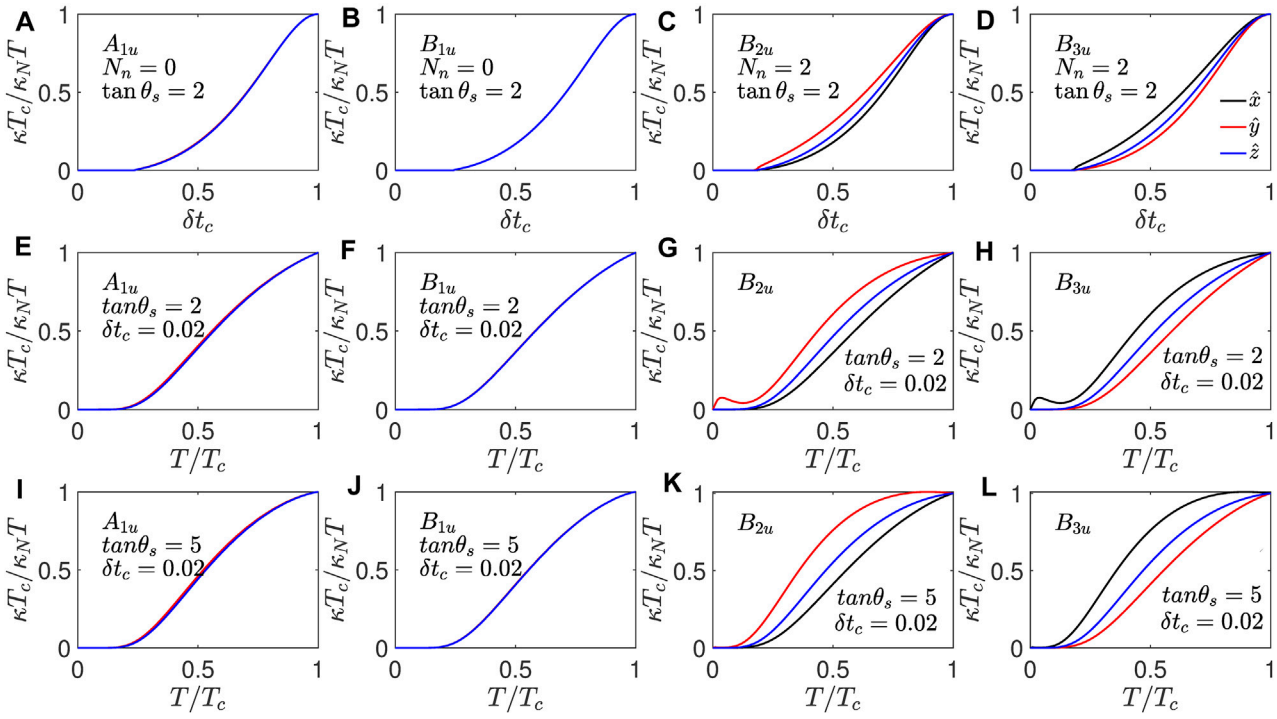

FIGURE 1
Thermal conductivity for the single-component unitary states allowed by the D_{2h} point group. The thermal conductivity normalized to its value at T_c for the four irreducible representations of the D_{2h} point group shown column-wise for the A_{1u}, B_{1u}, B_{2u}, and B_{3u} representations from **(A–D)**, respectively. The first row shows the residual thermal conductivity in the zero-temperature limit as a function of relative reduction in the transition temperature δt_c. **(E–H)** in the second row show $\kappa T_c/\kappa_N T$ for the weak scatterers with $\tan\theta_s = 2$ and for the intermediate-strength scatterers with $\tan\theta_s = 5$ from **(I–L)** in the third row. For the temperature dependence, the T_c is reduced by 2% ($\delta t_c = 0.02$) with respect to the clean limit.

from the $\hat{x}$-axis, and the positions of four nodes are determined by $\tan\phi = \pm\sqrt{r^2-1}$, where ϕ is the polar angle on the cylindrical Fermi surface. As the mixing parameter r increases, additional pairs of nodes appear in the yz plane at $\sin(k_z/2) = \pm 1/\sqrt{r^2-1}$. In the $r \to \infty$ limit, only two point nodes along the $\hat{y}$-axis survive, as expected for a pure B_{2u} state. The low-energy DOS remains quadratic in all these cases. For $1 \le r < \sqrt{2}$, the nodes remain closer to the $\hat{x}$-axis, and for $r \ge \sqrt{2}$, the nodes move closer to the $\hat{y}$-axis. The $A_{1u} + irB_{3u}$ state also shows similar DOS to the $A_{1u} + irB_{2u}$ state, but it has a different nodal structure. It has gap minima in the quasiparticle spectrum near the $\hat{y}$-axis, and nodes appear along the $\hat{y}$-axis. For $r > 1$, a set of four nodes appear near the $\hat{y}$-axis at $\phi = \pm\cot^{-1}\sqrt{r^2-1}$ and move toward the $\hat{x}$-axis in the xy-plane as the value of r increases. For $r > \sqrt{2}$, four more nodes appear at $k_z = \pm 2\sin^{-1}(1/\sqrt{r^2-1})$ in the xz-plane. Both these states are chiral and show finite quasiparticle spin density along $\hat{y}$ and $\hat{x}$ directions in the spin space. The last AF nonunitary state is $A_{1u} + irB_{1u}$, which is not a chiral state. It has nodes along the $\hat{x}$ and $\hat{y}$ directions for $r = 1$, a set of four point nodes in the xz-plane and another set of four point nodes in the yz-plane, where the k_z for the nodal position is determined by $\sin(k_z/2) = \pm\sqrt{r^2-1}$. The DOS shows quadratic behavior at low energies (see Supplementary Material).

Next, we consider the ferromagnetic nonunitary states on the cylindrical Fermi surface, which are chiral states with finite Cooper pair spin moment. Figure 2D shows the DOS for the $B_{1u} + irB_{2u}$ state along with the Δ_- in Figures 2E–F. This state is gapped for $r < 1/\sqrt{2}$, and a set of four point nodes appear in the yz-plane for $1/\sqrt{2} \le r < 1$, whose positions are determined by $\sin(k_z/2) = r/\sqrt{1-r^2}$. For $r > 1$, a set of four point nodes appear in the xy-plane at $\phi = \pm\tan^{-1}\sqrt{r^2-1}$ close to the $\hat{x}$-axis and move toward the $\hat{y}$-axis as r increases. These states show quadratic DOS at low energies. For $r = 1$, this state shows point nodes along the $\hat{x}$-axis, but these are the quadratic point nodes. The first derivative of Δ_- vanishes at the nodes for quadratic or second-order point nodes. This leads to linear DOS at low energies, as shown in Figure 2D. Similarly, for $B_{1u} + irB_{3u}$, a twin pair of quadratic point nodes appear along the $\hat{y}$-axis and shows linear DOS at low energies for $r = 1$. For $1/\sqrt{2} \le r < 1$, four point nodes appear at $\sin(k_z/2) = \pm\sqrt{1-r^2}/r$ in the yz-plane, and for $r > 1$, a set of four point nodes appear in the xy-plane at $\cot\phi = \pm\sqrt{r^2-1}$, closer to the $\hat{y}$-axis for $r \ge 1$, which move toward the $\hat{x}$-axis for $r \gg 1$. The DOS remains quadratic, as expected. For the $B_{2u} + irB_{3u}$ state, four point nodes are either located in the yz-plane at $\sin(k_z/2) = \pm r/\sqrt{1-r^2}$ for $r \le 1/\sqrt{2}$ or in the xz-plane at $\sin(k_z/2) = \pm 1/\sqrt{r^2-1}$ for $r \ge \sqrt{2}$. These states show ω^2 behavior in the low-energy DOS. For $1/\sqrt{2} < r < \sqrt{2}$, a gap exists in the quasiparticle spectrum due to lack of nodes (see Supplementary Material). In contrast to the AF nonunitary states on the cylindrical Fermi surface, the FM nonunitary states can have at most four nodes and are expected to be more anisotropic.

We now discuss the zero-temperature limit of the thermal conductivity, which is very sensitive to the gap structure. We

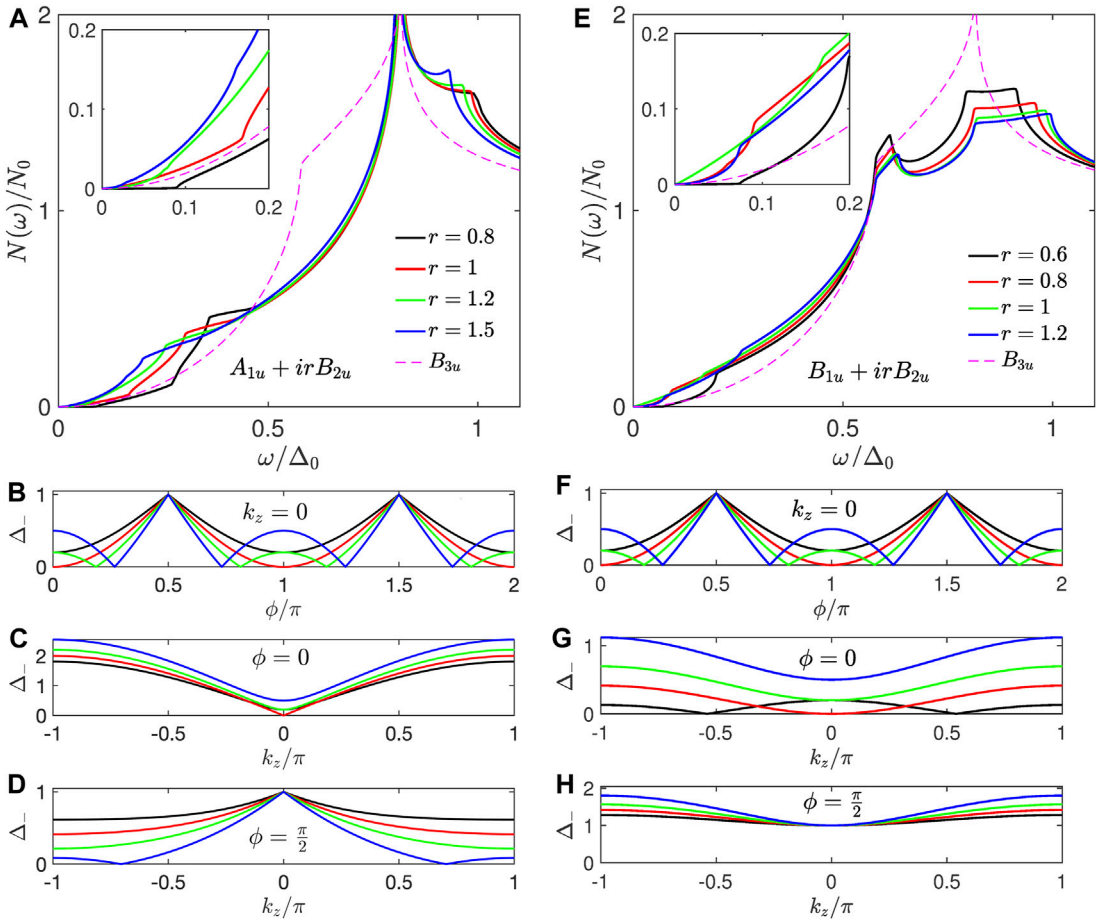

FIGURE 2
Density of states: **(A)** shows the density of states (DOS) per spin for the $A_{1u} + irB_{2u}$ state for different values of the mixing parameter r. The inset shows the energy dependence of the DOS at low energies. A dashed line illustrating the DOS for the unitary B_{3u} state is shown for comparison. **(B–D)** show the variation in Δ_- for different values of r in the xy, xz, and yz-planes, respectively. **(E)** shows the DOS per spin for the $B_{1u} + irB_{2u}$ state, and Δ_- in the xy, xz, and yz-planes is shown in panels **(F–H)**, respectively.

compare the normalized $\kappa T_c/T\kappa_N$ along three principal directions, where the thermal conductivity along a particular direction is normalized to its normal state value at T_c along that direction. This suppresses the intrinsic anisotropy present in the electronic structure and accentuates the effect of order parameter anisotropy. Figures 3A–D show $\kappa T_c/T\kappa_N$ in the zero-temperature limit for the $A_{1u} + irB_{1u}$ state as a function of the relative reduction in the transition temperature δT_c. For a weakly disordered system, κ/T vanishes in the zero-temperature limit, but as the disorder level increases and crosses Γ_{th}, $\kappa/T|_{T\to 0}$ becomes finite and reaches the normal-state value as the superconductivity vanishes. For the $A_{1u} + irB_{1u}$ state, $\kappa T_c/\kappa_N T$ shows isotropic behavior in the xy-plane. Note that for this state, the nodes are always along the $\hat{x}$ and $\hat{y}$ axes at the same k_z value. In contrast, the $B_{2u} + irB_{3u}$ state shows relatively weaker level anisotropy than a unitary state. Figures 3E–G show $\kappa T_c/\kappa_N T$ for the $B_{2u} + irB_{3u}$ state, while Figure 3H shows $\kappa T_c/\kappa_N T$ for the unitary B_{3u} state with nodes along the $\hat{x}$-axis. As shown in Figure 3E, with nodes in the yz-plane κ_{yy} and κ_{zz} exceeding κ_{xx}, and this behavior reverses as the nodes move to the xz-plane for the $B_{2u} + irB_{3u}$ state, as depicted in Figure 3H. As the value of r increases, the anisotropy also reduces, and for $r = 1$, the superconducting state becomes fully isotropic, as shown in Figure 3F. This is a special case, which has a four-fold symmetric Δ_-, leading to a very isotropic normalized thermal conductivity along the three principal directions. As r becomes larger than unity, the κ_{xx} starts to dominate.

Next, we look at the zero-temperature limit thermal conductivity for the $A_{1u} + irB_{2u}$ state for two different impurity potential strengths. Figures 4A–D show $\kappa T_c/\kappa_N T$ for s-wave scattering phase shift $\tan^{-1}(2)$, and panels Figures 4E–H show $\kappa T_c/\kappa_N T$ for $\theta_s = \tan^{-1}(5)$. $\kappa/T|_{T\to 0}$ becomes finite above a threshold disorder level, as in earlier cases. This threshold scattering rate is smaller for the stronger impurity potentials. This state has a minimum and maximum along the xz-plane, the energy gap is small in the yz-plane, and a weak maximum exists along the $\hat{y}$-axis in the xy-plane. This excitation energy spectrum is reflected in the thermal conductivity. As κ/T becomes finite, the in-plane anisotropy is very weak with a slightly larger value along the $\hat{x}$-axis as long as there is no node in the yz-plane. As the impurity-induced quasiparticles overcome the minima along the $\hat{y}$-axis, the thermal conductivity along the $\hat{y}$-axis starts to

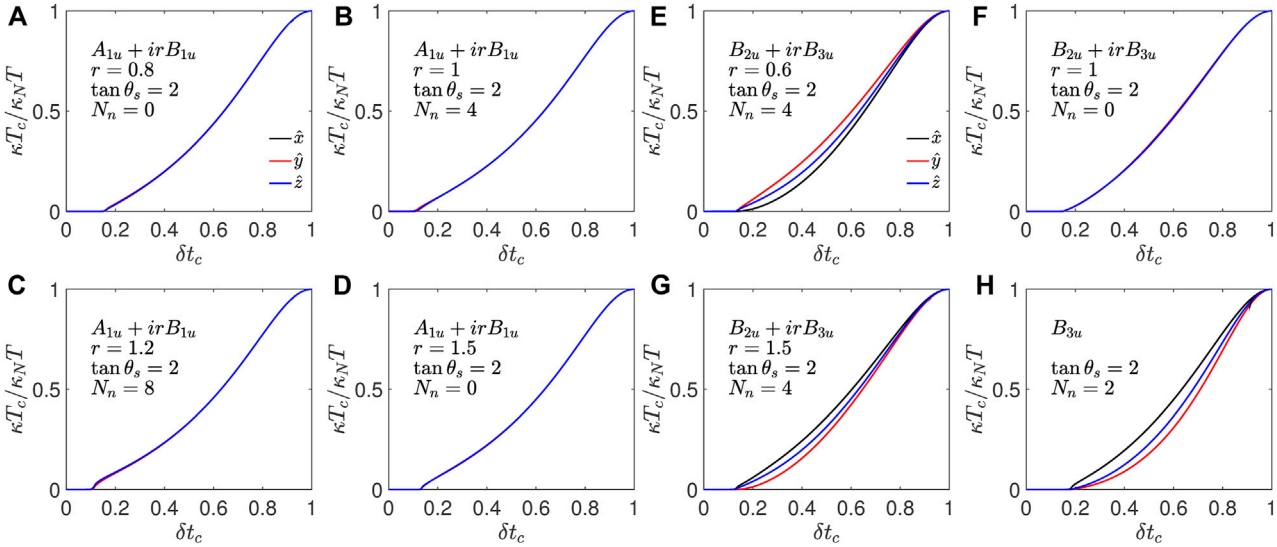

FIGURE 3
Residual thermal conductivity. Zero-temperature limit $\kappa T_c/\kappa_N T$ for the $A_{1u} + irB_{1u}$ in **(A–D)** and for the $B_{2u} + irB_{3u}$ state in **(E–G)** for various values of mixing parameter r. **(H)** shows $\kappa T_c/\kappa_N T|_{T\to 0}$ for the unitary B_{3u} state. The s-wave scattering phase shift is $\theta_s = \tan^{-1}(2)$ for all the panels. The number of nodes N_n is indicated for each case.

dominate. In the case of eight nodes, with four in the xy-plane and another four in the yz-plane, the thermal conductivity is always larger along the $\hat{y}$-axis. The $\hat{z}$-axis thermal conductivity remains close to the $\hat{x}$-axis thermal conductivity. For the $A_{1u} + irB_{3u}$ state, the thermal conductivity along the $\hat{x}$-axis and $\hat{y}$-axis shows the same behavior as κ_{yy}/T and κ_{xx}/T in the $A_{1u} + irB_{2u}$ state, respectively.

For the $B_{1u} + irB_{3u}$ state, in the gapped phase, i.e., $r < 1/\sqrt{2}$, the spectral gap on the Fermi surface is small in the yz-plane and near the $\hat{y}$-axis in the xy-plane, which leads to larger $\kappa/T|_{T\to 0}$ along the $\hat{y}$-axis, followed by the $\hat{z}$ direction, as shown in Figures 4I–M, for $\tan\theta_s = 2$ and $\tan\theta_s = 5$, respectively. As a set of four nodes appear in the yz-plane, the relative anisotropy remains the same, as shown in Figures 4J–N. This state also shows an elusive quadratic node for $r = 1$ along the $\hat{y}$-axis. Unlike the other states with linear point nodes, for this case, $\kappa/T|_{T\to 0}$ term remains finite along the nodes, and for other directions, residual thermal conductivity remains 0 below the threshold disorder level. This state shows linear DOS at low energies, like superconductors with line nodes. Finally, the nodes appear in the xy-plane for this state as r exceeds unity and remains closer to the $\hat{y}$-axis, and thermal conductivity along the $\hat{y}$-axis becomes dominant, while the other two directions show very similar $\kappa T_c/\kappa_N T$. As r increases, the in-plane anisotropy decreases, and the $\hat{x}$-axis κ increases and becomes stronger along the $\hat{y}$ direction in the $r \gg 1$ limit. For the $B_{1u} + irB_{2u}$ state, the in-plane anisotropy found for the $B_{1u} + irB_{3u}$ state gets interchanged.

3.2 Finite T electronic thermal conductivity

Now, we look at the temperature evolution of the normalized thermal conductivity for the nonunitary states. At very low temperatures, the elastic scattering by the impurities is the main mechanism of relaxation. However, as the temperature increases, the inelastic scattering also becomes important, which we discuss in the subsequent section. Apart from the electron contribution to thermal conductivity, phonon thermal conductivity can also become significant. Here, we focus on electronic thermal conductivity and the effect of impurity scattering on it and the effect of underlying spectral nodes on the anisotropy in the thermal conductivity. As shown in Figure 1, the thermal conductivity shows a weak maximum as a function of temperature at very low temperatures along the nodal directions. There is no evidence for such a feature in the experimental measurements [7, 34]; therefore, we set $\theta_s = \tan^{-1}(5)$ for the rest of our discussion (see Supplementary Material for the weaker impurity scatterers). We first consider the $A_{1u} + irB_{1u}$ state, which shows very isotropic residual thermal conductivity, and the thermal conductivity remains isotropic as a function of temperature, as shown in Figures 5A–D. For the clean system with $\delta t_c = 0.02$, at very low temperatures, the thermal conductivity remains negligibly small, and as the temperature increases, κ/T increases T^2 at very low temperatures. This behavior is observed for both nodal and gapped systems. Note that in superconductors with point nodes, there are very few states available at the Fermi energy, as shown in Figure 2. For dirtier systems such as $\delta t_c = 0.15$, there are sufficient quasiparticle states at the Fermi level to provide nonzero thermal conductivity, which is depicted in Figures 5E–H. At low temperatures, κ/T remains independent of temperature, and as it increases, once more, quasiparticles become relevant for transport as the temperature increases.

Next, we consider the $A_{1u} + irB_{2u}$ state, which shows enhanced thermal conductivity along the $\hat{y}$-axis. The zero-

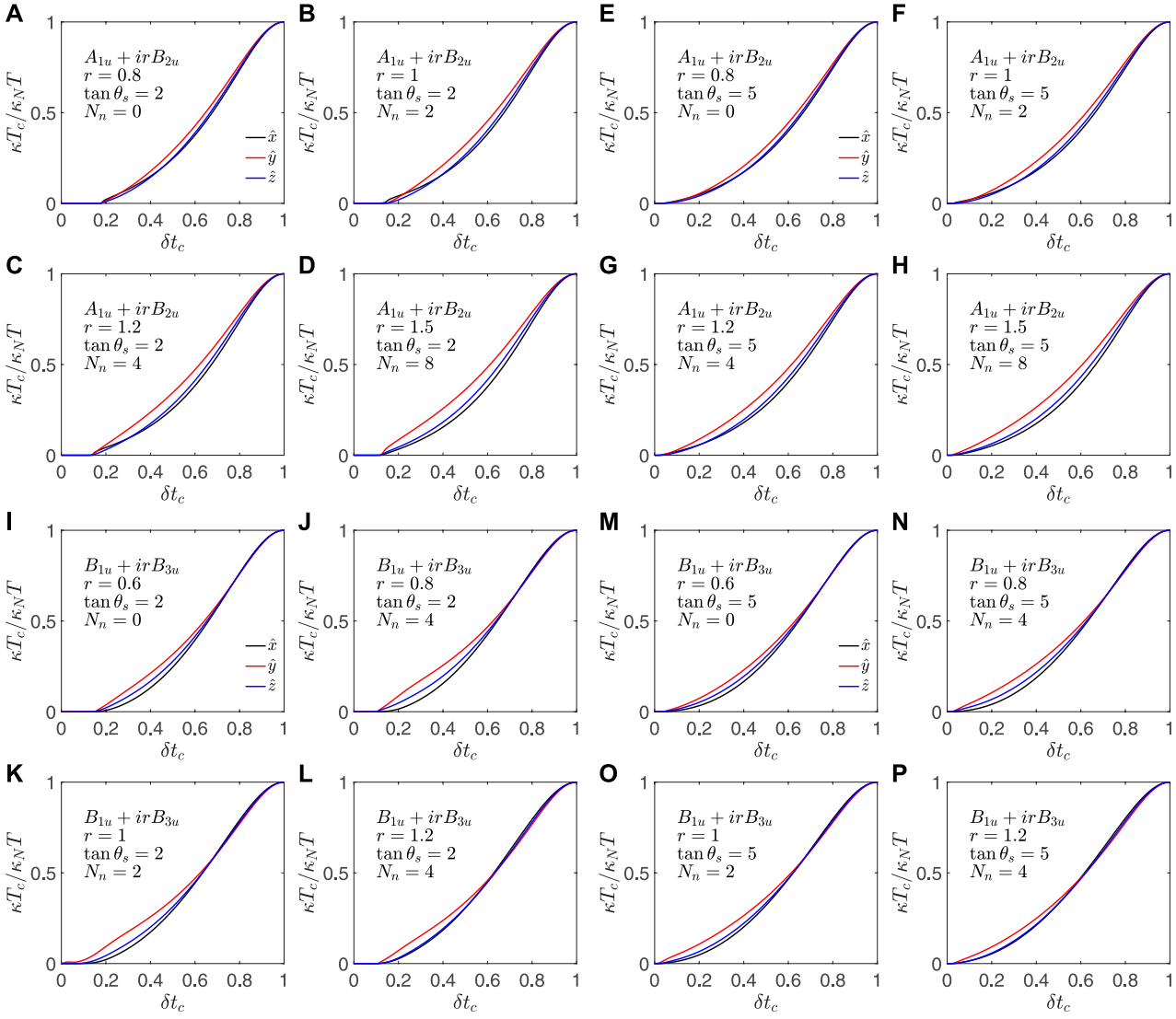

FIGURE 4
Residual thermal conductivity: **(A–H)** show κ/T in the zero-temperature limit normalized to κ_N/T at T_c as a function of relative T_c reduction δt_c for the $A_{1u} + irB_{2u}$ state for different values of the mixing parameter r. The s-wave scattering phase for **(A–D)** is $\theta_s = \tan^{-1}(2)$ and for panels **(E–H)** is $\theta_s = \tan^{-1}(5)$. For the $B_{2u} + irB_{3u}$ state, $\kappa T_c/\kappa_N T|_{T\to 0}$ is shown for various values of parameter r for the s-wave scattering phase shift $\theta_s = \tan^{-1}(2)$ in **(I–L)** and with $\theta_s = \tan^{-1}(5)$ in **(M–P)**. The number of nodes N_n is indicated for each case.

temperature trends in anisotropy continue as the temperature increases, as shown in Figure 6. For $\delta t_c = 0.02$, κ/T is close to 0 and increases as temperature increases beyond a critical value. For the gapped case ($r < 1$) and for the $\hat{x}$-axis nodes ($r = 1$), κ/T is slightly larger than that in the other two directions, but as the temperature increases, the other two directions begin to increase and dominate because the temperature overcomes the gap minima in the yz-plane. For $r > 1$, there are four point nodes that move toward the $\hat{y}$ axis, and it is reflected as a larger κ/T along the $\hat{y}$-axis. For $r > \sqrt{2}$, four more nodes in the yz-plane make κ/T along $\hat{y}$ and $\hat{z}$ directions larger than that in the $\hat{x}$ direction. For dirtier systems, thermal conductivity becomes finite and T-independent at very low temperatures, as in the earlier case, but the anisotropy remains similar to its zero-temperature limit. For $A_{1u} + iB_{3u}$, the behavior of $\hat{x}$ and $\hat{y}$ directions gets interchanged (see Supplementary Material).

Next, we consider the $B_{2u} + irB_{3u}$ state, which is one of the FM nonunitary chiral states. For this state, there are four point nodes in the yz-plane for $r < 1/\sqrt{2}$, and for $r > \sqrt{2}$, there is a set of four point nodes in the xz-plane. Figure 7 shows the thermal conductivity as a function of temperature, and as expected, κ/T along the nodal directions dominates. For $r < 1$, the thermal conductivity is enhanced along the $\hat{y}$ and $\hat{z}$ directions, and as r increases, the system becomes gapped with enhanced thermal conductivity in the $\hat{y}$ and $\hat{z}$ directions, but the anisotropy reduces. The state $r = 1$ shows completely isotropic behavior, and as r exceeds unity, this state shows a $\hat{x}$-axis-dominated

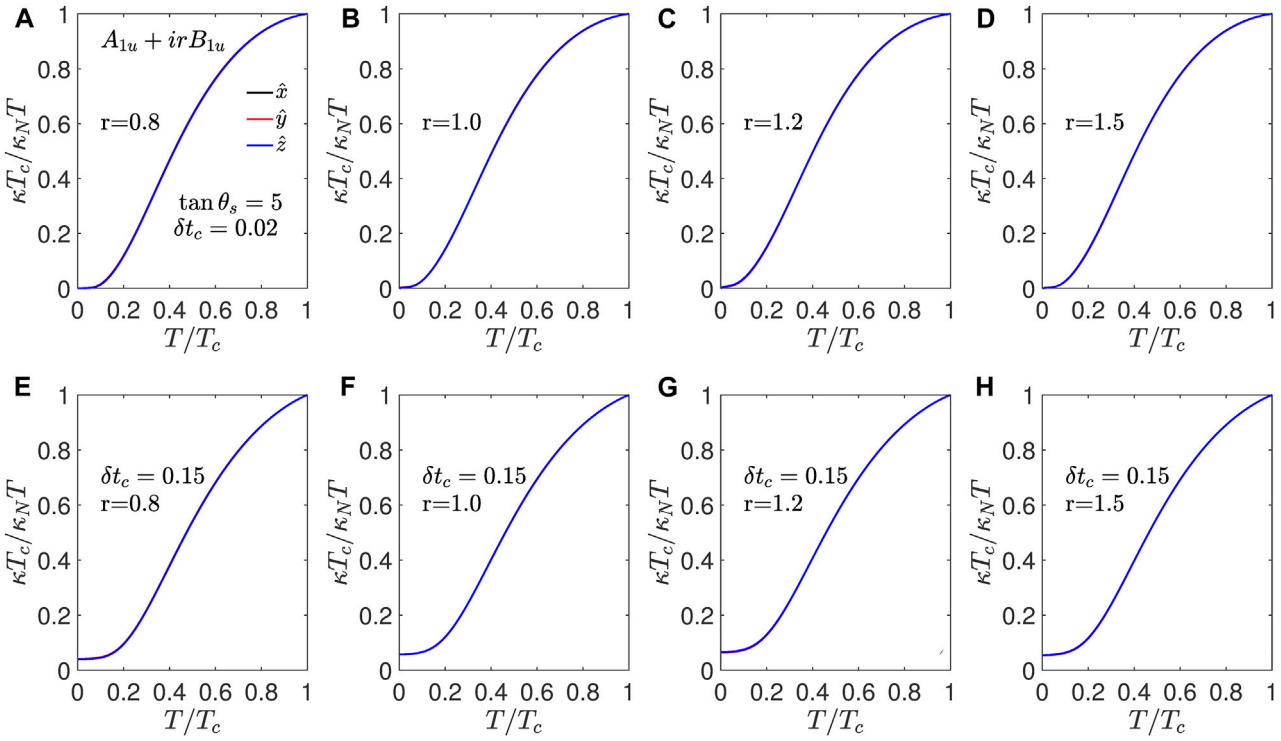

FIGURE 5
$A_{1u} + irB_{1u}$: Thermal conductivity normalized to its normal state value at T_c for $A_{1u} + irB_{1u}$ shown as a function of temperature normalized to T_c for scatterers with $\tan\theta_s = 5$ for $\delta t_c = 0.02$ from **(A–D)** and for $\delta t_c = 0.15$ in **(E–H)** for various values of mixing parameter r.

thermal response, as the nodes reappear in the xz-plane. The anisotropy remains qualitatively same as the temperature increases. Finally, we consider the $B_{1u} + irB_{3u}$ state, which is another possible FM nonunitary state that shows enhanced thermal conductivity along the $\hat{y}$ direction, as shown in Figure 8. Here, the anisotropy changes significantly as the temperature increases. At low temperatures, the $\hat{y}$-axis dominates due to its vicinity to the point nodes; however, as the temperature increases, $\kappa T_c/\kappa_N T$ increases along the $\hat{x}$ directions. This happens because at lower temperatures, the lower-energy branch of the quasiparticle excitations $\sqrt{\xi_{\mathbf{k}}^2 + \Delta_-^2}$ dominates, which has more quasiparticle states along the $\hat{y}$ directions, but at higher temperatures, the $\sqrt{\xi_{\mathbf{k}}^2 + \Delta_+^2}$ branch of the quasiparticle excitations begins to contribute, which, for this state, has minima along the $\hat{x}$-axis. The overall anisotropy for this state is relatively less compared to other states, except those that show fully isotropic behavior as a function of temperature or disorder. For the $B_{1u} + irB_{2u}$ state, κ/T along the $\hat{x}$ and $\hat{y}$ directions gets interchanged by the anisotropy shown by the $B_{1u} + irB_{3u}$ state.

3.3 Inelastic scattering effects

As mentioned in the previous section, at very low temperatures, i.e., $T \ll T_c$, the elastic scattering from impurities is the only mechanism that determines the scattering rate. However, at higher temperature, inelastic scattering from a bosonic mode is possible. We consider a simple scenario where there is a dispersionless bosonic mode that couples with the fermions with an effective coupling constant g_{fb}. We further assume that the coupling does not depend on the spin degree of freedom of the fermion. The lowest-order self-energy for the fermions reads

$$\Sigma_{in}(i\omega_n, \mathbf{k}) = g_{fb}^2 T \sum_{m,\mathbf{q}} G(i\omega_n - i\Omega_m, \mathbf{k} - \mathbf{q}) D(i\Omega_m, \mathbf{q}). \tag{30}$$

Here, D is the bosonic Green's function and ω_n and Ω_m are the fermionic and bosonic Matsubara frequencies, respectively. After performing the Matsubara summation, we obtain

$$\Sigma_{in}(\omega) = -\frac{g_{fb}^2}{2\pi}\int_{-\infty}^{\infty} dx \int_{-\infty}^{\infty} dy \frac{N(y)D''(x)}{x + y - \omega - i\eta} (\coth(\beta x/2) + \tanh(\beta y/2)). \tag{31}$$

Here, the real part of the self-energy contributes to mass renormalization, and the imaginary part modifies the scattering rate, which is a function of quasiparticle energy and temperature. Noting that UTe_2 has very high effective mass, we ignore the real part of the self-energy. The imaginary part of the self-energy is

$$\Sigma_{in}''(\omega) = -\frac{g_{fb}^2}{2}\int_{-\infty}^{\infty} dx N(\omega - x) D''(x) \times (\coth(\beta x/2) + \tanh(\beta(\omega - x)/2)), \tag{32}$$

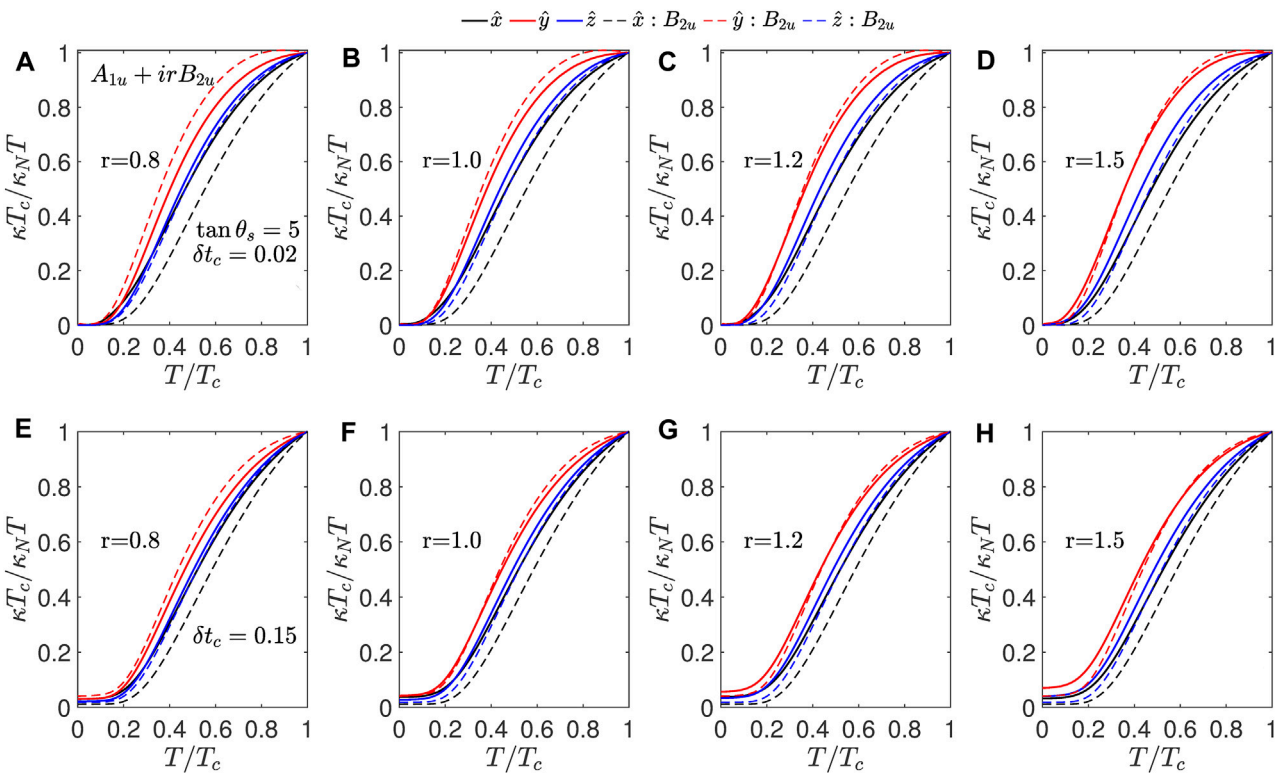

FIGURE 6
$A_{1u}+irB_{2u}$: Thermal conductivity normalized to its normal state value at T_c for $A_{1u}+irB_{2u}$ shown as a function of temperature normalized to T_c for scatterers with $\tan\theta_s=5$ for $\delta t_c=0.02$ from **(A–D)** and for $\delta t_c=0.15$ in **(E–H)** for various values of mixing parameter r. The dashed lines show the normalized thermal conductivities for the B_{2u} state with the same impurity parameters.

where $D''(x)\equiv x/(x^2+\Omega_0^2)$ is the bosonic DOS and Ω_0 is the characteristic energy scale associated with the bosonic mode. In the context of UTe_2, we expect $\Omega_0 \gg T_c$; therefore, we approximate the bosonic DOS as $D''(x)\approx x/\Omega_0^2$. In the zero-temperature limit, $\Sigma_{in}''\propto\omega^{n+2}$, where the DOS for the superconducting state behaves like ω^n at low energies. For linear point nodes, $\Sigma_{in}''\propto\omega^4$, and for quadratic point nodes or line nodes, it behaves like ω^3. Similarly, in the static limit ($\omega\to 0$), the imaginary part of the inelastic self-energy reads

$$\Sigma_{in}''(\omega=0,T)=-2g_{fb}^2\int_0^\infty dx\frac{N(x)D''(x)}{\sinh\beta x}. \tag{33}$$

Since the thermal response integrand is peaked at $\omega=0$, we only retain the temperature dependence of the inelastic self-energy at $\omega=0$. At very low temperatures, the inelastic scattering rate behaves likes T^4 for the point nodes and T^3 for the line nodes in the static limit. This is sufficient to understand the qualitative effect of inelastic scattering. The prefactor in Eq. 33 is fixed by the value of the inelastic scattering rate at T_c.

Figure 9 shows the effect of inelastic scattering on the electronic thermal conductivity. We show the results for two cases as the rest of the cases are qualitatively similar. The first row of Figures 9A–D shows the normalized thermal conductivity for the $A_{1u}+irB_{2u}$ state, which shows enhanced thermal conductivity along the $\hat{y}$-axis. Note that the normal state thermal conductivity includes the inelastic scattering. We fixed the value of r at 1.2, which leads to four point nodes in the xy-plane. The primary effect of inelastic scattering is the formation of a peak below T_c. This peak appears first for the directions that have larger thermal conductivity, as shown in Figure 9A for $\delta=0.02$. As the system becomes dirtier, the peaks get smeared, as depicted in Figure 9B for $\delta t_c=0.15$. If the strength of inelastic scattering increases, the peaks also strengthen, as shown in Figure 9C, and it may survive in dirtier systems, as illustrated in Figure 9D. Similar trends continue for the other states as well. Figures 9E–H show the normalized thermal conductivity for the $B_{1u}+irB_{3u}$ state, which shows the same qualitative behavior as a function of disorder and inelastic scattering strength. However, this state shows a nonmonotonic variation of anisotropy, and the peaks for different directions remain quite close to each other.

4 Summary and concluding remarks

We studied low-energy quasiparticle excitations and thermal transport for the single-component and two-component pairing states allowed by the irreducible representations of the D_{2h} point group symmetry, which is relevant for the orthorhombic UTe_2 crystals. Since D_{2h} has only one-dimensional representations, the four single-component pairing states corresponding to the

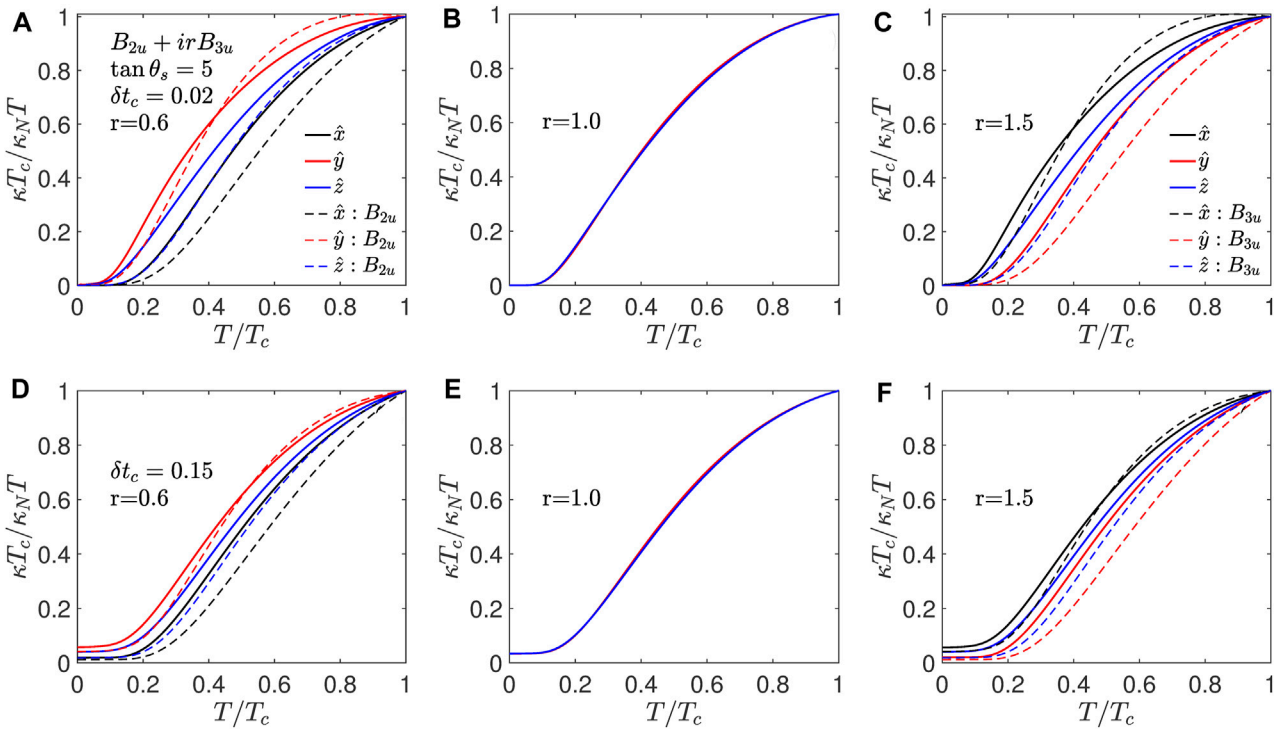

FIGURE 7
$B_{2u} + irB_{3u}$: Thermal conductivity normalized to its normal state value at T_c for $B_{2u} + irB_{3u}$ shown as a function of temperature normalized to T_c for scatterers with $\tan\theta_s = 5$ for $\delta t_c = 0.02$ from **(A–C)** and for $\delta t_c = 0.15$ in **(D–F)** for various values of mixing parameter r. The dashed lines show the normalized thermal conductivities for the B_{2u} state in **(A,D)** and for the B_{3u} state in **(C,F)**. The impurity parameters are the same for the single-component superconducting states.

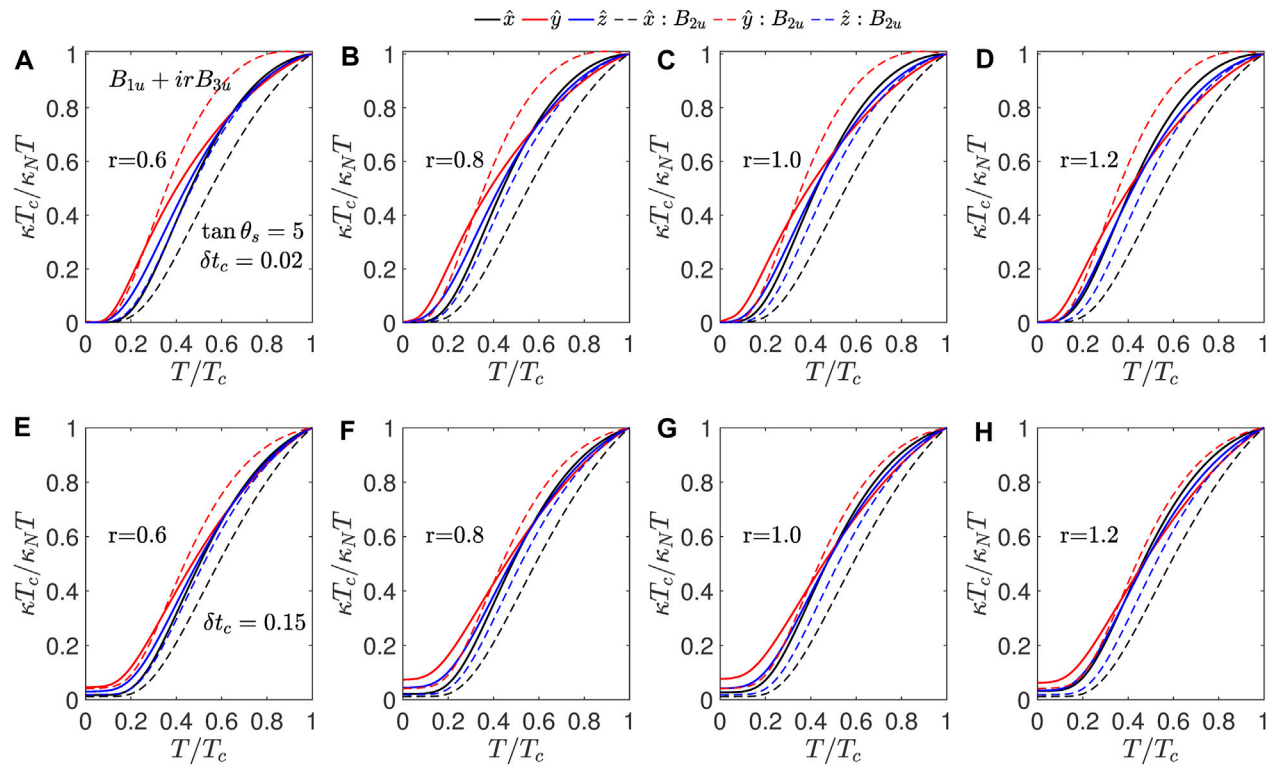

FIGURE 8
$B_{1u} + irB_{3u}$: Thermal conductivity normalized to its normal state value at T_c for $B_{1u} + irB_{3u}$ shown as a function of temperature normalized to T_c for scatterers with $\tan\theta_s = 5$ for $\delta t_c = 0.02$ from **(A–D)** and for $\delta t_c = 0.15$ in **(E–H)** for various values of mixing parameter r. The dashed lines show the normalized thermal conductivities for the B_{2u} state with same impurity parameters.

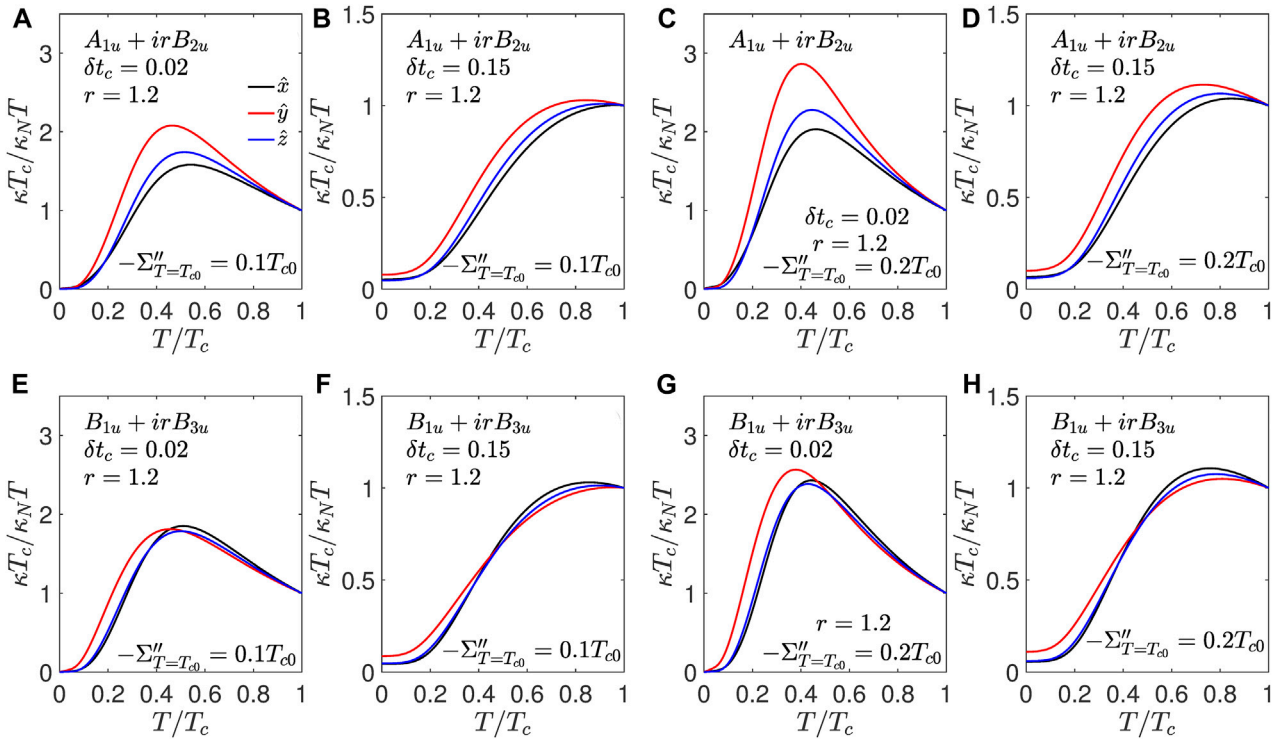

FIGURE 9
Effect of inelastic scattering: **(A–D)** show the temperature dependence of normalized thermal conductivity for the $A_{1u} + irB_{2u}$ state for $r = 1.2$. **(E–H)** show the temperature dependence of the normalized thermal conductivity for the $B_{1u} + irB_{3u}$ state. The imaginary part of the inelastic self energy at $T = T_{c0}$ and relative reduction in T_c are indicated in each panel. For brevity, we denote $\Sigma''_{in}(T = T_{c0})$ as $\Sigma''_{T=T_{c0}}$ The s-wave scattering phase is $\tan^{-1}(5)$. The relative reduction in T_c is indicated in each of the panels.

irreducible representations cannot break the time-reversal symmetry and describe unitary triplet pairing states. Therefore, we also considered the pairing states that are combinations of two of the four irreducible representations using a single mixing parameter r. We examined all six two-component superconducting states as a function of r on a cylindrical Fermi surface, which describe either gapped states or states with spectral point nodes depending on the value of the mixing parameter. The spectral point nodes are not necessarily the zeros of order parameters, but they are the points on the Fermi surface hosting quasiparticle excitations. The spectral nodes are identical to the gap nodes in the case of single-component or unitary states. These six states can be divided into AF or FM categories depending on the Fermi surface average of the Cooper pair spin moment, which vanishes for the AF states and remains finite for the FM states. Except for the $A_{1u} + irB_{1u}$ state, all other states are chiral on the cylindrical Fermi surface as the average angular momentum of the Cooper pairs remains finite.

After introducing the single-parameter model for the two-component states, we calculated the effect of impurity scattering within the self-consistent T-matrix approximation. One of the new findings is the spin-dependent impurity scattering rate for the chiral states. This happens due to finite quasiparticle spin densities for the chiral states. This can be interpreted as accumulation of magnetization near the impurity sites and this leads to qualitative changes in the quasiparticle excitation spectrum. For the two-component states, the nodes are accidental, not symmetry-imposed, like the single-component states, and the spin-dependent self-energy or the impurity-pinned magnetization can change the position of the spectral nodes. In principle, the removal of spectral point nodes by impurity scattering is possible in the chiral superconducting states, but we have not found such an effect for the cases that we considered. Next, we calculate the thermal conductivity using the Kubo formula for the thermal–current response function. Due to spin-dependent impurity self-energies, the thermal conductivity significantly differs from the thermal conductivity reported for the unitary states. We examine the thermal transport for all the single- and double-component states that are possible for the D_{2h} point group.

We have considered a single band with a cylindrical Fermi surface in our theoretical calculations. The quantum oscillation experiment reports two cylindrical Fermi surfaces, where one is an electron-like and the other is a hole-like Fermi surface with comparable effective masses [35]. However, we expect our analysis to be valid for a two-band system as well because interband scattering is always pair-breaking due to odd-parity order parameters. The impurity will renormalize the quasiparticle energies, and there will not be any off-diagonal impurity self-energy. Therefore, multiple bands will lead to a higher impurity scattering rate; this should not affect the

anisotropy of the thermal transport. There are also some speculations about a closed Fermi surface near the **Z** point; therefore, we also considered a spherical Fermi surface (see Supplementary Material). The key qualitative difference is the possibility of nodes along the $\hat{z}$-axis and strong thermal conductivity along that direction; however, there are no experimental data available to support that scenario.

Based on our thermal transport study and some recent experimental data, we can identify some states that could possibly describe the gap structure in UTe_2. Definitive conclusions are not possible at this time due to a lack of sufficient direction-dependent data on the newer samples, but we can make some qualitative statements and rule out some states. For the $A_{1u} + irB_{1u}$ state on a cylindrical Fermi surface, the normalized thermal conductivity shows isotropic behavior as a function of impurity scattering in the zero-temperature limit and in its temperature dependence for a fixed disorder level. The limited data that are available for the thermal conductivity indicate weak in-plane anisotropy, but not absolute isotropic behavior [7]. The thermal conductivity measurements obtained by [34] claim a fully gapped superconducting state. In contrast, another independent thermal conductivity measurement obtained by Hayes et al. shows evidence for point nodes without finding any residual thermal conductivity in the zero-temperature limit [8]. Therefore, the absence of finite zero-temperature limit thermal conductivity in high-quality samples is not sufficient to rule out point nodes. Other probes such as the field dependence of specific heat suggest a superconducting state with nodes closer to the $\hat{y}$-axis [36]. The superfluid density measurement indicates stronger low-energy quasiparticle excitations along the $\hat{y}$ directions and weakest along the $\hat{x}$-axis [29]. The relative anisotropy in the penetration depth measurements is weaker than that in the single-component states. We find that the $A_{1u} + irB_{2u}$, $B_{2u} + irB_{3u}$ state with a dominant B_{2u} component and the $B_{1u} + irB_{3u}$ state show stronger quasiparticle excitations along the $\hat{y}$-axis. The $B_{1u} + irB_{3u}$ state shows a change in anisotropy as a function of temperature, which can be used to distinguish it from the other two states. This state also shows a quadratic point node for $r = 1$, which shows linear DOS at low energies; hence, it can also be ruled out. The two ferromagnetic states show higher thermal conductivity along the $\hat{y}$ direction than the B_{2u} state, which has point nodes along the $\hat{y}$-axis.

As mentioned earlier, the phonon thermal conductivity could be significant, especially in the low T_c samples. At very low temperatures, the scattering of phonons from defects dictates the phonon mean free path, and hence the phonon thermal conductivity [37–39]. Phonon thermal conductivity is expected to be insignificant in the high-quality samples due to the low concentration of defects. Therefore, a systematic measurement of thermal conductivity along all three directions in the samples with high residual resistivity ratios is highly desirable. One common feature among all these superconducting phases is zero κ/T in the zero-temperature limit in clean samples. For sufficient disorder, even point nodal states acquire a very small residual κ/T, which would require very careful low-T measurements to detect.

Data availability statement

The original contributions presented in the study are included in the article/Supplementary Material; further inquiries can be directed to the corresponding authors.

Author contributions

VM: writing–original draft and writing–review and editing. GW: writing–original draft and writing–review and editing. PH: writing–original draft and writing–review and editing.

Funding

The author(s) declare that financial support was received for the research, authorship, and/or publication of this article. PH was supported by the NSF under DMR-2231821.

Acknowledgments

The authors thank S. Anlage, I. Hayes, T. Metz, J.P. Paglione, and T. Shibauchi for useful discussions.

Conflict of interest

The authors declare that the research was conducted in the absence of any commercial or financial relationships that could be construed as a potential conflict of interest.

Publisher's note

Supplementary material

The Supplementary Material for this article can be found online at: https://www.frontiersin.org/articles/10.3389/fphy.2024.1397524/full#supplementary-material

References

1. Ran S, Eckberg C, Ding QP, Furukawa Y, Metz T, Saha SR, et al. Nearly ferromagnetic spin-triplet superconductivity. *Science* (2019) 365:684–7. doi:10.1126/science.aav8645

2. Aoki D, Ishida K, Flouquet J. Review of U-based ferromagnetic superconductors: comparison between UGe_2, URhGe, and UCoGe. *J Phys Soc Jpn* (2019) 88:022001. doi:10.7566/JPSJ.88.022001

3. Aoki D, Brison JP, Flouquet J, Ishida K, Knebel G, Tokunaga Y, et al. Unconventional superconductivity in UTe_2. *J Phys Condensed Matter* (2022) 34: 243002. doi:10.1088/1361-648X/ac5863

4. Fujibayashi H, Nakamine G, Kinjo K, Kitagawa S, Ishida K, Tokunaga Y, et al. Superconducting order parameter in ute2 determined by knight shift measurement. *J Phys Soc Jpn* (2022) 91:043705. doi:10.7566/JPSJ.91.043705

5. Matsumura H, Fujibayashi H, Kinjo K, Kitagawa S, Ishida K, Tokunaga Y, et al. Large reduction in the a-axis knight shift on UTe_2 with $T_c = 2.1$ k. *J Phys Soc Jpn* (2023) 92:063701. doi:10.7566/JPSJ.92.063701

6. Aoki D, Nakamura A, Honda F, Li D, Homma Y, Shimizu Y, et al. Unconventional superconductivity in heavy fermion ute2. *J Phys Soc Jpn* (2019) 88:043702. doi:10.7566/JPSJ.88.043702

7. Metz T, Bae S, Ran S, Liu IL, Eo YS, Fuhrman WT, et al. Point-node gap structure of the spin-triplet superconductor ute_2. *Phys Rev B* (2019) 100:220504. doi:10.1103/PhysRevB.100.220504

8. Hayes IM, Metz TE, Frank CE, Saha SR, Butch NP, Mishra V, et al. Robust nodal behavior in the thermal conductivity of superconducting UTe_2. *arXiv:2402* (2024): 19353. doi:10.48550/arXiv.2402.19353

9. Volovik GE, Gorkov LP. Superconducting classes in heavy-fermion systems. *Zh Eksp Teor Fiz* (1985) 88:1412–28.

10. Ueda K, Rice TM. p-wave superconductivity in cubic metals. *Phys Rev B* (1985) 31: 7114–9. doi:10.1103/PhysRevB.31.7114

11. Blount EI. Symmetry properties of triplet superconductors. *Phys Rev B* (1985) 32: 2935–44. doi:10.1103/PhysRevB.32.2935

12. Ran S, Liu IL, Eo YS, Campbell DJ, Neves PM, Fuhrman WT, et al. Extreme magnetic field-boosted superconductivity. *Nat Phys* (2019) 15:1250–4. doi:10.1038/s41567-019-0670-x

13. Wang Z, Rodriguez JO, Jiao L, Howard S, Graham M, Gu GD, et al. Evidence for dispersing 1D Majorana channels in an iron-based superconductor. *Science* (2020) 367: 104–8. doi:10.1126/science.aaw8419

14. Kitaev AY. Unpaired majorana fermions in quantum wires. *Physics-Uspekhi* (2001) 44:131–6. doi:10.1070/1063-7869/44/10S/S29

15. Wilczek F. Majorana returns. *Nat Phys* (2009) 5:614–8. doi:10.1038/nphys1380

16. Ivanov DA. Non-abelian statistics of half-quantum vortices in *p*-wave superconductors. *Phys Rev Lett* (2001) 86:268–71. doi:10.1103/PhysRevLett.86.268

17. Chung SB, Zhang HJ, Qi XL, Zhang SC. Topological superconducting phase and majorana fermions in half-metal/superconductor heterostructures. *Phys Rev B* (2011) 84:060510. doi:10.1103/PhysRevB.84.060510

18. Hayes IM, Wei DS, Metz T, Zhang J, Eo YS, Ran S, et al. Multicomponent superconducting order parameter in UTe_2. *Science* (2021) 373:797–801. doi:10.1126/science.abb0272

19. Rosa PFS, Weiland A, Fender SS, Scott BL, Ronning F, Thompson JD, et al. Single thermodynamic transition at 2 k in superconducting UTe_2 single crystals. *Commun Mater* (2022) 3:33. doi:10.1038/s43246-022-00254-2

20. Sakai H, Opletal P, Tokiwa Y, Yamamoto E, Tokunaga Y, Kambe S, et al. Single crystal growth of superconducting ute_2 by molten salt flux method. *Phys Rev Mater* (2022) 6:073401. doi:10.1103/PhysRevMaterials.6.073401

21. Ajeesh MO, Bordelon M, Girod C, Mishra S, Ronning F, Bauer ED, et al. The fate of time-reversal symmetry breaking in UTe_2. *Phys. Rev. X* (2023) 13:041019. doi:10.1103/PhysRevX.13.041019

22. Azari N, Yakovlev M, Rye N, Dunsiger SR, Sundar S, Bordelon MM, et al. Absence of Spontaneous magnetic fields due to time-reversal symmetry breaking in Bulk superconducting UTe_2. *Phys. Rev. Lett.* (2023) 131:226504. doi:10.1103/PhysRevLett.131.226504

23. Theuss F, Shragai A, Grissonnanche G, Hayes IM, Saha SR, Eo YS, et al. Single-component superconductivity in UTe_2 at ambient pressure. *Nat. Phys.* (2024). doi:10.1038/s41567-024-02493-1

24. Ambegaokar V, Griffin A. Theory of the thermal conductivity of superconducting alloys with paramagnetic impurities. *Phys Rev* (1965) 137:A1151–67. doi:10.1103/PhysRev.137.A1151

25. Kadanoff LP, Martin PC. Hydrodynamic equations and correlation functions. *Ann Phys* (1963) 24:419–69. doi:10.1016/0003-4916(63)90078-2

26. Schmitt-Rink S, Miyake K, Varma CM. Transport and thermal properties of heavy-fermion superconductors: a unified picture. *Phys Rev Lett* (1986) 57:2575–8. doi:10.1103/PhysRevLett.57.2575

27. Hirschfeld P, Vollhardt D, Wölfle P. Resonant impurity scattering in heavy fermion superconductors. *Solid State Commun* (1986) 59:111–5. doi:10.1016/0038-1098(86)90190-0

28. Hirschfeld PJ, Wölfle P, Einzel D. Consequences of resonant impurity scattering in anisotropic superconductors: thermal and spin relaxation properties. *Phys Rev B* (1988) 37:83–97. doi:10.1103/PhysRevB.37.83

29. Ishihara K, Roppongi M, Kobayashi M, Imamura K, Mizukami Y, Sakai H, et al. Chiral superconductivity in UTe_2 probed by anisotropic low-energy excitations. *Nat Commun* (2023) 14:2966. doi:10.1038/s41467-023-38688-y

30. Marchenko VI. On the theory of gauge symmetry of superconductors. *Zh Eksp Teor Fiz* (1986) 93:583–9.

31. Sigrist M, Rice TM. Symmetry classification of states in high temperature superconductors. *Z Phys B* (1987) 68:9–14. doi:10.1007/BF01307857

32. Annett JF. Symmetry of the order parameter for high-temperature superconductivity. *Adv Phys* (1990) 39:83–126. doi:10.1080/00018739000101481

33. Fledderjohann A, Hirschfeld P. Thermal conductivity anisotropy in superconducting UPt_3. *Solid State Commun* (1995) 94:163–7. doi:10.1016/0038-1098(95)00050-X

34. Suetsugu S, Shimomura M, Kamimura M, Asaba T, Asaeda H, Kosuge Y, et al. Fully gapped pairing state in spin-triplet superconductor UTe_2. *Sci Adv.* (2024) 10: eadk3772. doi:10.1126/sciadv.adk3772

35. Aoki D, Sakai H, Opletal P, Tokiwa Y, Ishizuka J, Yanase Y, et al. First observation of the de haas–van alphen effect and fermi surfaces in the unconventional superconductor UTe_2. *J Phys Soc Jpn* (2022) 91:083704. doi:10.7566/JPSJ.91.083704

36. Lee S, Woods AJ, Rosa PFS, Thomas SM, Bauer ED, Lin SZ, et al. Anisotropic field-induced changes in the superconducting order parameter of ute2. *arXiv:2310.04938.* (2023). doi:10.48550/arXiv.2310.04938

37. Klemens PG. The scattering of low-frequency lattice waves by static imperfections. *Proc Phys Soc London, Sect A* (1955) 68:1113–28. doi:10.1088/0370-1298/68/12/303

38. Bardeen J, Rickayzen G, Tewordt L. Theory of the thermal conductivity of superconductors. *Phys Rev* (1959) 113:982–94. doi:10.1103/PhysRev.113.982

39. Uher C Thermal conductivity of high-tcsuperconductors. *J Superconductivity* (1990) 3:337–89. doi:10.1007/BF00617463

frontiers | Frontiers in Physics

TYPE Review
PUBLISHED 05 September 2024
DOI 10.3389/fphy.2024.1406242

OPEN ACCESS

EDITED BY
Nigel Hussey,
University of Bristol, United Kingdom

REVIEWED BY
Peter Hirschfeld,
University of Florida, United States
Sergio Caprara,
Sapienza University of Rome, Italy
Matthias Eschrig,
University of Greifswald, Germany

*CORRESPONDENCE
Henri Alloul,
alloul@lps.u-psud.fr

RECEIVED 24 March 2024
ACCEPTED 05 August 2024
PUBLISHED 05 September 2024

CITATION
Alloul H (2024) What do we learn from impurities and disorder in high-T_c cuprates? *Front. Phys.* 12:1406242.
doi: 10.3389/fphy.2024.1406242

What do we learn from impurities and disorder in high-T_c cuprates?

Henri Alloul*

Université Paris-Saclay, CNRS, Laboratoire de Physique des Solides, Orsay, France

A series of experimental studies established that the differing morphologies of the phase diagrams *versus* hole doping n_h of the various cuprate families are mostly controlled by defects and disorder. In the minimally disordered cuprate Yttrium Baryum Copper Oxide (YBCO) we introduced controlled detfects that allowed us to probe the metallic and superconducting states. We demonstrate that the extent of the spin glass phase and the superconducting dome can be controlled by the concentration of spinless (Zn, Li) impurities substituted on the planar Cu sites. NMR frequency shift measurements establish that these defects induce, in their vicinity, a cloud with a Kondo-like paramagnetic behavior. Its "Kondo" temperature and spatial extent differ markedly between the pseudogap and strange metal regimes. We have performed transport measurements on single crystals with a controlled content of in-plane vacancies introduced by electron irradiation. At high T, the inelastic scattering of the carriers has been found independent of disorder and completely governed by the excitations of the correlated electronic state. The low T upturns in the resistivity associated with single-site Kondo-like scattering are qualitatively in agreement with local magnetism induced by spinless impurities. The apparent metal insulator crossover is only detected for a very large defect content, and part of the large resistivity upturn remains connected with Kondo-like paramagnetism. In the superconducting state, the defect-induced reduction of T_c scales linearly with the increase in residual resistivity induced by disorder. High-field magnetoresistance experiments permit us to determine the paraconductivity due to superconducting fluctuations. The latter vanishes beyond a temperature T'_c and a field H'_c that both decrease with increasing in-plane defect content. In the pseudogap regime, the weaker decrease of T'_c with respect to that of T_c reveals a large loss of superconducting phase coherence in the presence of disorder. In light of our experimental results, we initiate a discussion of its interplay with pair breaking. Our data also permit us to confirm that the differing phase diagrams are due to competing orders or disorders that are family-specific. In the ideal phase diagram of a disorder-free cuprate, 2D superconductivity should persist at low doping. This ensemble of experimental results provides serious challenges for the theoretical understanding of superconductivity in these correlated electron systems.

KEYWORDS

cuprates, phase diagrams, strange metal behavior, pseudogap and impurity effects, Kondo-like effects, paraconductivity, fluctuations, superconductivity

1 Introduction

Impurities and disorder play a major role in solid state physics, as could be already shown in materials for which an independent electron approximation holds. They govern the mechanical and optical properties of most materials. The chemical nature of impurities determines, for instance, the beautiful colors of gems that are large bandgap insulators. The transport properties of semiconductors were only under control when it became clear that the carrier content is associated with the chemical properties of the impurities and their concentration. The low-temperature electronic and thermal conductivity of metals are limited by the scattering of carriers on impurities and lattice defects. In the metals that display a superconducting state at low T, the disorder favors the type II state and plays a major role in the pinning of vortices and so on.

One does naturally expect then to find that disorder has a strong influence on the original physical properties displayed by materials in which electronic interactions are dominant, such as high-T_c cuprates [1]. These are materials involving a large number of atomic species. They are then likely expected to house a variety of impurities or lattice defects. On the experimental side, they are quasi unavoidable and intrinsic to the growth of the materials. The basic structure of cuprates is a set of layered CuO_2 planes separated by charge reservoir layers. The former is responsible for the original physical properties, while the latter is essential to control the electron or hole doping of the CuO_2 planes. On the theory side, one faces a sufficiently complex theoretical challenge in trying to explain the properties of a single CuO_2 plane with increasing doping. One generally considers impurities and disorder as unwanted complications.

In actual cuprates, defects are always present and, for experimentalists, the real difficulty is to decide whether the observed physical properties are generic, that is, due to the ideal defect-free cuprate plane. Most of the works reported in this article are attempts to isolate those from the extrinsic effects related to the chemical doping procedure. It can altogether be shown as well that defects or impurities injected in a controlled manner can be excellent probes of the properties of the pure material.

An essential approach to reach this aim is to eliminate as much as one can the sources of disorder that smear or influence the measured properties. Improving the sample preparation procedure is an obvious method to achieve this task. An alternative approach is to compare the properties of different cuprate families to sort out the generic properties from those that are specific or marginal. Once this has been performed, that is, a rather disorder-free compound or family has been selected, one might then try to introduce defects in a controlled manner in that pure material. One may then use both thermodynamic and local probes to determine the influence of specific defects on the physical properties. I shall show that those observations sometimes bring new information hardly accessible experimentally on the pure material [2].

I have initiated such an orientation in my research group since the early days of the discovery of high T_c superconductivity and encouraged many researchers in the Orsay-Saclay area to follow this approach over the last 35 years. I summarize here the various important results obtained that allowed some understanding of the experimental properties of cuprates and still raise important questions to be resolved on the theory side.

I shall consider first in Section 2 the (T,n_h) phase diagram of diverse hole doped cuprate families and show that its morphology is driven by the existing disorder, which raises the question about the actual phase diagram which should represent the hypothetical disorder-free cuprate. This will further allow me to categorize the cuprate families with increasing disorder. I shall then show that the Yttrium Baryum Copper Oxide (YBCO) family is among the cleanest cases where one could investigate the influence of an increasing content of defects. This allowed me to present in Section 3 the local NMR studies of the magnetic properties induced by Zn and Li spinless impurities in the metallic state of the CuO_2 planes. Using highly energetic electron irradiation allowed one to control the introduction of vacancies in the CuO_2 planes in cuprate single crystals. Their influence on the transport properties was identical to that produced by Zn chemical substitutions. We could, therefore, perform a refined comparison of the evolution with the defect content of the normal state transport and magnetic properties. In Section 4, I shall then present results on the corresponding modifications of the SC properties such as the decrease of T_c. Similarly, I shall describe a detailed investigation of the evolution with a disorder of the superconducting fluctuation range, using high magnetic fields when necessary. The importance of the loss of phase coherence in the 2D SC state in the presence of disorder will be underlined. A discussion of this ensemble of results, done in Section 5, will permit to summarize that one cannot any more consider disorder effects as unnecessary complications. They rather permit to raise many essential questions and give useful guidance for theory.

2 Cuprate phase diagrams and disorder

Let me perform first a small historical survey about the discovery of cuprates and of their phase diagram and discuss hereafter my present understanding of the influence of disorder.

2.1 Early phase diagrams of cuprates

The first cuprate discovered by Bednorz and Muller has been the family of 124 compounds [3]. The parent La_2CuO_4 is an AF Mott insulator with T_N = 240 K that can be doped by substitution of a concentration x of La^{3+} by Ba^{2+} or Sr^{2+} [4]. The long-range ordered AF state is destroyed for x = 2%, and an SC dome appears for $0.07 < x < 0.3$ with a maximum T_c = 38 K for $x \sim 0.19$. From simple chemical arguments, the concentration of holes in the CuO_2 planes is merely $n_h = x$ and most researchers have immediately considered that this (T,n_h) phase diagram is generic of the cuprate plane. One noticed as well that the material displays in the intermediate range $0.02 < x < 0.07$ a low T disordered frozen spin state of the Cu $3d^9$ magnetic sites labeled as spin glass (SG).

A year later, the $YBa_2Cu_3O_{6+x}$ family has been discovered [5], with a parent AF state as well with T_N = 410 K for $x = 0$ and part of a SC dome with a maximum T_c = 93 K. This compound involves two CuO_2 layers with an intermediate Y^{3+} layer. Successive bilayers are separated by a square lattice layer of non-magnetic Cu^+ for $x = 0$. The

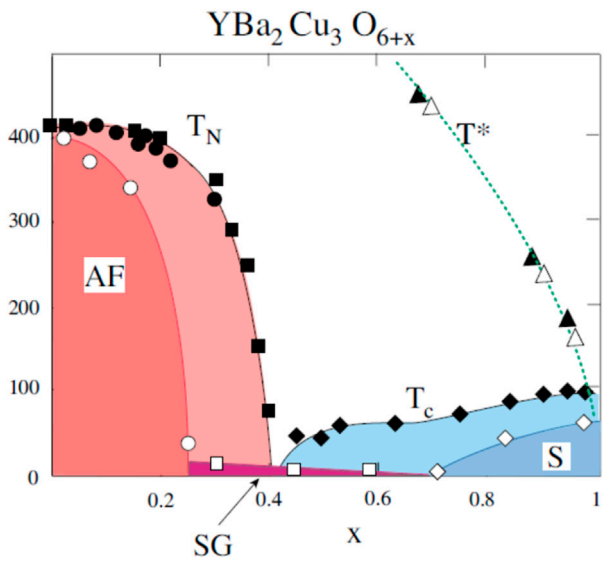

FIGURE 1
Phase diagrams of the AF Néel temperature T_N, spin glass transition T_{SG}, SC transition T_c, and pseudogap T^* for pure YBCO samples (filled symbols) and for 4% Zn substitution (empty symbols). From Ref. [6].

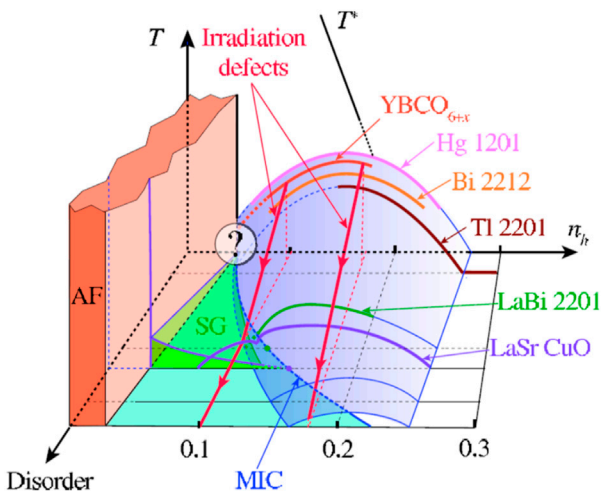

FIGURE 2
Variation in the (T,n_h) phase diagram for increasing disorder. The red lines represent the T_c variation with disorder induced by electron irradiation in YBCO (See Section 3 in the text). The doping range of the AF state slightly shrinks with increasing disorder for instance with Zn content, or with Ca content in Y_{1-y} Ca_yBCO_6 (see text in Section 2.2). The T_c domes reported for the various cuprate families are limited to the experimentally accessible doping ranges. Their positions on the disorder axis are chosen in order to roughly match their SG ranges with those expected with increasing Zn-induced disorder in YBCO. From Ref. [12].

hole doping for $x > 0$ results from the extra oxygen atoms introduced in this intermediate Cu layer. The relation between x and n_h is not straightforward as the Cu^{2+}-O^{2-}- Cu^{2+} chain segments formed do not transfer charge in the CuO_2 planes. The phase diagram displayed in Figure 1 is quite similar to that of La_2CuO_4, but the AF phase is contiguous to the SC phase [7]. An important difference is therefore the absence of an intermediate SG regime. Although this is a very important distinction, many researchers mostly interested by the SC properties considered that as a minor difference and mapped the n_h ranges in the 124 and YBCO phase diagrams by an artificial parabolic fit of the SC domes [8].

In our preliminary experiments with Zn impurities in $YBa_2Cu_3O_{6+x}$, we immediately found that the reduction of T_c was larger in the underdoped regime than in the optimally doped case. This Zn induced in plane disorder has then led us to notice changes in the morphology of the phase diagram (PD), as displayed in Figure 1 [9]. Then, we plotted together the PD *versus* oxygen content x for pure samples and for 4% Zn substitution [6]. One can see that both extents of the AF phase and the SC dome shrink and disclose a wide SG regime. The morphology of the PD resembles then markedly that of the 124 family upon this introduction of disorder. The latter, therefore, plays a major role in defining the extent of the SG regime in the cuprates. This observation also implied that the n_h mapping between phase diagrams is not accurate.

This occurred at the very time of the PG discovery in the underdoped pure YBCO using ^{89}Y NMR shift data [10]. I initiated these Zn substitution experiments mostly to try to understand whether the PG had any relation with superconductivity. With 4% Zn substitution, our ^{89}Y NMR data immediately convinced us that T^* unchanged even for the underdoped $YBCO_{6.6}$ sample, for which SC is fully suppressed [9]. This total independence of the two effects suggested that the PG is a phenomenon that competes with the SC state. This powerful indication revealed by introduction of Zn impurities does not, however, allow to conclude whether T^* corresponds to a phase transition in the defect-free compound. The actual disorder introduced by the Zn substitution might indeed prevent a long-range ordering.

We were, at that time, most concerned by an important question concerning the PG. What could explain the large T_c difference at optimal doping between the 124 and YBCO families? Could that be associated with an intrinsic difference between compounds with single CuO_2 layers and those with bilayers in the unit cell? We completely cleared that question by performing the first study of powder samples of the single-layer Hg1201 cuprate family, for which the optimum T_c is approximately 85 K. We could synthesize samples covering a large range of doping from the underdoped to the overdoped regime. The comparison of ^{17}O NMR shift data with that taken in the YBCO family allowed us to demonstrate that PG T^* are, in all aspects, quantitatively identical in both families [11].

In this Hg cuprate family, doping proceeds again from an increase in the O content in the Hg layer that is far from the CuO_2 plane so that the dopant-induced disorder should be weaker than in the 124 family. These experiments confirmed, therefore, that the PG is a robust phenomenon independent not only on the number of CuO_2 layers but also on the disorder induced by dopants or substitutions.

2.2 A 3D phase diagram

The Zn substitution experiments of Figure 1 indicate that the SC dome shrinks with increasing plane disorder. This was shown as well

using electron irradiation to increase progressively the in-plane defect content (see Section 3). These experiments have led us altogether to understand that the morphology of the PD evolves with the increase in disorder induced by the increase in the Zn content. We could then propose the 3D phase diagram of Figure 2, in which the third axis represents the increase in the Zn content [12]. Transport experiments given in detail in Section 3 allowed to follow the iso-n_h red lines plotted in Figure 2 that confirm the average displacement of the SC dome to the right in the PD while the SG range broadens and the PG T^* is unchanged.

We shall consider hereafter the various cuprate families and try to anticipate where their phase diagram could be located on such a 3D scheme. We discarded there the PD for homovalent substitutions of rare earths on the Y^{3+} sites in $YBCO_{6+x}$ as they do not significantly modify T_c and the PD. We did not consider either the peculiar case of Pr that was shown to display a 4+ valence that changes the oxygen content and hole doping for both AF and SC [13, 14]. For heterovalent substitutions, one can assume that the disorder due to the Coulomb interaction with the dopants decreases as their distance to the CuO_2 planes increases.

For all the single-layer or bilayer cuprate families, the PG T^* variation observed by various experimental techniques were found to match with those observed for YBCO. For those families that display $T_c \sim 90$ K at optimal doping, the dopants are located in the interlayers. So for these families, the mapping of the (T_c, n_h) SC domes usually assumed by parabolic fits might be acceptable. In Figure 2, their SC domes are located very near that of YBCO.

Let me point out that a weak dopant-induced disorder remains in those actual compounds, for which the optimum T_c value is approximately 90 K. The AF and SG domains for those families could not be probed except for YBCO as they could not be sufficiently underdoped experimentally. We cannot say, at this stage, whether in the absence of disorder, the T_c dome would reach $T_c = 0$ before the onset of the AF state. Would the clean phase diagram display a first-order transition from the AF to the SC state? In Figure 2, we introduced, therefore, the question mark near the 2D phase diagram for vanishing disorder.

The heterovalent substitutions in (LaSr)124 and (La-Bi) 2201 families occur on sites adjacent to the CuO_2 planes. We assumed that the disorder is large in these systems, and we consequently located their 2D PD along the "disorder" axis at points for which their SG ranges approximately match those for YBCO + Zn.

We also considered another PD for $Y_{1-y}Ca_yBCO_6$, in which the n_h doping proceeds from a partial substitution of Ca^{2+} on the Y^{3+} site inserted between the CuO_2 layers in the parent $YBCO_6$ [15]. We again found that the AF state disappears for a Ca content $y = 2n_h$ of about 7%. A SG range was disclosed for $0.03 < n_h < 0.09$, and a maximum T_c value of approximately 30 K is reached for $y = 0.25$ that unfortunately appears to be the Ca chemical solubility limit. Here, the large disorder induced by the substitution site between the CuO_2 planes again generates a PD that maps even quantitatively that of (LaSr)124 for $n_h < 0.15$. We did not plot it in Figure 2 to keep the figure clear.

In our proposed 3D PD, the quantitative definition of the disorder for a given family is, of course, rather rough. The disorder magnitude depends on the defect types and even evolves with doping inside many cuprate families. The data for a given family should be on a distorted surface in Figure 2 rather than on parallel flat planes.

The 3D representation, however, gives a reliable indication on the actual trend followed in the real materials. The systematic analysis conducted allows us to conclude that the disorder governs the morphology of the (T, n_h) phase diagram by opening the spin glass regime.

This 3D phase diagram even suggests that the disorder governs the optimal T_c value of the diverse cuprate families. In-plane disorder produced by Zn leads to a subsequent decrease in optimum T_c. The out-of-plane disorder also has an influence on T_c values, as illustrated for instance within the 124 family. Then, $T_c \sim 45$ K are obtained by electrochemical intercalation of excess oxygen [16] that induces less disorder than Sr^{2+} substitution on the La^{3+} sites.

From the above phase diagram analysis, we cannot, however, conclude whether the difference of optimal T_c is solely due to the existing disorder. Further data will allow us to discuss again that point later in Section 5.

Here, I did not discuss so far the interesting low T-phases detected well below T^* that have been thoroughly studied during the last decades. Soon, after the cuprate discovery, a stripe charge order has been highlighted in the 124 phase [17]. It is strongly pinned for Ba^{2+} substitution on the La^{3+} site and fully depresses the SC state for $x = 0.12$. For Sr^{2+} substitution, this stripe phase is less pinned and only seen as a small dip in the T_c (n_h) variation.

In YBCO, many unexpected phenomena were detected at low T in high-quality samples with $x \sim 0.6$, starting by quantum oscillations on the resistivity [18], corresponding to a small Fermi surface orbit and a negative Hall effect [19]. Then, NMR in a high applied field allowed to show a charge ordering below T_c = 60 K [20]. The latter could possibly be associated with the 2D CDW order detected for T as high as 150 K by RIXS experiments in zero field [21]. Extension of these measurements in high field [22] provide final evidence that the 2D CDW transforms below 60 K into the 3D CDW seen by NMR. The present understanding is that a reconstruction of the Fermi surface occurs below the SC dome, in a narrower dome-shaped region of the phase diagram [19] centered at about x = 0.6. This original coexistence of SC and CDW order parameters has been underlined and has justified extensive theoretical studies [23, 24].

Independently of the originality of this situation, I anticipated early on that these electronic orders occurred well below T^* and, therefore, could not be responsible for the pseudogap that is highly related to Mott physics [25]. Nowadays, an emerging consensus is that the cuprates can display diverse low T electronic orders in the PG regime [19]. These compete with SC and are somewhat distinct in the diverse cuprate families, as found in 124 and $YBCO_{6.6}$ families.

I have always suggested that the actual disorder or the order introduced by the hole dopants plays a great role in selecting the ground states [25]. The CDW dome in YBCO occurs for a hole doping nearby that for which a slight singularity occurs in the $T_c(x)$ variation, as shown in Figure 1. Structural studies have also shown that in this range of oxygen contents in YBCO, a Cu-O chain ordering occurs in the interlayer Cu plane [26]. I am, however, not aware of any careful experimental effort to search whether some

correlation holds between the oxygen structural order and the CDW. In any case, I still suggest that these competing charge orders are, therefore, not generic of the ideal CuO_2 plane conceived by theoreticians.

3 Point defects in the pseudogapped and strange metals

The *d*-wave superconductivity, PG, and strange metal with a *T* linear behavior of the resistivity for optimal doping are the actual generic physical properties of cuprates still requiring a thorough understanding. Experimentally, one still needs to gather all possible information on the cleanest materials, which, from the above analysis, should be among the families with the highest optimal T_c value.

The family of $YBCO_{6+x}$ appears to be a favorable case as the full range from the AF to the slightly overdoped regime is accessible without the occurrence of the intermediate SG phase. This indicates that disorder effects are minimal as we anticipated from NMR studies of the various nuclei of the unit cell [27].

For some specific oxygen content, the disorder might even be rather weak. The AF state for $x = 0$ is undoped with a half-filled Cu level in the CuO_2 planes and is not modified by a weak excess oxygen content. For $x = 1$, the unit cell is stoichiometric with filled ordered chains. It is situated in the slightly overdoped regime with $T_c = 92$ K, approximately 1 K below that at optimal doping. In the PG regime, we found out that sample reproducibility is extremely good with a large $T^* \sim 350$ K value for $x = 0.6$. This slightly exceeds the composition 0.5 with alternative full and empty chains, but one anticipates again that the excess Cu^{2+}-O^{2-}- Cu^{2+} chain segments do not contribute significantly to the charge transfer, hence the flat part of the $T_c(x)$ curve in the phase diagram in Figure 1. We have subsequently considered for years that these three oxygen contents were among the purest references for the AF, strange metal, and large PG metal phases of the cuprates. The highly overdoped regime has been mostly accessible in the Tl2201 family [28]. We concluded, therefore, for long, that one might then use these starting materials to introduce controlled defects and study in some detail their influence on the physical properties.

Why should we introduce defects? In classical physics, when we perfectly know the properties of a material, we might anticipate the influence of the defects introduced. For instance, if one drops a stone on a pond of a given liquid, one knows that a set of waves is created and propagates as circles on the surface. Their period and damping explains about the viscosity of the liquid of the pond. Similarly, introducing an impurity in a metal gives the Friedel charge density oscillations [29] or RKKY oscillations of spin density if the impurity is magnetic [30, 31]. If one considers now a poorly understood correlated electron compound, one may not anticipate the disturbance created. Then, the study of the response to the impurity is all the more important as it provides information on the properties of the pure material [2]. This is what we have been performing for years in cuprates. I shall summarize hereafter first in Section 3.1 the information on the magnetic properties gained mostly by NMR techniques using impurity substitutions. In Section 3.2, I shall present the influence on the transport properties of impurities and vacancies in the CuO_2 planes. The latter, obtained in a controlled manner by electronic irradiation of single crystals, allowed us to probe the properties of the distinct metallic regimes.

3.1 Magnetic properties induced by spinless impurities

In the 2D cuprates, the largest perturbations are induced, of course, by defects located in the CuO_2 planes. The substitution of Cu^{2+} by Zn^{2+} performed from the early days of HTSC introduces a spin vacancy without any charge defect. In the AF state of $YBCO_6$, these spinless defects only suppress spins on the AF lattice. This spin dilution effect is sufficient to explain the reduction of T_N with the increasing Zn content [32].

For a given Zn content, the introduction of oxygen on the intermediate Cu plane leads to the same hole doping, as for the pure material. Apart from the appearance of the SG phase, we could immediately detect an increase in the ^{89}Y NMR linewidth that increases with decreasing *T* down to T_c. Such broadening can only be associated with the appearance of local magnetic moments [9].

In that regime when the oxygen content is large enough, the spin glass temperature T_{SG} becomes negligible above $x = 0.6$, as shown in Figure 1. Spinless impurities never induce such paramagnetic local states in standard independent electron metals. SQUID measurements of the spin susceptibility allowed a determination of an upper limit of its magnitude [33]. An increase in the NMR experimental sensitivity enabled us then to reveal for x = 0.6 weak ^{89}Y NMR signals shifted from the main ^{89}Y NMR line, with a *T*-dependent NMR shift. We could attribute those "satellite" lines to ^{89}Y nuclei located near the Zn substitution site [34].

The characteristic pseudogap *T* dependence of the NMR shift has been found unmodified for sites at some distance from the Zn impurities, up to 4% Zn content. This suggests that the establishment of a robust PG behavior requires at most a sample size of about 25 unit cells. The Zn-induced paramagnetic moments appear then as a cloud of Cu sites around Zn with at most a similar spatial extent. They are characteristic of the correlated electronic nature of the PG regime.

In the slightly overdoped $YBCO_7$ samples, a weak broadening of the Y NMR line has been detected but no satellite could be resolved in this strange metal regime above T^* and T_c so that the magnitude and/or the spatial extent of the moments is weaker/smaller.

We then performed an important step in order to test the eventual influence of a charged defect. We used Li^+ substitution on the Cu^{2+} site of the CuO_2 planes and surprisingly discovered that the ^{89}Y NMR spectra were identical for 1% substitution of Li or Zn [35]. Both types of defects induced the same paramagnetism in their vicinity. The extra electron given by Li, therefore just fills a hole state in the bath band. This only slightly modifies the overall hole content for dilute Li substitution. This experimental result allowed us to show that the dominant defect in the CuO_2 plane is the spin vacancy associated with the substituent rather than its local charge.

As this was remarkable, we performed a similar comparison in another correlated electron system, Y_2BaNiO_5, in which Ni^{2+} is ordered in chains of $S = 1$ spins that constitute a prototype of the Haldane chain [2]. Here, the substitutions on the Ni site disrupt the

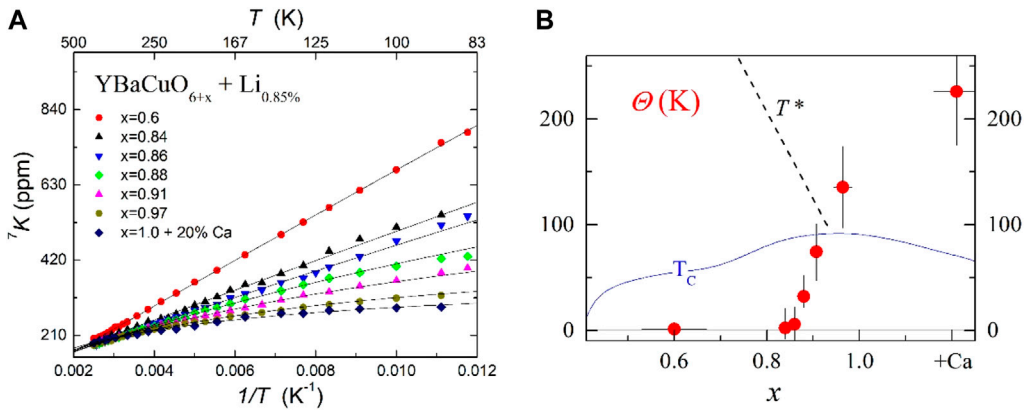

FIGURE 3
(A) ^{7}Li NMR shift ^{7}K plotted *versus* $1/T$ for increasing doping in $YBCO_{6+x}$, up to the overdoped regime with 20% Ca. The full lines are least square Curie Weiss fits. **(B)** Comparison of the Θ values deduced from the fits with the T_c and T^* data from Figure 1. From Ref. [35].

chains, a staggered paramagnetism occurs near the chain ends, and the ^{89}Y NMR then displays many satellite lines [36, 37]. These were identical for Zn, Cu, and Mg substitutions so that any disruption of the spin chain always induces the same staggered paramagnetism on the chain ends. The NMR data allowed a measure of the extension ξ_{imp} of this staggered perturbation. Its T dependence accurately fits the theoretically computed magnetic correlation length ξ for the pure chain.

Assuming a similar staggered local 2D paramagnetic cloud with an exponential correlation length for the cuprates, we have estimated that ξ_{imp} would increase from about two to five lattice constants in the PG range from T^* to T_c for $x = 0.6$ [38]. The intrinsic width of the ^{89}Y NMR forbids any accurate fit with such a model for the $x = 1$ strange metal, but ξ_{imp} would not exceed two lattice constants and would be roughly T-independent. Such a model-dependent determination is rough but establishes a qualitative difference between the PG and strange metal regimes. These $\xi_{imp}(T)$ would also agree with evaluations of the magnetic correlation length ξ determined from inelastic neutron scattering experiments in single crystals of pure YBCO [39, 40]. Therefore the staggered response detected around spinless impurities monitors the actual correlation length of pure cuprates, as found for the Haldane chain from both theory and experiments [2, 37].

We disclosed a further advantage of the Li substitution as the ^{7}Li NMR signal magnitude and intrinsic resolution are larger than those for ^{64}Zn. We could, therefore, detect its NMR shift ^{7}K for the Li content as small as 1%, regardless of the hole doping in the metallic range of $YBCO_{6+x}$. This NMR shift ^{7}K results from the transferred hyperfine coupling from the four Cu nearest neighbors of Li in the CuO_2 plane. These are the Cu sites exhibiting the largest paramagnetic response, in an exponentially staggered paramagnetic cloud model. We could measure accurately the T variation in ^{7}K for any hole doping [35]. As shown in Figure 3A, it can be fitted quite accurately with a Curie Weiss dependence $^{7}K\text{-}K_0 = C\ (T+\Theta)^{-1}$.

The effective moment given by C is found independent of hole doping within experimental accuracy. The Weiss temperature Θ shown in Figure 3B exhibits a large change from the PG to the strange metal regime. Although Θ is very small in the PG regime, it abruptly increases through the PG "critical" doping point.

We did notice that this T dependence of the local magnetic response is somewhat analogous to that known for Kondo magnetic impurities in classical Fermi liquid metals. The evolution with hole doping of the apparent Kondo temperature Θ is similar to that found when changing $3d$ impurities in pure copper metal, for which the Kondo temperature T_K changes from a few mK for Mn to 30 K for Fe [41].

Let me point out that all these data given in Figure 3A were taken above T_c and that for x = 0.6, they do not show any singularity at 150 K, the onset temperature of the 3D CDW detected by RIXS experiments [21]. The variation in Θ with hole doping of Figure 3B is obvious even from the data taken above 150 K so that the magnetic response is not influenced by this charge order, if present in our samples. This response to Li impurities is, therefore probing a specific property of the PG regime. Similar studies in other cuprate families have not been performed so far as an intrinsic disorder due to chemical doping complicates the experimental situation. More material research efforts on Li substitutions in favorable cases such as BiSCO2212 or Hg1201 would be required.

I believe that this paramagnetic response to spinless impurity substitutions characterizes an abrupt evolution of the metallic state from the PG to the strange metal regime in cuprates. It remains an important challenge for any theoretical interpretation of the correlated electronic properties of cuprate physics. ^{17}O NMR experiments show that this paramagnetic behavior persists in the superconducting state of the PG phase, while the Kondo-like screening is quite reduced in the SC state of the strange metal [42].

3.2 Influence of in-plane defects on the normal state transport

I shall consider hereafter the influence of impurities and vacancies in the CuO_2 plane on the transport properties in $YBCO_{6+x}$ single crystals.

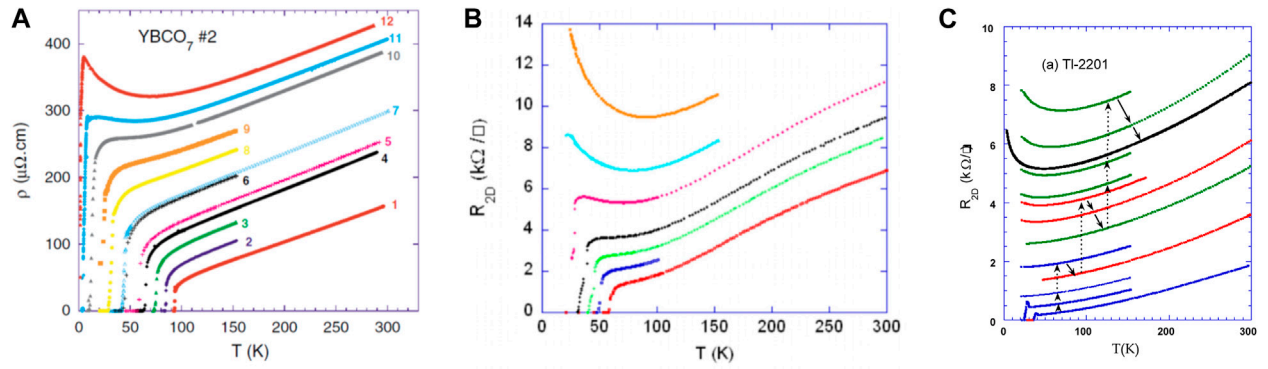

FIGURE 4
Planar resistivity data taken **(A)** on a virgin $YBCO_7$ (curve 1) and after steps of *in situ* electron irradiation at 20 K. The curves from 2 to 12 are data taken while cooling after annealing at 150 K or 300 K **(B)** on a $YBCO_{6.6}$ sample. The two upper data curves correspond to special heat treatments (see text) **(C)** on an overdoped sample of Tl2201 with T_c = 31 K. The arrows trace the thermal path followed during the experiment. The final black curve is a record after a long room *T* annealing. Figures respectively from Refs. [46, 47].

3.2.1 Experimental techniques

F. Rullier-Albenque had been using homogeneous irradiation with a highly energetic (2Mev) electron beam to produce defects in classical metallic superconductors [43]. She has extended her expertise to create vacancies in controlled content in thin cuprate crystal platelets. She checked first that the dominant defects acting on the planar transport are the vacancies produced in the CuO_2 planes by ejecting atoms out of these planes. A comparison with initial work conducted with Zn substitutions established that both resistivity and Hall effect are similarly modified in these two cases [44, 45].

I present in Figure 4 clear evidence for the important advantages of this electron irradiation technique. Herein, the resistivity curves $\rho(T)$ are taken on $YBCO_7$ [46], $YBCO_{6.6}$, and Tl2201 [47] samples, in which the damage created by electron irradiation is progressively increased. One notices immediately on these $\rho(T)$ data some important features that will be discussed in detail hereafter:

(1) The data are accurately parallel to each other at high *T*.
(2) Low *T* upturns appear with increasing damage. They suggest metal insulator crossovers (MICs).
(3) The SC transition can be suppressed by disorder down to $T_c = 0$.
(4) A downturn of $\rho(T)$ onsets above T_c at a temperature T'_c that signals the extension of the superconducting regime.

I shall analyze first, in detail, hereafter, points (1) and (2) related to the normal state properties. Experiments performed with large pulse field did allow us to suppress fully the superconducting fluctuations (SCFs) and follow the variation in the normal state resistivity below T_c. This also allowed us then to evaluate the contribution of the SCF to the conductivity, as described in Section 4.

The 12 $\rho(T)$ curves reported in Figure 4A had been measured *in situ* on a single $YBCO_7$ crystal within the cryostat where electron irradiation was performed at 20 K. After recording a first cooling curve, $\rho(T)$ was measured after each irradiation step. The defects created at 20 K are stable up to 150 K, and the resistivity curves are reversible, but heating to room *T* produces a partial annealing of some vacancies. The procedure was similar for the $YBCO_{6.6}$ sample of Figure 4B. Before recording the upper data curve, the sample was annealed at 400 K to achieve a clustering of the defects and a new irradiation was performed to fully suppress superconductivity. For the overdoped Tl2201 sample of Figure 4C, the last curve has been taken in a distinct cryostat after a long room *T* annealing.

As detailed in Section 4, high fields allow us to suppress the SC contributions (3) and (4) to the conductivity, once T_c has been highly reduced for a large enough defect content. We could then separate three contributions to the normal state resistivity:

$$\rho_n(T) = \rho_0 + \Delta\rho(T) + \rho_{pn}(T). \quad (1)$$

Here, $\rho_{pn}(T)$ is the normal state resistivity measured for the pure sample. Both the *T* independent increase of "residual" resistivity ρ_0 and the low *T* upturn $\Delta\rho(T)$ depend on the concentration of defects. The "Matthiessen-like" rule, especially the robustness of the high *T* variation in $\rho_n(T)$ with increasing defect content, is a totally unexpected observation.

3.2.2 Resistivity of the "pure" samples

In $YBCO_{6.6}$, the *S*-shaped contribution to $\rho_{pn}(T)$ is linked with the existence of the pseudogap, and application of fields as large as 60 T was not sufficient to suppress SC, except when T_c has been decreased by irradiation. The inflection point at high *T* has been found to occur approximately at $T^*/2$ and is seen to be independent of defect content. This confirms the independence of the PG on the disorder established by NMR for Zn substitution, as recalled in Figure 1, but also points out that the hole carrier content n_h in the CuO_2 planes is not modified by the irradiation damage, at least in the high *T* range.

This conclusion is therefore valid for the slightly overdoped $YBCO_7$ as well in as much as the *T* linear strange metal behavior is independent of disorder. Similarly, in the overdoped regime of Tl2201, the variation in $\rho_{pn}(T) = bT^p$ *with* $p \sim 1.5$ applies rather well, which supports an approach toward a Fermi liquid behavior.

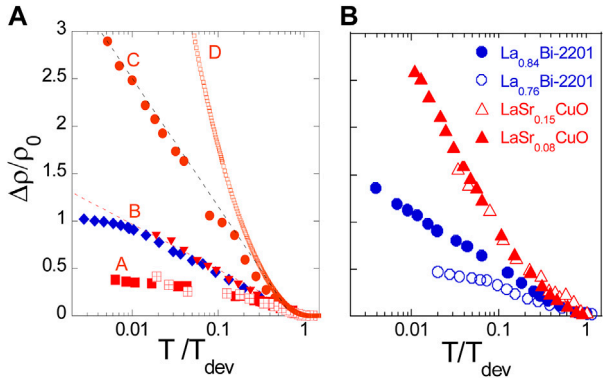

FIGURE 5
Low T upturn $\Delta\rho$ normalized by the increase in residual resistivity ρ_0 plotted *versus* T on a log scale. To permit quantitative comparisons, T is referred to T_{dev}, the onset T of $\Delta\rho$ whose values are between 100 and 150 K [12] **(A)** for $YBCO_{6.6}$ (red curves A to D) and $YBCO_7$ (blue diamonds). **(B)** Similarly analyzed data for (LaSr)124 and (LaBi) 2201 that are cuprates with low optimal T_c (see Ref. [12] and text).

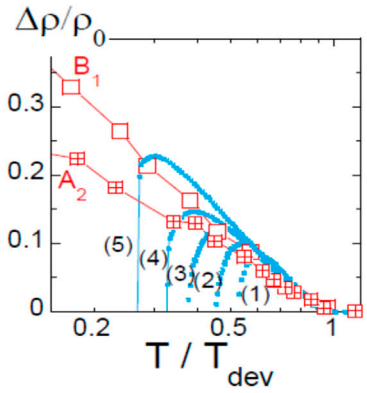

FIGURE 6
Detailed high T behavior of $\Delta\rho(T)/\rho_0$ of Figure 5A taken for moderate point defect content on three distinct $YBCO_{6.6}$ samples. The five small blue square curves involving the SC contribution are zero-field data taken *in situ* for the same sample with increasing vacancy content from (1) to (5). Those for samples B1 and A2 taken in 60T pulse field allowed to suppress the contribution of SCF to the conductivity (see text Section 4). From Ref. [12].

In all three cases, as will be shown in Section 4, a 60-T field is sufficient to suppress the SCF contributions to the conductivity but does not allow a direct determination of $\rho_{pn}(T)$ below T_c down to $T = 0$. In some cuprate families with low optimal T_c, the linearity with T apparently extends down to rather low T without an applied field. We found that linear fits of our high T data in our best pure $YBCO_7$ samples would imply a negative value of $\rho_{pn}(0)$. The T linear dependence of the strange metal behavior would, therefore, break down at low T. For the Tl2201, extending the bT^p fit at low T would be compatible with $\rho_{pn}(0) = 0$. On the contrary, for $YBCO_{6.6}$, one does get a residual resistivity of about $\rho_{pn}(0) = 1k\Omega/\square$. The symbol square should be introduced as for the vertical scale in Fig4B or 4C.

3.2.3 Metal insulator crossover (MIC)

We have taken data in large enough applied field to suppress the SCF contribution to the conductivity for many defect contents. After subtracting the measured or extrapolated $\rho_{pn}(T)$ values, we have determined the ρ_0 and $\Delta\rho(T)$ values defined in Equation 1. As ρ_0 was found to be a good measure of the defect content, the ratio $\Delta\rho(T)/\rho_0$ has been reported *versus* T, as shown in Figure 5A [12].

We have displayed there the analyzed data of Figure 4B for the $YBCO_{6.6}$ sample for limiting defect concentrations. For the lower defect contents A and B, a metallic behavior persists. When the SC state has been nearly completely suppressed (C and D), the data still suggest an insulating state. For the optimally doped $YBCO_7$ of Figure 4A, this procedure was not applicable [46] except after the final irradiation that lowered T_c to 1.9 K. In that case, a metallic behavior persists, as seen in Figure 5A (blue diamonds).

We have similarly analyzed some published data taken on low-T_c compounds (LaSr)124 [48, 49]and (LaBi)2201 [50]. Those presented in Figure 5B show that the resistivity upturns for these "pure" samples are quite similar to those found for YBCO after heavy electron irradiation. This analogy implies that a large disorder affects the physical properties even in the optimally doped (LaSr) 124 family [49], as anticipated from the phase diagrams in Section 2.

Let us further note that in Figure 5A, the "insulating" behavior in the PG regime occurs only for very high in-plane defect contents exceeding 5% per Cu. The disorder is then indeed at the origin of the apparent MIC. Contrary to conclusions taken from data on some low T_c cuprates [49], large applied fields do not induce the MIC. They only usefully suppress SC and reveal the underlying MIC associated with the specific intrinsic or extrinsic disorder.

3.2.4 Resistivity upturns for low defect content

We have shown that sizable resistivity upturns revealed by the applied field remain, however, for 1.6% defect content (curve A in Figure 5A). In that case, $\Delta\rho(T)$ onsets at T_{dev} of approximately 100 K and saturates at low T. An enlarged presentation of this low-defect content regime is displayed in Figure 6. Herein, we display data taken on a sample in zero field, for which the SC contributions cannot be corrected, so that only ρ_0 and $\rho_{pn}(T)$ have been subtracted (five blue square curves). They are shown together with data taken on two distinct samples in pulse fields that allowed us to suppress the SC contribution. One can see that the upturn of $\Delta\rho(T)/\rho_0$ is reproducible, weakly depends on the field used to suppress SC, increases initially as -log$T$ with decreasing T, and appears nearly independent of defect content. This trend toward single impurity scattering behavior resembles the initial observations performed in dilute Cu–Mn alloys that revealed the occurrence of Kondo effect in simple metallic states [51].

The ^{7}Li NMR experiments provide evidence for a paramagnetic response with a Curie Weiss Θ value that also resembles the case of Kondo effect for magnetic impurities in metals. These similar findings on the transport and magnetism give a strong weight to this analogy.

The absence of variation in T^* with defect content has led us to conclude that the doping n_h is not modified upon introduction of disorder. We might assume that n_h is T-independent as well. In a single carrier band model with $\rho_n(T) = m^*(n_h e^2\tau)^{-}$,[1] the T dependence would exclusively be due to the carrier's scattering rate. With this assumption, the experimental results imply that the data involve two contributions $\tau^{-1} = \tau_{el}^{-1} + \tau_{in}^{-1}$. The elastic rate τ_{el}^{-1} responsible for ρ_0 scales with the defect content. The inelastic

rate τ_{in}^{-1} would be the sum of the inelastic rate of the pure compound $\tau_{in,p}^{-1}$ and of the Kondo-like $\Delta\rho(T)$ contribution that also initially scales with the defect content.

One does expect changes in the latter contribution for a large defect content, due to the modification of their nanostructure. The interactions between impurities yield changes in scattering rates. Our estimate of a correlation length ξ_{imp} of five lattice constants at low T in $YBCO_{6.6}$ would indicate that a departure from the isolated defect regime should already occur for about 1% vacancy content.

Similarly, in $YBCO_7$, an upturn of $\rho(T)$ is only seen in Figure 4A for an estimated defect content of about 8%. Even if ξ_{imp} is about two lattice constants, one would expect strong interactions between the defects. The observed saturation at low T of $\Delta\rho(T)/\rho_0$ seen in Figure 5A has been found independent of applied field in the initial experiments of Ref. [12]. An analogy with the Kondo effect would suggest a Θ value much smaller than that of approximately 100 K found by ^{7}Li NMR in the strange metal regime for a low Li concentration. For Kondo alloys, such as CuFe, clusters of Fe impurities acquire a lower Kondo temperature than T_K = 30 K of isolated impurities [52]. The resistivity upturns for a high defect content in $YBCO_7$ would again appear quite similar to the situation encountered in CuFe alloys.

In Figure 4, the resistivity upturns are much larger in the YBCO samples than in the overdoped Tl2201 sample. A thorough analysis permitted us to show that weak localization induced by purely elastic scattering explains quantitatively the resistivity upturns in that case [47]. This is again a good indication that the electronic properties approach a Fermi liquid behavior for highly overdoped cuprates.

3.3 Conclusion on the normal state properties

We have been able to disclose the influence of dilute in-plane point defects in the three considered "clean" materials that allowed us to probe, respectively, the PG, strange metal, and Fermi liquid regimes. The Curie–Weiss magnetic perturbation induced by spinless defects and the low T saturation of the carriers scattering behave quite similarly with Kondo effect in classical Fermi liquids. The sharp increase in the Kondo-like temperature Θ through the pseudogap line is a striking generic feature of cuprates.

For large concentrations of defects, their mutual interactions might induce a MIC. We could enhance defect clustering and show the importance played by the defect morphology in driving the insulating state. The comparison with data taken on "pure" lower T_c compounds demonstrates that the dopant out-of-plane disorder induces similar upturns of the resistivity and an apparent MIC. This confirms our anticipations performed from simple comparisons of the phase diagrams in Section 2.

Can we reduce the disorder effects to study the metal insulator transition in the small doping part of the phase diagram? Within our study of in-plane defects, we have shown that this disorder is well-quantified by the residual resistivity ρ_0, but we do not know accurately the action of out-of-plane defects. The present results prove that those play an overwhelming role for low doping. The organization of the dopants certainly drives the stabilization of the family-specific low T-competing phases in the PG regime as well.

4 Influence of disorder on the superconducting state

From the 3D phase diagrams proposed in Section 2, we have noticed the existence of a correlation between the optimum T_c value and the morphology of the phase diagram for the various cuprate families. It is then important to analyze the evolution with an increasing disorder of the superconducting properties that are available in our data given in Figure 4. Such data could give indications on the actual origin of the pair condensed state, which is still poorly understood. In these 2D metallic compounds with low superfluid density, superconducting fluctuations are expected to persist above T_c. It has even been suggested that superconducting pair formation could occur at T^*, while T_c would be the onset of phase coherence between superconducting pairs. For me, this did not appear to be the case as our early experiments with Zn substitutions revealed that T^* is not affected by disorder.

I shall consider hereafter in Section 4.1, the evolution of T_c with controlled disorder that can be followed here until $T_c = 0$. In Section 4.2, I shall address the evolution of pairing strength through a study of the T-range of the superconducting fluctuations. This will allow me to discuss if there is any influence on the SC properties of the Kondo-like induced magnetism or of the resistivity upturns in the metallic PG regime.

4.1 Variation in T_c with in-plane disorder

Magnetic point defects usually induce pair breaking in classical superconductors. Here, $YBCO_7$ exhibits a strange metal behavior with nearly zero residual resistivity in its normal state. Electron irradiation allowed us a full suppression of superconductivity, although a metallic state persists. As displayed in Figure 7, we found that T_c scales linearly with the residual resistivity ρ_0 that scales

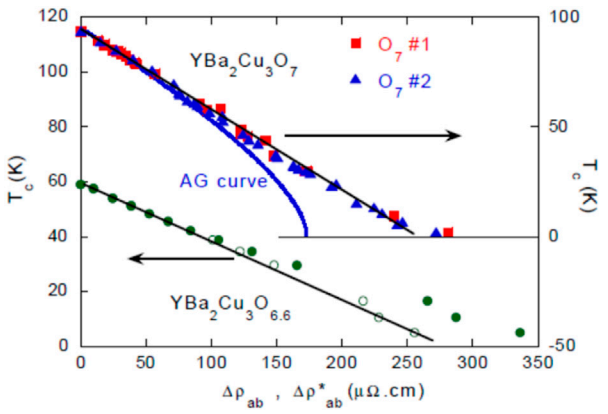

FIGURE 7
Variation in T_c with the excess residual resistivity ρ_0 induced by electron irradiation The upper curve is for $YBCO_7$. There, $\rho_0 = \Delta\rho_{ab}$ is a measure of the defect content n_d. For comparison, the full line reports the expected pure pair breaking (AG) theoretical dependence. The lower data curves for $YBCO_{6.6}$ are plotted for two distinct estimates of the defect resistivity $\Delta\rho_{ab}$ (full circles) and $\Delta\rho_{ab}$* (empty circles). From Ref. [46].

itself with n_d, the defect content [46]. Such a behavior disagrees qualitatively with the Abrikosov–Gorkov (AG) variation [53] expected for pair breaking that implies a sharp downturn of $T_c(n_d)$ before reaching $T_c = 0$.

We provided further evidence for the inadequacy of AG from the low magnitude of the $\Delta T_c/\rho_0$ slope and the observed variation in the width of the SC transition. The latter, being due to the inhomogeneous distribution of defects, remains narrow and does not broaden when approaching $T_c = 0$.

The quasi linear measured variation in T_c (ρ_0) is a somewhat unexpected result. One would hardly obtain it as accurately by other means, such as impurity substitutions. It surprisingly applies also for the underdoped $YBCO_{6.6}$ samples, as shown also in Figure 7, provided one takes for ρ_0, the high T-value of the extra resistivity.

Emery and Kivelson (EK) have proposed [54] that a peculiarity of the cuprates is their weak superconducting carrier density. They suggested that in such a case, phase fluctuations of the superconducting order parameter could be the source of T_c reduction. The phase coherent SC transition should then occur when the resistivity reaches a critical value [55].

In [46], we provided a detailed discussion indicating that such a correlation between T_c and $\rho(T_c)$ might be compatible with the quasi-linear variation. We were led, however, to conclude that the experimental situation probably requires taking *both pair breaking and phase fluctuations* into account. The influence of phase fluctuations should be more important for large defect contents and in the underdoped PG regime, but the existence of a single slope of $\Delta T_c/\rho_0$ at all defect contents appears awkward. I shall show hereafter that more information is available from quantitative studies of the magnitude of the SCF.

4.2 Superconducting fluctuations and disorder

Nernst effect [56], diamagnetism [57, 58], or paraconductivity [59, 60] measurements have been used to study the SCF above T_c. The main difficulty in such experiments resides in subtracting the normal state or spurious contributions from the data. Nernst effect data involve vortex motion contributions, while spurious paramagnetic phases can counterbalance the diamagnetic signal.

4.2.1 Paraconductivity experiments

We have rather preferred to use magnetoresistance (MR) measurements. As shown first in [59], it permits us to obtain the paraconductivity accurately. Using 60T pulse fields on an $YBCO_{6.6}$ sample, we demonstrated that the H^2 field dependence of the normal state MR known at high T extends at temperatures well below T_c.

Low-field departures from the H^2 dependence progressively appear for decreasing T, when SC fluctuations contribute to the low-field conductivity, as shown in Figures 8A, B respectively for a pure $YBCO_{6.95}$ and an irradiated $YBCO_{6.6}$ sample. Such departures appear below an onset temperature T'_c. At each T, the normal state H^2 variation is recovered at a field $H'_c(T)$ [60].

The increase in conductivity $\Delta\sigma(T)$ associated with the SCF in zero applied field is easily obtained from the decrease of $\rho(T)$ with respect to the extrapolated normal state behavior. Typical results for $\Delta\sigma(T)$ and $H'_c(T)$ are displayed, respectively, in Figures 9A,B for pure and irradiated YBCO samples. As shown there, both T'_c and H'_c decrease after reduction of T_c *by* electron irradiation. Although the critical field $H'_c(T)$ cannot be determined at low T for most samples, we could show that $H'_c(0)$ can be estimated using the "usual" variation

$$H'c(T) = H'c(0)\left[1 - (T/T'c)^2\right] \quad (2)$$

that fits the data for low-T'_c samples (see Figure 9B and Ref. [59]).

4.2.2 SCF range and disorder

The onset value T_ν of the SCF that we obtained on the same samples by Nernst effect [61] was smaller than T'_c deduced from the paraconductivity. The onset values obtained by a given technique are somewhat determined by the experimental sensitivity. Here, they would decrease by approximately 10–20 K for one order of magnitude decrease in the cutoff sensitivity. To the best of our knowledge, the T'_c values given here are among the highest reported

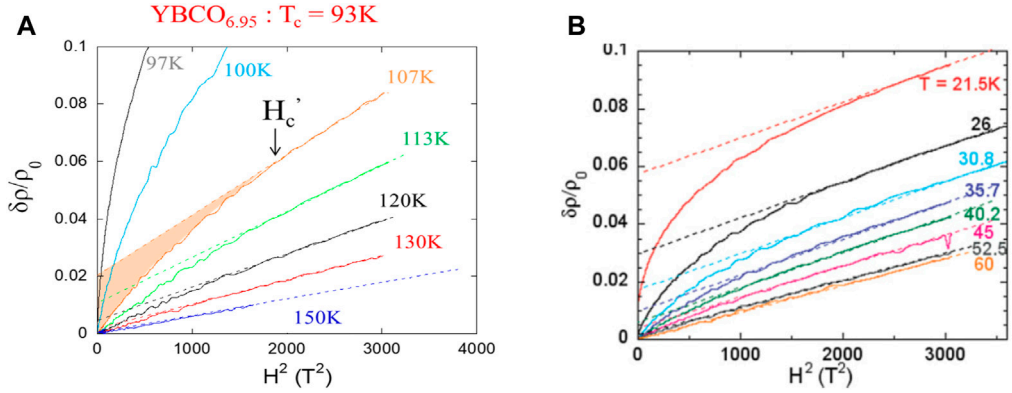

FIGURE 8
Plot of the magnetoresistance $[\rho(H)-\rho(0)]/\rho(0)$ *versus* H^2 at various temperatures **(A)** for pure $YBCO_{6.95}$. Here, the orange area indicates the SCF contribution to the conductivity. **(B)** Data taken on $YBCO_{6.6}$ after decreasing T_c to 5 K by electron irradiation. Here, the SCF appear below an onset of T'_c = 60 K and are suppressed at fields H'_c *(T)* that increase with decreasing T. From Ref. [60].

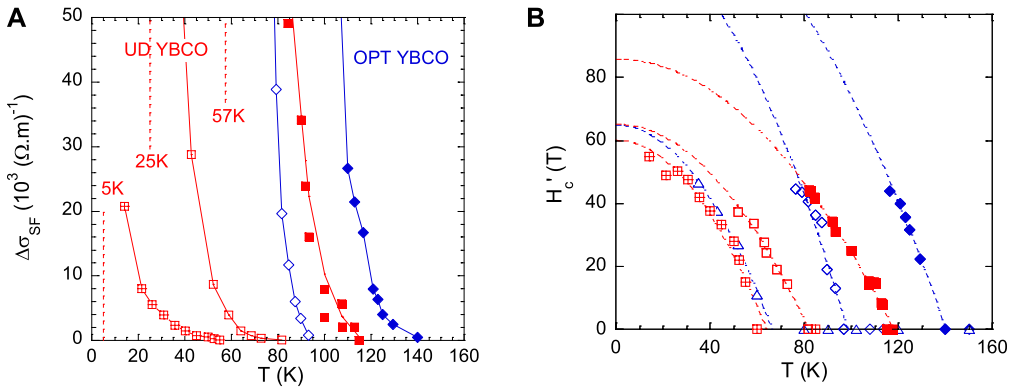

FIGURE 9
(A) Zero-field paraconductivity $\Delta\sigma(T)$ reported for pure and irradiated $YBCO_7$ and $YBCO_{6.6}$. It vanishes for distinct T'_c values. **(B)** $H'_c(T)$ data for the same samples. $H'_c(0)$ is estimated from the parabolic fits with Equation 2 shown as dotted lines. From Ref. [60].

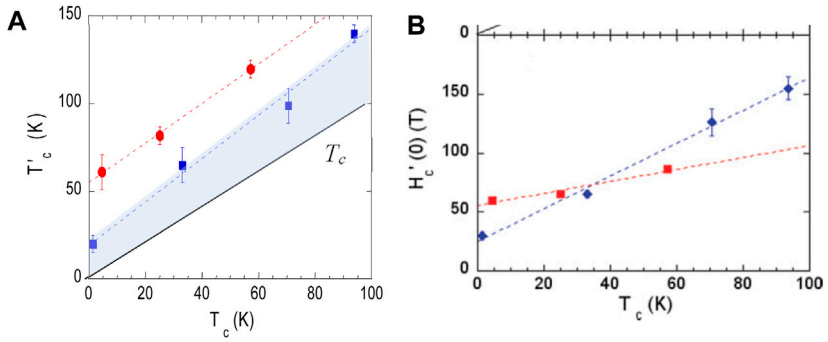

FIGURE 10
Variation with in-plane disorder of the SCF in the PG (red) and strange metal (blue) regimes. **(A)** Onset temperature T'_c plotted *versus* T_c. The blue range is the SCF range for the $YBCO_7$ sample. **(B)** Critical field value $H'_c(0)$ plotted *versus* T_c. It remains large for an increasing disorder for underdoped $YBCO_{6.6}$. From Ref. [60].

in YBCO. More importantly, our experimental approach benefits of a significant technical advantage. Using a single sample and identical criteria for all defect contents ensures the reliability in the T'_c data comparisons.

We report in Figure 10 the results for T'_c and $H'_c(0)$ *versus* T_c obtained from the data on Figure 9 for the $YBCO_{6.95}$ and $YBCO_{6.6}$ "pure" samples and after electron irradiation. One can easily notice that the SCF temperature range is quite similar for the different defect contents but does not scale with the actual T_c values. The ratio T'_c/T_c increases steadily with defect content so that the range of SCF increases markedly with respect to T_c in samples with in-plane disorder. In the underdoped PG regime, T'_c remains as large as 60 K for the $YBCO_{6.6}$ sample with T_c = 5 K, and a large ratio T'_c/T_c ~ 14 persists for the $YBCO_7$ sample in the strange metal regime for T_c = 1.5 K.

From these simple observations, it appears quite clearly that the increase of in-plane disorder does not reduce T'_c as much as T_c. The fact that SCF remain important even if T_c is highly depressed implies that superconducting pairs remain above T_c, while full 3D SC is not established. This suggests that phase fluctuations become more important in the presence of disorder, as suggested by EK in "bad metals" [55]. A full quantitative study of the magnitude of the SCF conductivity helps better clarify that point.

4.2.3 Amplitude and phase fluctuations in YBCO

In an applied field H, the SCF paraconductivity is obtained by subtracting the normal state conductivity $\Delta\sigma_{SF}(T,H) = \rho^{-1}(T,H) - \rho_n^{-1}(T,H)$. Assuming that YBCO samples were among the cleanest cuprates, we have studied the T and H dependences of $\Delta\sigma_{SF}$ in [60] for four samples from the PG to the slightly overdoped regime. We have analyzed first the zero field data reported in Figure 9A in the Ginzburg–Landau framework. The SCF is associated with pair braking in that approach, and the paraconductivity reflects the T dependence of the superconducting coherence length

$$\xi s(T) = \xi s(0)/\varepsilon^{1/2}, \quad (3)$$

with $\varepsilon = ln(T/T_c) \sim (T - T_c)/T_c$ for $T > T_c$. This 3D paraconductivity should diverge at T_c on a very small T-range inaccessible experimentally, which evolves for a 2D compound toward a 2D Aslamazov Larkin (AL) regime [62] for which

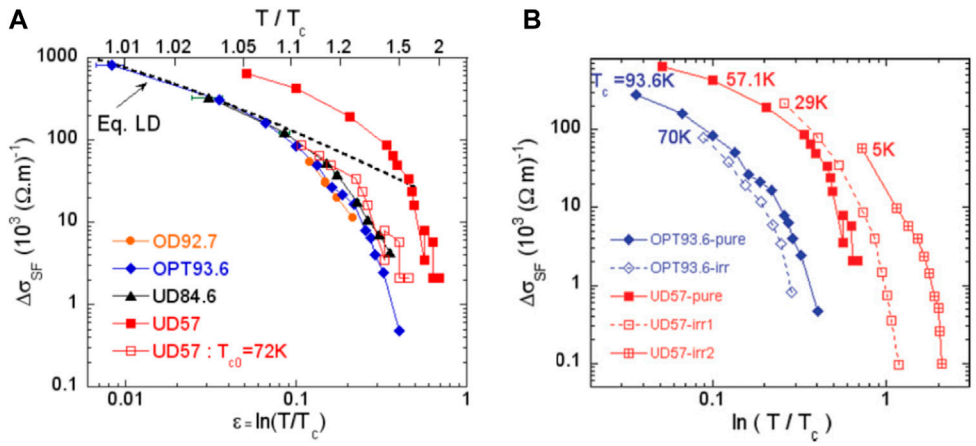

FIGURE 11
(A) Paraconductivity $\sigma_{SF}(T,0)$ is plotted *versus* $\varepsilon = ln(T/T_c)$ for the four "pure" YBCO samples with the indicated T_c values. The dashed line represents the expected variation for the LD Gaussian fluctuations assuming $\xi_c(0) = 0.9$ Å. For the underdoped sample UD57 with $T_c = 57$ K, the data are also plotted by replacing T_c by $T_{c0} = 72$ K (see text). **(B)** Similar plots for pure optimal (OPT) and underdoped (UD) samples and after electron irradiation that reduced T_c to 70 K for the OPT sample and to 29 and 5 K for the UD sample. From Ref. [60].

$$\sigma_{SF}(T,0) = e^2/(16\hbar s\varepsilon). \quad (4)$$

Here, s is the interlayer spacing. The AL expression has been extended by Laurence and Doniach (LD) [63] to include a c direction coherence length $\xi_c(0)$. One can see in Figure 11A that assuming $\xi_c(0) = 0.9$ Å, the LD/ AL analysis of Equation 4 applies for three of the YBCO samples in the range $0.01 < T/T_c < 1.1$. The T dependence of $\Delta\sigma_{SF}(T,0)$ for the $YBCO_{6.6}$ sample is shifted to the right in Figure 11A but coincides with the other if T_c is replaced by $T_{c0} = 72$ K. I point out here that in [59] the normal state resistivity displays a T dependence with a non-zero residual resistivity ρ_0 for that "pure" sample, as can be seen also in Figure 4B. Considering the linear relation between T_c and $\Delta\rho_{ab}$ of Figure 7, this ρ_0 value corresponds to a 10 K decrease of T_c so that a defect-free sample could indeed have a critical temperature $\sim T_{c0}$.

As underlined in [59], these data allowed us to point out that the existing uncontrolled disorder leads to an intermediate SCF regime between T_c and $\sim T_{c0}$. Phase fluctuations initially suppress T_c in that T range, while amplitude fluctuations of the superconducting order parameter take over beyond $\sim T_{c0}$.

The similar plots shown in Figure 11B for the underdoped UD irradiated samples provide evidence that systematic shifts to the right occur and increase with increasing defect content. Here, again, one could use values of $T_{c0} > T_c$ to obtain rough estimates of the increasing T range, for which phase fluctuations are dominant. For the optimally doped sample, the T variation in the SCF does follow the same pair breaking behavior, as for the pure sample even though T_c has been reduced from 93.6 K to 70 K.

These results indicate in the "pure" $YBCO_{6.6}$ sample the small T-range of phase fluctuation is presumably due to the residual native disorder. It broadens markedly with increasing in-plane defect content. The GL amplitude fluctuations only become dominant at high temperatures in this PG regime. A totally coherent conclusion has been drawn from a quantitative comparison of the Nernst effect and $\sigma_{SF}(T,0)$ data, as detailed in [60]. It fully supports a disorder-induced large phase fluctuations range in the PG regime and the applicability of Gaussian fluctuations for the strange metal regime even in the presence of disorder.

Let us consider now the case of the clean samples beyond the applicability of the LD amplitude fluctuations regime that applies up to 1.1 T_c in Figure 11A. Beyond that temperature, $\sigma_{SF}(T,0)$ decreases markedly and vanishes quite sharply at T'_c that might be assigned to a cutoff in the pairing. From Equation 2, the latter might be linked with a minimal superconducting coherence length, as discussed in [60].

We are still lacking a full theoretical approach, in which the influence of disorder on both phase and amplitude fluctuations would be treated on an equal footing. One can anticipate that the interplay between these two depends on the microscopic sources of superconductivity and disorder. However, the present qualitative experimental information implies that T'_c is a sharp temperature beyond which pair formation is energetically prohibited. T'_c appears, therefore, as one of the best determinations of the upper limit of the superconducting regime.

4.2.4 Magnetoconductance and superconducting gap

Another important thermodynamic entity that characterizes the superconducting state is the field $H'_c(T)$ beyond which the SCF is suppressed. The highest measurable value of H'_c is so far about 45T in the experimentally available 60T applied pulse fields. We have proposed that a natural extension down to $T = 0$ may apply using Equation 2 as usually done below T_c for the H_{c2} of classical 3D superconductors. This choice is supported by the data given in Figure 9B taken on an OD sample with T_c reduced to 5 K by electron irradiation, for which we obtained $H'_c(0) = 60$T.

In the LD Gaussian fluctuation analysis, one expects an independent determination of H_{c2} from the low field behavior of

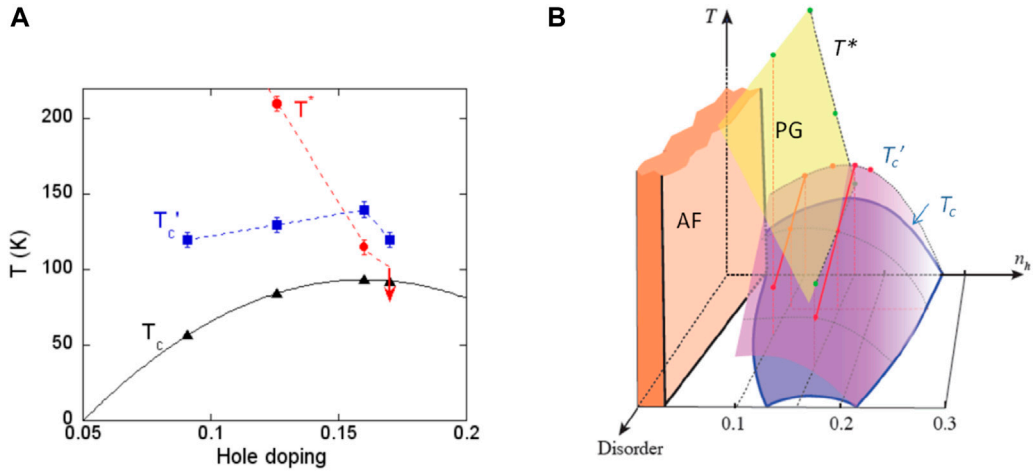

FIGURE 12
(A) Doping dependence of the 3D T_c, pseudogap T^*, and SCF onset T'_c for four "pure" YBCO samples and **(B)** 3D phase diagram displaying the evolution of these temperatures with the concentration of in-plane defects. The red lines are actual data for T'_c of underdoped and optimally doped YBCO. In the overdoped range, T_c are those for Tl2201 and the T'_c variations are anticipated by extrapolation of the optimally doped behavior (see text). From Ref. [60].

the magnetoconductance $\Delta\sigma_H(T,H)= \sigma_{SF}(T,H)- \sigma_{SF}(T,0)$. We have reported in [60] an analysis of such data that surprisingly establishes that $H_{c2}(0)$ and $H'_c(0)$ are identical within experimental accuracy for the four pure samples considered in [60].

For a large applied field, $\Delta\sigma_H(T,H)$ is also found to depart from the LD behavior and displays then a sharp $exp[-(H/H_0)^2]$ decay. This provides evidence that $H'_c(T)$ is a field beyond which pair formation is inhibited in analogy with the finding conducted for T'_c. This applies in the disordered cases, and the validity of this evaluation of $H'_c(0)$ is a confirmation of the reliability of the extrapolation of Equation 2.

The important conclusion drawn from this detailed analysis is that $H_{c2}(0)$ or equivalently $H'_c(0)$ increases with doping. $H_{c2}(0)$, being a measure of $\xi(0)^{-2}$, one finds that the superconducting gap Δ_{SC}, which scales with $\xi(0)^{-1}$, also increases with hole doping. From the $H'_c(0)$ data displayed in Figure 10B, the influence of disorder on the gap is found much smaller for the underdoped sample than for the optimally doped one. This appears in accordance with the corresponding data for T'_c on Figure 10A and with a dominance of phase fluctuations in the PG regime.

4.3 Disorder in the 3D YBCO phase diagram

Although we have clearly shown that the underdoped $YBCO_{6.6}$ sample is not a perfectly clean cuprate, we have still confirmed that the YBCO family is not far from being clean enough to yield important conclusions on the differences between the PG and strange metal regimes. The detailed investigation of the SCF conducted in [60] and reported here allowed us to determine reliably the temperature T'_c beyond which superconducting pairing is suppressed as the coherence length becomes presumably very small.

As seen in Figure 12A, T'_c only displays a small decrease below optimal doping but follows T_c and not the pseudogap T^*. We have also shown that the latter crosses the T'_c *versus* doping line (Figure 12A). This again confirms that the pseudogap is not a precursor to SC, as anticipated from the Zn experiments. The SC gap, as determined by H'_c from thermodynamic arguments, increases steadily with hole content up to optimal doping. This appears in line with the doping dependence of the small gap observed by some spectroscopic experiments in other cuprate families [64, 65].

Our studies of the SCF in the "pure" samples also allowed us to point out that in the PG regime of $YBCO_{6.6}$, the native disorder slightly reduces T_c that should be 10–15 K higher in a "cleaner" sample.

The detailed investigations with increasing controlled disorder allow us, by analogy with Figure 2, to propose the 3D phase diagram of Figure 12B specific to YBCO with in-plane disorder. Here, the disorder axis is better monitored than in Figure 2, using the concentration of defects introduced by electron irradiation or equivalently the increase of residual resistivity ρ_0, for instance at optimal doping. In this phase diagram, one should consider that T'_c is a better identifier of the 2D pairing than T_c that marks the 3D coherent superconducting state.

The analysis of the SCF conducted in [60] and shortly reviewed here has further allowed us to differentiate the influence of disorder on the SCF in the PG and strange metal regimes. In the latter, the disorder induces essentially a pair breaking so that T'_c, T_c, and H'_c decrease markedly altogether, as seen in Figure 10. In the PG regime of underdoped $YBCO_{6.6}$, a large T_c decrease is observed, while T'_c and H'_c are only moderately reduced. This indicates that pairing remains while a loss of phase coherence suppresses 3D superconductivity. The disorder induces in the PG phase a large SCF range that extends from the reduced T_c up to T'_c.

These conclusions about the phase diagram in the PG to strange metal regime are quite important as they result from experimental studies on the YBCO family that is a clean cuprate family, as discussed in Section 2. For lower hole content n_h<0.1, the 3D T_c decreases until the interplay between SC and AF occurs, as displayed in Figure 1. In that range, the doping n_h is, however, not easy to control as it depends on the formation in the intermediate Cu^+ layer

of Cu^{2+} - O^{2-} - Cu^{2+} segments that do not produce any charge transfer in the CuO_2 planes. The metal insulator transition could only be investigated with significant native out-of-plane disorder in $YBCO_{6+x}$ for x < 0.45 or in $YBCO_6$ with Ca^{2+} substitution on the Y^{3+} site. Unfortunately, the investigation of the overdoped range cannot be performed either in the YBCO family as it can only be reached by Ca^{2+} substitution that also introduces a sizable disorder. In Figure 12B, we have reported in that range a T_c variation analogous to that observed for Tl2201 and assumed that amplitude fluctuations remain dominant to anticipate the T'_c variation.

5 Discussion

I shall summarize first hereafter the various results concerning the phase diagram and underline the experimental questions that remain open. I shall analyze then the important information disclosed by using controlled defects as probes of the original properties of the distinct states of the phase diagram.

5.1 Phase diagrams and low T_c cuprates

We have conducted systematic investigations of the evolution of the cuprate phase diagrams with increasing controlled disorder in the CuO_2 planes. Our initial Zn substitution experiments demonstrated that the disorder opens a large spin glass regime, as displayed in the 3D phase diagram of Figure 2. The controlled increase in the vacancy content in single crystals allowed us then to show that SCF persist above T_c up to a temperature T'_c that decreases less than T_c with increasing disorder. The normal state residual resistivity ρ_0 increases markedly altogether and low T upturns appear mostly in the underdoped regime for large disorder.

All these features had been observed in the "pure" singular low-T_c cuprate families such as LSCO [48] or (LaBi)2201 [50]. Large residual resistivity ρ_0 was clearly apparent in the data for those cuprate families, for which the large fields applied to suppress T_c disclosed resistivity upturns even at optimum T_c [49]. Nernst effect data revealed a large range of SCF above T_c in the underdoped rPG regime as well [56]. In LSCO, THz conductivity experiments have also been performed to probe the SCF range [66]. The maximum range of 10–20 K is smaller than that found by Nernst effect all-over the SC dome. All these results confirm our initial guess that had led us to propose the 3D phase diagram of Figure 2 and to anticipate the presence of a large disorder that diminishes T_c in those specific cuprate families.

Comparing ρ_0 of these low-T_c compounds with those induced by electron irradiation in our YBCO samples even suggests that the linear relation, as shown in Figure 7, between T_c and ρ_0 might have an extended validity. Choosing then to use the ρ_0 value at optimal doping to fix the position of the PD of the diverse cuprate families on the disorder axis in Figure 2 would not modify it significantly [67]. In the phase fluctuation scenario, a relationship between T_c and $\rho(T_c)$ is indeed expected. This ensemble of arguments therefore leads me to conclude that the dopant disorder is mostly at the origin of the reduced T_c values in the cuprate families with anomalously low optimal T_c.

5.2 Toward disorder-free cuprates?

Once we have considered that we should put aside the low-T_c cuprates, the question raises as to whether we can decide what family better represents clean cuprates. For YBCO, Bi2212, Hg1201, and Tl2201 that display the highest $T_c \sim 90$ K, we noticed that the extrapolated ρ_0 is nearly zero at optimal doping [67]. These families are therefore nearly equivalent in that doping range. We could indeed initially establish the universality of the transition T^* between the PG and the strange metal regimes in YBCO and Hg1201 [11].

Our phase diagram of Figure 2 provides evidence that determination of the hole contents n_h by mapping the SC "domes" between different cuprate families is certainly incorrect, except for the higher T_c families. Unfortunately, it appears difficult to underdope the Tl2201 family that is the only "clean" cuprate, for which the overdoped to non-SC transition is accessible. As indicated in Section 4, we have not been able so far to perform a full study of the variation in the thermodynamic properties of the SC state through that transition.

$YBCO_{6+x}$ is similarly the only family on which the metal-to-insulator transition occurs without a spin glass intermediate regime. We have, however, seen here that for $x = 0.6$, native disorder effects already appear as T'_c remains large with respect to T_c. Low T upturns of the resistivity occur for oxygen contents $x < 0.4$ [12], but we do not know how the insulator state sets in. We do not have any reliable control on the influence of the oxygen disorder during this crossover. One cannot anticipate whether a first-order SC insulator transition would occur in a disorder-free cuprate, hence the question mark we have introduced in the 3D phase diagram in Figure 2.

So although huge progress has been performed since the discovery of the cuprates, we only have, at hand, a limited number of cuprates that allow us to explore independently some characteristic clean compositions in the phase diagram of Figure 2. We were not able to discover so far a batch that would play for the cuprates a similar role to that played by silicon single-crystal wafers for semiconductors.

I like to point out that the present critical concern is even more pertinent if one considers the actual disorder that occurs on the sample surfaces. The latter are investigated using novel techniques restricted to easily cleavable single crystals. ARPES [68] and STM [69] experiments allow to thoroughly study the doping dependence of the **k**-space surface band structures of Bi2212 crystals. One can beautifully see there the dopant disorder in the spatially resolved STM spectra [69] that have been helpful to correlate electronic structure with the local order. This unavoidable dopant disorder probably limits the energy resolution in ARPES spectra. The bulk and surface dopant disorder are not necessarily identical so that refined comparisons between bulk thermodynamic properties and surface energy spectra might be misleading. Local STM and NMR experiments have been achieved on Zn substituted cuprates. NMR could give information mostly on the bulk YBCO normal state properties, while STM permitted to probe the SC local states on the Bi2212 surface [70].

5.3 Point defects in the normal state

The change in the normal state transport properties has initially revealed the difference between the PG, strange metal, and quasi

Fermi liquid regimes in the "pure" cuprates. The introduction of point defects has allowed us to highlight those differences by providing clear evidence that the scattering of the carriers splits into two distinct contributions. *The contribution observed in the pure compound is totally unmodified by the defects introduced.* It adds to the specific scattering of the carriers by the dilute impurities. An unexpected difference with the situation encountered in classical metals is that in the latter case, the scatterings are associated with two different processes, an elastic scattering on the defects and an inelastic one mediated by phonon modes. In the cuprates, both processes deal with electronic states controlled by the correlated electronic properties of the pure compound.

This stems from the fact highlighted by the NMR experiments that the impurity substitutions or vacancies in the CuO_2 planes induce a modification in their vicinity, which has a significant spatial extension that varies with temperature and doping [38]. This is certainly unambiguous evidence that the cuprates are strongly correlated electron systems.

We gave evidence for low T upturns of the resistivity as well when introducing in-plane vacancies by electron irradiation. These correspond to scattering rates on the defects similar to those observed for Kondo magnetic impurities in classical metals. As recalled in Section 3, these upturns scale with defect content as long as their concentration is small enough to avoid overlaps between the clouds induced by the vacancies.

We have shown, both by NMR and transport, that a sharp modification of the defect state occurs when the hole doping of YBCO is switched from the PG to the strange metal regime. We assign that to a reduction of the paramagnetism similar to a large increase in the Kondo-like temperature. In the strange metal regime, the cloud size does not exceed two lattice constants and the resistivity upturns decrease, in agreement with an increased "Kondo" temperature. We assume that paramagnetism should disappear when reaching the pure Fermi liquid regime for large hole doping. This crossover still needs, however, to be carefully studied for instance on the Tl2201 cuprate family.

5.4 Disorder in the SC state

The data analysis of Section 4 reports an original study of the destruction of the 2D superconductivity by a controlled disorder. The GL or Lawrence–Doniach pair breaking approach explains rather well the 2D SCF up to 1.1 or 1.2 T_c in the pure or disordered YBCO near-optimal doping. This would apparently also hold for very clean underdoped samples.

In that PG regime, any disorder native or produced by electron irradiation, induces a large SCF range as compared to T_c that mostly originates from a loss of phase coherence [60]. [55] had proposed a major importance of phase fluctuations for SC with either a low superfluid density or a large resistivity at T_c. Our study indicates that the disorder is mainly responsible for the phase fluctuations in underdoped YBCO. I therefore suggest that the Kondo-like inelastic defect scattering of the hole carriers is the main player in the T_c reduction that occurs before the SC insulator transition.

One should notice finally that our study of the field dependence of the SCF gives a measure of $H'_c(0)$, the critical 2D magnetic field. Thermodynamic arguments allow us to connect it with $\Delta_{SC,}$ the SC gap magnitude. In clean YBCO, Δ_{SC} increases with doping up to the optimum T_c, and correspondingly, the coherence length $\xi(0)$ diminishes. One would expect to reach a cutoff value of $\xi(0)$ and then a decrease in the gap in the overdoped regime. One should still probe that experimentally in the Tl2201 family and altogether whether the transition at the endpoint of the SC dome is smeared out by disorder.

6 Conclusion

We have recalled here that the cuprates are correlated electron systems in which native disorder occurs naturally due to chemical doping. This disorder has introduced great difficulties in the understanding of the very phase diagram of the hypothetically clean cuprate plane. Immediately after the discovery of YBCO, we have highlighted that the pseudogap to strange metal transition is robust to disorder at high temperatures. We have given evidence that it is generic, which means identical for all hole doped cuprate families. A long time has been required although [25] to see that fact accepted by the community.

Wide attention has been devoted to the original and interesting ground states discovered, such as stripes in the 124 family and later on CDW in YBCO. This diversity of ground states in the cuprate families testifies the richness of the underlying physics of these correlated electron systems. Meanwhile, we have been performing with collaborators an extensive work on Na_xCoO_2 [71, 72] that demonstrated that the physical properties of the CoO_2 layers were highly influenced in these compounds by their interactions with the Na dopants. Although similar detailed investigations haves not been achieved so far in the cuprates, I got convinced that, there too, the order of the dopants may analogously play a great role in stabilizing the different ground states. The fact that these states compete with SC complicated our understanding of the variety of cuprate phase diagrams.

As recalled here, we proposed the 3D phase diagram of Figure 2 with some Orsay-Saclay colleagues. We suggested that the AF insulator, PG, strange metal, and Fermi liquid metallic regimes were the actual phases that characterize the high T part of the disorder free cuprate phase diagram. Among those, all the metallic states display a superconducting ground state except for large doping in the Fermi liquid range. On experimental grounds, the less understood part of the phase diagram is the transition from the metallic PG regime to the insulating state, presumably because even the weak native disorder has a strong influence there on the physical properties.

In my research group, we have always considered that the intentional introduction of controlled impurities or defects allowed us to disclose physical properties of the cleanest phases. The original "Kondo-like" magnetic and transport responses induced by spinless impurities are strong signs for a connection with Mott physics. The step change of its characteristic temperature Θ has been somewhat overlooked so far by the community, although it characterizes a generic part of the clean cuprate phase diagram.

This sharp transition at a doping p* recalled in Figure 3B is so abrupt that it is legitimate to wonder whether it marks a phase transition rather than a crossover. Although T^* is not modified by disorder, it could still correspond to a transition that would only be

slightly smeared by the weak native disorder always present in the cleanest compounds. The sharp drop of the T^* line *versus* n_h near-optimal doping with a quantum critical point could agree with such a possibility. Whether orbital currents [73, 74] appear at T^* remains an open question, and one should like to understand how such a collective state would induce a Kondo-like magnetic cloud around spinless defects. Any further experimental input on such a matter would certainly require extremely clean samples.

If I consider now the SC state, we have shown that the onset of 2D superconducting pair formation occurs rather sharply at a higher temperature T'_c than the 3D superconductivity at T_c. Most researchers considered that the $T_c(n_h)$ dome shape is universal for the cuprates, with differing T_c magnitudes. In contrast, we have shown that T'_c is always large, even in the anomalous cuprate families, for which the disorder (or order) imposes a low T_c value. As shown in Figure 12A, we have even demonstrated that one might hardly define a dome for the T'_c (n_h) variation for the cleanest cuprates.

This study of the influence of defects has, therefore, disclosed two apparently contradictory observations. The PG line marks a high T transition between different electronic states, while the low T pairing energy is nearly unaffected by the opening of the pseudogap, which does not therefore compete directly with SC. Our SCF experiments with controlled disorder allowed us to show that the main difference in the SC states appears to be the influence of in-plane defects. They induce pair breaking in the strange metal while they furthermore enhance phase fluctuations in the PG regime. As recalled previously, we do not know whether T'_c would decrease and vanish before reaching the SC to insulator transition in a "clean" cuprate.

It has been suggested [54] that the low carrier density and the associated low phase stiffness is a possible source of phase fluctuations and T_c reduction in cuprates. Our data rather imply that large impurity-induced carrier scattering rates are required to promote a bad metal behavior. This leads me to speculate that the distinct influences of disorder on SC could be due to the actual difference in the normal state Kondo-like response. This would qualitatively be consistent with the decrease in the 3D T_c on the left of the dome-like SC regime in the supposedly pure cuprate families.

I noticed more than 10 years ago [25] that the occurrence of the pseudogap and the SC states in the cuprates finds some theoretical justification in computations conducted by Cluster DMFT within the simple one-band Hubbard model [75]. Within the three-band Emery model [76], similar computations give analogous results and introduce realistic extra parameters, such as the charge transfer gap or the hole occupancies of the oxygen and copper orbitals. These are considered nowadays to try to justify the difference of optimum T_c between the diverse cuprate families [77]. Our work establishes that disorder is a dominant factor in this differentiation of the low T_c cuprates, while T_c only marginally differs for cleaner cuprate families with low residual resistivity. The actual influence of the planar structure is therefore less important on the optimal T_c than might be anticipated from the data. Given the numerical computations being conducted on clean models, it would appear quite interesting to see if the three-band parameters have any influence on the SC dome shape for the clean compounds. Such computations could help suggest a behavior for the SC–insulator transition that is at present obscured by disorder in the real materials.

As for the relation between the normal and SC state properties, I hope that the present experimental results will stimulate extensions of the thermodynamic developments taking into account random disorder, amplitude, and phase fluctuations on the same footing. This could permit hopefully to relate the normal state scattering properties with T'_c or T_c and to open a route toward an understanding of the microscopic origin of the pairing energy.

Author contributions

HA: writing–original draft and writing–review and editing.

Funding

The author declare that no financial support was received for the research, authorship, and/or publication of this article.

Acknowledgments

The author would like to acknowledge here his collaborators and students who have participated in the large set of experiments mentioned here. Florence Rullier-Albenque (FRA), from CEA (Saclay) has been responsible for most experimental work on transport properties and would have been a co-author on this article if she did not pass away too early in 2016. P. Mendels has been an efficient collaborator on the NMR experiments done during many years after the cuprate discovery, and J. Bobroff has done essential contributions for his PhD and well after with A. Mac Farlane and with his student S. Ouazi. Collaborations with G. Collin, J. F. Marucco (ICMO Orsay), N. Bamchard, D. Colson, and A. Forget (CEA Saclay) have been essential for all the preparation and characterization of the NMR and single-crystal samples. F. Balakirev initiated us to perform the first pulsed high-field transport measurements achieved at the NHMFL in Los Alamos. FRA and the author complemented them by many runs performed at the SNCI (Toulouse), with the help of B. Vignolles, D. Vignolles, and C. Proust. Over the years, the author has benefited of numerous exchanges on the experiments with K. Behnia, P. Bourges, and Y. Sidis and on theoretical matters with M. Civelli, M. Gabay, A. Georges, M. Héritier, P. Hirschfeld, C. Pépin, H. Schulz, G. Sordi, and A. M. Tremblay.

Conflict of interest

The author declares that the research was conducted in the absence of any commercial or financial relationships that could be construed as a potential conflict of interest.

Publisher's note

References

1. Lee PA, Nagaosa N, Wen X-G. Doping a Mott insulator: physics of high-temperature superconductivity. *Rev Mod Phys* (2006) 78:p17–85. doi:10.1103/revmodphys.78.17

2. Alloul H, Bobroff J, Gabay M, Hirschfeld P. Defects in correlated metals and superconductors. *Rev Mod Phys* (2009) 81:45–108. doi:10.1103/revmodphys.81.45

3. Bednorz JG, Müller KA. Possible high Tc superconductivity in the Ba-La-Cu-O system. *Condensed Matter* (1986) 64:p189–93. doi:10.1007/bf01303701

4. Shirane G, Birgeneau RJ. In: Ginsberg DM, editor. *Physical properties of high temperature superconductor*. Singapore: World Scientific (1989). p. p151.

5. Wu MK, Ashburn JR, Torng CJ, Hor PH, Meng RL, Gao L, et al. Superconductivity at 93 K in a new mixed-phase Y-Ba-Cu-O compound system at ambient pressure. *Phys Rev Lett* (1987) 58:p908–10. doi:10.1103/physrevlett.58.908

6. Alloul H, Bobroff J, Mac Farlane WA, Mendels P, Fullier-Albenque F. Impurities and defects as probes of the original magnetic properties of the cuprates. *J Phys Soc Jpn suppl B* (2000) 59:p114.

7. Rossat-Mignod J, Buffet P, Jurgens MJ, Vettier C, Regnault LP, Henry JY, et al. Antiferromagnetic order and phase diagram of Yba2Cu3O6+x. *J Phys (Paris)* (1988) C8: 2119.

8. Tallon JL, Obertelli SD, Cooper JR. Systematics in the thermoelectric power of high-T, oxides. *Phys Rev B* (1992) 46:14928–31. doi:10.1103/physrevb.46.14928

9. Alloul H, Mendels P, Casalta H, Marucco JF, Arabski J. Correlations between magnetic and superconducting properties of Zn substituted YBa2Cu3O6+x. *Phys Rev Lett* (1991) 67:3140–3. doi:10.1103/physrevlett.67.3140

10. Alloul H, Ohno T, Mendels P. 89Y NMR evidence for a fermi-liquid behavior in YBa2Cu3O6+x. *Phys Rev Lett* . (1959) 63:1700–3. doi:10.1103/PhysRevLett.63.1700

11. Bobroff J, Alloul H, Mendels P, Viallet V, Marucco J-F, Colson D. 17O NMR evidence for a pseudogap in the monolayer HgBa2CuO4+d. *Phys Rev Lett* (1997) 78: 3757–60. doi:10.1103/physrevlett.78.3757

12. Rullier-Albenque F, Alloul H, Balakirev F, Disorder CP. Disorder, metal-insulator crossover and phase diagram in high-T_c cuprates. *Europhysics Lett.ers.* (2008) 81:37008. doi:10.1209/0295-5075/81/37008

13. Maple MB, Lee BW, Neumeier JJ, Nieva G, Paulius LM, Seaman CL. Extraordinary behaviour of the Y_{1-x} Pr_x $Ba_2Cu_3O_{7-\delta}$ system. *J Alloys Compd* (1992) 181:135–52. doi:10.1016/0925-8388(92)90305-s

14. Mac Farlane WA, Bobroff J, Mendels P, Collin G, Marucco JF, Cyrot L, et al. Planar 17O NMR study of PryY1-yBa2Cu3O6+x. *Phys Rev B* (2002) 66:024508.

15. Casalta H, Alloul H, Marucco JF. Measurement of the Néel temperature of (Y1yCay)Ba2Cu3O6 versus Calcium content: evidence for the importance of charge dynamics in the destruction of TN. *Physica C* (1993) 204:331–40. doi:10.1016/0921-4534(93)91017-p

16. Johnston DC, Borsa F, Canfield PC, Cho JH, Chou FC, Miller LL, et al. In: Sigmund E, M¨uller KA, editors. *Phase separation in cuprate superconductors*. Heidelberg: Springer-Verlag (1994). p. p82.

17. Tranquada JM, Sternlieb BJ, Axe JD, Nakamura Y, Uchida S. Evidence for stripe correlations of spins and holes in copper oxide superconductors. *Nature* (1995) 375: 561–3. doi:10.1038/375561a0

18. Doiron-Leyraud N, Proust C, LeBoeuf D, Levallois J, Bonnemaison JB, Liang R, et al. Quantum oscillations and the Fermi surface in an underdoped high-Tc superconductor. *Nature* (2007) 447:565–8. doi:10.1038/nature05872

19. Proust C, Taillefer L. The remarkable underlying ground states of cuprate superconductors. *Annu Rev Condens Matter Phys* (2019) p10409.

20. Wu T, Maya H, Kramer S, Horvatic M, Berthier C, Hardy WN, et al. Magnetic-field-induced charge-stripe order in the high-temperature superconductor YBa2Cu3Oy. *Nature* (2011) 477:p191–4. doi:10.1038/nature10345

21. Blanco-Canosa S, Frano A, Schierle E, Porras J, Loew T, Minola M, et al. Resonant x-ray scattering study of charge-density wave correlations in YBa2Cu3O6+x. *Phys Rev B* (2014) 90:054513. doi:10.1103/physrevb.90.054513

22. Gerber S, Jang H, Nojiri H, Matsuzaw S, Yasumura H, Bonn DA, et al. Three-Dimensional charge density wave order in YBa2Cu3O6.67 at high magnetic fields. *Science* (2015) 350:949–52. doi:10.1126/science.aac6257

23. Meier H, Einenkel M, Pépin C, Efetov KB. Effect of magnetic field on the competition between superconductivity and charge order below the pseudogap state. *Phys.Rev B* (2013) 88:020506. doi:10.1103/physrevb.88.020506

24. Hayward LE, Hawthorn DG, Melko RG, Sachdev S Angular fluctuations of a multicomponent order describe the pseudogap of YBa_2 Cu_3 O_6 + *x*. *Science* (2014) 343: 1336–9. doi:10.1126/science.1246310

25. Alloul H. What is the simplest model which captures the basic experimental facts of the physics of underdoped cuprates? *C R Physique* (2014) 15:519–24. doi:10.1016/j.crhy.2014.02.007

26. Zimmermann Mv., Schneider JR, Frello T, Andersen NH, Madsen J, Ka¨ll M, et al. Oxygen-ordering superstructures in underdoped YBa2Cu3O 6¿x studied by hard x-ray diffraction. *Phys Rev B.* (2003) 68:104515. doi:10.1103/physrevb.68.104515

27. Bobroff J, Alloul H, Ouazi S, Mendels P, Mahajan A, Blanchard N, et al. Absence of static phase separation in the high Tc cuprate YBa2Cu3O6+x. *Phys Rev Lett* (2002) 89: 157002. doi:10.1103/physrevlett.89.157002

28. Kubo Y, Shimakawa Y, Manako T, Igarashi H. Transport and magnetic properties of TlzBa2Cu06+d showing a d -dependent gradual transition from an 85-K superconductor to a non superconducting metal. *Phys Rev B* (1991) 43:7875–82. doi:10.1103/physrevb.43.7875

29. Friedel J. On some electrical and magnetic properties of metallic solid solutions. *Can J Phys* (1956) 34:1190–211. doi:10.1139/p56-134

30. Yosida K. Magnetic properties of Cu-Mn alloys. *Phys Rev* (1957) 106:893–8. doi:10.1103/physrev.106.893

31. Alloul H. From Friedel oscillations and Kondo effect to the pseudogap in cuprates. *Jsupercond Nov Mag* (2012) 25:585–608. doi:10.1007/s10948-012-1472-x

32. Mendels P, Alloul H, Marucco JF, Arabski J, Collin G. Antiferromagnetism in YBa2Cu3O6+x: Ga and Zn substitutions II. zero field NMR of the Cu magnetic sites. *Physica C* (1990) 171:p429–37. doi:10.1016/0921-4534(90)90252-a

33. Mendels P, Bobroff J, Collin G, Alloul H, Gabay M, Marucco JF, et al. Normal-state magnetic properties of Ni and Zn substituted in $YBa_2Cu_3O_{6+x}$: hole-doping dependence. *Europhysics Lett* (1999) 46:678–84. doi:10.1209/epl/i1999-00319-x

34. Mahajan AV, Alloul H, Collin G, Marucco JF. 89Y NMR probe of Zn induced local moments in YBa2(Cu1-yZny)3O6+x. *Phys Rev Lett* (1994) 72:3100–3. doi:10.1103/PhysRevLett.72.3100

35. Bobroff J, Mac Farlane A, Alloul H, Mendels P, Blanchard N, Collin G, et al. Spinless impurities in high Tc cuprates: Kondo like behaviour. *Phys Rev Lett* (1999) 83: 4381–4. doi:10.1103/physrevlett.83.4381

36. Tedoldi F, Santachiara R, Horvatic M. Y89 NMR imaging of the staggered magnetization in the doped Haldane chain Y2BaNi1-xMgxO5. *Phys Rev Lett* (1999) 83: 412–5. doi:10.1103/physrevlett.83.412

37. Das J, Mahajan AV, Bobroff J, Alloul H, Alet F, Sorensen E. Comparison of S=0 and S=1/2 impurities in the Haldane chain compound Y2BaNiO5. *Phys Rev B* (2004) 69:144404. doi:10.1103/physrevb.69.144404

38. Ouazi S, Bobroff J, Alloul H, MacFarlane WA. Correlation length in cuprate superconductors deduced from impurity-induced magnetization. *Phys Rev B* (2004) 70: 104515. doi:10.1103/physrevb.70.104515

39. Balatsky AV, Bourges P. Linear dependence of peak width in $\chi(\bq, ω)$ vs T_c for YBCO superconductors. *Phys Rev Lett* (1999) 82:5337–40. doi:10.1103/physrevlett.82.5337

40. Sidis Y, Bourges P, Hennion B, Regnault LP, Villeneuve R, Collin G, et al. Zinc-induced modification of the dynamical magnetic susceptibility in the superconducting state of YBa2 Cu3 O61x as revealed by inelastic neutron scattering. *Phys Rev B* (1996) 53: p6811–8. doi:10.1103/physrevb.53.6811

41. Alloul H. Hyperfine studies of the static and dynamic susceptibilities of Kondo systems. *Physica* (1977) 86-88B:449–54. doi:10.1016/0378-4363(77)90382-5

42. Bobroff J, Alloul H, Mac Farlane WA, Mendels P, Blanchard N, Collin G, et al. Persistence of Li induced Kondo moments in the superconducting state of cuprates. *Phys Rev Lett* (2001) 86:4116–9. doi:10.1103/physrevlett.86.4116

43. Rullier-Albenque F, Quéré Y. An experimental argument — in Nb3Ge — for the Labbé-Barisic-Friedel theory of A-15 superconductors. *Phys Lett A* (1981) 81:232–4. doi:10.1016/0375-9601(81)90248-6

44. Legris A, Rullier-Albenque F, Radeva E, Lejay P. Effects of electron irradiation on YBa[Formula: see text]CU[Formula: see text]0[Formula: see text] superconductor. *J Phys (France)* (1993) 3:1605–15. doi:10.1051/jp1:1993203

45. Mizuhashi K, Takenaka K, Fukuzumi Y, Uchida S. Effect of Zn doping on charge transport in YBa2Cu307-d. *Phys Rev B* (1995) 52:R3884–7. doi:10.1103/physrevb.52.r3884

46. Rullier-Albenque F, Alloul H, Tourbot R. Influences of pair breaking and phase fluctuations in disordered high Tc cuprates. *Phys Rev Lett* (2003) 91:047001. doi:10.1103/physrevlett.91.047001

47. Rullier-Albenque F, Alloul H, Tourbot R. Disorder and transport in cuprates: weak localization and magnetic contributions. *Phys Rev Lett* (2001) 8:157001. doi:10.1103/physrevlett.87.157001

48. Ando Y, Boebinger GS, Passner A, Kimura T, Kishio K. Logarithmic divergence of both in-plane and out-of-plane normal-state resistivities of superconducting La2–xSrxCuO4 in the zero-temperature limit. *Phys Rev Lett* (1995) 75:4662–5. doi:10.1103/physrevlett.75.4662

49. Boebinger GS, Ando Y, Passner A, Kimura T, Okuya M, Shimoyama J, et al. Insulator-to-Metal crossover in the normal state of of La 22xSrxCuO4 near optimum doping. *Phys Rev Lett* (1996) 77:5417–20. doi:10.1103/physrevlett.77.5417

50. Ono S, Ando Y, Murayama T, Balakirev FF, Betts JB, Boebinger GS. Metal-to-Insulator crossover in the low-temperature normal state of Bi2Sr2−xLaxCuO6+δ. *Phys Rev Lett* (2000) 85:638–41. doi:10.1103/physrevlett.85.638

51. Daybell MD, Steyert WA. Localized magnetic impurity states in metals: some experimental relationships. *Rev Mod Phys* (1968) 40:380–9. doi:10.1103/revmodphys.40.380

52. Tholence JL, Tournier R. One-impurity and interaction effects on the Cu:Fe magnetization. *Phys.Rev.Letters* (1970) 25:867–71. doi:10.1103/physrevlett.25.867

53. Borkowski LS, Hirschfeld PJ. Distinguishing d-wave superconductors from highly anisotropic s-wave superconductors. *Phys Rev B* (1994) 49:15404–7. doi:10.1103/physrevb.49.15404

54. Emery VJ, Kivelson SA. Importance of phase fluctuations in superconductors with small superfluid density. *Nature (London)* (1995) 374:434–7. doi:10.1038/374434a0

55. Emery VJ, Kivelson SA. Superconductivity in bad metals. *Phys Rev Lett* (1995) 74: 3253–6. doi:10.1103/physrevlett.74.3253

56. Wang Y, Li L, Ong NP. Nernst effect in high-T c superconductors. *Phys Rev B* (2006) 73:024510. doi:10.1103/physrevb.73.024510

57. Wang Y, Lu L, Naughton MJ, Gu GD, Uchida S, Ong NP. Field-enhanced diamagnetism in the pseudogap state of the cuprate Bi2Sr2CaCu2O8+δ superconductor in an intense magnetic field. *Phys Rev Lett* (2005) 95:247002. doi:10.1103/physrevlett.95.247002

58. Li L, Wang Y, Komiya S, Ono S, Ando Y, Gu GD, et al. Diamagnetism and Cooper pairing above T c in cuprates. *Phys Rev B* (2010) 81:054510. doi:10.1103/physrevb.81.054510

59. Rullier-Albenque F, Alloul H, Proust C, Lejay P, Colson D, Forget A. Total suppression of superconductivity by high magnetic fields in YBa2Cu3O6.5. *Phys Rev Lett* (2007) 99:027003. doi:10.1103/physrevlett.99.027003

60. Rullier-Albenque F, Alloul H, Rikken G. High field studies of superconducting fluctuations in high-Tc cuprates: evidence for a small gap distinct from the large pseudogap. *Phys Rev B* (2011) 84:014522. doi:10.1103/physrevb.84.014522

61. Rullier-Albenque F, Tourbot R, Alloul H, Lejay P, Colson D, Forget A. Nernst effect and disorder in the normal state of high-Tc_cuprates. *Phys Rev Lett* (2006) 96: 067002. doi:10.1103/physrevlett.96.067002

62. Larkin A, Varlamov AA. *Theory of fluctuations in superconductors*. Oxford: Oxford University Press (2005).

63. Lawrence WE, Doniach S. In: Kanda E, editor. *Proceedings 12th international conference on low temperature physics, kyoto 1970*. Tokyo: Kaigaku (1971). p. 361.

64. Le Tacon M, Sacuto A, Georges A, Kottliar G, Gallais Y, Colson D, et al. Two energy scales and two distinct quasiparticle dynamics in the superconducting state of underdoped cuprates. *Nat Phys* (2006) 2:537–43. doi:10.1038/nphys362

65. Kondo T, Khasanov R, Takeuchi T, Schmalian J, Kaminski A. Competition between the pseudogap and superconductivity in the high-Tc copper oxides. *Nature (London)* (2009) 457:296–300. doi:10.1038/nature07644

66. Bilbro LS, Valdés Aguiolar R, Logvenov G, Pelleg O, Božovi´c I, Armitage NP. Temporal correlations of superconductivity above the transition temperature in La2-xSrxCuO4 probed by terahertz spectroscopy. *Nat Phys* (2011) 7:p302.

67. Rullier'Albenque F. *Unpublished private communication* (2024).

68. Damascelli A, Hussain Z, Shen ZX. Angle-resolved photoemission studies of the cuprate superconductors. *Rev Mod Phys* (2003) 75:473–541. doi:10.1103/revmodphys.75.473

69. Hoffman JE, McElroy K, Lee D-H, M Lang K, Eisaki H, Uchida S, et al. Imaging quasiparticle interference in $Bi_2Sr_2CaCu_2O_{8+\delta}$. *Science* (2002) 297:1148–51. doi:10.1126/science.1072640

70. Pan SE, Hudson EW, Lang KM, Eisaki H, Uchida S, Davis J. Imaging the effects of individual zinc impurity atoms on superconductivity in Bi2Sr2CaCu2O8+δ. *Nature (London)* (2000) 403:746–50. doi:10.1038/35001534

71. Alloul H, Mukhamedshin IR, Platova TA, Dooglav AV. Na ordering imprints a metallic kagomé lattice onto the Co planes of Na2/3CoO2. *Europhysics Lett* (2009) 85: 47006. doi:10.1209/0295-5075/85/47006

72. Gilmutdinov IF, Schonemann R, Vignolles D, Proust C, Mukhamedshin IR, Balicas L, et al. Interplay between strong correlations and electronic topology in the underlying kagome lattice of Na2/3CoO2. *Phys Rev B* (2021) 104:L201103. doi:10.1103/physrevb.104.l201103

73. Varma CM. Pseudogap phase and the quantum-critical point in copper-oxide metals. *Phys Rev Lett* (1999) 83:3538–41. doi:10.1103/physrevlett.83.3538

74. Bourges P, Sidis Y. Novel magnetic order in the pseudogap state of high-T c copper oxidessuperconductors. *Comptes Rendus Physique* (2011) 12:461–79. doi:10.1016/j.crhy.2011.04.006

75. Séùmon P, Haule K, Tremblay AMS. Strong coupling superconductivity, pseudogap, and Mott transition. *Phys Rev Lett* (2012) 108:216401. doi:10.1103/physrevlett.108.216401

76. Fratino L, S´emon P, Sordi G, Tremblay A-MS. Pseudogap and superconductivity in two-dimensional doped charge transfer insulators. *Phys Rev B.* (2016) 93:245147. doi:10.1103/physrevb.93.245147

77. Kowalski N, Dash SS, Sémon P, Sénéchal D, Tremblay AM. Oxygen hole content, charge-transfer gap, covalency, and cuprate superconductivity. *PNAS* (2021) 118: 2106476118. doi:10.1073/pnas.2106476118

Frontiers in Physics

Investigates complex questions in physics to understand the nature of the physical world

Addresses the biggest questions in physics, from macro to micro, and from theoretical to experimental and applied physics.

Discover the latest Research Topics

See more →

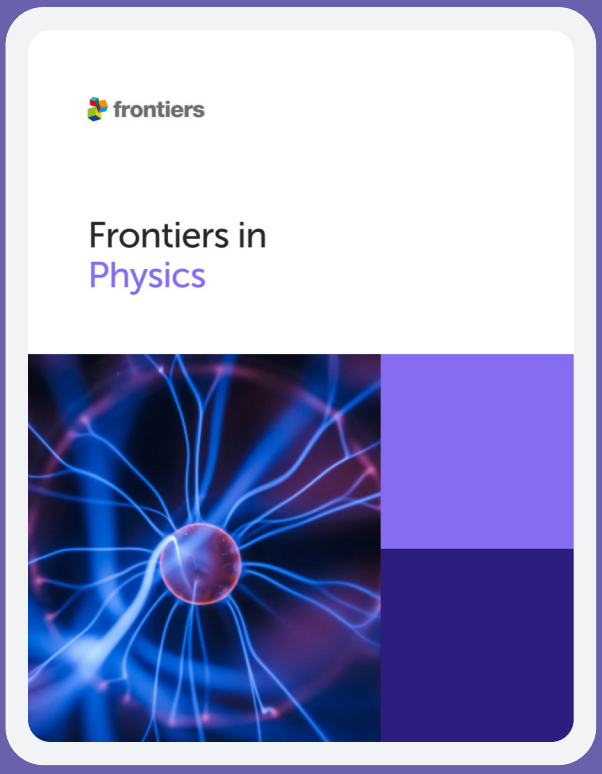

Frontiers

Avenue du Tribunal-Fédéral 34
1005 Lausanne, Switzerland
frontiersin.org

Contact us

+41 (0)21 510 17 00
frontiersin.org/about/contact